

**Framework for the Utilization of Forward and Inverse Airflow Models in
Systematic Sensor System Design for Indoor Air**

A Thesis

Submitted to the Faculty

of

Drexel University

by

Lisa (Yung Hua) Chen Ng

in partial fulfillment of the
requirements for the degree

of

Doctor of Philosophy

August 2010

VOLUME 1 of 2

UMI Number: 3430596

All rights reserved

INFORMATION TO ALL USERS

The quality of this reproduction is dependent upon the quality of the copy submitted.

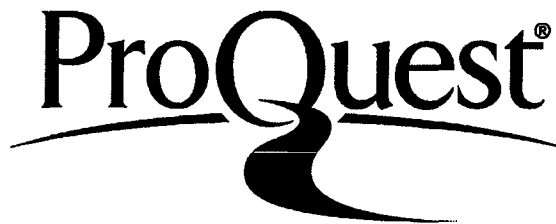
In the unlikely event that the author did not send a complete manuscript and there are missing pages, these will be noted. Also, if material had to be removed, a note will indicate the deletion.



UMI 3430596

Copyright 2010 by ProQuest LLC.

All rights reserved. This edition of the work is protected against unauthorized copying under Title 17, United States Code.



ProQuest LLC
789 East Eisenhower Parkway
P.O. Box 1346
Ann Arbor, MI 48106-1346



Office of Graduate Studies Dissertation/Thesis Approval Form

This form is for use by all doctoral and master's students with a dissertation/thesis requirement. Please print clearly as the library will bind a copy of this form with each copy of the dissertation/thesis. All doctoral dissertations must conform to university format requirements, which is the responsibility of the student and supervising professor. Students should obtain a copy of the Thesis Manual located on the library website.

Dissertation/Thesis Title: Framework for the Utilization of Forward
and Inverse Airflow Models in Systematic
Sensor System Design for Indoor Air

Author: Lisa (Yung Hua) Chen Ng

This dissertation/thesis is hereby accepted and approved.

Signatures:

Examining Committee

Chair

Jin Wen Jin Wen

Members

Michael Waring Michael Waring

Patrick Gurian Patrick Gurian

Charles W. Haas Charles W. Haas

Andrew Pensky Andrew Pensky

Academic Advisor

Jin Wen

Department Head

Charles W. Haas

© Copyright 2010

Lisa (Yung Hua) Chen Ng. All rights reserved.

TABLE OF CONTENTS

TABLE OF CONTENTS.....	iii
LIST OF TABLES	vii
LIST OF FIGURES	xi
ABSTRACT.....	xvi
1. CHAPTER 1: INTRODUCTION	1
1.1 Background	1
1.2 Framework for systematic indoor air sensor system design	2
1.3 Literature review	4
1.3.1 Airflow and contaminant transport simulation	4
1.3.2 Optimization	19
1.3.3 Sensor system design methods.....	20
1.3.4 Characterizing contaminant source.....	29
1.3.5 Building airflow network.....	34
1.4 Research needs and motivation.....	35
1.4.1 Framework for utilizing a forward airflow model	35
1.4.2 Framework for developing and utilizing an inverse airflow model.....	36
1.5 Research scope and hypotheses	39
2. CHAPTER 2: TESTING HYPOTHESIS #1 – SELECTING A FORWARD AIRFLOW MODEL	41
2.1 Preliminary studies.....	41
2.2 Chapter 2 outline.....	42
2.3 Zones simulated	42
2.3.1 Diffuser characteristics (location, <i>A</i>)	45
2.3.2 Furniture (<i>B</i> and <i>C</i>)	48

2.3.3	Airtightness (D)	50
2.4	Computer experiments	54
2.5	Model setup: multizone and zonal models.....	56
2.6	Model setup: CFD model.....	58
2.6.1	Zone $A[-]$	59
2.6.2	Zone $A[+]$	61
2.7	Contaminant releases	62
2.8	Designing indoor air sensor systems.....	63
2.8.1	Genetic algorithm (GA)	65
2.8.2	Design objectives (objective functions).....	66
2.9	Validation of sensor systems	69
2.10	Results and discussion	71
2.10.1	Zone $A[-]$	72
2.10.2	Zone $A[+]$	82
2.10.3	Effects of furniture and infiltration on sensor system design	93
2.10.4	Effects of test space characterization on sensor system design	95
2.11	Conclusions.....	97
2.12	Plans for publication	99
2.13	Future work.....	100
3.	CHAPTER 3: TESTING HYPOTHESIS #2 – DEVELOPING AND UTILIZING AN INVERSE AIRFLOW MODEL FOR SINGLE ZONE.....	103
3.1	Chapter 3 outline.....	103
3.2	Inverse models	104
3.2.1	Singular value decomposition (invSVD0 and invSVD1)	104
3.2.2	Inverse-multizone (invC).....	106

3.3	Zones simulated	106
3.4	Synthetic sensor data.....	108
3.4.1	Pre-selected velocity sensor locations	108
3.4.2	Optimized sensor locations	109
3.5	Results and discussion	112
3.5.1	Comparing inverse models	112
3.5.2	Best sensor locations (from pre-selected configurations).....	120
3.5.3	Best sensor locations (from optimization)	124
3.5.4	Using synthetic temperature data.....	129
3.5.5	Limitations of invSVD model.....	129
3.6	Conclusions.....	130
3.7	Future work.....	132
3.8	Plans for publication	133
4.	CHAPTER 4: TESTING HYPOTHESIS #3 – DEVELOPING AND UTILIZING INVERSE MODEL FOR WHOLE BUILDING.....	134
4.1	Current methods and limitations for determining a building airflow network .	134
4.2	Framework for developing a building airflow network inverse model	137
4.3	Chapter 4 outline.....	140
4.4	Proposed building airflow network inverse model	141
4.4.1	Deterministic inverse model	141
4.4.2	Stochastic inverse model.....	144
4.4.3	Additional relationships	146
4.4.4	Summary of equations	147
4.4.5	Solving the mathematical models (parameter estimation).....	148
4.4.6	Solution condition.....	151

4.4.7	Uncertainty in building airflow network inverse model	152
4.5	Study methods.....	153
4.5.1	Sensor models	155
4.5.2	Reporting uncertainty.....	155
4.5.3	Reporting building airflow network inverse model performance.....	157
4.6	Test cases	159
4.6.1	Test case 1 – steady-state system.....	160
4.6.2	Test case 2 – transient system.....	172
4.7	Conclusions.....	190
4.8	Future work.....	191
4.8.1	Validation.....	194
4.9	Plans for publication	195
5.	CONCLUSIONS AND RECOMMENDATIONS	196
6.	LONG TERM RESEARCH GOALS AND ENGINEERING IMPACT	198
7.	LIST OF REFERENCES	199
APPENDIX A	Preliminary sensor system studies	208
APPENDIX B	Sensor system design results for Test Cases in Chapter 2	228
APPENDIX C	Published portions of Chapter 3 (in Proceedings of Indoor Air 2008 and ANCRiSST).....	294
APPENDIX D	Detailed RSS values for airflow estimates in Chapter 3	313
APPENDIX E	Matlab codes for Chapter 4.....	315
APPENDIX F	Detailed reports of building airflow network estimates for transient test case for Chapter 4	320
APPENDIX G	Published portions of Chapter 4 (in proceedings of <i>1st International High Performance Buildings Conference</i>)	328
VITA	337

LIST OF TABLES

Table 2-1. Air leakage values for one-story U.S. houses.....	51
Table 2-2. Summary of zones characteristics varied in this research.	54
Table 2-3. Summary of test cases and responses using multizone model.	55
Table 2-4. Sensor system designs for Test Case 1 using multizone model data.	75
Table 2-5. Sensor system designs for Test Case 1 using zonal model data.	75
Table 2-6. Sensor system designs for Test Case 7 using multizone model data.	80
Table 2-7. Sensor system designs for Test Case 7 using zonal model data.	80
Table 2-8. Summary of 1-sensor systems designed to minimize detection time using data from three airflow models for Zone $A[-]$	84
Table 2-9. Sensor system designs for Test Case 9 using multizone model data.	86
Table 2-10. Sensor system designs for Test Case 9 using zonal model data.	86
Table 2-11. Sensor system designs for Test Case 15 using multizone model data.	91
Table 2-12. Sensor system designs for Test Case 15 using zonal model data.	91
Table 2-13. Sensor design designs for Test Case 16 using multizone model data.	92
Table 2-14. Sensor design designs for Test Case 16 using zonal model data.	92
Table 2-15. Summary of 1-sensor systems designed using three airflow models for Zone $A[+]$	93
Table 2-16. Mean age of air for test cases in Chapter 2	96
Table 3-1. Summary of bins used in evaluation of estimation accuracy of airflow results.	111
Table 3-2. Summary of skewness of error distributions resulting from use of invSVD0, invSVD1, and invC models to inversely estimate airflow for Zone A.	113
Table 3-3. Summary of skewness of error distributions resulting from use of invSVD0, invSVD1, and invC models to inversely estimate airflow for Zone B.	116
Table 3-4. Summary of skewness of error distributions resulting from use of invSVD0, invSVD1, and invC models to inversely estimate airflow for Zone C.	118

Table 3-5. Mean age of air for test cases in Chapter 3	127
Table 4-1. Number of occupants modeled in CONTAM for 3-zone synthetic test building (training data).....	164
Table 4-2. Steady-state CO ₂ concentrations (ppm) simulated by CONTAM for 3-zone synthetic test building (training data).	164
Table 4-3. Rank of CO ₂ training data datasets (steady-state).	164
Table 4-4. Testing data for 3-zone synthetic test building.....	166
Table 4-5. Estimated building airflow network using synthetic perfect CO ₂ measurements (steady-state, LSQ model).	166
Table 4-6. Estimated building airflow network using 1,000 sets of synthetic imperfect CO ₂ measurements with precision error (steady-state, LSQ model).	168
Table 4-7. Estimated building airflow network using 1,000 sets of synthetic imperfect CO ₂ measurements with precision error and bias (steady-state, LSQ model).....	168
Table 4-8. Summary of uncertainty and performance of building airflow network inverse model (steady-state, LSQ).	170
Table 4-9. Summary of error in infiltration rates.....	171
Table 4-10. Rank of CO ₂ training data datasets (transient).	176
Table 4-11. Summary of error in infiltration rates (LSQ, transient).....	187
Table 4-12. Summary of error in infiltration rates (NONLINOPTIM, transient).	187
Table 4-13. Summary of error in infiltration rates (SDE, transient).....	187
Table B-1. Sensor system designs for Test Case 2 using multizone model data.....	286
Table B-2. Sensor system designs for Test Case 2 using zonal model data.	286
Table B-3. Sensor system designs for Test Case 5 using multizone model data.....	287
Table B-4. Sensor system designs for Test Case 5 using zonal model data.	287
Table B-5. Sensor system designs for Test Case 6 using multizone model data.....	287
Table B-6. Sensor system designs for Test Case 6 using zonal model data.	288
Table B-7. Sensor system designs for Test Case 8 using multizone model data.....	289
Table B-8. Sensor system designs for Test Case 8 using zonal model data.	289

Table B-9. Sensor system designs for Test Case 10 using multizone model data.....	291
Table B-10. Sensor system designs for Test Case 10 using zonal model data.	291
Table B-11. Sensor system designs for Test Case 13 using multizone model data.....	292
Table B-12. Sensor system designs for Test Case 13 using zonal model data.	292
Table B-13. Sensor system designs for Test Case 14 using multizone model data.....	293
Table B-14. Sensor system designs for Test Case 14 using zonal model data.	293
Table D-1. Summary of RSS values from use of invSVD0, invSVD1, and invC models to inversely estimate airflow for Zone A	313
Table D-2. Summary of RSS values from use of invSVD0, invSVD1, and invC models to inversely estimate airflow for Zone B	314
Table D-3. Summary of RSS values from use of invSVD0, invSVD1, and invC models to inversely estimate airflow for Zone C	314
Table F-1. Estimated building airflow network using synthetic perfect CO ₂ measurements (transient, LSQ model).....	320
Table F-2. Estimated building airflow network using 1,000 sets of synthetic imperfect CO ₂ measurements with precision error only (transient, LSQ model).	321
Table F-3. Estimated building airflow network using 1 set of synthetic imperfect CO ₂ measurements with precision error only (transient, LSQ model).	321
Table F-4. Estimated building airflow network using 1,000 sets of synthetic imperfect CO ₂ measurements with precision error & bias (transient, LSQ model).....	322
Table F-5. Estimated building airflow network using 1 set of synthetic imperfect CO ₂ measurements with precision error & bias (transient, LSQ model).....	322
Table F-6. Estimated building airflow network using synthetic perfect CO ₂ measurements (transient, NONLINOPTIM model).	323
Table F-7. Estimated building airflow network using 1,000 sets of synthetic imperfect CO ₂ measurements with precision error only (transient, NONLINOPTIM model).	323
Table F-8. Estimated building airflow network using 1 set of synthetic imperfect CO ₂ measurements with precision error only (transient, NONLINOPTIM model).	324
Table F-9. Estimated building airflow network using 1,000 sets of synthetic imperfect CO ₂ measurements with precision error & bias (transient, NONLINOPTIM model).	324

Table F-10. Estimated building airflow network using 1 set of synthetic imperfect CO ₂ measurements with precision error & bias (transient, NONLINOPTIM model).	325
Table F-11. Estimated building airflow network using synthetic perfect CO ₂ measurements (transient, SDE model).....	325
Table F-12. Estimated building airflow network using synthetic imperfect CO ₂ measurements with precision error only (transient, 1,000 iterations of SDE model).	326
Table F-13. Estimated building airflow network using synthetic imperfect CO ₂ measurements with precision error only (transient, 1 iteration of SDE model). .	326
Table F-14. Estimated building airflow network using synthetic imperfect CO ₂ measurements with precision error & bias (transient, 1,000 iterations of SDE model).	327
Table F-15. Estimated building airflow network using synthetic imperfect CO ₂ measurements with precision error & bias (transient, 1 iteration of SDE model).	327

LIST OF FIGURES

Figure 1-1. Framework for systematic indoor air sensor system design and outline for this research.	4
Figure 2-1. Diagram of actual diffusers.	47
Figure 2-2. Two diffuser/exhaust layouts for simulated zone.	48
Figure 2-3. Example of how furniture was modeled in multizone and zonal models.	49
Figure 2-4. CFD models of air leakage paths in simulated zones with two diffuser/exhaust layouts.	53
Figure 2-5. Alternative CFD models of air leakage paths (not used in this research).	53
Figure 2-6. Subdivision of Zones (a) $A[-]$ and (b) $A[+]$ (not to scale).	58
Figure 2-7. Velocity profile across middle of Zone $A[-]$ (uniform meshes).	60
Figure 2-8. Velocity profile across middle of Zone $A[+]$ (uniform meshes).	62
Figure 2-9. Locations of contaminant releases (underlined) and occupant exposures (italics).	63
Figure 2-10. Flow chart of sensor system design.	64
Figure 2-11. Genetic algorithm flow chart [90].	66
Figure 2-12. Connection between terminologies in research and airflow models.	70
Figure 2-13. Contaminant contour plots for Test Case 1, Release #3.	77
Figure 2-14. Contaminant contour plots for Test Case 7, Release #1.	83
Figure 2-15. 1-sensor systems designed to minimize detection time using data from three airflow models for Zone $A[-]$	84
Figure 2-16. Contaminant contour plots from CFD model at $t = 1.0$ min sec for Release #1.	88
Figure 2-17. 1-sensor system designed using three airflow models for minimizing detection time for Zone $A[+]$	93
Figure 2-18. Flow chart of computer experimental process.	102
Figure 3-1. Simulated Zones A, B, and C.	107

Figure 3-2. Pole configurations where synthetic velocity data were taken.	109
Figure 3-3. Using genetic algorithm to optimize the quantity and location of velocity data.	111
Figure 3-4. Error distribution plots for Pole Config. #8 and 11 and for invSVD1 and invC models (Zone A).	114
Figure 3-5. Error distribution plots for Pole Config. # 12 and 14 and for invSVD1 and invC models (Zone B).....	117
Figure 3-6. Error distribution plots for Pole Config. 9 for invSVD1 and invC models (Zone C).	119
Figure 3-7. Flow pattern through diffuser in Zone A for invSVD1, Pole Config. #1 and 5, and for the CFD results.	123
Figure 3-8. Flow pattern through diffuser in Zone B for invSVD1, Pole Config. #1 and 4, and for the CFD results.	123
Figure 3-9. Flow pattern through diffuser in Zone C for invSVD1, Pole Config. #1 and 4, and for the CFD results.	124
Figure 3-10. Skewness values for Trials 1 and 2 with various numbers of sensors in Zone A.....	127
Figure 4-1. Example of blower-door test results.	135
Figure 4-2. Framework for developing building airflow network inverse model.	138
Figure 4-3. Flow diagram of study process.	154
Figure 4-4. Example of synthetic perfect and imperfect CO ₂ measurements.....	156
Figure 4-5. CONTAM model of synthetic 3-zone test building.....	162
Figure 4-6. Building airflow network to be estimated for synthetic 3-zone test building.	163
Figure 4-7. Parameter values for known airflow rates over time (RLS model).	174
Figure 4-8. (a) Occupancy and (b) simulated CO ₂ concentrations in each simulated physical zone for 3-zone test building (training data).	176
Figure 4-9. Example of testing data in Zone B.....	177
Figure 4-10. Comparing <i>mean error in Q</i> for three transient inverse models.	180

Figure 4-11. Comparing $RSME$ in C and R^2 values for three transient inverse models (training data).....	183
Figure 4-12. Comparing $RSME$ in C and R^2 values for three transient inverse models (testing data).....	185
Figure B-1. Contaminant contour plots for Test Case 1, Release #1.....	229
Figure B-2. Contaminant contour plots for Test Case 1, Release #2.....	230
Figure B-3. Contaminant contour plots for Test Case 1, Release #4.....	231
Figure B-4. Contaminant contour plots for Test Case 2, Release #1.....	232
Figure B-5. Contaminant contour plots for Test Case 2, Release #2.....	233
Figure B-6. Contaminant contour plots for Test Case 2, Release #3.....	234
Figure B-7. Contaminant contour plots for Test Case 2, Release #4.....	235
Figure B-8. Contaminant contour plots for Test Case 5, Release #1.....	236
Figure B-9. Contaminant contour plots for Test Case 5, Release #2.....	237
Figure B-10. Contaminant contour plots for Test Case 5, Release #3.....	238
Figure B-11. Contaminant contour plots for Test Case 5, Release #4.....	239
Figure B-12. Contaminant contour plots for Test Case 6, Release #1.....	240
Figure B-13. Contaminant contour plots for Test Case 6, Release #2.....	241
Figure B-14. Contaminant contour plots for Test Case 6, Release #3.....	242
Figure B-15. Contaminant contour plots for Test Case 6, Release #4.....	243
Figure B-16. Contaminant contour plots for Test Case 7, Release #1.....	244
Figure B-17. Contaminant contour plots for Test Case 7, Release #3.....	245
Figure B-18. Contaminant contour plots for Test Case 7, Release #4.....	246
Figure B-19. Contaminant contour plots for Test Case 8, Release #1.....	247
Figure B-20. Contaminant contour plots for Test Case 8, Release #2.....	248
Figure B-21. Contaminant contour plots for Test Case 8, Release #3.....	249
Figure B-22. Contaminant contour plots for Test Case 8, Release #4.....	250

Figure B-23. Contaminant contour plots for Test Case 9, Release #1.....	252
Figure B-24. Contaminant contour plots for Test Case 9, Release #2.....	253
Figure B-25. Contaminant contour plots for Test Case 9, Release #3.....	254
Figure B-26. Contaminant contour plots for Test Case 9, Release #4.....	255
Figure B-27. Contaminant contour plots for Test Case 10, Release #1.....	256
Figure B-28. Contaminant contour plots for Test Case 10, Release #2.....	257
Figure B-29. Contaminant contour plots for Test Case 10, Release #3.....	258
Figure B-30. Contaminant contour plots for Test Case 10, Release #4.....	259
Figure B-31. Contaminant contour plots for Test Case 13, Release #1.....	260
Figure B-32. Contaminant contour plots for Test Case 13, Release #2.....	261
Figure B-33. Contaminant contour plots for Test Case 13, Release #3.....	262
Figure B-34. Contaminant contour plots for Test Case 13, Release #4.....	263
Figure B-35. Contaminant contour plots for Test Case 14, Release #1.....	264
Figure B-36. Contaminant contour plots for Test Case 14, Release #2.....	265
Figure B-37. Contaminant contour plots for Test Case 14, Release #3.....	266
Figure B-38. Contaminant contour plots for Test Case 14, Release #4.....	267
Figure B-39. Contaminant contour plots for Test Case 15, Release #1.....	268
Figure B-40. Contaminant contour plots for Test Case 15, Release #2.....	269
Figure B-41. Contaminant contour plots for Test Case 15, Release #3.....	270
Figure B-42. Contaminant contour plots for Test Case 15, Release #4.....	271
Figure B-43. Contaminant contour plots for Test Case 16, Release #1.....	272
Figure B-44. Contaminant contour plots for Test Case 16, Release #2.....	273
Figure B-45. Contaminant contour plots for Test Case 16, Release #3.....	274
Figure B-46. Contaminant contour plots for Test Case 16, Release #4.....	275
Figure B-47. Contaminant contour plots for Release #1 without infiltration	277

Figure B-48. Contaminant contour plots for Release #1 with infiltration	278
Figure B-49. Contaminant contour plots for Release #2 without infiltration	279
Figure B-50. Contaminant contour plots for Release #2 with infiltration	280
Figure B-51. Contaminant contour plots for Release #3 without infiltration	281
Figure B-52. Contaminant contour plots for Release #3 with infiltration	282
Figure B-53. Contaminant contour plots for Release #4 without infiltration	283
Figure B-54. Contaminant contour plots for Release #4 with infiltration	284

ABSTRACT

Framework for the Utilization of Forward and Inverse Airflow Models in
Systematic Sensor System Design for Indoor Air

Lisa (Yung Hua) Chen Ng

Advisor: Jin Wen, Ph.D.

The building industry faces many challenges, including maximizing energy efficiency and improving the health and safety of building occupants. Indoor air sensor systems can be used to regulate ventilation rates, monitor indoor air quality, and detect and eliminate harmful contaminants. However, current sensor system design is intuitively-based. This research presents the framework for utilizing airflow modeling techniques in *systematic* indoor air sensor system design.

Airflow modeling is used to simulate the contaminant data necessary for systematic sensor system design. Forward airflow models require detailed information about an indoor space in order to simulate airflow and contaminant transport. If this information is not available, inverse airflow models can estimate airflow patterns using measurements from commonly installed sensor systems. Thus, this research was divided into three parts: develop a framework for utilizing (1) *forward* airflow models in systematic sensor system design; (2) *inverse* airflow models for estimating airflow patterns in a single zone; and (3) *inverse* airflow models for estimating airflow patterns in a whole building.

In Part 1, it was found that data from simple airflow models could be used to design sensor systems that performed *just as well* as those designed using more complex airflow models for sensor systems with *more than one sensor*. Thus, saving modeling

time without compromising sensor system performance. In Part 2, it was found that velocity sensors placed on the *wall closest to the exhaust* in a single zone most improved the airflow estimation accuracy of the developed inverse model. Thus, offering practicality in experimental setup without sacrificing estimation accuracy. In Part 3, it was found that the proposed building airflow network inverse model could be applied to a building of any size if the rank of the known-information matrix was greater than or equal to the number of unknown airflow rates. The estimated building airflow network was in good agreement with a synthetic building airflow network, and its contaminant concentration prediction ability comparable to similar studies published in the literature. The proposed building airflow network inverse model also offered computational advantages over methods published in the literature.

1. CHAPTER 1: INTRODUCTION

1.1 Background

The building industry faces many challenges. It has been reported that a majority of Americans spend about 90% of their lifetimes indoors [1]. A building that was built or retrofitted around the time of the energy crisis of the 1970s would most likely be supplied with an outdoor air ventilation rate lower than today's standard. The building would also most likely be "airtight" in order to improve energy efficiency. However, such construction practices reduce the amount of outdoor air, which can pass through the building envelope. A newer building may be supplied with an outdoor air ventilation rate at today's standard. However, the use of modern technology (fax machines, printers, etc.) also means the presence of more indoor contaminants. Products such as paint, particleboard, and carpets also emit volatile organic compounds (VOCs) that can cause adverse health symptoms ranging from minor irritation to cancer.

Indoor air quality (IAQ) is the totality of attributes of indoor air that affect a person's health and well-being [2]. It includes measurable quantities like temperature, relative humidity, and contaminant levels. Unsatisfactory IAQ is harmful to public health and the economy. An estimated \$50 to \$100 billion is spent annually on IAQ-related health care costs, while losses in productivity are estimated between \$20 and \$70 billion [3].

During these very real times of rising energy prices, the building industry also faces increasing demands for more efficient buildings. Whereas under-ventilation results in inadequate IAQ, over-ventilation wastes energy by conditioning excess outdoor air. Demand control ventilation (DCV), which utilizes IAQ sensor systems to control

ventilation rates, has demonstrated great potential to balance IAQ and energy use. With new ventilation control mechanisms, a reduction in individual building energy consumption (as little as 1%) could lead to a 10% reduction in wholesale electricity prices [4] since the building industry is a large consumer of the nation's energy. However, *a framework for the systematic design of indoor air sensor systems* for the control of DCV and other non-traditional ventilation systems is still lacking in this field.

After the tragic events of September 11th and subsequent terrorist attacks, the public expects buildings to be safer. The ventilation system that delivers necessary air to occupants is also an effective distributor of chemical and biological warfare (CBW) agents to a building in the event of an attack. Thus, it is important to develop a *framework for systematic indoor air sensor system design* to quickly detect the presence of such agents and warn building occupants.

The next section presents the framework for systematic indoor air sensor system design that has applications for improving IAQ, reducing energy use, and detecting foreign and dangerous contaminants, among other applications.

1.2 Framework for systematic indoor air sensor system design

Figure 1-1 outlines the framework for systematic indoor air sensor system design. Systematic sensor system design first requires an understanding of the airflow pattern within a space or a building. This can be determined one of three ways: (1) by specialized experiments such as tracer gas tests; (2) by the use of a *forward* airflow model; or (3) by the use of an *inverse* airflow model. Experiments are time-consuming and expensive and may not provide as much information as an airflow model. *Forward* airflow models utilize specific details about a space or building to estimate airflow patterns. Details

include physical dimensions, layout, diffuser and exhaust locations, supply airflow rates, etc. Forward models also utilize "typical" building data, such as building envelope airtightness for a given construction type and year. *Inverse* airflow models, on the other hand, could utilize information collected from commonly installed sensor systems, such as airflow rates and/or velocity, temperature, or carbon dioxide (CO₂) concentration, along with physical dimensions, layout, diffuser and exhaust locations, etc. to estimate airflow patterns. Once the airflow pattern within a space or building is known, information such as contaminant distribution, air change rates, infiltration levels, etc. can be predicted. One use for contaminant distribution is systematic sensor system design. Uses for air exchange rates and infiltration levels are building commissioning and retrofitting.

Sec. 1.3.1 summarizes the literature on forward and inverse airflow models. The development and utilization of forward airflow models has been more established in the literature than for inverse airflow models. Therefore, Part 1 of this research (Chapter 2) presents a framework for utilizing *forward* airflow models in systematic sensor system design for different types of *zones*. To utilize the abundance of information provided by commonly installed sensor systems, Part 2 of this research (Chapter 3) presents a framework for utilizing *inverse* airflow models in estimating airflow patterns for different types of *zones*. Though the work in Chapter 3 can provide important findings, a more practical and wider application of inverse modeling is to estimate the airflow pattern within a *whole building*. Therefore, Part 3 of this research (Chapter 4) presents a framework for utilizing *inverse* airflow models for estimating the airflow pattern within a *whole building*.

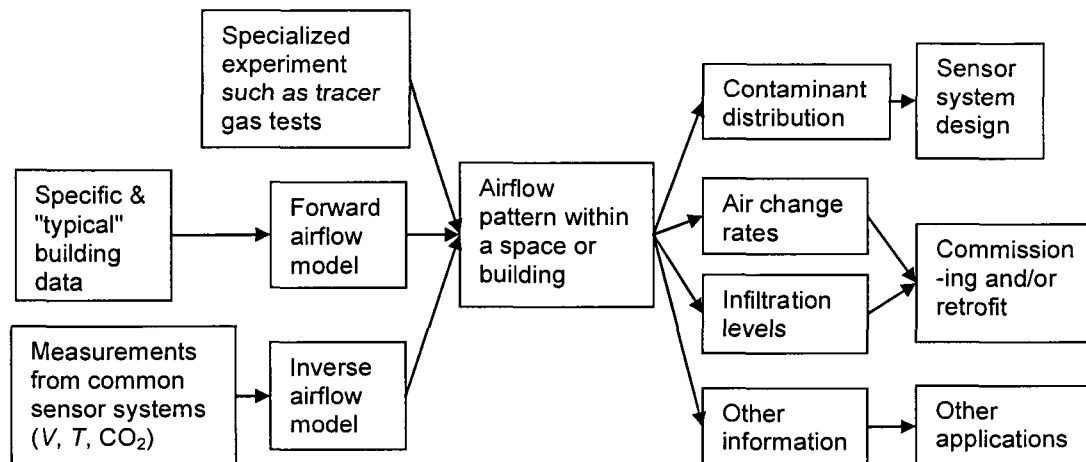


Figure 1-1. Framework for systematic indoor air sensor system design and outline for this research.

Sec. 1.3 reviews the literature on the components of systematic sensor system design, which include airflow modeling and sensor system design methods. Sec. 1.4 discusses the research needs and motivation behind this research. Sec. 1.5 discusses the scope and hypotheses that were tested in this research. Chapters 2-4 discuss the results of testing each research hypothesis. Each chapter concludes with possible publications to be generated, conclusions, and recommendations for future work. Chapter 5 provides general conclusions and recommendations for future work. Finally, Chapter 6 discusses the long-term goals of this research.

1.3 Literature review

1.3.1 Airflow and contaminant transport simulation

Obtaining airflow patterns and contaminant distribution from an experimental setup can be cumbersome and expensive. Depending on the measurements desired, obtaining them might also be difficult. Therefore, it is advantageous to the researcher to

use airflow and contaminant transport simulation models (now further referred to only as "airflow models") in order to obtain airflow patterns and contaminant distribution. These models can either be forward or inverse models. *Forward* modeling starts with known initial and boundary conditions. Airflow and contaminant transport calculations are then carried out through space and time. On the other hand, *inverse* models start with information about current conditions, most likely *partial* measurements of airflow patterns or contaminant distribution. The inverse model then makes estimates about the past, provide additional information on current conditions, or makes predictions about the future.

Three major types of forward airflow models exist: multizone (Sec. 1.3.1.1), zonal (Sec. 1.3.1.2), and computational fluid dynamics (CFD) (Sec. 1.3.1.3). Specialized experiments, such as fan pressurization and tracer gas tests, have been used to improve the performance of *multizone* airflow models (Sec. 1.3.1.4). Contaminants are either mathematically modeled by an Eulerian or Lagrangian approach (Sec. 1.3.1.5). The multizone and zonal models use the former approach while CFD can use either one. Coupling between multizone and CFD models has been performed in order to simultaneously exploit the advantages of and overcome the drawbacks of each airflow model (Sec. 1.3.1.6). Inverse modeling methods are discussed in Sec. 1.3.1.7.

1.3.1.1 Multizone modeling

The multizone model considers a building as a network of interconnected nodes. Each node represents a physical space, called a *zone*. Each zone is considered well-mixed, which means that parameters such as temperature, pressure, and contaminant concentration are spatially uniform within a zone. Zones are connected to one another via

flow elements, which can be cracks, windows, doors, fans, etc. At least one zone must connect directly to a constant pressure zone, often the ambient zone. The constant pressure zone serves as a boundary condition, giving the solution algorithm a starting point for solving the unknown airflow network.

Two popular multizone software are CONTAM [5] and COMIS [6]. CONTAM was developed by the National Institute of Standards and Technology (NIST), and COMIS was developed by the Lawrence Berkeley National Laboratory (LBNL). Both were developed in the 80s. Each multizone model has been used in a variety of applications and validated in the literature. The ability of multizone models to couple with other software, such as energy simulation software, has also made their use popular [7].

Multizone models have been evaluated in terms of: (1) program integrity; (2) comparison with experimental data collected in controlled environments; and (3) comparison with experimental data collected in field studies. The first test (program integrity) ensured that the flow equations which form the backbone of the models were executed correctly [8]. The second test showed that results from multizone model simulations were in reasonable agreement with data from controlled experiments [8]. Lastly, the third test showed that multizone models made reasonable predictions of airflow even when experiments were performed in real-world environments [8-11].

The well-mixed assumption is often times not a valid one. Spaces with strong velocity or thermal jets and large spaces, such as atria and auditoria, are obvious candidates for more sophisticated airflow models. Nevertheless, it has been shown that the well-mixed assumption can hold under certain conditions [12]. For instance, upper

limits for temperature gradients and Archimedes number exist for which the well-mixed assumption is still valid [12]. Further, under certain conditions, the air momentum effect (from a strong velocity jet) can be neglected too [12].

1.3.1.2 Zonal modeling

Many of the same principles and assumptions used in the multizone models are applied in zonal models. Buildings are represented by a network of nodes, each node representing a well-mixed zone. The difference, however, is that each node in the zonal model is a *subzone*, which is a non-physical section of a physical zone. There are two types of subzones: *standard* and *mixed*. The *standard* subzone is considered well-mixed and flow between standard subzones is pressure-driven, just like in multizone models. The *mixed* subzone contains a well-mixed portion and a driving element, such as velocity jet or thermal plume. Flow between the portions with a driving element is governed by designated mass flow relationships, depending on the type of element. Multizone models do not include driving elements.

The inclusion of driving elements in zonal models has been shown to improve their accuracy over multizone models. Comprehensive validation studies have been performed for zonal models. Both two-dimensional and three-dimensional environments, as well as natural and mixed convection conditions have been used to test the performance of zonal models [13-16]. Within zonal models are different variations: power-law (PL) models, specific driven flow (SDF) models, and surface drag (SD) models [17-18]. PL models represent the flow between subzones as a function of pressure, just like in multizone models. SDF models include equations that describe *ideal* velocity jet and thermal plume flow. Finally, SD models account for drag forces on airflow caused

by nearby surfaces. These variations resulted in different estimates of airflow patterns – some better than others. Empirical constants in zonal models have been varied in order to improve performance [19].

Since each physical zone is subdivided for zonal modeling, questions arise as to the appropriate size of the subzones. It was shown that decreasing the size of subzones *did not* significantly improve results when compared to experimental data, as is often the case when using more sophisticated airflow models like CFD [13]. Nevertheless, it has been recommended that the size of a *standard* subzone be between 0.25 and 1.5 m [20]. The size of a *mixed* subzone should capture the entire flow element [21]. Being able to accurately mathematically represent flow between subzones, where no physical wall/crack/opening exists and experimental values are nearly impossible to obtain, challenges the accuracy of zonal models [14].

Various simulation environments have been used to execute zonal models. They include MACSYMA [13] and SPARK [16]. Enhancements to the multizone model COMIS resulted in the model, COwZ (COMIS with subzones), developed by the QUESTOR Environmental Modeling Group [22].

Multizone and zonal models are suitable for whole building and whole heating, ventilating, and air-conditioning (HVAC) system simulation. They are useful for modeling different types of ventilation strategies and certain dynamic effects. Dynamic effects include HVAC operating schedules and changes in occupancy and weather conditions, among others. These effects are currently much more difficult or even impossible to model in more sophisticated models such as CFD.

1.3.1.3 Computational fluid dynamics (CFD)

Computational fluid dynamics (CFD) is a sophisticated airflow and contaminant transport model that has been around since the 70s. First developed for use in aircraft design, it has since been utilized in many other applications, including indoor air applications.

CFD numerically solves the partial differential equations governing fluid flow and contaminant transport (Navier-Stokes equations). On the other hand, multizone and zonal models algebraically solve governing equations that neglect momentum and mass transfer. Many numerical methods have been developed to solve these equations. Especially challenging is the modeling of *turbulence* in fluid flow, which is random disturbance in fluid flow. In order to account for turbulence, additional equations and approximations to the Navier-Stokes equations are included in the solution procedure. There are three major classes of CFD models: direct numerical simulation (DNS), large eddy simulation (LES), and Reynolds-averaged Navier-Stokes (RANS) [23]. DNS directly solves the Navier-Stokes equations without approximation. Thus, DNS requires a fine grid and a small time step in order to carry out the solution procedure. DNS requires a significant amount of computing power for real-world applications. LES simulates the large-scale eddies caused by turbulence but makes approximations for the small-scale eddies. Thus, a coarser grid compared to that necessary for a DNS model can be utilized. RANS utilizes mean flow parameters in the solution procedure. Thus, solution time is shorter compared to DNS and LES. The appropriateness of any CFD model is dependent upon the application. Those that have been found appropriate for indoor airflow will be discussed below.

For indoor airflow, most of the literature utilizes the RANS class of CFD models [23-26]. Given the size of typical indoor spaces, requiring the fine grids necessary to utilize the DNS and LES could lead to computational spaces beyond the capability of current desktop computers. Studies that have evaluated the performance of RANS for indoor airflow will be discussed below. RANS models are classified into two types: eddy viscosity and Reynolds stress models [23]. The RANS models described below are the standard κ - ε , standard κ - ω , SST κ - ω , RNG κ - ε , and zero-equation models.

The standard κ - ε model is a commonly used CFD model for a wide variety of applications [26]. It was developed for fully turbulent and high Reynolds number flows [23, 27]. It requires the solution of two additional equations for turbulent kinetic energy κ and dissipation rate ε . In contrast, the standard κ - ω model (ω being turbulence frequency) can be used for low Reynolds number flow [27]. The Shear-Stress Transport (SST) κ - ω model combines the modeling principles of both the standard κ - ε and κ - ω models [27]. Near the wall, the model uses κ - ω principles, where the flow is relatively slow. The remainder of the space uses κ - ε principles. The SST κ - ω model showed the best agreement with experimental data compared to the standard κ - ε , RNG κ - ε , and laminar model [27].

The standard κ - ε , standard κ - ω , and SST κ - ω models are eddy viscosity models. They fail to capture complex flow structures, such as swirling, which commonly found in indoor airflow [23]. Thus, Reynolds stress models were developed. One Reynolds stress model is the Renormalization Group (RNG) κ - ε model. It has shown to be more accurate and reliable for a wider class of indoor airflows than the standard κ - ε model [25-27]. Though the RNG κ - ε model outperforms the standard κ - ε model, its drawbacks are: (1) a

greater number of additional equations need to be solved; (2) computations are less stable; (3) computing effort is five to twenty times greater than using the standard κ - ε model; and (4) improvements to the results that the RNG κ - ε model makes over the standard κ - ε model are often not significant enough to warrant the additional computational effort [26].

The additional equations in CFD models are used to model turbulence. Recently, there has been an emergence of a new zero-equation eddy-viscosity model [23, 28]. Instead of representing turbulence with partial differential equations, zero-equation models represent turbulence with algebraic functions. The zero-equation turbulence model has shown great potential for use in indoor airflow because of its simplicity and reduction in computing time compared to the standard κ - ε model [28]. The indoor zero-equation model performed well, in terms of airflow pattern and temperature profile, under mixed convection conditions and low Reynolds number flow [24], which is typical of indoor air flow.

1.3.1.4 Multizone model tuning

Efforts have been made to improve the performance of forward airflow models, namely the multizone models, using specialized experiments such as fan pressurization and tracer gas tests (discussed briefly in Sec. 1.3.5 and in more detail in Chapter 4). Airflow model tuning focuses on reducing the *uncertainty* in the parameters of a multizone model in order to improve the accuracy of the estimated airflow patterns and contaminant transport.

Musser et al. [29] proposed a four-stage tuning process for improving the performance of a CONTAM model of a building:

- (1) Utilize construction documents and building leakage data found in the literature to assign building envelope airtightness values to the CONTAM model.
- (2) Modify simulated building envelope airtightness values with actual ones obtained from fan pressurization tests.
- (3) Modify simulated bulk airflow rates from fan-driven flows, such as at an air handling unit, with measured ones.
- (4) Modify simulated zone supply airflow rates so that simulated air change rates match those obtained from tracer gas tests. Smoke tests can be used to verify pressurization of zones.

The performance of the tuned CONTAM model was evaluated using a correlation coefficient and mean square error as defined by the ASTM D5157 [30]. These metrics quantify the difference between measured and predicted concentration of a contaminant.

The measurements of bulk airflow rates in Step 3 for a mechanically ventilated building required about one day and were more helpful in improving the accuracy of the tuned CONTAM model than the other measurements/experiments. The tracer gas tests in Step 4 required the most time and effort, and the fan pressurization test in Step 1 required a half-day. Thus, the effort required to tune CONTAM model parameters *did not always translate into an equal improvement* in model performance.

Firrantello et al. [31-32] proposed a formal approach for CONTAM model tuning. Factorial analysis was used to test the effect of CONTAM parameters on model performance for a synthetic test building. Those parameters that were found to significantly affect model performance would be subject to tuning. Model performance was evaluated using the percentage of incorrect interzonal airflow *direction*. It was

assumed that actual interzonal airflow direction was known prior to tuning. The magnitude of any errors was not taken into account.

Values for tuning the CONTAM model of the synthetic test building was taken from a synthetic target building. The researchers did not recommend any techniques to obtain these values in a real building, such as interior/exterior door leakage and interior/exterior wall leakage. In fact, when tuning the CONTAM model for a *real* test building, the researchers did not tune the parameters found significant for model performance for the synthetic test building. They measured airflow rates through the air handling unit, diffusers, and exhausts. Leakage properties were taken from construction documents and typical leakage data in the literature. The actual interzonal airflow directions for their real test building were obtained using chemical smoke bottles. Jeong et al. [33] demonstrated that smoke gun tests did not give reliable indication of interzonal airflow, especially when the pressure difference between two spaces was less than the uncertainty in the pressure measurement. Nevertheless, Farrantello et al. [31-32] reported a 50% improvement in the prediction of interzonal airflow direction for their *synthetic* test building, and 10-30% improvement for their *real* test buildings. They showed that the formal approach to tuning improved the performance of a CONTAM model better than using randomly selected measurements.

As Price et al. [34] summarized: (1) there are hundreds of parameters in any building; (2) their values are subject to, sometimes large, uncertainty – to the point where the value cannot always be determined; (3) experiments to tune the parameters are often time-consuming, expensive, and do not translate into an equal improvement in results (as

demonstrated in [29]); and lastly (4) large uncertainties in the results can still remain even after careful measurements or parameter estimation are made.

1.3.1.5 Modeling chemical biological warfare (CBW) agents

Contaminants are found in gaseous and particulate forms. To model them using CFD, the differences in the transport mechanism of each contaminant type must be considered. Gaseous contaminants are modeled in the same way as the airflow. Particulate contaminants, on the other hand, are modeled either one of two ways: Eulerian or Lagrangian. The Eulerian approach treats a group of particulates as a continuum. The Lagrangian approach treats each particulate as a discrete element. One study found that both approaches produced similar concentration distributions in enclosed spaces [35]. The Eulerian approach tended to "smooth" out concentration distributions and gradients. The Lagrangian approach could provide information on each individual particle. Due to this level of detail, it is not surprising that the Lagrangian approach requires a higher computational time than the Eulerian approach.

1.3.1.6 Coupled CFD models

To use CFD successfully, one must possess specific knowledge about fluid dynamics theory and numerical techniques. Further, executing CFD can require great computational effort. Therefore, researchers have attempted to find a middle ground between simple models, like multizone model, and more complex models, like CFD. Coupling of CONTAM and the indoor zero-equation CFD model has been tested with good performance [36]. The coupled model performed just as well as the standard κ - ϵ model with regards to air velocity prediction. As for contaminant distribution, the

coupled model compared well with experimental results and better than the multizone model alone. A coupled multizone-CFD model used in natural ventilation applications also performed well compared to a standalone CFD model [37]. A study has been completed coupling CFD with COMIS [38]. Computational time for a coupled CFD-multizone model is significantly less than using CFD alone. Research continues on this topic, such as where information from the two models is coupled and how much information is exchanged [39].

1.3.1.7 Inverse airflow and contaminant modeling methods

Whether using the simpler multizone and zonal models, or the more complex CFD model, forward modeling requires gathering information on a zone or building. Information includes architectural and mechanical plans and specifications. If the building is in the design or construction phase, this information may be fairly accessible. In contrast, this information may be inaccurate, incomplete, or missing for existing buildings. Gathering the information by field measurements can be tedious and time-consuming.

Forward modeling methods start with initial and boundary conditions. Airflow and contaminant transport calculations are then carried out in space and time. Inverse airflow modeling methods use complete or partial information about current conditions to make estimates about the past, provide additional information about current conditions, or make predictions about the future. Inverse modeling is often less computationally intense than CFD and even multizone or zonal models. Inverse modeling methods found in the literature are discussed in this section.

Nonlinear least-squares minimization method was used to fit mass balance equations of airflow and concentration equations to experimental tracer gas data [40]. Interzonal airflow rates (or the airflow rates between zones) were estimated. Estimated interzonal airflow rates agreed well with the experimental data. The experiment was conducted using two tracer gases in a real two-zone building. A total of four equations were simultaneously fit. The solution was subject to two continuity equations, one for each zone. As the number of zones increases, the use of this method may prove both experimentally and mathematically challenging. Thus, this inverse modeling method may be *limited* to small buildings.

Maximum likelihood estimation (MLE) was used to determine a space air change rate and supply CO₂ concentration using CO₂ measurements inside a synthetic single zone [41]. MLE equations were derived from mass balance equations in order to determine the unknown parameters that maximized the probability (or likelihood) of obtaining the actual CO₂ measurements. The estimated space air change rate and supply CO₂ concentration was then used heuristically to determine CO₂ generation rates. This inverse modeling method was *not extended to multiple zones*. Further, its proposed heuristic method to estimate CO₂ generation rates was *not shown to be robust*.

A direct search optimization method was used to fit three inverse models to CO₂ concentrations from CFD simulations [42]. The inverse models were mathematically based on mass balance relationships for a synthetic single zone. The first inverse model tested was a quasi-static equilibrium model, the second one was a two-zone transient model (the synthetic single zone was subdivided into two non-physical zones), and the third one was a three-zone transient model (the synthetic single zone was subdivided into

three non-physical zones). Subdivision of the synthetic single zone was performed in order to test the effects of imperfect mixing on the performance of the inverse models. The number of unknown parameters was smallest in the first model and largest in the third model. The CO₂ predictions made by the *simplest* of the mathematical models were sufficiently accurate for DCV system control purposes. Estimated energy use of a simulated DCV system, and subsequent cost savings, using the CO₂ predictions from the three tested inverse models were similar. Thus, the effects of imperfect mixing did not affect inverse model performance for DCV system control purposes. This inverse modeling method was *not extended to multiple zones*.

Both steepest descent and simulated annealing were used to determine the subzonal volumes and inter-subzonal airflow rates of a partitionless building [43], similar to the study just discussed. The objective was to determine the unknown parameters that minimized the sum of squared differences between the synthetic and predicted subzonal tracer gas concentrations. The synthetic tracer gas concentrations provided to the inverse model varied in amount (i.e., how many tracer gas releases), accuracy, and frequency. In essence, the study tested the effects of limited and inaccurate concentration data on the performance of the inverse model. The authors showed that even large uncertainties in the estimated subzonal volumes and inter-subzonal airflow rates could still result in reasonable predictions in tracer gas concentration. This study was designed for use in large, partitionless areas of buildings such as atria or gymnasiums. The authors reported that their results *may not be applicable* to spaces that exhibit significantly different volumes or airflow rates from the ones tested in their study.

Artificial neural networks (ANN) have also been used as an inverse modeling method. ANN is essentially a black-box that determines input-output relationships by first training itself using *known* input-output relationships. Complete training sets must be available in order for input-output relationships to be established by ANN. Obtaining complete training sets may *prove challenging* for indoor air applications, depending on the measurements needed. Nevertheless, ANN was shown to have potential in accurately determining input-output relationships for a complex system such as airflow in an urban environment [44]. ANN used historical NO_x measurements gathered in an urban environment as *training* sets. After training, the ANN showed promise in being able to *predict* hourly NO_x concentrations.

The governing equations that describe indoor airflow and contaminant transport can also be "reversed" in inverse CFD modeling. Utilizing velocity and contaminant data from a current time, the inverse CFD model was able to determine the location and start of a contaminant release. More details can be found in Sec. 1.3.4.

1.3.1.8 Summary

Both forward and inverse airflow modeling methods were discussed. Multizone, zonal, and CFD models are forward modeling models. Multizone and zonal models are relatively easy to set up and computationally efficient. However, the literature has shown that their results are not as accurate as CFD results when compared to experimental data. Efforts have been made to tune, or improve the performance of, multizone airflow models using building data and measurements. CFD is more challenging to set up and more computationally intense than multizone and zonal models. Inverse modeling methods have the potential to take advantage of the simplicity of multizone and zonal

models and the accuracy of CFD models. Requiring far less setup and computational effort than forward models, inverse models have been shown to be acceptably accurate for certain applications.

1.3.2 Optimization

Optimization methods seek to locate points within a search domain that are either maxima or minima. Optimization methods can be broadly categorized into three types: calculus-based, enumerative, and heuristic [45].

Calculus-based searching methods are distinguished into indirect and direct approaches [45]. Indirect methods search for a point in the domain where the slope in all directions is zero. Direct methods start from a single point and continue the search in the direction of the steepest gradient. Calculus-based methods require the existence of first and second derivatives, and continuity in the domain. Further, if the search space contains multiple *local* minima or maxima, calculus-based methods may get "stuck" in these points and not find the *global* minima or maxima.

Whereas the calculus-based methods start at a random location, enumerative methods search the domain one location at a time [45]. These methods, though not constrained to the need for derivatives and continuity, require large search times when the domain is large. They are also prone to being "stuck" in local minima or maxima. Because of this, they have not been applied to large search domains, such as indoor air applications.

The last type of optimization method is heuristic (or stochastic/probability-based). Random choice (or probability) is used as a tool during the search process. Stochastic optimization methods have been shown to be very useful in solving problems that exhibit

high nonlinearity and may have many local minima/maxima [46]. The example problems in [46] were taken from material science, chemical engineering, and applied statistics.

In [47], simulated annealing (SA), simultaneous perturbation stochastic approximation (SPSA), and genetic algorithm (GA) were considered for indoor air sensor system design. The authors chose GA as the most suitable method of the three. GA is a robust optimization method for four reasons [45]: (1) it codes the parameter set into finite-length strings instead of using the parameters themselves; (2) the method searches from a population of points, not just one point at a time. This avoids the finding of local maxima/minima; (3) the method uses payoffs or objective function/fitness values, not derivatives or other auxiliary information; (4) the method uses probabilistic, not deterministic rules. Though it is not the most efficient optimization method for solving nonlinear problems [48], GA is an optimization method that is useful in a wide variety of applications.

1.3.3 Sensor system design methods

Sensors are used to collect different types of information in different applications. The applications discussed here are in municipal water networks (Sec. 1.3.3.1), the chemical process plant industry (Sec. 1.3.3.2), outdoor air applications (Sec. 1.3.3.3), and indoor air applications (Sec.1.3.3.4). Studying these applications highlights the design methods and criteria that are used to develop sensor systems that help to protect human health and well-being. Selecting appropriate sensors for each of these applications is not a trivial task. A report by the Department of Defense's (DoD) Defense Advanced Research Projects Agency (DARPA) identified at least twelve sensor characteristics important in sensor selection [49]. They are: sensitivity, size, weight, power consumption, unit cost,

reliability factor (in months and in weeks), operating cost, false positive rate (low and high disruption response), response time, and detection confidence. Initial cost of a sensor is one of the most important factors in the selection process. Thus, engineers designing sensor systems need to adopt design methodologies that optimize placement of a limited number of sensors.

1.3.3.1 Municipal water applications

Municipal water networks are vulnerable to water contamination, either accidental or intentional. Their large coverage area also makes them effective carriers of such contamination to a large, diverse population if the event is not dealt with in a reasonable amount of time. Thus, researchers have been working to find ways to determine sensor or monitoring locations along municipal water networks that can quickly detect contamination.

Design objectives include minimizing sensor system cost, minimizing detection time, minimizing exposure to the population served by the water network, minimizing consumption of contaminated water prior to detection, and maximizing the likelihood of detection. These objectives are met over a set of *probable* contaminant events, which are simulated using contaminant transport models [50]. Sensor system design to minimize the impact of "high-consequence" (though perhaps not as probable) events, such as terrorist attacks, were explicitly considered in [51] and compared to sensor systems designed for probable events.

It was shown that many design objectives exhibit diminishing returns, or *submodularity*, as sensors are added to a system [52]. The same study also accounted for the unit *and* installation costs associated with each additional sensor when evaluating

submodularity. Another study explored the effects of designing with imperfect sensors [53].

Besides contaminant detection, sensor system design methods were also employed to optimize the placement of booster stations [54-55]. The objective was to minimize the total mass of chlorine supplied to the system while maintaining an acceptable level of disinfection at particular locations in the water network. In [56], an additional objective was simultaneously met: maximize the volume of water, that has minimal disinfectant by-products, supplied to customers.

Sensor system design (optimization) methods used in municipal water applications included mixed integer programming, greedy algorithm, branch and bound techniques, genetic algorithm, and enumeration.

1.3.3.2 Chemical process plant applications

Chemical process plants rely on sensor data for the control of its systems, quality assessment, and failure detection. Bagajewicz [57] gave a good summary of the factors that affect the performance of chemical process plant sensor systems, which can be extended to many other fields as well. Any data collected by a sensor system should be *accurate, precise, and reliable* (i.e., accurate and precise even under sensor failure). A sensor system includes both the instrumentation/ sensors (hardware) used to collect and software used to reconcile the data.

Sensor system performance indices, such as *redundancy, observability, and robustness* are commonly found in the literature on sensor system design for chemical process plants. Designing for redundancy ensures that in the presence of a sensor failure, the quantity of interest (or variable) is still able to be measured or estimated by some

other means (sensor or software) (i.e., the variable remains *observable*). Designing for redundancy also ensures that the most reliable measure of a variable is obtained. For instance, if the measurement of a variable is obtained by more than one method (sensor or software), redundancy allows the software to utilize the precision of each method and statistical tools to produce the most reliable estimate of the variable. Lee [58] devised a method to evaluate the validity of a sensor measurement based on the spatial redundancy of sensors.

The process model used to design a sensor system will not be (and cannot be) an exact representation of the actual process. It will contain approximations and errors. Thus, designing for sensor system *robustness* means any changes or errors in the process model will not significantly compromise the performance of the sensor system [59]. Also, the performance of each sensor in a sensor system, such as its fault occurrence and failure probability, may be uncertain. This can affect the *reliability* of the sensor measurements. And so the performance of a sensor system should not be significantly affected by sensor uncertainties. Ali and Narasimhan [60] studied the effects of using sensors of equal and unequal sensor failure probabilities on reliability. Bagajewicz and Sánchez [61] studied the effects of adding sensors in different locations and of different type on reliability.

With many design objectives, *lexicographic optimization* has been used [59], which optimizes design objectives in decreasing order of preference.

1.3.3.3 Outdoor air applications

Monitoring outdoor air contaminant levels is met with many challenges. Outdoor weather conditions, such as wind, temperature, and precipitation, can vary continuously and affect the accuracy of measurements collected by monitoring equipment.

Furthermore, the capital cost of the monitoring equipment is large, as is the cost of maintenance. Thus, a limited number of monitoring stations are sparsely located throughout any particular region of interest. The selected locations for these monitoring stations are critical in the detection of contaminants.

In an outdoor application, buildings, trees, and other elements are obstacles to air and contaminant flow. They are also obstacles to detection by a static sensor network. Nevertheless, two studies designed sensor networks for outdoor monitoring without considering airflow patterns [62-63]. The first study superimposed a uniform grid onto the desired monitoring area. The authors assumed that the probability of detecting a contaminant by any sensor varied with the distance between the sensor and the release location. The objective was to arrange sensors such that every grid point was covered by a threshold probability of detection. The second study arranged sensors such that each grid point was covered by at least the coverage area of a sensor. Both studies showed that a systematic approach to sensor placement outperformed random sensor placement in determining the minimum number of sensors needed for the same level of protection.

Taking into account airflow patterns within a city block, CFD was used to determine optimal sensor locations [64]. Simulations accounted for various wind conditions (direction and speed). Optimal sensor network configurations were determined for each wind condition. Exposure to the contaminant was then calculated. It was found that the sensor network configuration that minimized exposure for all wind conditions was not as effective compared to configurations optimized for each wind condition. The authors recommended that sensors could be moved depending on season, and thus prevailing wind direction, to optimize detection throughout a year. Another CFD study of

a city block utilized a heuristic approach to optimal sensor placement [65]. The study demonstrated that as the number of wind directions and release locations increased, so did the number of required sensors. The approach required multiple iterations of computationally-intensive simulations.

Over time, the accuracy of sensors diminishes due to environmental factors, such as humidity and dust accumulation. Calibration of each sensor in a network can be very time-consuming. Thus, it would be beneficial to develop an auto-calibration method. Using only measurements from nearby government monitoring stations during conditions when measured contaminant levels were low, a private monitoring station was able to auto-calibrate its sensor at least once a month throughout a year [66]. Contaminant measurements compared well between the calibrated monitoring station and a gas analyzer placed near the same station. This method may be extended to auto-calibration of indoor sensors.

1.3.3.4 Indoor air applications

Indoor air sensor systems can be used to monitor indoor air parameters, such as temperature, relative humidity, and contaminant concentration. The information collected can be used to: (1) evaluate IAQ and maximize energy efficiency and (2) detect the presence of harmful indoor contaminants. The contaminants used to evaluate IAQ are usually present during normal occupancy and building operation. Common contaminants are: CO₂, dust, and VOCs. Indoor air sensor systems could also detect the presence of harmful contaminants, which are not present during normal occupancy, including those used for terroristic purposes, such as anthrax and sarin gas.

IAQ and energy efficiency are considered one application because the two should be balanced in building system design. In order to maintain acceptable IAQ, ventilation (or outdoor airflow) rates are modulated. Higher ventilation rates have been shown to improve IAQ [67]. However, higher ventilation rates also require greater energy expenditure. A ventilation system used increasingly more in the building industry that attempts to balance acceptable IAQ with energy use is called demand-controlled ventilation (DCV) systems. Sensor systems for ventilation purposes could have great benefits for DCV systems. Ventilation rates are modulated in DCV systems in accordance to measured parameters inside the building. Modulating ventilation rates helps to maintain adequate IAQ while also reducing energy consumption [68]. Indoor measurements used as control parameters for DCV include CO₂, water vapor, VOC, and particles [3]. The most widely used parameter is CO₂.

An article published in the ASHRAE Journal, which is a publication written by and for practicing mechanical engineers, provides guidelines for CO₂ sensor placement [69]. Systematic decisions on the number of sensors and their placement within a zone or building is currently not common practice. The effects of intuitively-designed sensor systems on IAQ and energy use are often never verified with simulation models nor quantified after installation. Therefore, it is necessary to develop a design methodology for indoor air sensor systems that will, in actual operation, best maintain IAQ and reduce energy waste.

To design sensor systems for protecting indoor environments, airflow modeling has been used along with optimization techniques. Airflow models provide the concentration data for which an optimization method identifies sensor locations based on

given objective functions. The average predictions of contaminant concentration of a multizone model was the search domain for GA to optimally locate a limited number of sensors in an office level [47]. Detailed contaminant concentration results from a CFD model provided data for sensor placement [70-71]. However, in the studies using CFD, no systematic approach to sensor placement was used. Sensor placement was decided upon based on concentration profiles taken at a few selected locations. These locations were most likely chosen based on experience or intuition.

In these studies, there was no systematic selection of an airflow model for sensor system design. A sensor system design using multizone and zonal model data *may* not meet design objectives during actual operation since it has been shown that their results are not as accurate as CFD results when compared to experimental data (Sec. 1.3.1). A sensor system design using CFD model data *may* meet design objectives during actual operation, but the time and effort required to simulate a building in CFD may be impractical. Thus, the utilization of either a multizone or CFD model for sensor system design is a cost-benefit decision that requires a systematic comparison between the performances of the sensor systems designed by the different airflow models.

For indoor applications, *inverse models have yet to be studied for use in sensor system design*. Inverse models could potentially estimate airflow patterns and contaminant transport based on a limited number of sensor readings. No longer would time-consuming forward modeling be required in order to obtain contaminant data for sensor system design. Inverse models could provide this data with the ease and efficiency of multizone and zonal models, but with the accuracy of CFD models.

Sensor systems for protecting the indoor environment have been designed to minimize detection time [47, 70-72]. However, due to the highly harmful and even deadly effects of exposure to CBW agents, design objectives should also include minimizing occupant exposure. As more data becomes available on the human dose-response relationships for CBW agents, sensor systems could be designed to minimize risk. Risk is the probability of an outcome, such as an adverse health symptom or even death, at given exposure levels. Decision makers will need to determine the maximum level of risk, and thus the maximum occupant exposure, acceptable in each case. How the distribution of risk changes with time (given more sensor data) can also be evaluated [73].

1.3.3.5 Summary

Sensor systems have been shown to be useful in many applications. In municipal water networks, appropriately located sensors reduce the detection time of contaminants and thus reduce exposure to the public. For chemical process plants, formal metrics ensure certain levels of sensor system performance. Studies of sensor system design for outdoor applications have utilized both statistical and CFD models to predict the transport of contaminants in order to locate sensors. For indoor applications, sensor systems have been designed for either IAQ purposes or for protecting the indoor environment. However, sensor selection and placement is currently intuitively-based. Further, the literature has not discussed systematic selection of the airflow model used to generate the contaminant data for sensor system design. Lastly, the potential for utilizing inverse models in sensor system design has not been reported in the literature.

1.3.4 Characterizing contaminant source

Characterizing a contaminant source includes its location, and strength (or rate) and duration of release. It is important information for first responders who seek to contain and eliminate a contaminant, whether indoors or outdoors. The methods reviewed here for characterizing a contaminant source are *inverse* in nature. They utilize information on current conditions to estimate the characteristics of a contaminant release event.

1.3.4.1 Outdoor air applications

Outdoor air contamination can spread quickly and affect large populations – many more people than would be inside a building. It is important to locate sources of outdoor air contamination to both protect an exposed region and also to assign responsibility for the contaminant release when necessary.

Using simulation models, synthetic source emission data can be simulated as a result of possible release locations. Synthetic measurements are "taken" at possible monitoring sites. An optimization method is then employed to select the release location that most likely resulted in a given set of synthetic measurements. GA was used in [74-75] to determine source apportionment factors, which are assigned to each possible release location that could have resulted in the measurement at a monitoring site. Thus, the release location(s) with the highest source apportionment factors are the most probable location(s) of contaminant release. Single releases were more easily identified than multiple releases [74]. GA was also used to determine the wind direction, two dimensional coordinates of the source location, and the source strength [76].

Improvements in prediction could be made by implementing a hybrid GA. Hybrid GA couples GA with other optimization methods. Hybrid GA was shown to improve results over using stand-alone optimization methods. For instance, in [77], the researchers coupled GA with a gradient-based optimization method. Using the hybrid GA improved convergence time and resulted in the correct identification of the global minima. In addition to using hybrid GA, sensitivity analyses on GA parameters also helped to expedite convergence [76].

1.3.4.2 Indoor air applications

The methods that have been used to characterize contaminant sources in indoor air applications are: Bayesian statistics, artificial neural networks (ANN), Kalman filtering, inverse CFD modeling, inverse probabilistic modeling, and hypothesis tracking.

Bayesian statistics was used for source locating [78-79]. It utilized a two-stage process. In the first stage, a number of release scenarios were simulated using a forward airflow model. In the second stage, synthetic measurements were collected over time for one of the simulated release scenarios. Bayesian statistics was then used to update (over time) the probability of each simulated release scenario producing the synthetic measurements. It was very similar to the study using GA and source apportionment factors to location an outdoor source.

The effect of sensor accuracy, threshold level, and response time on the performance of the two-stage Bayesian method for source locating was studied [79]. It was shown that trade-offs must be made between different sensor characteristics.

The advantages of the two-stage Bayesian method were: (1) stage one could be completed offline; and (2) depending on the airflow model selected, many release

scenarios could be simulated to cover a large range of release scenarios. The disadvantages were: (1) every possible release scenario cannot be simulated due to uncertainty in many factors, such as release location, release amount, etc.; and (2) as building size increases, the data set in stage one would increase. The time to complete stage two would also increase. This, this method may be *impractical* for real-world indoor applications.

Instead of Bayesian statistics, ANN was used to perform a similar "matching" of release scenario to synthetic measurements [80]. However, as discussed in Sec. 1.3.1.7, complete training sets must be available in order for input-output relationships to be established by ANN. Thus, ANN may not be able to correctly identify a release scenario that is significantly different from the ones used to train the model.

Kalman filtering was used to estimate source characteristics given certain inputs. There were many advantages to using Kalman filtering, as listed by [81]: (1) the method allowed solution of time-varying inputs and parameters; (2) it was able to treat some parameters as time-varying and others as time invariant; (3) it allowed for inclusion of noise in data; and (4) it generated statistics that were used to evaluate its own performance. Kalman filtering is most suited to *linear* problems. Many problems involving indoor air are neither linear nor well-conditioned, i.e., it is often the case that there are more unknowns than equations [78].

In inverse CFD modeling, the governing equations that describe contaminant transport are "reversed" in order to determine source characteristics. Two inverse CFD modeling approaches were found in the literature: quasi-reversibility (QR) and pseudo-reversibility (PR) [82-83]. Both approaches require detailed information on airflow

patterns and contaminant distribution. These can be obtained from sensor data. However, for the studies, they were obtained from forward CFD simulations. The QR method locates sources by time-reversing contaminant transport. In contrast, PR locates sources by first reversing airflow and then estimating contaminant transport. Both inverse CFD approaches were able to correctly identify source locations. However, because inverse CFD modeling requires adequate airflow and contaminant data of a space to act as initial conditions, the approach may be *impractical* where large amounts of sensor data are unavailable. In addition, both studies were performed for aircraft cabins where the air change rate is 20-30 air changes per hour so that contaminant transport is dominated by convection and thus contaminant molecular *diffusion was neglected* in the inverse equations. Inverse CFD modeling may not be appropriate for indoor applications where diffusion is not always negligible [83].

Liu and Zhai [84] gave a summary of inverse modeling methods for indoor pollutant tracking, including the QR method just described. Another method is an inverse probabilistic approach called the adjoint probability method. The researchers applied the adjoint probability method to both CFD and multizone models. A probability-based inverse CFD model was able to successfully identify the source location in an office space [85], as opposed to the QR and PR methods which were shown not to be appropriate for buildings. A probability-based inverse multizone model was able to successfully identify the source location in a multiple-family residence and an institutional building [86]. The computational time for these inverse probabilistic approaches was no doubt significantly less than that for the inverse CFD model. Nevertheless, as with the QR and PR methods, the proposed inverse probabilistic

approaches also required a large amount of information, like the airflow field, in order to identify the source location.

Multiple hypothesis tracking (MHT) [87] technique determined the probability that an observation at time t_i from one sensor location came from the same source as an observation at time t_{i-1} at another sensor location. In essence, MHT back-traced the transport of a contaminant from its source. Various contaminant transport tracks were hypothesized during sensor data collection. As more sensor data arrived, the algorithm converged on the most likely contaminant transport track, thus identifying the source location. To test MHT, source transport was modeled using by Fick's Law of diffusion, and thus the method is currently limited to gas transport. A constant release was simulated in the study. All simulations were performed in two-dimensions. Wind was also introduced as a pseudo-random variable. Wind arrived from only eight possible directions at a uniform, constant rate. There was no mention of turbulence or how it would affect the source plume or the results of the study.

The uniform linear array (ULA) delay-and-sum beamformer technique utilized sensor data to determine the direction-of-arrival (DOA) of a contaminant plume [88]. The approach was based on the propagation delay of signals between sensors, which were placed at known distances apart. By observing the output gain of a given sensor array, the time and direction of an arriving contaminant plume was identified. Similar to MHT, this method is also currently limited to gas transport. Only a constant release of the source was simulated in the study. However, unlike MHT method, this study introduced turbulence, though it was modeled as intermittent "events" in the plume and not as an

additional mathematical model. The ULA method was able to predict the DOA in the presence of "turbulence" as well.

1.3.4.3 Summary

Characterizing contaminant sources is important to first responders who seek to contain and eliminate a contaminant. This information also helps them to reduce exposure to the population affected. Methods both in outdoor and indoor applications were discussed. Many of the methods required some amount of forward modeling. Reducing the amount or complexity of simulations would improve the efficiency of these source characterization methods. Inverse models discussed in Sec. 1.3.1.7 may provide the accuracy and efficiency needed for time-sensitive contaminant source characterization. The two methods that required no forward modeling, MHT and ULA, were limited to gaseous transport and did not account for or approximated turbulence.

1.3.5 Building airflow network

An appropriate estimate of a *building airflow network* is important when determining IAQ and energy use, and for indoor air sensor system design. It can be determined using forward airflow models, but detailed information about a building is required. Specialized experiments can also be used. Fan pressurization tests are used to determine building envelope airtightness, which is characteristic of the envelope construction. Tracer gas tests are used to determine building air change rate under specific outdoor and indoor conditions. Tracer gas tests can also be used to determine interzonal airflows.

The limitation to current blower-door tests is that they are designed for use with single-zone or small multi-zone buildings. The limitations to current tracer gas tests are:

they use specialized equipment; and their results cannot be generalized to indoor and outdoor conditions that are significantly different from the test conditions. The current methods for determining a building airflow network are limited in their application. They either require a large amount of time and effort or are limited in the size of the building that can be considered. A more detailed review of the literature on blower-door and tracer gas tests is given in Chapter 4, which discusses the framework for developing a building airflow network inverse model.

1.4 Research needs and motivation

Sec. 1.2 presented the framework for systematic indoor air sensor system design, which first requires an understanding of indoor airflow patterns. Indoor airflow patterns are used to predict contaminant distribution, which in turn is used for systematic sensor system design. As reviewed in Sec. 1.3.1, both forward and inverse airflow models are available, but no systematic selection of a *forward* airflow model for sensor system design has been found in the literature. Further, the potential for utilizing inverse models for sensor system design has also not been found in the literature. Therefore, the first research need is to develop a framework for utilizing *forward* airflow models for systematic sensor system design. The second research need is develop a framework for utilizing *inverse* airflow models for systematic sensor system design. This includes developing an appropriate inverse model as well.

1.4.1 Framework for utilizing a forward airflow model

The available forward airflow models for the systematic design of indoor air sensor systems are multizone, zonal, and CFD models. "Indoor air sensor systems" will be further referred to only as "sensor system" in the text for brevity. Multizone and zonal

models are relatively easy to set up and computationally efficient. However, they do not provide as *detailed* airflow and contaminant results as those provided by CFD models. Experimental studies also show that well developed CFD models provide more *accurate* airflow and contaminant distribution results than multizone and zonal models. However, CFD models are more difficult to set up and more computationally intense.

The first research need is to develop a framework for utilizing *forward* airflow models for systematic sensor system design. This involves establishing criteria for selecting the most appropriate forward airflow model for a given zone or building. In Sec. 1.3.3.4, the selection of an airflow model was either out of convenience (thus choosing the multizone model) or for proven accuracy (thus choosing the CFD model). However, selecting the most appropriate airflow model should not be limited only to ease in setup, model accuracy, and model efficiency. The selection process should also evaluate the model's effect on the output. The desired output here is whether or not the selected airflow model can provide adequate data for designing sensor systems that can meet design criteria. For instance, if sensor systems designed using multizone data could perform just as well as those designed using CFD data, there would be no justifiable reason to recommend using CFD models for sensor system design.

1.4.2 Framework for developing and utilizing an inverse airflow model

Forward airflow models all have one thing in common: they produce results specific for each zone or building. With each new zone or building, a new model of the physical system needs to be created. For rooms with regular geometry (e.g. rectangular) and small buildings, creation of a model may be straight-forward. However, for more complex geometries and larger buildings, creating a model is not a trivial task. Further,

for existing buildings, where accurate, up-to-date architectural and mechanical plans may be incomplete or missing, creating a model would first require time for field inspection. Thus, the development of accurate inverse models would be beneficial. Inverse models have the potential to provide the information on airflow patterns and contaminant transport for systematic sensor system design without the need for time-consuming forward modeling.

The second research need is to develop a framework for utilizing *inverse* airflow models for systematic sensor system design. This involves first, the *development of an inverse airflow model* that is easy to use, computationally efficient, and also accurate. Inverse airflow models have several advantages over forward airflow models. (1) They reduce the time and effort for set up that forward models require each time a new zone or building configuration is encountered. (2) Interior obstructions to airflow, which include furniture and people, can affect contaminant transport and thus sensor system performance. Inverse models can use actual sensor measurements located in real spaces to estimate airflow patterns and contaminant transport within that space or between spaces. These measurements inherently capture the effects of interior obstructions, where forward airflow models may not be able to capture correctly or even at all. Inverse models could utilize information collected from commonly installed sensor systems, such as airflow rates and/or velocity, temperature, or carbon dioxide (CO₂) concentration.

For a single zone: One can use the estimated airflow pattern within a single zone for *systematic sensor system design*. One would like to place sensors in locations where the information collected is most useful. For instance, if a DCV (see Sec. 1.3.3.4) relies on indoor CO₂ measurements to determine an appropriate ventilation rate, then the CO₂

sensors should be placed where the measurements will best represent the indoor CO₂ level. One would not want to place the sensors in "dead" area of spaces where uncharacteristically high or low CO₂ concentrations may exist. This would cause the DCV system to supply either too low or too high a ventilation rate, which adversely affects IAQ and energy use. The estimated airflow pattern can also be used for *disinfection purposes*. For instance, it can help to determine where a disinfectant should be released to maximize decontamination effectiveness.

For a whole building: One can use the estimated airflow pattern within a building to determine *building envelope airtightness* – overall values and also in specific parts of a building. It can also be used to provide a quick estimate of the *transport of other unmeasured contaminants*. In an experimental study at an empty school building, researchers found that intuitive HVAC control measures to control the spread of a contaminant released at an outdoor air intake duct could actually increase the level of contamination [89]. An inverse model of the building could have been used to *inform HVAC control* since it could have predicted the spread of the contaminant and what measures to take to reduce the level of contamination, etc. The estimate provided by the inverse model could also *direct first responders* to the areas of highest contamination before starting decontamination. It can also be helpful in reporting the effectiveness of decontamination – if it is safe for people to re-enter a building. The estimated airflow pattern from an inverse model also has the potential to provide *insight into the pressure distribution* of a building, which is critical in spaces such as laboratories and hospitals. Lastly, it can be used for *building commissioning*.

1.5 Research scope and hypotheses

Based on the identified research needs, this research was divided into three parts. The first part examined the effect of different forward airflow models and different zone characteristics on sensor system design. It identified the most appropriate forward airflow model for systematic sensor system design in a variety of single zones. The second part of this research examined inverse model development for a single zone and the sensor system design that collects the information for developing the inverse model. The third part of this research extended Part 2 by examining inverse model development for a *whole building*. It also presented a framework for utilizing information from a distributed sensor network to develop such an inverse model.

The following three hypotheses were tested, each one associated with each part of the research:

1. For each class of zone or building configuration, there exists a simplest *forward* airflow model to simulate indoor airflow patterns and contaminant transport for systematic sensor system design.
2. There exists an *inverse* airflow model that is able to efficiently and accurately estimate indoor airflow patterns and contaminant transport utilizing measurements from an indoor air sensor system.
3. There exists a framework for efficiently and accurately determining the airflow pattern within a whole building using a distributed sensor network.

Chapter 2 will discuss the results of testing Hypothesis #1, Chapter 3 will discuss the results of testing Hypothesis #2, and Chapter 4 will discuss the results of testing

Hypothesis #3. Each chapter concludes with recommendations for future work. General conclusions and recommendations for future work are given in Chapter 5.

2. CHAPTER 2: TESTING HYPOTHESIS #1 – SELECTING A FORWARD AIRFLOW MODEL

2.1 Preliminary studies

Two preliminary studies were published in *Building and Environment*, a peer-reviewed journal with impact factor of 1.192. They are included in APPENDIX A. The first study [90] performed systematic sensor system design on a medium-sized building using a subzoned-multizone model. That is, each physical zone was subdivided into subzones, similar to using a zonal model, but no mixed subzones with driving elements were modeled as is done in zonal modeling (Sec. 1.3.1.2). The study demonstrated the feasibility of using a subzoned-multizone airflow model and genetic algorithm (GA) for sensor system design. The effect of different sensor sensitivities on resulting sensor system designs was also studied. The second study [91] performed sensor system design on three test spaces (typical single office, large single hall, and a three-office suite). The study compared the performance of sensor systems designed using contaminant data from three forward airflow models: a subzoned-multizone, zonal, and CFD model. It was shown that unless a unique sensor system was needed, sensor systems designed using data from simpler airflow models performed just as well as those designed using more accurate CFD data for the single office and three-office suite, but not for the large hall. If there was *one and only one* sensor system that gave the minimum objective function value, that sensor system was given the description "unique". Only limited layouts were tested in these test spaces, and there was no internal furniture considered.

From these preliminary studies, it could be seen that there were limitations to using the simpler airflow models for designing sensor systems that could perform as well

as those designed using more complex airflow models. Thus, this chapter examines those limitations in regards to different zone characteristics.

2.2 Chapter 2 outline

Sec. 2.3 presents the zone characteristics that were varied in order to observe which ones contributed to whether or not data from a simpler airflow model could be used to design sensor systems that performed just as well as those designed using more accurate CFD data. Sec. 2.4 presents the experimental design method used to generate the various test zones. Sec. 2.5 and 2.6 describe how each test zone was modeled in the multizone, zonal, and CFD models. Sec. 2.7 describes the contaminant releases simulated in each test zone. Sec. 2.8 describes how the contaminant data from an airflow model were used to design sensor systems. In lieu of experimental data, Sec. 2.9 describes how the performance of the designed sensor systems was validated/benchmarked. The results are discussed in Sec. 2.10, conclusions in Sec. 2.11, and future work in Sec. 2.13.

2.3 Zones simulated

The variation among zone and building shapes, sizes, interior layout, and uses is nearly endless. No two zones/buildings are identical. Currently, a new computer representation would need to be set up for every zone or building that is to be evaluated. Further, each of the three available airflow models requires a different setup. For indoor air sensor system design, one would like to use the simplest airflow model. This saves time without compromising design objectives. Currently, to determine the simplest airflow model, one would set up three representations for each of the three airflow models, and then simulate airflow patterns and contaminant transport. This methodology does not compromise design objectives, but it also does not save time. Therefore, it is

desirable to determine the simplest airflow model needed for systematic sensor system design for different classes of zones and buildings based on specific characteristics of the zone or building.

This research is an initial step in classifying zones and buildings for the purpose of selecting the simplest forward airflow model for sensor system design. With future development, given any zone or building, one can use such classification to determine the simplest airflow model for the purposes of sensor system design without needing to simulate the zone or building in multiple airflow models.

This research focused on commercial-use zones only. A suite of zones, like a small building, was tested in a preliminary study [91]. It was found that a sensor system designed using data from a simpler airflow model could perform just as well as one designed using more accurate CFD data *only* when the total number of sensors was not too small (reported to be two in [91]). The simpler airflow models were limited in their capabilities to provide data for designing sensors systems that could perform just as well as those designed using CFD data. Therefore, the effect of zone characteristics in *buildings* on systematic sensor system design was not tested in this research.

Larger zones sizes were tested in [91-92]. It was found that a sensor system designed using data from a simpler airflow model could perform just as well as one designed using more accurate CFD data *only* when the total number of sensors was equal to the number of simulated contaminant releases. Thus, the simpler airflow models were limited in their capabilities to provide data for designing sensors systems that could perform just as well as those designed using CFD data. Therefore, the effect of zone characteristics on *larger* zones was not tested in this research, and the zone size was fixed.

The size of the zone that was tested in this research was selected based on architectural design guidelines. Thus, a **12 × 12 ft (3.7 × 3.7 m)** zone was selected from [93] as the base value for the size. It was the size of a typical private office. The ratio of L/W for this zone size was 1:1. Architectural standards also report that heights of ceilings range from [8.0, 13] ft ([2.5, 4.0] m), depending on whether the ceiling is finished or not. For this research, the standard **8 ft (2.5 m) finished ceiling** was chosen since finished ceilings are more likely to be found in commercial spaces.

"Zones" were defined as a space:

- That had a stand-alone HVAC system. In this research, the HVAC system supplied 100% outdoor air to the zone. Ducts in the multizone and zonal model were modeled using the Darcy-Colebrook model with average roughness of 0.15 mm. Ducts were of unit length, 1.0 m. No modeling of ductwork was needed when using the CFD model.
- Where the pressure inside and outside are *not* equal. Thus, infiltration was modeled. Openings on the exterior walls were modeled as small cracks. The same weather conditions were imposed on all sides of the zone. Thus, temperature differences due to solar radiation and pressure differences due to wind conditions were not modeled. During a year-long study of air change rates in an occupied house, it was found that wind speed and direction had very little influence on the air change rates [94].

Zones differ in innumerable ways. Some of them include: size, diffusers (airflow rate, shape, size, and location), exhausts (shape, size, and location), furniture (types, sizes, and placement), ventilation system (type, amount of outdoor air), and airtightness (tight,

leaky). In this research, zones were classified by *three* characteristics: the diffuser, furniture, and level of airtightness. The literature has shown that these three characteristics can have a great impact on the indoor airflow and thus contaminant transport [95-96].

Given an airflow rate, the shape and size of a diffuser will affect the speed through which air is delivered to a zone. This in turn affects the flow condition (e.g., turbulence, mixing effects). The location of the diffuser and exhaust will also affect the circulation pattern. Lastly, furniture is present in almost all real indoor environments. They present obstructions to indoor airflow and can affect circulation patterns. The following sections discuss the range of "values" for diffuser (airflow rate, shape, size, and location), presence of furniture, furniture placement, and airtightness level used in this research. The letter assigned to each respective characteristic (i.e., input factor) was *A*, *B*, *C*, and *D*.

2.3.1 Diffuser characteristics (location, *A*)

The first zone characteristic evaluated was the diffuser. Diffusers can be specified by airflow rate, shape, size, and location. Most diffusers for commercial spaces are either round or square. Titus, a manufacturer of diffusers, recommends round diffusers for large spaces such as gymnasiums and atriums. Square diffusers are suitable for most other applications. Thus, for this research, **square diffusers were selected** as the selected zone size was not large enough to warrant the use of round diffusers.

Diffusers have louvers that are angled in order to more effectively deliver air to the occupied space within a zone (Figure 2-1). A simple method to model the complicated geometry of a diffuser is to represent it as an opening with the same area as

the *effective* area of the actual diffuser. This approach can be taken in any of the three available forward airflow models. A more complex method, and one that is the subject of much research [97-99], is including the louvers in a CFD model. The "rectangular grille" diffuser macro in Airpak [100] was selected to model diffusers in this research. It is modeled by the momentum method [97, 100]. Details on this method will be given below.

The airflow rate and size of the diffuser were assigned values that remained constant through all test cases. These were fixed so that turbulence effects caused by the diffuser would be similar for all test cases. The airflow rate through a diffuser can be calculated by knowing the desired number of air changes per hour (ACH) in the zone. ACH is the number of volumes of air changed in an hour. For example, one ACH for a 100 m³ zone would be equal to 100 m³/hr through the diffuser. For commercial spaces, a typical range of 4 to 10 ACH was reported [101]; thus an average value of **7 ACH was chosen**. The effective size (or area) of a diffuser can be calculated by dividing the desired airflow rate (m³/hr) by the desired air speed (m/s). A guideline of 25-45 fpm is recommended for commercial spaces [101]; thus an average value of 35 fpm (640 m/h) was chosen. Given the ACH, zone volume, and desired air speed, a single square diffuser would be modeled with a volumetric flow rate of **150 cfm (0.7 m³/s)** and an effective area of **4.0 ft² (0.37 m²)**.

In Airpak, additional parameters (throw, terminal velocity, effective area ratio or velocity decay constant) need to be specified in order to model a diffuser using the *momentum method* [100]. By this method, the airflow from a diffuser is modeled as:

$$\frac{u_m}{u_0} = K_1 \frac{\sqrt{A_0}}{x} \quad (1)$$

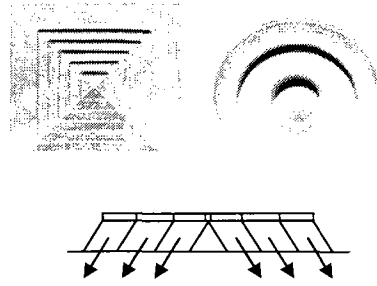
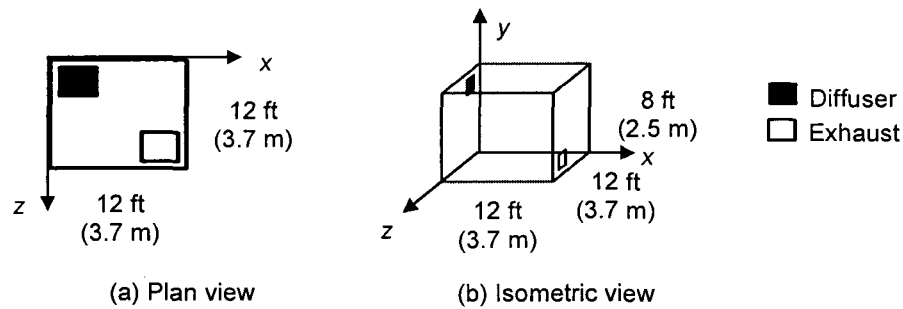


Figure 2-1. Diagram of actual diffusers.
Source: Titus

where u_m is the terminal velocity a distance x (or throw) from the diffuser, u_0 is the initial jet velocity, A_0 is the effective area, and K_I is an empirically-determined velocity decay constant. The throw and terminal velocity of the diffuser were selected from manufacturer catalogs for the specified flow rate of 150 cfm ($0.7 \text{ m}^3/\text{s}$). The throw was specified as 10 ft (3.0 m) and the terminal velocity specified as 150 fpm (0.8 m/s). The effective diffuser area in Eq. (1) is a function of the effective area ratio, if specified, and the overall dimensions of the diffuser. The velocity decay constant would then be calculated by Airpak. If, on the other hand, a velocity decay constant is specified, then the effective area is calculated by Airpak. In this research, each diffuser was limited to one louver. Therefore, the effective area ratio was specified as 1.0. For a ceiling-mounted diffuser, air was delivered at an angle of 30° from the ceiling. For a wall-mounted diffuser, air was delivered 30° from horizontal. Additional louver set-ups were tested but resulted in numerically unstable CFD solutions.

The location of a diffuser and exhaust affect the indoor airflow pattern. This subsequently affects contaminant removal efficiency. Diffusers and exhausts can be wall-



**Figure 2-2. Two diffuser/exhaust layouts for simulated zone.
(not to scale)**

or ceiling-mounted. Both types are used in this research. Figure 2-2(a) shows the locations of a single ceiling-mounted diffuser and exhaust at opposite corners of the zone. Figure 2-2(b) shows the locations of a single ceiling-mounted diffuser and exhaust on opposite walls and opposite corners of the zone. Here, the diffuser is mounted near the ceiling while the exhaust is mounted near the floor. These layouts were chosen since they are two common design practices for locating diffusers/exhausts for a room of this size. Because the ceiling-mounted diffuser was placed in the corner, it was modeled as a 2-way diffuser in CFD. The wall-mounted diffuser was modeled as two separate 1-way diffusers in CFD. See Figure 2-4 for a graphic of the CFD models.

2.3.2 Furniture (*B* and *C*)

The second zone characteristic, *B*, was whether the zone was empty or contained a piece of furniture. It was assumed that a single piece of furniture was placed in the zone, when applicable. The furniture was represented as a 2-D surface, resembling a table top with no legs. The third zone characteristic, *C*, was whether the piece of furniture was located under the exhaust or under the diffuser, when applicable.

Two techniques have been found in the literature to model furniture: solid and resistance. Using the solid technique, furniture is modeled as distinct objects, such as table surfaces, chairs, etc. and have impermeable surfaces. This means that no air is allowed to pass through the surfaces, which is a realistic assumption. Using the resistance technique, furniture is modeled as a single group of objects and has permeable surfaces. This means that a specified amount of air is allowed to pass through the surfaces. The resistance technique is most often used to model, for example, auditoria seating, when modeling each individual seat is impractical. A study that used the resistance technique to model furniture was [102]. In this study, furniture was limited to a single piece and so the solid modeling technique was utilized.

Modeling furniture in CFD requires the addition of solid no-slip surfaces to the model. Modeling furniture in the subzoned-multizone and zonal models requires that no flow path be specified between subzone interfaces where the piece of furniture is placed. Figure 2-3 shows a zone divided into four subzones. Figure 2-3 shows the top surface of a subzone "black-out" because it is to be modeled as a 2-D furniture surface.

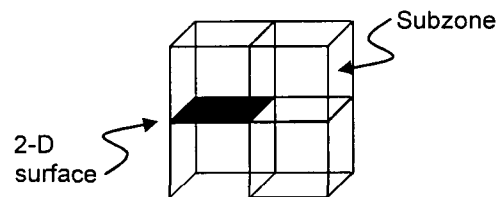


Figure 2-3. Example of how furniture was modeled in multizone and zonal models.

2.3.3 Airtightness (*D*)

Building airtightness can affect the transport of contaminants, IAQ, and operation effectiveness and efficiency of the ventilation system. Thus, it is important to evaluate the effect of different levels of airtightness on sensor system design. Table 2-1 lists some values of air leakage for one-story homes in the U.S. Since the zone simulated was also one-story and relatively small, it was assumed that this data would be appropriate for this research. Each of the airtightness values should be multiplied by the envelope area in order to determine the volumetric flow rate of the total leakage from the zone at the specified pressure difference.

The air leakage values in Table 2-1 can be converted from $\text{m}^3/\text{h}\cdot\text{m}^2$ to effective leakage area (ELA) at 0.016 in H_2O (4 Pa), in cm^2/m^2 of wall area, by multiplying by 0.16. ELA was a concept developed by the Lawrence Berkeley National Laboratory. It is essentially the total area of orifices (with discharge coefficient of 1) that would result in the same leakage airflow rate as that measured at the reference pressure difference. ELA is often calculated at 0.016 in H_2O (4 Pa), especially in houses, since this is the order of magnitude of typical indoor-outdoor pressure differences. The ELA at 0.016 in H_2O (4 Pa) for a "leaky" condition would be equal to $5.6 \text{ cm}^2/\text{m}^2$ ($0.08 \text{ in}^2/\text{ft}^2$) (Table 2-1).

To model infiltration in the multizone and zonal models, the air leakage values in Table 2-1 were converted to a mass flow coefficient (kg/s @ 1 Pa/m^2). First, the air leakage values given at 50 Pa were converted to values at 1 Pa using the power-law equation:

$$F = K(\Delta P)^n \quad (2)$$

where F is the air leakage value ($\text{m}^3/\text{h}\cdot\text{m}^2$) from Table 2-1, K is the constant to be determined, n is the flow exponent (dimensionless), and ΔP the reference pressure for which F was determined. In this case, ΔP was 50 Pa. Therefore, for the leaky condition, K was 2.115 using a typical value for $n=0.65$ [5]. Thus, at 1 Pa, $F=2.115(1 \text{ Pa})^{0.65}=2.115 \text{ m}^3/\text{h}\cdot\text{m}^2$. Multiplying by the density of air ($1.204 \text{ kg}/\text{m}^3$) and converting from hours to seconds, this resulted in a mass flow coefficient of $0.0007 \text{ kg}/\text{s} @ 1 \text{ Pa}/\text{m}^2$. The airflow model then calculated the leakage rate through a crack using this mass flow coefficient and the area of the wall using the power-law equation given above.

To model infiltration in CFD, the ELA at 0.016 in H_2O (4 Pa) was first converted to ELA at 0.004 in H_2O (1 Pa), in order to be consistent with the air leakage value specified in the multizone and zonal models. It was calculated to be $5.04 \text{ cm}^2/\text{m}^2$ ($0.072 \text{ in}^2/\text{ft}^2$), which is very similar to the ELA at 0.016 in H_2O (4 Pa).

Figure 2-4 shows that on each wall, three air leakage paths were modeled in CFD. The literature on modeling air leakage in CFD is limited, if not non-existent. Therefore, the choice of three air leakage paths was selected from studies of air leakage in manufactured homes using a multizone airflow model [104]. Given that the ELA at 0.016 in H_2O (4 Pa) was calculated to be $5.04 \text{ cm}^2/\text{m}^2$ ($0.072 \text{ in}^2/\text{ft}^2$), and that the area of a wall

Table 2-1. Air leakage values for one-story U.S. houses.

	Air leakage @ 75 Pa (0.03 in H_2O) [$\text{m}^3/\text{h}\cdot\text{m}^2$]	Equivalent air changes per hour @ 50 Pa (0.02 in H_2O) [h^{-1}]
Tight	3.5	2
Moderately tight	8.8	5
Typical	17.5	10
Leaky	35.0	20

Source: [103].

was 144 ft^2 (13.7 m^2), each of the three air leakage paths was modeled as an opening of $1.08 \times 0.016 \text{ ft}$ ($0.33 \times 0.005 \text{ m}$) in CFD. Other configurations of air leakage paths were also considered. Figure 2-5(a) shows the air leakage paths modeled as window sashes. Figure 2-5(b) shows the air leakage paths modeled as extending the width of a wall. These configurations were not used, however, because the grid size around such air leakage paths in CFD would be much less than 0.016 ft (0.0005 m) in order to maintain the same ELA. This would have resulted in mesh sizes, and thus solution spaces, that exceeded the computing power of the desktop used in this research. In the multizone and zonal models, three leakage paths were also modeled. However, only the area of the *wall* needed to be specified. Therefore, for three leakage paths, each wall was divided into three portions.

Table 2-2 is a summary of the input factors that were used to simulate and classify different zones in this research, along with their various "values". The "-" and "+" will be explained in the following section. If the value of an input factor was held constant, it traversed both "-" and "+" columns. The value of these constant input factor values could be varied in future work.

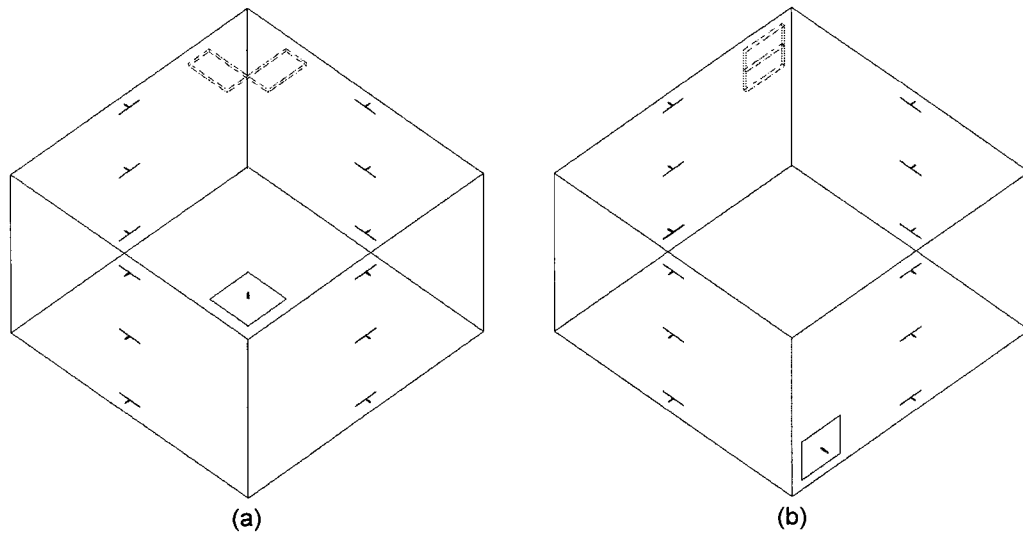


Figure 2-4. CFD models of air leakage paths in simulated zones with two diffuser/exhaust layouts.

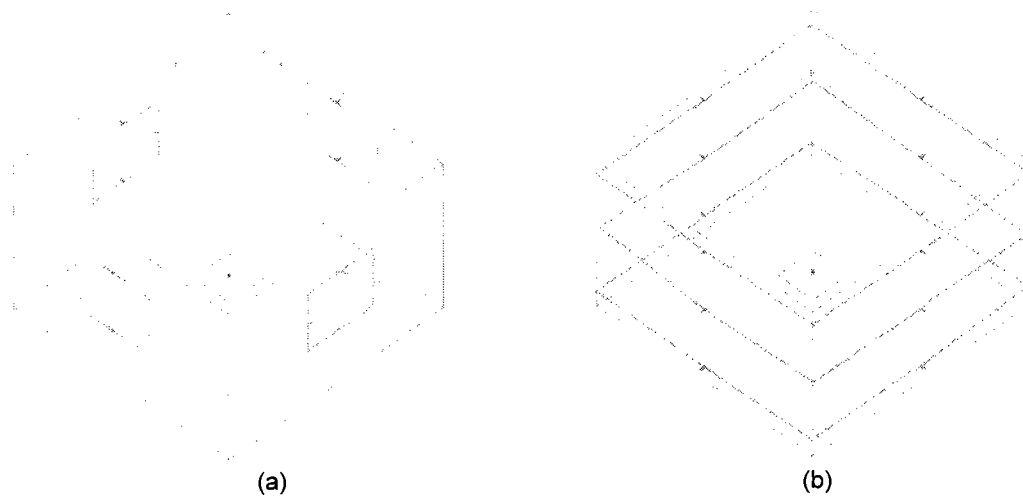


Figure 2-5. Alternative CFD models of air leakage paths (not used in this research).

Table 2-2. Summary of zones characteristics varied in this research.

Input factor designation	Zone characteristic	Parameter	"-" values assigned	"+" values assigned
A	Diffuser	Location Shape Airflow rate Size	Ceiling 150 cfm (0.7 m ³ /s) 4.0 ft ² (0.37 m ²)	Wall Square
B	Furniture	Present/Not present	Not present	Present
C		Location Modeling technique	Under exhaust Solid	Under diffuser
D	Airtightness		No leakage	Leaky

2.4 Computer experiments

Methods for designing physical experiments were applied to this research in order to systematically test the effect of each input on the output, or response. The inputs here were the zone characteristics. The response was the resulting sensor systems designed using contaminant transport data from an airflow model. A qualitative response was used in this research: whether or not the sensor system designed using data from a simpler airflow model could perform just as well as one designed using data from a more complex airflow model.

Two levels ("- and "+") for each input factor were described in Sec. 2.3 and summarized/assigned in Table 2-2. The number of experiments ran was n^k , where n is the number of levels and k is the number of inputs. Since there are four input factors (A =diffuser location, B =presence of furniture, C =location of furniture, and D =airtightness) and two levels each, the number of experiments to run would have been 2^4 or 16. But, when there was no furniture present (input factor B), the location of the furniture (input factor C) could not be varied (in Table 2-3, these simulations are darkened). Thus, the number of experiments ran was $2^4 - 4 = 12$. This design had three replications because

Table 2-3. Summary of test cases and responses using multizone model.

Test case	Input factors				Response
	Diffuser/ Exhaust Location	Furniture Presence	Furniture Location	Airtightness	
	(A)	(B)	(C)	(D)	
1M	-	-	-	-	$Y_{1,M}$
2M	-	-	-	+	$Y_{2,M}$
3M	-	-	-	-	$Y_{3,M}$
4M	-	-	+	+	$Y_{4,M}$
5M	-	+	-	-	$Y_{5,M}$
6M	-	+	-	+	$Y_{6,M}$
7M	-	+	+	-	$Y_{7,M}$
8M	-	+	+	+	$Y_{8,M}$
9M	+	-	-	-	$Y_{9,M}$
10M	+	-	-	+	$Y_{10,M}$
11M	-	-	+	+	$Y_{11,M}$
12M	-	-	+	+	$Y_{12,M}$
13M	+	+	-	-	$Y_{13,M}$
14M	+	+	-	+	$Y_{14,M}$
15M	+	+	+	-	$Y_{15,M}$
16M	+	+	+	+	$Y_{16,M}$

Note: "-" indicates low level; "+" indicates high level; subscript "M" indicates multizone model. A subscript "Z" would indicate zonal model, and subscript "CFD", the CFD model. Tables for zonal and CFD models are identical to this one except for the subscripts. They are not shown for brevity.

there three airflow models were tested, giving a total of $12 \cdot 3 = 36$ zone simulations. This number did not account for the number of contaminant releases (i.e., locations). In the text, each test case will be referred to by its input factor and level. For instance, test case 1M is for Zone $A[-]$, $B[-]$, $C[-]$, and $D[-]$.

The multizone model used was COMIS [6], the zonal model COWZ [20], and the CFD model FLUENT Airpak [100]. All simulations were performed on a Dell Dimension desktop with Intel Duo-Core Processor and 3GB RAM. The turbulence models available in Airpak were the standard κ - ϵ , RNG κ - ϵ , and indoor zero-equation models (Sec. 1.3.1.3). Both the RNG κ - ϵ and indoor zero-equation turbulence models have been recommended for indoor airflow in the literature. For this research, the

standard $\kappa\text{-}\varepsilon$ and the indoor zero-equation turbulence models were tested. The RNG $\kappa\text{-}\varepsilon$ model was not tested since convergence difficulties have been met when using it [26].

2.5 Model setup: multizone and zonal models

A subzonal modeling approach was taken when utilizing the multizone and zonal models. However, in the text, they have simply been referred to as multizone and zonal model. As discussed in Sec. 1.3.1.2, mixed subzones contain a well-mixed (or standard) portion and a driving element. In this research, the driving element was a velocity jet. Flow between the portions with a driving element is governed by designated mass flow relationships. For a vertical jet, the equation that described velocity distribution along the axis of the jet was [21]:

$$\frac{w_m}{w_o} = \frac{K_a}{\sqrt{2}} \frac{\sqrt{A_o}}{z} \left[1 \pm 0.09 \frac{|\Delta T_o| \sqrt{A_o}}{K_a w_o^2} \left(\frac{z}{\sqrt{A_o}} \right)^2 \right]^{1/3} \quad (3)$$

where the index m refers to the axis of the jet and the index o to the initial position of the jet (at the ceiling where $z = 0$ m). The area of the inlet is A_o (m^2). The constant K_a represents the apparent length of the constant velocity zone measured from the inlet [105]. The initial temperature difference, ΔT_o , is the difference between the inlet and room temperature ($^{\circ}\text{C}$). In this research, isothermal flow was assumed, therefore, ΔT_o was zero. The velocity along the jet axis is w_m , and the initial jet velocity is w_o . Finally, z is the distance from the inlet measured along the jet axis (m). The plus sign inside the brackets is used when the momentum of the jet is in the same direction as gravity, as it was in this research. Conversely, when the forces are in opposite directions, the minus sign is used.

The increase in jet radius, r , was assumed to be approximately linear and was:

$$\frac{w}{w_m} = \exp \left[-k \left(\frac{r}{z} \right)^2 \right] \quad (4)$$

where k is a dimensionless coefficient determined experimentally to be 77 for three dimensional jets [21]. Thus, the volumetric flow rate, $q(z)$, was:

$$q(z) = \int_0^{\infty} 2\pi r w \, dr \quad (5)$$

Substituting the expression for w in (4) into this equation and remembering that $q_o = A_o w_o$, the volumetric flow rate was:

$$\frac{q(z)}{q_o} = \frac{z_m(z)}{z_{mo}} = \frac{\pi}{\sqrt{2}} \frac{K_a}{k} \frac{z}{\sqrt{A_o}} \left[1 \pm 0.09 \frac{|\Delta T_o| \sqrt{A_o}}{K_a w_o^2} \left(\frac{z}{\sqrt{A_o}} \right)^2 \right]^{1/3} \quad (6)$$

Thus, the relationship between r and z was:

$$r = \sqrt{\frac{z^2}{k A_o}} \quad (7)$$

Since volumetric flow rate was related to mass flow rate, (6) is also the ratio of the mass flow rate at any distance z from the inlet ($z_m(z)$) to the initial mass flow rate (z_{mo}). Thus, given the distance from the inlet to the bottom of the jet, one can determine the width of the subzone required to capture the entire inlet jet. In selecting the sizes of the standard subzones, guidelines found in [20] were followed. For the tested zone size of $12 \times 12 \times 8$ ft high ($3.7 \times 3.7 \times 2.5$ m), a $5 \times 5 \times 5$ subzone layout was used (Figure 2-6).

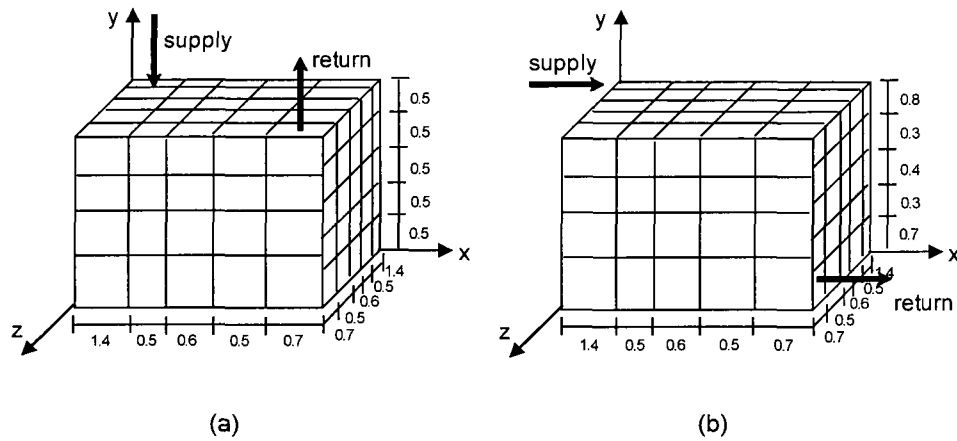


Figure 2-6. Subdivision of Zones (a) $A[-]$ and (b) $A[+]$ (not to scale).

Testing the sensitivity of the airflow results to changes in subzone size was not performed when using the multizone and zonal models because it has been shown that increasing the number of subzones did not improve the accuracy of resulting velocity [13]. Sensitivity tests where time step was varied, however, were performed. The time steps tested were 1, 5, 15, 30, and 60 seconds. No change was found for the airflow and contaminant transport results using different time steps in the multizone and zonal models. Both grid size and time step analyses were performed for the CFD models.

2.6 Model setup: CFD model

The grid size used to model typical indoor spaces found in the literature varied widely. Therefore, an optimal grid size and time step must be determined on a case by case basis. As mentioned in Sec. 2.4, the standard κ - ϵ and the indoor zero-equation turbulence models were tested. However, due to convergence issues with the indoor zero-equation turbulence model when modeling the diffusers, this research was performed using the standard κ - ϵ turbulence model.

2.6.1 Zone A[-]

For the test cases with the ceiling-mounted diffuser and exhaust (A[-]), grid and time step independence analyses were performed using several meshes and time steps. The meshes used were: $10 \times 10 \times 10$ cm uniform, $8 \times 8 \times 8$ cm uniform, $6 \times 6 \times 6$ cm uniform, and each uniform mesh with three refinements. The "refined meshes" included different levels of clustering around the diffuser and exhaust. For each refinement, the initial grid perpendicular to the surface(s) of the inlet, outlet, and contaminants was 3.0 cm. For the R1 meshes, the grid sizes continued to increase toward the center of the test zone at a ratio of 1.5. For the R2 meshes, the ratio decreased to 1.25, and for the R3 meshes, the ratio decreased to 1.03. The number of nodes in the meshes considered varied from 50,000 to 200,000. The time steps used were 0.25, 0.1, 0.05, and 0.01 seconds.

Resulting velocity profiles from the various meshes were compared for several locations around the room. It was found that velocity profiles across the middle of this zone along the x -direction were more affected by the change in grid size than other selected locations, even near the diffuser. Thus, only velocity profiles across the middle the zone were used in the selection of an optimal mesh. Figure 2-7 shows that the 10cm and 8cm uniform meshes produced airflow results more similar to each other than did the 6cm uniform mesh (steady-state, or SS, results). The difference in velocity, u_y , at the peak was 5% when the results were compared between the 10cm and 8cm uniform mesh. The reduction in grid size down to 6cm began capturing airflow effects near the walls, which consequently affected flow everywhere else. Since experimental data was not

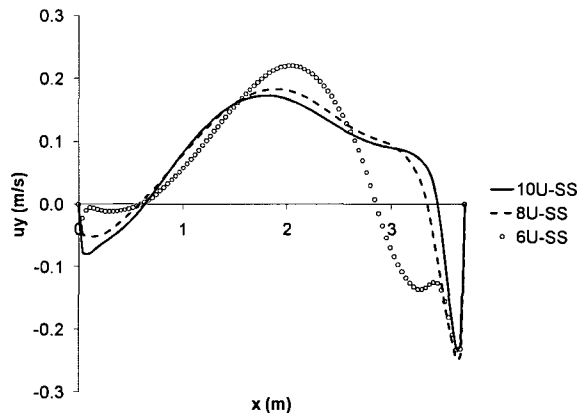


Figure 2-7. Velocity profile across middle of Zone A[-] (uniform meshes).

available to validate these CFD results, it was not possible to conclude which mesh was the "right" one or which one "should be" utilized. Thus, the 8cm uniform mesh was selected for grid refinement around the diffuser and exhaust since it would allow for savings in computational time since multiple CFD simulations needed to be performed for this research.

Velocity profiles resulting from the use of the refined 8cm meshes (steady-state) were compared. It was found that with greater refinement, the resulting velocity profiles converged. The differences between the velocity profiles resulting from the use of the first (R1) and second refinement (R2) of the 8cm uniform mesh was 5%. The difference was even smaller (1%) when velocity profiles using the 8R2 and 8R3 meshes were compared. **Thus, it was concluded that the 8R2 mesh would be used for the simulation of Zone A[-].**

The 8R2 mesh was subsequently used to determine the optimal time step for CFD simulations. The steady-state airflow results from the use of the 8R2 mesh were selected as the starting conditions for the transient simulations in order to conserve computational

time. Velocity profiles under the diffuser and in the center of the zone were compared in order to determine the optimal time step. The differences between the velocity profiles resulting from the use of $\Delta t = 0.25$ and $\Delta t = 0.10$ sec was approximately 10%. The differences between the velocity profiles resulting from the use of $\Delta t = 0.10$ and $\Delta t = 0.05$ sec was <5%. **Therefore, it was concluded that $\Delta t = 0.10$ sec was the optimal time step for Zone A[-].**

2.6.2 Zone A[+]

For the test cases with the wall-mounted diffuser and exhaust (A[+]), grid and time step independence analyses were performed using the same meshes and time steps for Zone A[-] (previous section). The number of nodes in the meshes considered for Zone A[+] varied from 99,000 to 250,000. Similar comparisons to the ones made in the previous section for Zone A[-] were made here in order to select the optimal mesh and time step for Zone A[+]. Figure 2-8 shows that using the 8cm and 6cm uniform meshes resulted in airflow more similar to one another than using the 10cm uniform mesh (SS results). The difference in velocity, u_y , at the peak was small ($3e-3$ m/s) when the results were compared between the 8cm and 6cm uniform mesh. Thus, the 8cm uniform mesh was selected for grid refinement around the diffuser and exhaust. **It was concluded that the 8R2 mesh would be used for the simulation of the Zone A[+].**

The 8R2 mesh was used to determine the optimal time step for CFD simulations. The steady-state airflow results from the use of the 8R2 mesh were selected as the "initial guesses" for the transient simulations in order to conserve computational time. Velocity profiles under the diffuser and in the center of the zone were compared in order to

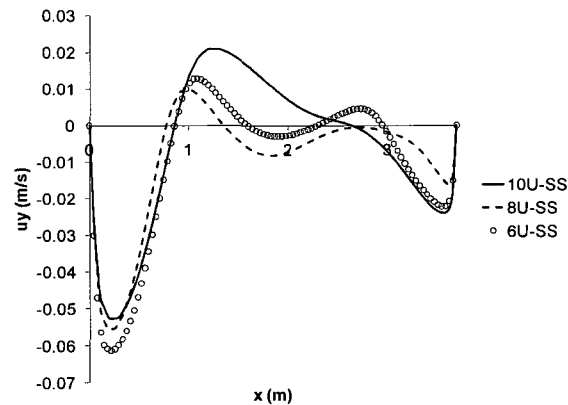


Figure 2-8. Velocity profile across middle of Zone A[+] (uniform meshes).

determine the optimal time step. The differences between the velocity profiles resulting from the use of $\Delta t = 0.25$ and $\Delta t = 0.10$ sec was $< 5\%$. The differences between the velocity profiles resulting from the use of $\Delta t = 0.10$ and $\Delta t = 0.05$ sec was even less, about 2% . **Therefore, it was concluded that $\Delta t = 0.25$ sec was the optimal time step for this Zone A[+].**

2.7 Contaminant releases

The release of a CBW agent was modeled as a constant source (5 mg/s) that was present from $t=0$ to $t=1.0$ min. The same four release locations were considered for each test case (Figure 2-9). Release location 1 was under the supply diffuser. Release location 2 was near the center of the test zone. Release location 3 was chosen near an occupant. Release location 4 was near the exhaust.

Subzone location names are given by their respective x , z , and y cell index. For instance, in Figure 2-9, the first release location was in subzone 111. The second release location was in subzone 321, and so on. In CFD, the contaminants are modeled as volumetric sources of size $0.25 \times 0.25 \times 0.25\text{m}$.

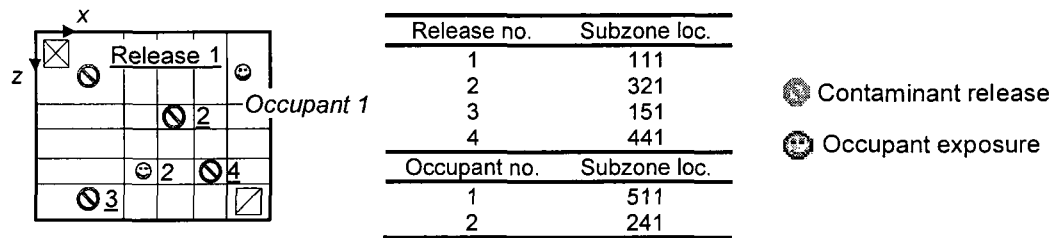
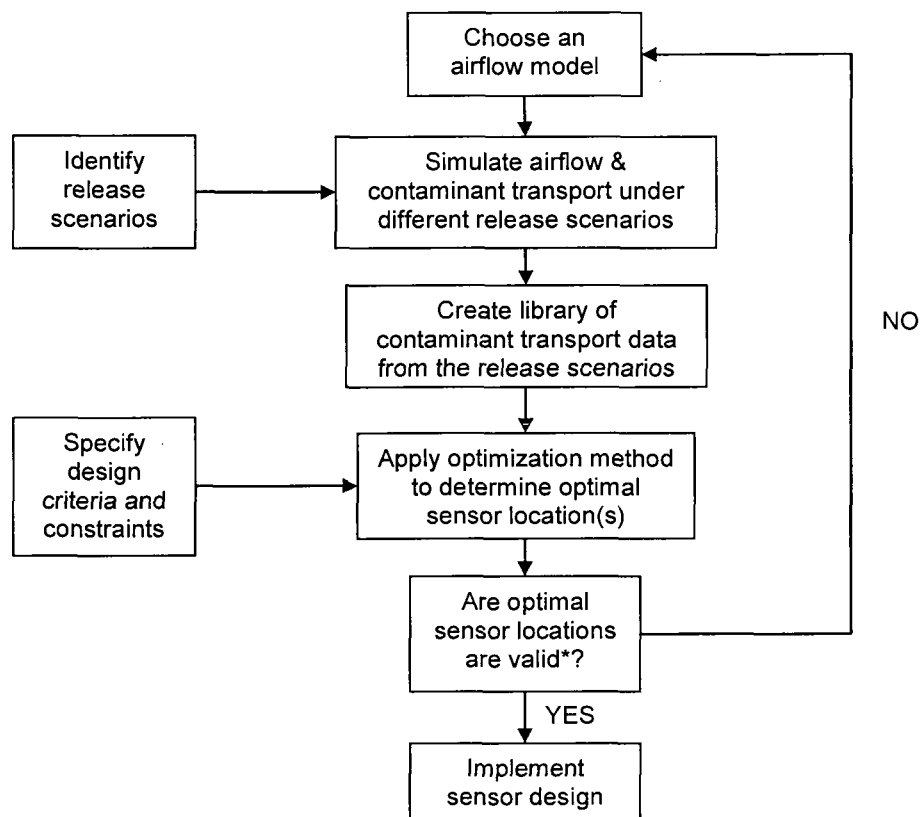


Figure 2-9. Locations of contaminant releases (underlined) and occupant exposures (*italics*). Subdivisions shown (not to scale). See text for subzone naming convention.

All contaminants were released on the floor. The release locations were designed for effective transport or ease of accessibility. They were also designed to test the simpler models based on differences in the airflow calculated by the three models. Large differences in airflow could lead to large differences in contaminant transport. Thus, by specifying contaminant releases in the subzones where the largest differences between the calculated airflow of the simpler airflow model and CFD model existed, it can be shown whether or not even the largest differences between the airflow models affected sensor system design. Tests Cases 1 and 9 (no furniture, no infiltration) (Table 2-3) were used to design the contaminant release locations.

2.8 Designing indoor air sensor systems

Upon completion of each simulation, a sensor system was designed according to the procedure in Figure 2-10. Selecting an optimization method, selecting design objectives, identifying constraints, and validating the sensor system design were some of the key components.



* A "valid" sensor system design here means that its performance is validated, either with experimental data or other benchmark, and will meet design objectives when implemented under real conditions.

Figure 2-10. Flow chart of sensor system design.

Designing sensor systems for indoor air applications requires an optimization method that can solve non-linear problems and is computationally efficient. As discussed in Sec. 1.3.2, the stochastic class of optimization methods were very useful in solving nonlinear problems from different areas of physical science and engineering [46]. Stochastic optimization methods were also considered in a study for indoor sensor placement [47]. Therefore, for this research, genetic algorithm (GA) was selected as the optimization tool for sensor system design.

2.8.1 Genetic algorithm (GA)

This discussion is adapted from [90]. The contaminant dispersion process is a complicated non-linear process, and sensor system selection is a discrete process. Hence GA, a stochastic search algorithm was selected as the optimization approach because of its ability to handle complicated non-linear problems, as well as discrete processes..

Figure 2-11 shows the basic process of a GA optimization. An initial guess was supplied for the design variables (i.e., sensor system designs), which served as the initial population. For each vector of n of initial guesses, the objective function (the ones used in this research to be discussed in the following section) was calculated and compared. The vectors that generated the best values of the objective function had the highest probability of becoming "parents" to the next generation. "Reproduction" of the parents was performed through "crossover" and "mutation" (Figure 2-11). Crossover was an exchange of the members (i.e., sensor locations of each sensor system design) of the parents. To prevent premature converging to a local optimal solution, a process called "mutation", which generates a new vector randomly, was involved in the process. Once a new population was generated, the values of the objective function were calculated and compared again. New parents were then selected and the process was repeated until certain optimization criteria were satisfied.

GA was employed using the Genetic Algorithm and Direct Search Tool in Matlab

[106] with the following options:

- Population size: 20
- Elite count (or number of parents): 2
- Crossover fraction: 0.8
- Mutation function: Gaussian
- Mutation scale: 1.0
- Generations: Infinity

Time limit: Infinity
 Fitness limit: -Infinity
 Stall generations: 200
 Stall time limit: Infinity

2.8.2 Design objectives (objective functions)

The objective functions for designing sensor systems for building protection purposes should be able to detect contaminants within an amount of time that poses the least threat to the building occupants across multiple release locations. The first objective function used was to minimize detection time, J_{det} [90]:

$$J_{det} = \sum_{k=1}^N p_k \times t_{det-k} \quad (8)$$

where p_k is the probability for the k th release location to occur, t_{det-k} is the detection time for scenario k , and N is the number of release locations. t_{det-k} for a particular release

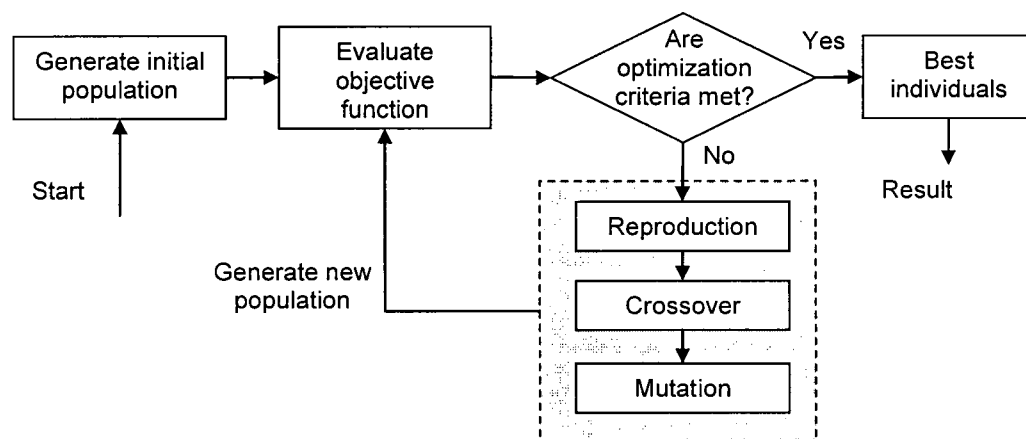


Figure 2-11. Genetic algorithm flow chart [90].

location k given a multiple-sensor system is the minimum detection time of all of the sensors. For example, for a 2-sensor system, the detection time for each release location might be (1) for sensor one: 1.0, 2.0, 1.5, and 1.0; and (2) for sensor two: 2.0, 1.0, 1.0, and 2.0. Thus, the detection time for each release location, $t_{\text{det-}k}$, given this 2-sensor system would be 1.0, 1.0, 1.0, and 1.0. In this study, p_k was $1/N$ for all release locations. Therefore the objective function value, J_{det} , was essentially the average detection time over all release locations, i.e., $\frac{1}{4}(1.0+1.0+1.0+1.0)=1.0$ min in the above example. The detection time for each release location was the **time when the measured contaminant concentration reached (or exceeded) the sensor threshold at a sensor location**. The sensor threshold was a fixed value, 0.03 mg/m^3 [107], for all sensor system designs. Thus, even if the three airflow models calculated *different* contaminant concentration at a sensor location at a specific time (say, 1.0 min), as long as the concentration at the sensor location was equal to or greater than the sensor threshold (0.03 mg/m^3), the detection time would be *equal* to 1.0 min. for all three airflow models Each sensor in the sensor systems designed in this research had the same threshold.

The second objective function used was to minimize occupant exposure, J_{exp} [90].

Total occupant exposure, E_k , for the k th release location was defined as:

$$E_k = \sum_{m=1}^S \sum_{t=0}^{t_{\text{det-}k}} \text{Exp}(m, t) \quad (9)$$

where $\text{Exp}(m, t)$ is the occupant exposure for the m th occupant at time t , and S is the number of occupants. For each occupant, the exposure is the total inhaled concentration up to the time when the sensor alarmed, i.e., when the contaminant concentration measured reached the sensor threshold at the sensor location.

$$E_k = \sum_{m=1}^S \sum_{t=0}^{t_{\text{det}}-k} B \cdot C(m, t) \quad (10)$$

where B is the inhalation rate, which was assumed to be constant for all occupants and all times, and $C(m, t)$ the local concentration at each occupant location. Thus, for all N release locations, the objective function based on total occupant exposure, J_{exp} , was defined as:

$$J_{\text{exp}} = \sum_{k=1}^N P_k \times E_k \quad (11)$$

Occupant exposures were evaluated at two locations in the test zone (Figure 2-9) at opposite corners. All occupant exposures were evaluated at the breathing level.

The sensor locations for which the contaminant concentration did *not* reach the sensor threshold within the simulation time period were penalized with a value of 1,000 for both detection time and occupant exposure. A penalty of 1,000 was used since it was at least an order of magnitude greater than the time for which concentration data was available. If the penalty value were set to be a value other than 1,000, some reported objective function values would change (those with a value larger than 100). However, as long as the penalty value was greater than the time for which concentration data was available, the results of this research would not change.

The constraints on a sensor system can include cost, quantity and location of sensors, and the types of sensors used. These constraints are interrelated and can affect the performance of a sensor system. Because the relationships between these constraints are complex, detailed evaluation of their interaction will be saved for future work. For this research, it was assumed that the cost of each sensor was the same, no matter its

location. Therefore, the constraint on the sensor system designs was the quantity of sensors.

2.9 Validation of sensor systems

Optimal sensor systems cannot be determined analytically, which is why optimization methods are employed for sensor system design. One way to validate a sensor system is to perform experiments. However, given the number of simulations in this research, a time-saving and often used method for validating airflow model data is to use CFD data. This assumes that CFD data is accurate. Initial studies have been done in order to verify Airpak, the CFD code used for this research. Published experimental studies that report velocity and/or contaminant data were used for verification purposes. CFD data thus took the place of actual experimental data.

Once a sensor system is designed, data from CFD models are used as synthetic experimental data to evaluate the detection times and occupant exposures (more generally referred to as "objective function values") associated with each sensor system. These objective function values were given different descriptive names in this research. The terminologies used were: multizone-optimal, zonal-optimal, CFD-optimal, and CFD-benchmarked objective function values. They differed in the airflow model data used to design the sensor system and the airflow model data used to calculate the objective function values. Figure 2-12 illustrates the connection between the terminology and the airflow models.

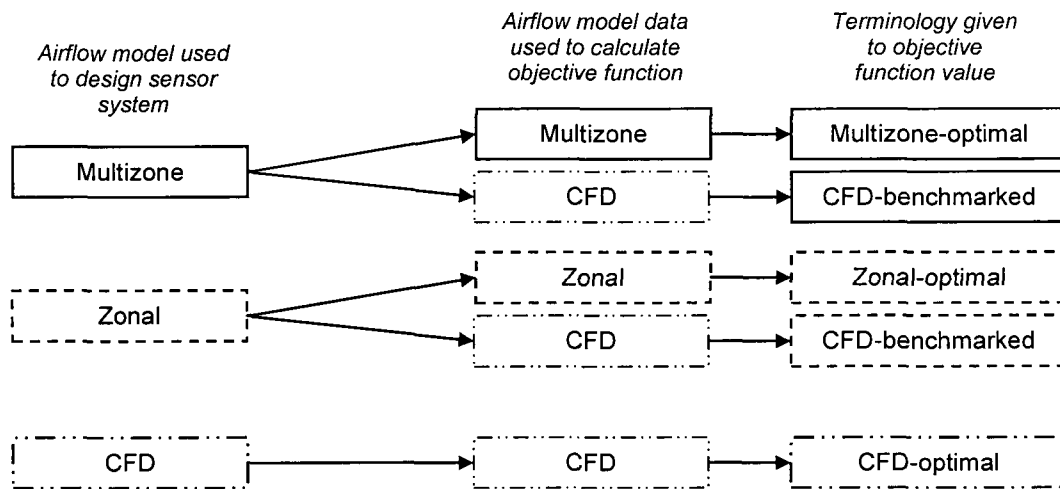


Figure 2-12. Connection between terminologies in research and airflow models.
Source [91].

When CFD data served as synthetic experimental data, volume-averaged CFD concentration data was calculated based on the subzone sizes used for the multizone and zonal models. The volume-averaged CFD concentration data was then used to calculate the detection time and occupant exposure for each sensor system designed using the multizone and zonal models (termed the "CFD-benchmarked" detection times and occupant exposures). Comparing CFD-benchmarked detection time and occupant exposure to CFD-optimal ones showed whether or not data from simpler airflow models could be used to design sensor systems capable of performing just as well as those designed using more accurate CFD data. Thus, the CFD-benchmarked values represented the potential performance of the simpler airflow models, whereas the multizone- and zonal-optimal values respectively represented the current capabilities of the multizone and zonal models.

2.10 Results and discussion

There were four contaminant release locations simulated in this research. Thus, up to 4-sensor systems for each design objective were reported for each test case. Table 2-4 to Table 2-14 summarize the sensor systems designed using the multizone and zonal model data for test cases that will be discussed in this main text. Similar tables for test cases not specifically discussed in this main text can be found in APPENDIX B. The results from some test cases were not specifically discussed in this main text because they shared similarities with those that were discussed.

The "Obj. func." (objective function) column in these tables referred to the design objective, either "D" for minimizing detection time or "E" for minimizing occupant exposure. For the sensor systems designed with the "D" objective, the units of the objective function value were in minutes. For the sensor systems designed with the "E" objective, the units of the objective function value were in kg of contaminant/kg of air (or kg/kg). The concepts of multizone-optimal, zonal-optimal, CFD-optimal, and CFD-benchmarked objective function values were introduced in Sec. 2.9 and Figure 2-12. A "complementary" objective function value was defined (denoted in parenthesis). They referred to the occupant exposure when "D" was the objective function used to design the sensor system, or detection time when "E" was the objective function value used to design the sensor system. The column "Locations using CFD data" were the sensor locations designed using CFD data alone. The last column indicated whether or not the CFD-benchmarked objective function value for each sensor system was equivalent to the CFD-optimal value for the same number of sensors. A "Y" indicated that the two values were equivalent, and thus the sensor system designed using data from the simpler airflow

model could perform just as well as one designed using more accurate CFD data. A "Y" also indicated that the sensor locations designed using either multizone or zonal model data were the same as those designed using CFD data.

If there was *one and only one* sensor system that gave the minimum objective function value, that sensor system was given the description "unique". It was marked with a "*". If there were multiple sensor systems that gave the same minimum objective function value, only one of the possible sensor systems was listed. The one listed was chosen based on similarity to the sensor systems designed using data from the other airflow models, thus allowing for a clearer comparison. In general, some 1-sensor systems were found to be unique, while multiple-sensor systems were found to be non-unique. Finally, "Eng" indicated a common engineering design practice. In this research, the 1-sensor system commonly employed in engineering design is to place a sensor at the exhaust. The location was subzone 555 for the test cases with the ceiling-mounted diffuser and exhaust (Zone A[-]). The location was subzone 551 for the test cases with the wall-mounted diffuser and exhaust (Zone A[+]).

2.10.1 Zone A[-]

Test Cases 1 – 8 are associated with the zone with the ceiling-mounted diffuser and exhaust. Keep in mind that Test Cases 3 and 4 were not simulated since there was no furniture and thus, its location could not be varied (see Sec. 2.4 and Table 2-3). Sec. 0 and 2.10.1.1 discuss the results for Test Cases 1 (no furniture, no infiltration) and 7 (furniture under diffuser, no infiltration), respectively. Details for the results of Test Cases 2 (no furniture, with infiltration), 5 (furniture under exhaust, no infiltration), 6 (furniture under exhaust, with infiltration), and 8 (furniture under diffuser, with

infiltration) were not presented since they shared similarities with either Test Case 1 or 7. In general, for Test Cases 1 – 8, sensor systems designed using data from the multizone and zonal models (i.e., simpler airflow models) were **able to perform just as well as those designed using more accurate CFD data, except for the 1-sensor systems**. In other words, the CFD-benchmarked detection time and occupant exposure were equal to the CFD-optimal ones. Keep in mind that any differences in the *values* of the contaminant concentration calculated by each airflow model did not affect the calculated detection time as long as the contaminant concentration *reached* (or *exceeded*) the sensor threshold.

Neither the absence nor presence of furniture or infiltration affected the ability of the simpler airflow models to provide the data for designing sensor systems capable of performing just as well as those designed using more accurate CFD data for sensor quantities greater than one. Lastly, the common engineering design practice of placing a sensor at the exhaust resulted in non-optimal performance when benchmarked with CFD data. Placing a sensor at the exhaust was no more, and no less, a robust design than placing a sensor at the location designed using multizone and zonal model data. Test Case 1 (no furniture, no infiltration)

Table 2-4 shows that the 2-, 3-, and 4-sensor systems designed using data from the multizone model was able to perform just as well as those designed using more accurate CFD data for Test Case 1. The 1-sensor system designed using multizone model data for Test Case 1 was subzone location 452 when minimizing detection time. It was the *only* location where the 1-sensor system was multizone-optimal and was thus marked

with an "*" in the table. Its CFD-benchmarked detection time was calculated as 1.5 min, which was **greater** than the CFD-optimal detection time of 1.0 min for a 1-sensor system.

Table 2-5 shows that the 2-, 3-, and 4-sensor systems designed using data from the zonal model was able to perform just as well as those designed using more accurate CFD data for Test Case 1. The 1-sensor system designed using zonal model data for Test Case 1 was *either* subzone location 451 or 452 when minimizing detection time. These locations were vertically adjacent subzones. These locations are marked with an "*" because these were the *only two* locations where a 1-sensor system was zonal-optimal. Their CFD-benchmarked detection times were calculated as 1.5 and 1.25 min, respectively, which were **greater** than the CFD-optimal detection time of 1.0 min for a 1-sensor system.

The common engineering design practice of placing a sensor at the exhaust resulted in non-optimal performance (CFD-benchmarked detection time of 1.5 min). The detection times for the sensor placed at the exhaust were 2.0, 2.0, 1.0, and 1.0 min, respectively for each release location. The multizone- and zonal-optimal 1-sensor systems (locations 451 or 452) also exhibited these detection times. Thus, placing a sensor at the exhaust was no more, and no less, a robust design than placing a sensor at the location designed using multizone and zonal model data.

Table 2-4. Sensor system designs for Test Case 1 using multizone model data.

Sensor sys. [1]	Qty [2]	Obj. func. [3]	Locations using multizone data [4]	Objective function value (complementary obj. func. value)			Locations using CFD data [8]	Col. [6] equiv. to [7]? [9]
				Multizone-optimal [5]	CFD-benchmarked [6]	CFD-optimal [7]		
1	4	D	151,251, 441,524	1.0 (5.9e-8)	1.0	1.0		Y
2	4	E	222,321, 433,555	5.9e-8 (1.25)	9.4e-4	9.4e-4		Y
3	3	D	151,423, 554	1.0 (5.9e-8)	1.0	1.0		Y
4	3	E	131,141, 455	5.9e-8 (1.5)	9.4e-4	9.4e-4		Y
5	2	D	231,552	1.0 (5.9e-8)	1.0	1.0		Y
6	2	E	121,553	5.9e-8 (1.5)	9.4e-4	9.4e-4		Y
7	1	D	452*	1.25 (1.0e-6)	1.5	1.0	252	N
8	1	E	331	5.9e-8 (500.5)	9.5e-4	9.4e-4	252	N
Eng	1	D (E)	555	2.25 (1.2e-5)	1.5 (1.1e-3)	1.0 (9.4e-4)	355	N

* unique sensor system

Table 2-5. Sensor system designs for Test Case 1 using zonal model data.

Sensor sys. [1]	Qty [2]	Obj. func. [3]	Locations using zonal data [4]	Objective function value (complementary obj. func. value)			Locations using CFD data [8]	Col. [6] equiv. to [7]? [9]
				Zonal-optimal [5]	CFD-benchmarked [6]	CFD-optimal [7]		
1	4	D	134,215, 453,533	1.0 (2.7e-6)	1.0	1.0		Y
2	4	E	134,351, 454,523	2.7e-6 (1.0)	9.4e-4	9.4e-4		Y
3	3	D	314,442, 553	1.0 (2.7e-6)	1.0	1.0		Y
4	3	E	235,434, 554	2.7e-6 (1.25)	9.4e-4	9.4e-4		Y
5	2	D	142,454	1.0 (2.7e-6)	1.0	1.0		Y
6	2	E	322,554	2.7e-6 (1.25)	9.4e-4	9.4e-4		Y
7	1	D	451 or 452*	1.0 (2.7e-6)	1.5 or 1.25	1.0	252	N
8	1	E	451 or 452	2.7e-6 (1.0)	1.10e-3 or 9.48e-4	9.4e-4	252	N
Eng	1	D (E)	555	1.5 (1.1e-5)	1.5 (1.1e-3)	1.0 (9.4e-4)	355	N

* almost unique sensor system

For Test Case 1, a sensor system designed to minimize detection time *did* also guarantee that occupant exposure was minimized, whether using multizone or zonal model data to design the sensor system. However, a sensor system designed to minimize occupant exposure *did not* also guarantee that detection time was minimized, whether using multizone or zonal model data to design the sensor system. For instance, the 4-sensor system designed to minimize detection time (Sensor sys. #1 in Table 2-4) had a detection time of 1.0 min and an occupant exposure of 5.0×10^{-8} kg/kg. Following the discussion in Sec. 2.8.2, the detection time was calculated as $\frac{1}{4}(1.0+1.0+1.0+1.0)=1.0$ min. The occupant exposure was calculated as $\frac{1}{4}(2.4 \times 10^{-7}+0+0+0) = 5.9 \times 10^{-8}$ kg/kg. Similar calculations were performed for Sensor sys. #2 in Table 2-4) (designed to minimize occupant exposure). Detection time was calculated as $\frac{1}{4}(1.0+1.0+2.0+1.0)=1.25$ min, and occupant exposure was calculated as $\frac{1}{4}(2.4 \times 10^{-7}+0+0+0)=5.9 \times 10^{-8}$ kg/kg (same value as for Sensor sys. #1). The detection time for release #3 was 1.0 min for Sensor sys. #1 and 2.0 min for Sensor sys. #2. Nevertheless, the occupant exposure for release #3 was always 0 kg/kg.

Figure 2-13 shows the contaminant contour plots for Test Case 1, Release #3 for all three airflow models at two times. When the contaminant was released from location #3, the contours plots of Test Case 1 modeled with the simpler airflow models showed that neither occupant was exposed to the contaminant (Figure 2-13a to d). Note that even though the contour lines may fall within the subzone of an occupant, the concentration there was always zero. On the other hand, the contour plots of the contaminant data simulated by the CFD model showed that at least one of the occupants was exposed to the

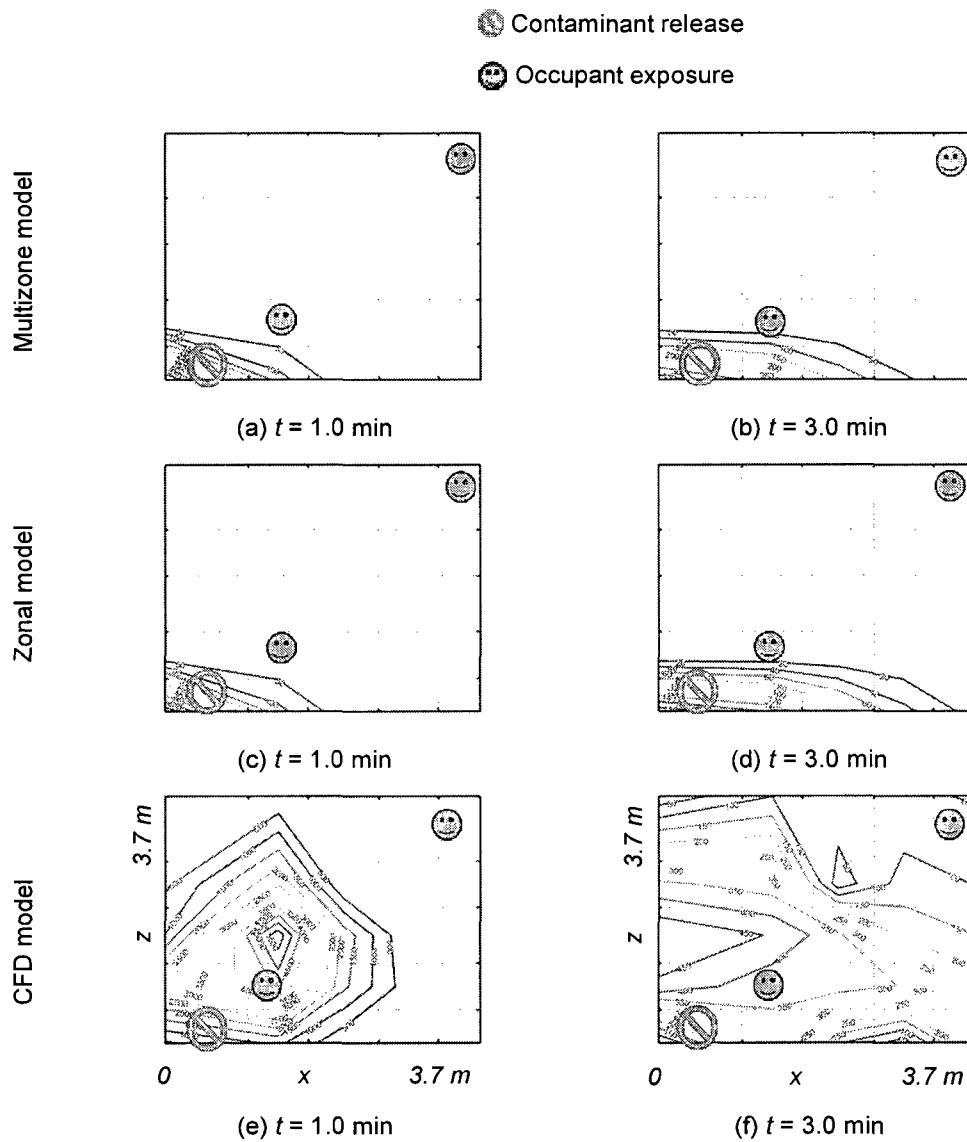


Figure 2-13. Contaminant contour plots for Test Case 1, Release #3.

contaminant within the first minute. Figures similar to Figure 2-13 can be found in the APPENDIX B for all the test cases and all of the contaminant releases. Since different detection times resulted in the same occupant exposure, minimizing occupant exposure could not also guarantee that detection time was also minimized. This was also observed

for the sensor systems designed using zonal model data (compare Sensor sys. #3 and 4 in Table 2-5).

In fact, for releases #2 to #4, the simpler airflow models calculated *zero* occupant exposure for *all* test cases simulated by the simpler airflow models for Zone A[-].

Therefore, for all test cases simulated by the simpler airflow models for Zone A[-], minimizing occupant exposure *did not guarantee* that detection time was also minimized.

The optimal 1-sensor location designed to minimize detection time using multizone model data for Test Cases 2, 5, and 6 were the same (subzone location 451). This location was vertically adjacent to the optimal 1-sensor location designed to minimize detection time using multizone model data for Test Case 1 (subzone location 452). The optimal 1-sensor locations designed to minimize detection time using zonal model data for Test Cases 2, 5, and 6 were the same (*either* subzone location 451 or 452). These locations were the same as the optimal 1-sensor locations designed to minimize detection time using zonal model data for Test Case 1. For Test Cases 2, 5, and 6, the 1-sensor systems designed using the simpler airflow models **did not** perform as well as those designed using more accurate CFD data. **Therefore, for all test cases simulated by the simpler airflow models for Zone A[-], the 1-sensor systems designed using data from the simpler airflow models did not perform as well as those designed using more accurate CFD data.**

The closest CFD-optimal subzone location for a 1-sensor system would have been subzone location 252 for Test Cases 1–6. This location was approximately 1.3 m away from the locations designed using data from the simpler airflow models. The 1-sensor

systems designed using data from three airflow models for the test cases for zone A[-] are summarized in Table 2-8 and shown graphically in Figure 2-15.

2.10.1.1 Test Case 7 (furniture under diffuser, no infiltration)

Table 2-6 shows that the 2-, 3-, and 4-sensor systems designed using data from the multizone model was able to perform just as well as those designed using more accurate CFD data for Test Case 7. The 1-sensor system designed using multizone model data for Test Case 7 was *either* subzone location 451, 452, 453, 551, or 552 when minimizing detection time. The first three and last two locations were vertically adjacent subzones. These locations were marked with an "*" because these were the *only five* locations where a 1-sensor system was multizone-optimal. Their CFD-benchmarked detections time ranged from 1.25 to 1.5 min, which were **greater** than the CFD-optimal detection time of 1.0 min for a 1-sensor system.

Table 2-7 shows that the 2-, 3-, and 4-sensor systems designed using data from the zonal model was able to perform just as well as those designed using more accurate CFD data for Test Case 7. The 1-sensor system designed using zonal model data for Test Case 7 was *either* subzone location 451, 452, or 453 when minimizing detection time. These locations were vertically adjacent. These locations were marked with an "*" because these were the *only three* locations where a 1-sensor system was zonal-optimal. Their CFD-benchmarked detections time ranged from 1.25 to 1.5 min, which were **greater** than the CFD-optimal detection time of 1.0 min for a 1-sensor system.

The common engineering design practice of placing a sensor at the exhaust resulted in non-optimal performance (CFD-benchmarked detection time of 1.25-1.5 min).

Table 2-6. Sensor system designs for Test Case 7 using multizone model data.

Sensor sys. [1]	Qty [2]	Obj. func. [3]	Locations using multizone data [4]	Objective function value (complementary obj. func. value)			Locations using CFD data [8]	Col. [6] equiv. to [7]? [9]
				Multizone-optimal [5]	CFD-benchmarked [6]	CFD-optimal [7]		
1	4	D	111,351, 442,544	1.0	1.0	1.0		Y
2	4	E		See note				
3	3	D	111,323, 452	1.0	1.0	1.0		Y
4	3	E		See note				
5	2	D	111,551	1.0	1.0	1.0		Y
6	2	E		See note				
7	1	D	451,452, 453,551, or 552	250.75	Range from 1.25 to 1.5	1.0	151,152, or 153	N
8	1	E		See note				
Eng	1	D (E)	555	251.25 (0)	1.5 (1.5e-3)	1.0 (1.2e-3)	144	N

Note: For *all* contaminant releases, occupant exposure is always 0 kg/kg. Therefore, all sensor systems designed using multizone model data result in the same occupant exposure, 0 kg/kg, and there are no "optimal" designs.

Table 2-7. Sensor system designs for Test Case 7 using zonal model data.

Sensor sys. [1]	Qty [2]	Obj. func. [3]	Locations using zonal data [4]	Objective function value (complementary obj. func. value)			Locations using CFD data [8]	Col. [6] equiv. to [7]? [9]
				Zonal-optimal [5]	CFD-benchmarked [6]	CFD-optimal [7]		
1	4	D	215,253, 444,521	1.0 (4.3e-6)	1.0	1.0		Y
2	4	E	131,241, 425,552	4.3e-6 (1.0)	1.2e-3	1.2e-3		Y
3	3	D	224,312, 552	1.0 (4.3e-6)	1.0	1.0		Y
4	3	E	334,422, 555	4.3e-6 (1.25)	1.2e-3	1.2e-3		Y
5	2	D	321,552	1.0 (4.3e-6)	1.0	1.0		Y
6	2	E	235,451	4.3e-6 (500.5)	1.2e-3	1.2e-3		Y
7	1	D	451,452, or 453*	1.0 (4.3e-6)	Range from 1.25 to 1.5	1.0	151,152, or 153	N
8	1	E	451,452, or 453	4.3e-6 (1.0)	Range from 1.3e-3 to 1.5e-3	1.2e-3	151,152, or 153	N
Eng	1	D (E)	555	1.5 (1.2e-5)	1.5 (1.5e-3)	1.0 (1.2e-3)	144	N

* almost unique sensor system

The detection times for the sensor placed at the exhaust were 2.0, 2.0, 1.0, and 1.0 min, respectively for each release location. Some of the multizone- and zonal-optimal 1-sensor systems (locations 451, 551, and 552) also exhibited these detection times. The remaining multizone- and zonal-optimal 1-sensor systems (locations 452 or 453) had detection times of 2.0 min, 1.0 min, 1.0 min, and 1.0 min, respectively for each release location. Thus, placing a sensor at the exhaust was no more a robust design than placing a sensor at the two of the locations designed using multizone and zonal model data.

Similar to Test Case 1, a sensor system designed for Test Case 7 to minimize detection time *did* also guarantee that occupant exposure was minimized, whether using multizone or zonal model data to design the sensor system. However, a sensor system designed to minimize occupant exposure *did not* also guarantee that detection time was minimized, whether using multizone or zonal model data to design the sensor system (compare Sensor sys. #3 and 4 in Table 2-7). For Test Case 7, the occupant exposure was 0 kg/kg for *all* releases, but only when multizone model data was used. In contrast, for Test Case 1, the occupant exposure was always 0 kg/kg *only* for releases #2 to #4, using data from either simpler airflow model.

Figure 2-14 shows the contaminant contour plots for Test Case 7, Release #1 for all three airflow models at two times. Test Case 7 was the case where furniture was placed beneath the diffuser. When the contaminant was released from location #1, the contours plots of Test Case 7 modeled with the multizone model showed that neither occupant was exposed to the contaminant (Figure 2-14a and b). Note that even though the contour lines may fall within the subzone of an occupant, the concentration there was always zero. On the other hand, the contour plots of the contaminant data simulated by

the zonal and CFD models showed that at least one of the occupants was exposed to the contaminant within the first minute.

The optimal 1-sensor locations designed to minimize detection time using multizone model and zonal model data for Test Case 8 was the same as that designed to minimize detection time for Test Case 7. The closest CFD-optimal subzone locations for a 1-sensor system would have been subzone location 151, 152, or 153 for Test Cases 7–8. This location was approximately 3.0 m away from the locations designed using data from the simpler airflow models. The 1-sensor systems designed to minimize detection time using data from three airflow models for the test cases for Zone A[-] are summarized in Table 2-8 and shown graphically in Figure 2-15. The values in the last column of Table 2-8 will be discussed in Sec. 2.10.3.

2.10.2 Zone A[+]

Test Cases 9 – 16 are associated with the zones with the wall-mounted diffuser and exhaust. Keep in mind that Test Cases 11 and 12 were not simulated since there was no furniture and thus, its location could not be varied (see Sec. 2.4 and Table 2-3). Sec. 2.10.2.1 and 2.10.2.2 will discuss the results for Test Cases 9 (no furniture, no infiltration), 15 (furniture under diffuser, no infiltration) and 16 (furniture under diffuser, with infiltration), respectively. Details for the results of Test Cases 10 (no furniture, with infiltration), 13 (furniture under exhaust, no infiltration), and 14 (furniture under exhaust, with infiltration) were not presented since they shared similarities with Test Cases 9, 15 or 16. In general, sensor systems designed using data from the multizone and zonal models (i.e., simpler airflow models) were **able to perform just as well as those**

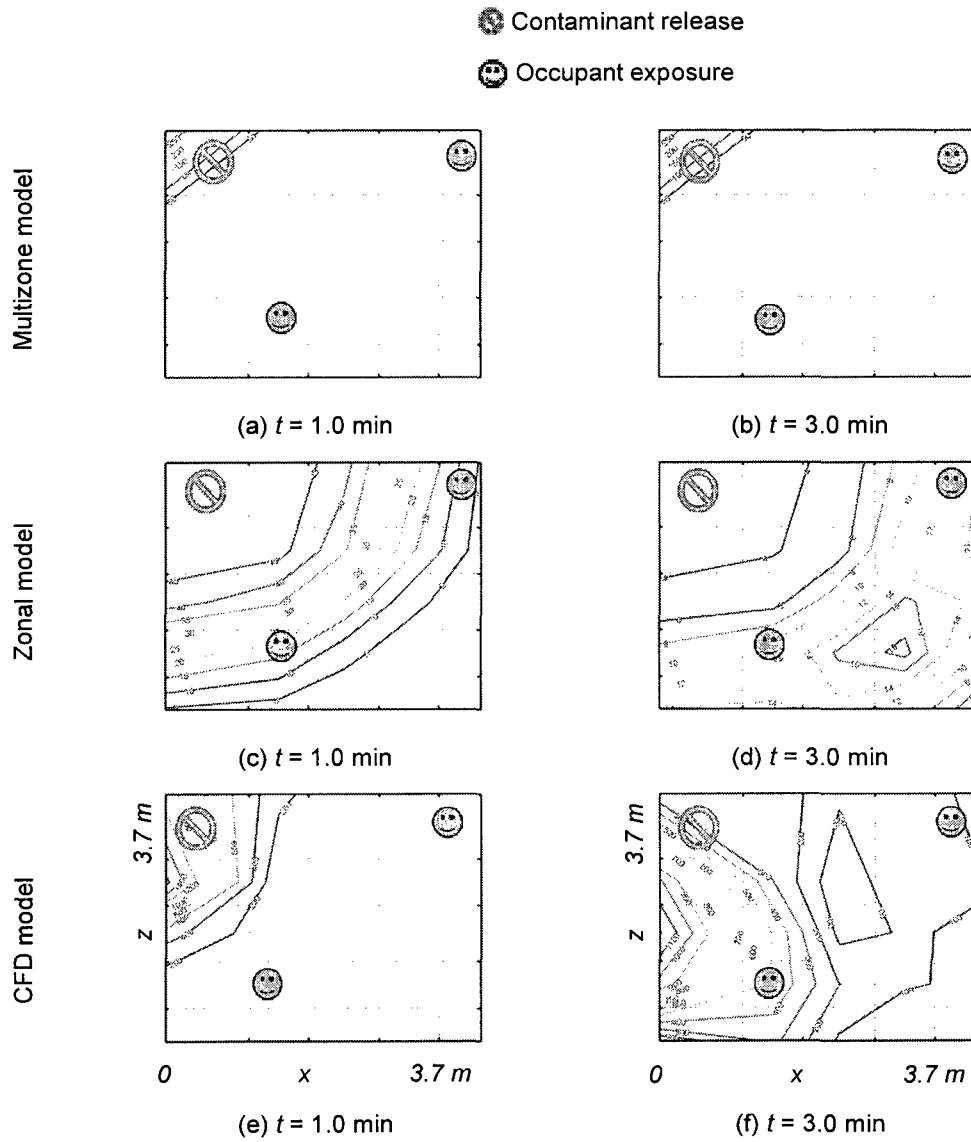


Figure 2-14. Contaminant contour plots for Test Case 7, Release #1.

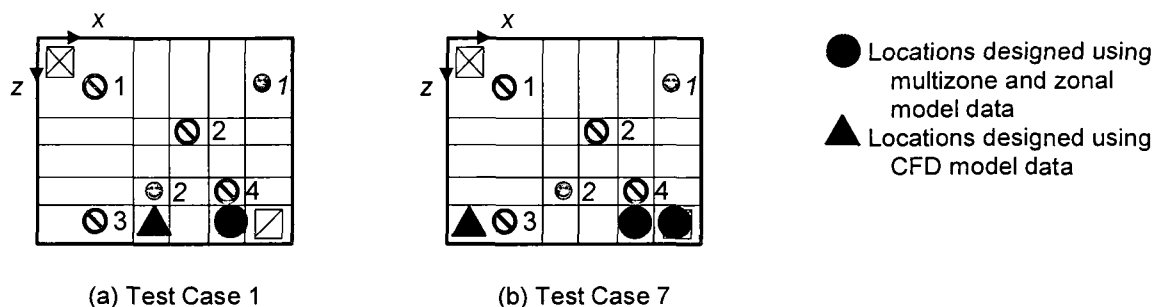


Figure 2-15. 1-sensor systems designed to minimize detection time using data from three airflow models for Zone A[-].

Table 2-8. Summary of 1-sensor systems designed to minimize detection time using data from three airflow models for Zone A[-].

Test Case	Furniture (Y/N)?	Furniture location	Infiltration (Y/N)?	Multizone Locations	Zonal Locations	Closest CFD location	Number of CFD-optimal 1-sensor sys.
1	N	n/a	N	452	451,452	252	45
2	N	n/a	Y	451	451,452	252	37
5	Y	Exhaust	N	451	451,452	251,252	52
6	Y	Exhaust	Y	451	451,452	252	46
7	Y	Diffuser	N	451,452, 453,551, 552	451,452, 453	151,152, 153	35
8	Y	Diffuser	Y	451,452, 453,551, 552	451,452, 453	151,152, 153	27

designed using more accurate CFD data for Test Cases 9 – 16, except for the 1-sensor systems for Test Cases 15 and 16. Also, **neither the absence nor presence of furniture or infiltration affected the ability** of the simpler airflow models to design sensor systems capable of performing just as well as those designed using more accurate CFD data, **except** for the 1-sensor systems for Test Cases 15 and 16. Lastly, **the common engineering design practice of placing a sensor at the exhaust resulted in optimal performance** when benchmarked with CFD data.

2.10.2.1 Test Case 9 (no furniture, no infiltration)

Table 2-9 and Table 2-10 show that the 2-, 3-, and 4-sensor systems designed using data from the multizone and zonal model, respectively, were able to perform just as well as those designed using more accurate CFD data for Test Case 9. The 1-sensor system designed using either multizone or zonal model data for Test Case 9 was *either* subzone location 451 or 551 when minimizing detection time. These locations were horizontally adjacent subzones. These locations were marked with an "*" because these were the *only two* locations where a 1-sensor system was both multizone- and zonal-optimal. Their CFD-benchmarked detection times were both calculated as 1.0 min, which were **equal** to the CFD-optimal detection time of 1.0 min for a 1-sensor system.

It should be noted that *all* of the sensor systems designed using the simpler airflow models for the test cases for the wall-mounted diffuser were optimal when benchmarked with CFD data, **except** for Test Cases 15 and 16. In fact, data from the CFD model indicated that *every* sensor location (i.e., every subzone) was an optimal location to place a sensor for *all* test cases for the wall-mounted ceiling diffuser, **except** for Test Cases 15 and 16. This was due to the fact that the CFD model calculated greater transport of each contaminant for the test cases for the wall-mounted diffuser when compared with the test cases for the ceiling-mounted diffuser. For instance, Figure 2-16(a-b) compares the contour plots of Test Cases 1 and 9. Both test cases were those with no furniture and no infiltration in Zone A[-] (ceiling-mounted diffuser and exhaust). Figure 2-16(c-d) compares the contour plots of Test Cases 5 and 13. Both test cases were those with furniture under the exhaust and no infiltration in Zone A[+] (wall-mounted

Table 2-9. Sensor system designs for Test Case 9 using multizone model data.

Sensor sys. [1]	Qty [2]	Obj. func. [3]	Locations using multizone data [4]	Objective function value (complementary obj. func. value)			Locations using CFD data [8]	Col. [6] equiv. to [7]? [9]
				Multizone-optimal [5]	CFD-benchmarked [6]	CFD-optimal [7]		
1	4	D	155,331, 414,551	1.0 (7.8e-8)	See note			
2	4	E	123,231, 252,551	7.8e-8 (1.0)				
3	3	D	151,433, 541	1.0 (7.8e-8)				
4	3	E	211,414, 551	7.8e-8 (1.0)				
5	2	D	551,211	1.0 (7.8e-8)				
6	2	E	111,451	7.8e-8 (1.0)				
7	1	D	451 or 551*	1.25 (1.14e-6)				
8	1	E	441	7.8e-8 (250.75)				
Eng	1	D (E)	551	1.25 (1.1e-6)				

Note (also applies to Table 2-10): Using CFD data, every sensor location (i.e., subzone locations) was an optimal location to place a sensor. *almost unique sensor system

Table 2-10. Sensor system designs for Test Case 9 using zonal model data.

Sensor sys. [1]	Qty [2]	Obj. func. [3]	Locations using zonal data [4]	Objective function value (complementary obj. func. value)			Locations using CFD data [8]	Col. [6] equiv. to [7]? [9]
				Zonal-optimal [5]	CFD-benchmarked [6]	CFD-optimal [7]		
1	4	D	144,321, 451,522	1.0 (8.1e-8)	See note			
2	4	E	211,321, 521,552	8.5e-8 (1.0)				
3	3	D	131,443, 551	1.0 (8.1e-8)				
4	3	E	145,211, 451	8.1e-8 (1.0)				
5	2	D	131,451	1.0 (8.1e-8)				
6	2	E	331,551	8.1e-8 (1.0)				
7	1	D	451 or 551*	1.25 (1.2e-6)				
8	1	E	441	8.1e-8 (250.75)				
Eng	1	D (E)	551	1.25 (1.2e-6)				

* almost unique sensor system

diffuser and exhaust). There was greater transport of the contaminant in Test Cases 9 and 13 (wall-mounted diffuser and exhaust) than in Test Cases 1 and 5 (ceiling-mounted diffuser and exhaust). Only for *two* cases did the CFD model *not* indicate that that *every* sensor location (i.e., every subzone) was an optimal location to place a sensor for Zone A[+]. They were Test Cases 15 and 16 (furniture under diffuser). More details can be found in Sec. 2.10.2.2.

Similar to Test Case 1, occupant exposure was always 0 kg/kg for releases #2 to #4 when using data from a simpler airflow model for Test Case 9. None of the sensor systems in Table 2-9 and Table 2-10 indicated that sensor systems designed to minimize occupant exposure did not also guarantee that detection time was minimized. This was due to the fact the sensor systems reported were non-unique (i.e., were *not* the only sensor systems that were multizone- or zonal-optimal for a given number of sensors). Therefore, sensor systems designed to minimize occupant exposure could not also minimize detection time given the fact that the occupant exposure was always 0 kg/kg for releases #2 to #4.

For releases #2 to #4, the simpler airflow models calculated *zero* occupant exposure for *all* test cases simulated by the simpler airflow models for Zone A[+]. **Therefore, for all test cases simulated by the simpler airflow models for Zone A[+], minimizing occupant exposure *did not guarantee* that detection time was also minimized.** This was also found for all test cases for Zone A[-].

The optimal 1-sensor location designed to minimize detection time using data from the simpler airflow models for Test Cases 10, 13, and 14 were the same (*either*

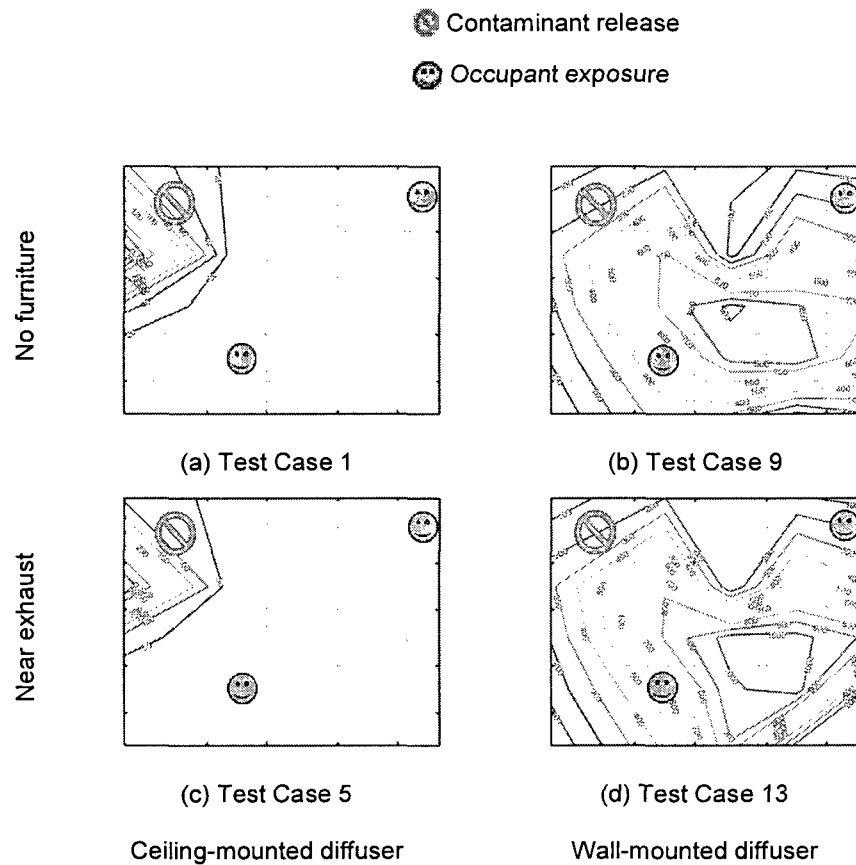


Figure 2-16. Contaminant contour plots from CFD model at $t = 1.0$ min sec for Release #1.

subzone location 451 or 551). These locations were the same as the optimal 1-sensor locations designed to minimize detection time using data from the simpler airflow models for Test Case 9. Thus, also for Test Cases 10, 13, and 14, the 1-sensor systems designed using data from the simpler airflow models **did** perform as well as those designed using more accurate CFD data. The 1-sensor systems designed to minimize detection time using data from three airflow models for the test cases for Zone A[+] are summarized in

Table 2-15 and shown graphically in Figure 2-17. The values in the last column of Table 2-15 will be discussed in Sec. 2.10.3.

2.10.2.2 Test Cases 15 (furniture under diffuser, no infiltration) and 16 (furniture under diffuser, with infiltration)

Table 2-11 and Table 2-12 show that the 2-, 3-, and 4-sensor systems designed using data from the multizone and zonal model, respectively, were able to perform just as well as those designed using more accurate CFD data for Test Case 15. Table 2-13 and Table 2-14 show that the 2-, 3-, and 4-sensor systems designed using data from the multizone and zonal model, respectively, were able to perform just as well as those designed using more accurate CFD data for Test Case 16.

The 1-sensor systems designed using multizone model data was *either* subzone location 451 or 551 when minimizing detection time for Test Case 15. The CFD-benchmarked detection time for only *one* of these locations was equal to the CFD-optimal detection of 1.0 min for a 1-sensor system. Therefore, a 1-sensor system designed using data from a multizone model **could not** perform just as well as one designed using more accurate CFD data. On the other hand, the 1-sensor system designed using zonal model data was subzone location 451 when minimizing detection time for Test Case 15. The CFD-benchmarked detection time for this location was equal to the CFD-optimal detection of 1.0 min for a 1-sensor system. Therefore, a 1-sensor system designed using data from a zonal model **could** perform as well as one designed using more accurate CFD data.

The 1-sensor systems designed using either multizone or zonal model data was *either* subzone location 451 or 551 when minimizing detection time for Test Case 16.

The CFD-benchmarked detection time for both of these locations was greater than the CFD-optimal detection of 1.0 min for a 1-sensor system. Therefore, a 1-sensor system designed using data from either simpler airflow model **could not** perform as well as one designed using more accurate CFD data for Test Case 16. The 1-sensor systems designed to minimize detection time using data from three airflow models for the test cases for Zone A[+] are summarized in Table 2-15 and shown graphically in Figure 2-17. The values in the last column of Table 2-15 will be discussed in Sec. 2.10.3.

The results for Test Cases 15 and 16 were different than for the rest of the test cases for Zone A[+] because in these two test cases, not every subzone location was an optimal one when calculated using CFD data. When there was furniture below the diffuser, as was the case for Test Cases 15 and 16, contaminant transport was not as great when compared to the cases without furniture or furniture placed below the exhaust.

In Test Case 15, there were only two subzone locations (321 and 551) where the detection time calculated by using CFD data was *not* 1.0 min for every release. In Test Case 16, there were even more subzone locations (131, 321, 321, 451, and 551) where the detection time calculated by using CFD data was *not* 1.0 min for every release. Test Case 16 included infiltration (which was negative in all test cases, meaning air was *leaving* the zone) while Test Case 15 did not. Thus, when there was infiltration *and* furniture under the diffuser (Test Case 16), contaminant transport was even less effective than when there was no infiltration (as calculated using CFD data).

Table 2-11. Sensor system designs for Test Case 15 using multizone model data.

Sensor sys. [1]	Qty [2]	Obj. func. [3]	Locations using multizone data [4]	Objective function value (complementary obj. func. value)			Locations using CFD data [8]	Col. [6] equiv. to [7]? [9]
				Multizone-optimal [5]	CFD-benchmarked [6]	CFD-optimal [7]		
1	4	D	111,232, 434,551	1.0	1.0	1.0		Y
2	4	E		See note				
3	3	D	111,332, 551	1.0	1.0	1.0		Y
4	3	E		See note				
5	2	D	111,451	1.0	1.0	1.0		Y
6	2	E		See note				
7	1	D	451 or 551*	250.75	1.0 or 1.25	1.0		Y or N
8	1	E		See note				
Eng	1	D (E)	551	250.75 (0)	1.0 (3.2e-4)	1.0 (3.2e-4)		Y

Note: For *all* contaminant releases, occupant exposure is always 0 kg/kg. Therefore, all sensor systems designed using multizone model data result in the same occupant exposure, 0 kg/kg, and there are no "optimal" designs. *almost unique sensor system

Table 2-12. Sensor system designs for Test Case 15 using zonal model data.

Sensor sys. [1]	Qty [2]	Obj. func. [3]	Locations using zonal data [4]	Objective function value (complementary obj. func. value)			Locations using CFD data [8]	Col. [6] equiv. to [7]? [9]
				Zonal-optimal [5]	CFD-benchmarked [6]	CFD-optimal [7]		
1	4	D	121,212, 351,541	1.0 (7.0e-9)	1.0	1.0		Y
2	4	E	111,132, 351,441	7.0e-9 (1.0)	3.2e-4	3.2e-4		Y
3	3	D	231,342, 551	1.0 (7.0e-9)	1.0	1.0		Y
4	3	E	131,224, 451	7.0e-9 (1.0)	3.2e-4	3.2e-4		Y
5	2	D	131,451	1.0 (7.0e-9)	1.0	1.0		Y
6	2	E	141,551	7.0e-9 (1.0)	3.2e-4	3.2e-4		Y
7	1	D	451*	1.25 (1.2e-7)	1.0	1.0		Y
8	1	E	331	7.0e-9 (500.5)	3.2e-4	3.2e-4		Y
Eng	1	D (E)	551	1.5 (5.0e-7)	1.0 (3.2e-4)	1.0 (3.2e-4)		Y

* unique sensor system

Table 2-13. Sensor design designs for Test Case 16 using multizone model data.

Sensor sys. [1]	Qty [2]	Obj. func. [3]	Locations using multizone data [4]	Objective function value (complementary obj. func. value)			Locations using CFD data [8]	Col. [6] equiv. to [7]? [9]
				Multizone-optimal [5]	CFD-benchmarked [6]	CFD-optimal [7]		
1	4	D	111,122, 451,542	1.0	1.0	1.0		Y
2	4	E	See note					
3	3	D	111,251, 541	1.0	1.0	1.0		Y
4	3	E	See note					
5	2	D	111,551	1.0	1.0	1.0		Y
6	2	E	See note					
7	1	D	451 or 551*	250.75	1.25	1.0	252	N
8	1	E	See note					
Eng	1	D (E)	551	250.75 (0)	1.0 (3.5e-4)	1.0 (3.5e-4)		Y

Note: For *all* contaminant releases, occupant exposure is always 0 kg/kg. Therefore, all sensor systems designed using multizone model data result in the same occupant exposure, 0 kg/kg, and there are no "optimal" designs. * almost unique sensor system

Table 2-14. Sensor design designs for Test Case 16 using zonal model data.

Sensor sys. [1]	Qty [2]	Obj. func. [3]	Locations using zonal data [4]	Objective function value (complementary obj. func. value)			Locations using CFD data [8]	Col. [6] equiv. to [7]? [9]
				Zonal-optimal [5]	CFD-benchmarked [6]	CFD-optimal [7]		
1	4	D	154,221, 451,554	1.0 (6.3e-9)	1.0	1.0		Y
2	4	E	221,335, 451,522	6.3e-9 (1.0)	3.5e-4	3.5e-4		Y
3	3	D	153,321, 551	1.0 (6.3e-9)	1.0	1.0		Y
4	3	E	321,433, 551	6.3e-9 (1.0)	3.5e-4	3.5e-4		Y
5	2	D	221,551	1.0 (6.3e-9)	1.0	1.0		Y
6	2	E	111,451	6.3e-9 (1.0)	3.5e-4	3.5e-4		Y
7	1	D	451 or 551*	1.5 (4.7e-7)	1.25	1.0	252	N
8	1	E	321	6.3e-9 (500.5)	3.9e-4	3.5e-4	252	N
Eng	1	D (E)	551	1.5 (4.7e-7)	1.0 (3.5e-4)	1.0 (3.5e-4)		Y

* almost unique sensor system

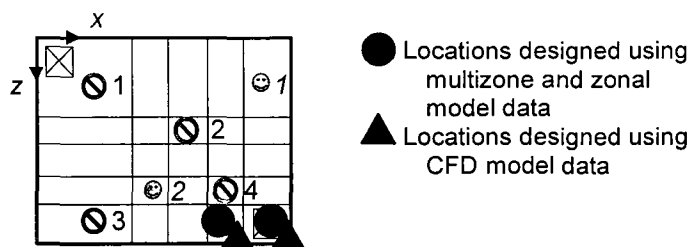


Figure 2-17. 1-sensor system designed using three airflow models for minimizing detection time for Zone A[+].

Table 2-15. Summary of 1-sensor systems designed using three airflow models for Zone A[+].

Test Case	Furniture (Y/N)?	Furniture location	Infiltration (Y/N)?	Multizone Locations	Zonal Locations	Closest CFD location	Number of CFD-optimal 1-sensor sys.
9	N	n/a	N	451,551	451,551	451,551	125
10	N	n/a	Y	451,551	451,551	451,551	125
13	Y	Exhaust	N	451,551	451,551	451,551	125
14	Y	Exhaust	Y	451,551	451,551	451,551	125
15	Y	Diffuser	N	451,551	451	451	123
16	Y	Diffuser	Y	451,551	451,551	452,552	120

* 125 is the total number of subzones.

2.10.3 Effects of furniture and infiltration on sensor system design

Table 2-8 and Table 2-15 summarize the 1-sensor systems designed to minimize detection time using the three airflow models for both zones tested. The last column shows the number of CFD-optimal 1-sensor systems for each test case. The pairs of test cases with and without infiltration to compare are 1 and 2; 5 and 6; and 7 and 8 for Zone A[-] (Table 2-8). The pairs of test cases with and without infiltration to compare are 9 and 10; 13 and 14; and 15 and 16 for Zone A[+] (Table 2-15). The tables show that for each pair, the test case with infiltration (Test Cases 2, 6, and 8) had *fewer* possible optimal 1-sensor systems than the test cases without infiltration (Test Cases 1, 5, and 7) for Zone

$A[-]$. For Zone $A[+]$, this was observed only when comparing Test Cases 15 and 16. For these two test cases, *not every* sensor location (i.e., subzone location) was an optimal location to place a sensor. Nevertheless, for both test zones, contaminant transport was **less effective when infiltration was modeled** as calculated using CFD data.

For the 2-, 3-, and 4-sensor systems designed using data from either multizone or zonal model data, **the inclusion of infiltration *did not* affect** the performance of the sensor systems designed using data from the simpler airflow models. Only the performance of the **1-sensor systems was affected** by the inclusion of infiltration, specifically for Test Cases 15 and 16.

Groups of test cases with and without furniture can also be compared using Table 2-8 and Table 2-15. The pairs of test cases with and without furniture to compare are 1, 5, and 7 (without infiltration); and 2, 6, and 8 (with infiltration) for Zone $A[-]$ (Table 2-8). The pairs of test cases with and without furniture to compare are 9, 13, and 15 (without infiltration); and 10, 14, and 16 (with infiltration) for Zone $A[+]$ (Table 2-15). These comparisons show that the inclusion of furniture under the exhaust *increased* the number of optimal 1-sensor locations designed using CFD data, with or without infiltration. Contaminant transport was ***more effective when furniture under the exhaust was modeled*** as calculated using CFD data. This could be attributed to the furniture allowing the contaminant to remain longer inside the zone before being exhausted out. In contrast, the inclusion of furniture under the diffuser *decreased* the number of optimal 1-sensor locations designed using CFD data, with or without infiltration. Contaminant transport was ***less effective when furniture under the diffuser was modeled*** as calculated using CFD data. Placing furniture under the diffuser did not allow the supply jet to reach the

floor of the zone, and thus did not allow effective distribution of the contaminant that was modeled as being released from the floor. The effect of furniture under the diffuser was more clearly observed in Zone A[-] (ceiling-mounted diffuser) than in Zone A[+] (wall-mounted diffuser) because the supply jet in Zone A[+] traveled horizontally along the ceiling.

For the 2-, 3-, and 4-sensor systems designed using data from either multizone or zonal model data, **the inclusion of furniture *did not* affect** the performance of the sensor systems designed using data from the simpler airflow models. Only the performance of the **1-sensor systems was affected** by the inclusion of furniture.

2.10.4 Effects of test space characterization on sensor system design

In addition the zone characteristics above, the zones tested in this research were also characterized more generally by *local mean age of air (LMA)* In order to calculate *LMA*, a uniform initial concentration of CO₂ was specified in the airflow model. The transient decay of SF₆ due to the ventilation system operation was then calculated by the airflow model. The local mean age of air was defined as [95]:

$$LMA = \frac{(\sum C_i) \delta_T + C_M / \beta_e}{C_o} \quad (12)$$

where β_e was the slope of the exponential decay of the contaminant, C_i was the concentration time i , C_o was the initial concentration, C_M was the final concentration, δ_T was the sampling interval, and M was the number of concentration readings. The local mean of air was calculated for each subzone.

Table 2-16 reports the mean±standard deviation of the local mean age of air calculated across all subzones for Test Case 1 (ceiling-mounted diffuser and exhaust, no

furniture, no infiltration), Test Case 9 (wall-mounted diffuser and exhaust, no furniture, no infiltration), as well as the three test spaces in the preliminary studies. *LMA* was calculated using CFD data.

Table 2-16 shows that for Test Case 1, the standard deviation was about 20% of the mean. For Test Case 9, the standard deviation was about 11% of the mean. Thus, it could be concluded that Test Case 9 was more well-mixed than Test Case 1 because its standard deviation value was relatively smaller. This was why *every* subzone in Test Case 9 was an optimal one. Nevertheless, for both test cases, the sensor systems designed using data from simpler airflow models performed just as well as those designed using CFD data even though neither test case would be considered well-mixed (standard deviation <6% of mean [108]), as evaluated using CFD data.

Table 2-16 shows that for the test spaces in the preliminary studies, the standard deviation of *LMA* was between 36-55% of the mean. Despite this fact, the sensor systems designed using data from simpler airflow models performed just as well as those designed using CFD data for the small office and office suite. **Therefore, it could be concluded that the degree of well-mixing, as evaluated by *LMA*, could not determine**

Table 2-16. Mean age of air for test cases in Chapter 2

Test Case	Local mean age of air (<i>LMA</i>) (sec) Mean±Standard Deviation
1	525±106
9	476±56
Preliminary: small office	370±135
Preliminary: large hall	472±207
Preliminary: office suite	376±206

whether or not sensor systems designed using data from simpler airflow models would perform just as well as those designed using more accurate data.

2.11 Conclusions

Four releases of a contaminant were modeled in a multizone and zonal model. Sensor systems were then designed using contaminant data simulated by each model, along with an optimization technique, genetic algorithm. The performance of these sensor systems was benchmarked with CFD contaminant data, in lieu of experimental data. It was found that for *both* Zone A[-] (ceiling-mounted diffuser and exhaust) and Zone A[+] (wall-mounted diffuser and exhaust):

- (1) Data from simpler airflow models that included *simple* diffusers were able to design sensor systems capable of performing *just as well* as those designed using more accurate CFD models that included more *complex* diffusers;
- (2) 2-, 3-, and 4-sensor systems designed using data from the simpler airflows were able to perform *just as well* as those designed using more accurate CFD data;
- (3) Sensor systems designed using data from the simpler airflow models to minimize detection time *did not* guarantee that detection time was also minimized. This was due in combination to the diffuser and exhaust layout, as well as the locations of the contaminants released. Both these factors resulted in *zero* occupant exposure for *three out of the four* simulated releases;
- (4) The inclusion of furniture and/or infiltration *did not* affect the performance of the 2-, 3-, and 4-sensor systems designed using data from the simpler airflow models;

- (5) The inclusion of furniture under the exhaust *increased* the number of CFD-optimal 1-sensor systems, indicating that furniture under the exhaust *improved* contaminant transport;
- (6) The inclusion of furniture under the diffuser *decreased* the number of CFD-optimal 1-sensor systems, indicating that furniture under the diffuser *reduced* contaminant transport;
- (7) The inclusion of infiltration *decreased* the number of CFD-optimal 1-sensor systems, indicating that infiltration *reduced* contaminant transport.

It was found that for *only* Zone A[+] (wall-mounted diffuser and exhaust):

- (1) Even 1-sensor systems designed using data from the simpler airflows were able to perform *just as well* as those designed using more accurate CFD data, but only for the cases where there was either no furniture or furniture under the exhaust;
- (2) CFD data indicated that *every* sensor location (i.e., every subzone) was an optimal location to place a sensor for all test cases, but only for the cases where there was either no furniture or furniture under the exhaust;
- (3) For the cases with furniture under the diffuser, the number of CFD-optimal 1-sensor systems *decreased* when compared to the cases without furniture. The inclusion of infiltration further *decreased* the number of CFD-optimal 1-sensor systems. This result was also found for Zone A[-] test cases.

The common engineering design practice of placing a sensor at the exhaust resulted in *non-optimal* performance for Zone A[-] (ceiling-mounted diffuser and exhaust). Placing a sensor at the exhaust was no more, and no less, a robust design than placing a sensor at the location designed using multizone and zonal model data. This

common engineering design practice resulted in *optimal* performance when benchmarked with CFD data for Zone A[+] (wall-mounted diffuser and exhaust).

Hypothesis #1 was: for each class of zone or building configuration, there exists a simplest *forward* airflow model to simulate indoor airflow patterns and contaminant transport for systematic sensor system design. In this research, it could be concluded that for sensor systems consisting of *more than one sensor, none of the zone characteristics tested in this research* affected the performance of sensor systems designed using data from simpler airflow models. Therefore, the simplest forward airflow model for designing multiple-sensor systems for the zone tested in this research, with or without furniture and/or infiltration, was the subzoned-multizone multizone model.

For sensor systems consisting of *one sensor, all of the zone characteristics tested in this research* affected the performance of sensor systems designed using data from simpler airflow models. Therefore, the simplest forward airflow model for designing 1-sensor systems for the zone tested in this research, with or without furniture and/or infiltration, was the CFD model.

2.12 Plans for publication

A possible publication would be "Method for classifying indoor spaces and the selection of simplest airflow model for systematic indoor air sensor system design". This work may be submitted to:

- *Indoor Air*, impact factor of 1.59
- *Building and Environment*, impact factor of 1.192

2.13 Future work

The conclusions drawn from the research in this chapter are very promising – for a small zone, even with furniture and/or infiltration, data from a simpler airflow could be used to design sensor systems that perform *just as well* as those designed using more accurate data. The sensor quantity should be greater than one. Nevertheless, the work was *limited* in the amount of variation between test cases. Only two diffuser and exhaust layouts, two furniture locations (and only one size), and two levels of airtightness (none to leaky) were tested.

Since the long-term objective of this research is to be able to select the simplest forward airflow model to simulate indoor airflow and contaminant transport for designing indoor air sensor systems for every class of zone, there are many more intermediate "levels" of (and additional) zone characteristics that need to be tested. Such levels include but are not limited to: variation in zone shape and size, (multiple) diffuser and exhaust layouts, furniture location and size, and other levels of infiltration. Additional zone characteristics include but are not limited to: non-isothermal cases and moving/more occupants (or contaminant sources).

Figure 2-18 shows the full computer experimental process that can be taken for future work. The first step is to include as many input factors (i.e., zone characteristics) as desired. Test cases can be set up using a factorial design. Sensor systems can then be designed using contaminant data from the simpler airflow models for each test case. Using benchmarked sensor system performance, input factors can be eliminated based on their effect on sensor system performance. If more input factors can be included, then new test cases can be set up with the additional input factors, leaving out the eliminated

ones. Fractional factorial design can be used to set up test cases if the number of input factors is large, and the time to run computer simulations of airflow and contaminant transport would be impractical, or a subset of the test cases can represent the entire set. The number of test cases in a fractional factorial design would be $2^k/2^f$, where f is the fraction. For instance, if $f=1$, then the number of test cases is reduced by half, and if $f=2$, then the number of tests cases is reduced by a fourth, etc. **In this manner, for any zone in the future, the simplest, but also most appropriate, forward airflow model may be used to simulate indoor airflow and contaminant transport for systematic indoor air sensor system design.** There will be no need to simulate contaminant transport in a multizone model *only* for its convenience. There will be no need to simulate contaminant transport in a CFD model *only* for its accuracy. A complete study such as the one proposed here for future work will have systematically selected an airflow model based on convenience *and* accuracy.

A qualitative analysis was performed in this research when discussing how various zone characteristics affected the appropriateness of a simpler airflow model to provide contaminant data for sensor system design. Since a factorial design was used to design the computer experiments in this research, a statistical test such as ANOVA may be used to quantitatively compare the performances of the sensor system designs in future work.

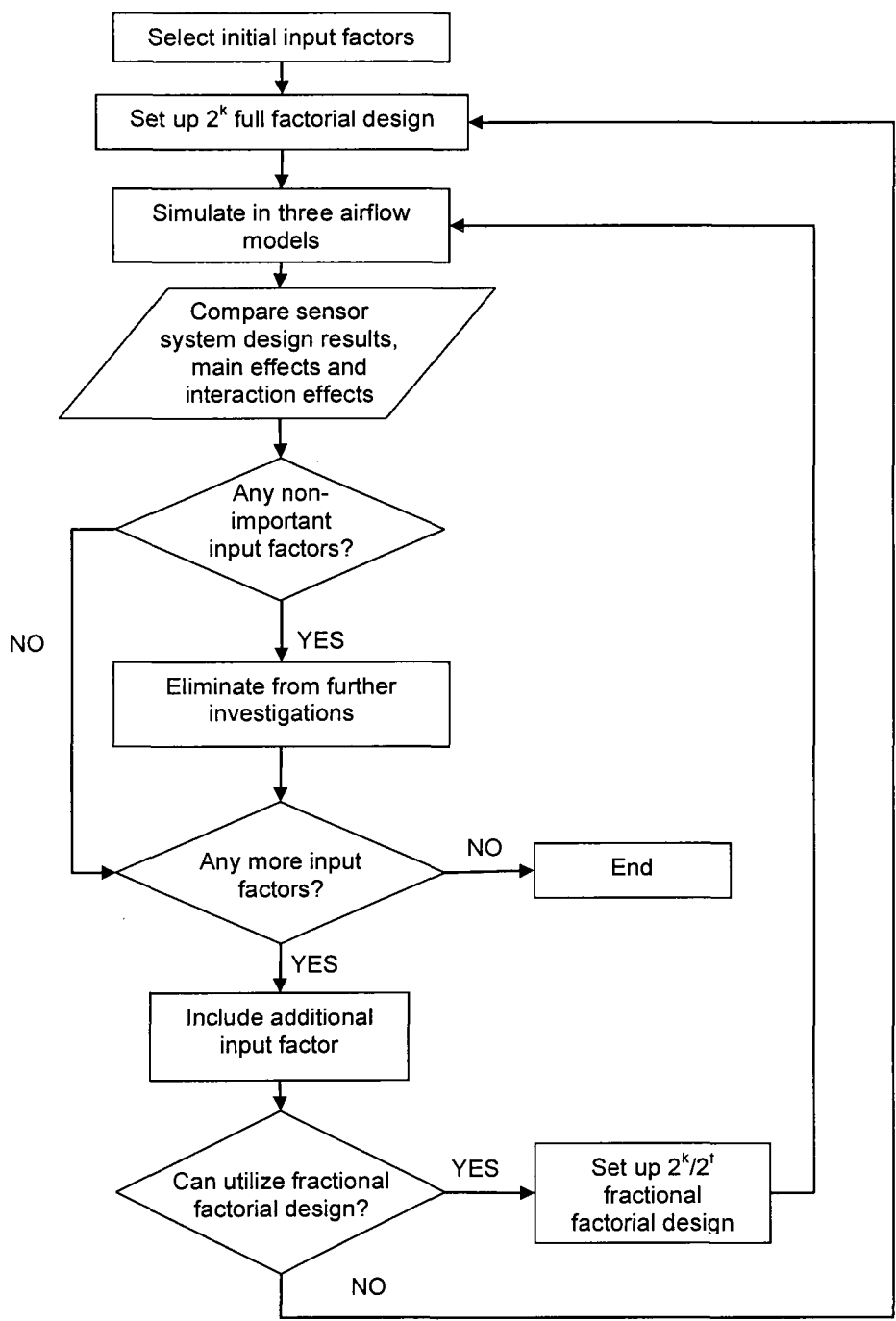


Figure 2-18. Flow chart of computer experimental process.

3. CHAPTER 3: TESTING HYPOTHESIS #2 – DEVELOPING AND UTILIZING AN INVERSE AIRFLOW MODEL FOR SINGLE ZONE

If one has the resources and information to perform a forward simulation of an indoor space, then the results reported in Chapter 2 can be very helpful in deciding which forward airflow model to use for sensor system design. However, if resources and information are limited, then one can use an appropriate inverse airflow model.

Inverse modeling is a potential tool for gathering the information needed for accurately estimating airflow and contaminant transport in real-time. It requires much less information than a forward model would. Utilizing the sensor readings from a selected number of locations, an inverse model may be able to estimate the measurements at non-sensored locations. Three methods were tested as inverse models. They were singular value decomposition without infiltration (invSVD0) and with infiltration (invSVD1) and inverse-multizone (invC, where the "C" stands for the CONTAM multizone model).

3.1 Chapter 3 outline

Sec. 3.2 presents inverse models used to inversely estimate indoor airflow using limited synthetic velocity measurements provided by CFD. Sec. 3.3 presents the test zones used to the inverse models. Sec. 3.4 describes the sensor locations where synthetic velocity measurements are taken. The results are discussed in Sec. 3.5, conclusions in Sec. 3.6, and future work in Sec. 3.6.

3.2 Inverse models

3.2.1 Singular value decomposition (invSVD0 and invSVD1)

SVD is a method for solving underdetermined systems [109]. The system of equations to inversely solve for indoor airflow are underdetermined. In the study of indoor airflow, for any control volume of air, the net mass flow, \dot{m} , must equal zero in order to satisfy continuity. Mathematically,

$$\sum_{i=1}^6 \dot{m}_i = \sum_{i=1}^6 \rho v_i A_i = 0 \quad (13)$$

where the subscript i indicates a face of a control volume (each control volume is assumed to have six sides), ρ is the density of air in kg/m^3 , v is the velocity of air in m/s , and A is a control surface. For a system of N control volumes,

$$\mathbf{A} \left[\rho \sum_{n=1}^N \mathbf{v} \right] = \mathbf{0} \quad (14)$$

where \mathbf{A} contains the areas of the control faces of each respective control volume. The boundary conditions and unknowns are contained in the quantity $\rho \sum \mathbf{v}$. Since there are up to six unknown v (left, right, up, down, front and back velocities) for any control volume, the system becomes underdetermined as N increases. The linear system in Eq. (14), if just- or over-determined, can be solved by inverting \mathbf{A} and multiplying by the right-hand-side. However, if the system is underdetermined, there are an infinite number of solutions to $\rho \sum \mathbf{v}$. Thus, to solve an underdetermined system, SVD uses the pseudoinverse of \mathbf{A} . \mathbf{A} can be factorized into:

$$\mathbf{A} = \mathbf{U} \mathbf{\Sigma} \mathbf{V}^T \quad (15)$$

where Σ contains the singular values of \mathbf{A} on its diagonal, \mathbf{U} and \mathbf{V} are orthogonal matrices containing corresponding singular vectors in their columns, and the superscript T is the transpose. These elements are used to calculate the pseudoinverse of \mathbf{A} , \mathbf{A}^* .

$$\mathbf{A}^* = \mathbf{V}\Sigma^+\mathbf{U}^T \quad (16)$$

where Σ^+ is the transpose of Σ with every non-zero entry replaced by its reciprocal. Thus, the original system represented by Eq. (14) can be solved by:

$$\rho\Sigma\mathbf{v} = \mathbf{A}^*\times\mathbf{b} \quad (17)$$

The accuracy of SVD can be checked by comparing the original "right hand side", \mathbf{b} , with the one obtained by multiplying \mathbf{A} with $\rho\Sigma\mathbf{v}$ from Eq. (17). Traditional forward airflow models satisfy continuity upon completion of the solution process. Their ultimate objective is to solve for airflow rates, but all take an indirect approach. In contrast, SVD is used to directly solve for airflow rates. To use SVD as an inverse model (invSVD), additional information about the unknowns, \mathbf{v} , can be provided by real or synthetic sensor data.

The invSVD model that did not include infiltration was called invSVD0. The invSVD model that did include infiltration was called invSVD1. A constant infiltration rate of -0.04 kg/s was included as an additional known boundary condition in addition to the inlet airflow rate.

Another set of equations describes energy balance for each subzone and can also be used to solve for airflow:

$$c \left[\rho \sum_{n=1}^N \mathbf{v} \right] \mathbf{T} = - \sum_{n=1}^N \mathbf{hA}(\mathbf{T}_w - \mathbf{T}) \quad (18)$$

where c is the specific heat of air, \mathbf{T} contains the temperature of each subzone, \mathbf{h} contains the convection coefficient for each surface (such as wall, floor, etc.) of a subzone, \mathbf{A} contains the area of each surface, and \mathbf{T}_w contains the temperature of each surface. It was assumed that all of the quantities are known except for \mathbf{v} .

3.2.2 Inverse-multizone (invC)

The inverse-multizone model, invC, was simply using the traditionally forward multizone model, CONTAM, "inversely". This was done by specifying constant mass flow elements in CONTAM where, traditionally one would not. Such locations may be in the center of a room or in a doorway, where a sensor might be located. A forward steady-state simulation was then run in order for CONTAM to solve the unknown airflow rates. It should be noted that the invSVD model utilizes linear relationships to solve for airflow, whereas the invC model utilizes nonlinear relationships to solve for airflow.

3.3 Zones simulated

Three zones were simulated. Zone A was $3\text{m} \times 2.7\text{m} \times 3\text{m}$ (Figure 3-1a). The zone has one inlet and one outlet. Both are $0.6\text{m} \times 0.6\text{m}$. Incoming flow is isothermal. The inlet velocity is 1 m/s and the density of air is constant throughout the room at 1.225 kg/m^3 . The zone size and airflow conditions are typical conditions for a small office [110]. Two additional zones were also simulated. The size of these two zones and sizes of the inlets and outlets are identical to those of Zone A. The only differences are the location of the inlet and outlet. For Zone B, the location of the inlet was moved toward the center of the ceiling while the location of the outlet remained the same. For Zone C, the location of the outlet was moved toward the center of the ceiling while the location of the inlet remained the same.

Each of the simulated zones was subdivided into $4 \times 4 \times 4$ subzones. The width of the subzones in the x - and z - directions were either 0.6 or 0.9m. The height of each subzone was 0.675m. This spacing ensured that the inlet and outlet were contained in a single subzone. The area of the control faces associated with each control volume was calculated given the subzone dimensions. Additional configurations of subzone size and number were evaluated as well. Unlike CFD modeling, however, the number and size of the subzones in algebraic models do not greatly affect the results of models using the subzonal approach. This conclusion was also reported by Mora et al. [17].

The invC model required specifying the pressure-flow relationship between subzones where no physical boundary, such as a wall, exists. The literature on subzonal modeling uses the power-law relationship with a discharge coefficient of 0.78 and an exponent of 0.5 [17].

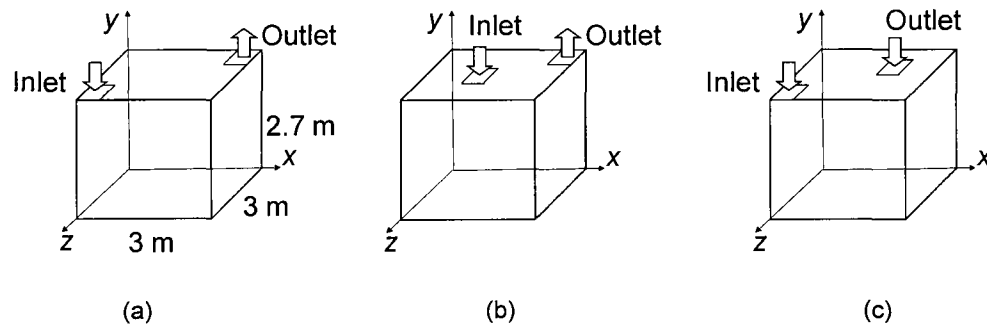


Figure 3-1. Simulated Zones A, B, and C.

3.4 Synthetic sensor data

In lieu of actual sensor data, synthetic velocity and temperature data from CFD simulations was provided to each of the inverse models. The grid size for the CFD model was $30 \times 26 \times 30$, roughly $0.1\text{m} \times 0.1\text{m} \times 0.1\text{m}$ cells. The standard $k-\varepsilon$ turbulence model was used to solve the steady-state airflow. The grid size and turbulence model here were also used by Murakami and Kato [110]. For the invSVD models, synthetic velocity data was provided to matrix \mathbf{v} in Eq. (14). Synthetic temperature data was provided to the matrix \mathbf{T} in Eq. (18). For the invC model, synthetic velocity data and subzone face area was used to specify constant mass flow elements in CONTAM.

Initially, the amount and location of the synthetic velocity data was pre-selected. Then, genetic algorithm (GA) was used to optimize the amount and location of the synthetic velocity data in order to optimize the estimation accuracy of the inverse airflow model. The temperature inside each subzone, as well as along the physical surfaces (ceiling, walls, and floor) of the zone were provided to the invSVD models. The use of temperature sensors to inversely estimate airflow using the invC model was not performed since CONTAM did not have the ability to perform thermal calculations.

3.4.1 Pre-selected velocity sensor locations

Eighteen pre-selected velocity sensor/pole configurations are shown in Figure 3-2. Each pole had four sensors, measuring velocities either both in the x - and y -direction, only in the x -direction, or only in the y -direction. The locations of the poles in Figure 3-2 were selected based on ideal situations, such as having a large number of sensors evenly distributed throughout the entire zone (Figure 3-2a), and based on more practical

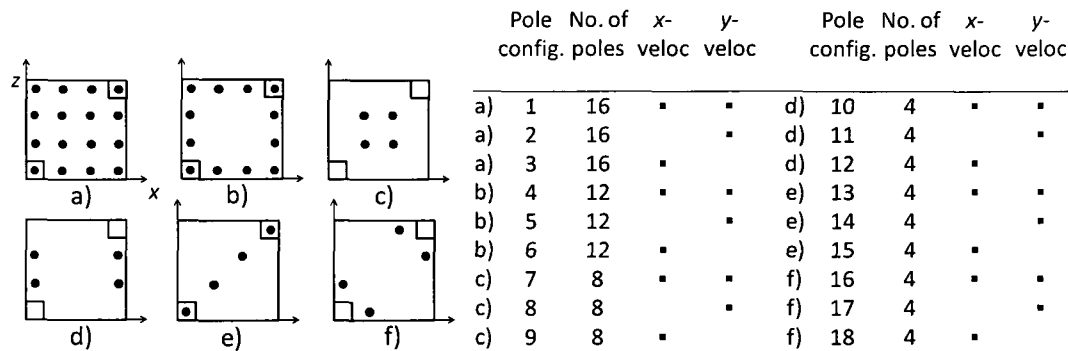


Figure 3-2. Pole configurations where synthetic velocity data were taken.

limitations on available sensor quantity (Figure 3-2d-f). The airflow solutions resulting from the use of these respective configurations provided insight into the relative importance of locating sensors close to the diffuser or exhaust and the relative importance of sensor measurements from the perimeter versus from the center of the room. When utilizing synthetic temperature data to estimate airflow, the temperature in every subzone and along all the surfaces of the zone were needed. Thus, only Pole config. #1 (Figure 3-2a) was tested.

3.4.2 Optimized sensor locations

Figure 3-3 shows the optimization process used to determine the optimal quantity and location of synthetic velocity data that maximized the indoor airflow estimation accuracy. Genetic algorithm (GA) was the optimization method used. All of the subzones were candidate locations. GA was employed using the Genetic Algorithm and Direct Search Tool in Matlab [106] with the following options:

Population size: 40
 Elite count (or number of parents): 6
 Crossover fraction: 0.8
 Mutation function: Gaussian
 Mutation scale: 1.5

Generations: Infinity
 Time limit: Infinity
 Fitness limit: -Infinity
 Stall generations: 1000
 Stall time limit: Infinity

Two trials were performed. In Trial 1, for each candidate location, only velocity measurements in one direction, either vertical or horizontal, were provided to each inverse airflow model as additional known data. In Trial 2, for each candidate location, *both* vertical and horizontal measurements were available.

3.4.2.1 Design objectives

The design objective when optimizing the sensor quantity and location was estimation accuracy. The first design objective utilized was maximizing skewness. The absolute error between the airflow results of each inverse airflow model and CFD at the interface between all of the subzones was calculated. Using these values, a histogram or error distribution, was created for each zone and pole configuration. The skewness was then calculated for each error distribution, defined as:

$$\frac{N}{(N-1)(N-2)} \sum_{i=1}^N \left(\frac{\bar{x}_i - x_i}{s} \right)^3 \quad (19)$$

where \bar{x}_i is the mean error, x_i is the error in each bin, N is the number of bins, and s is the sample standard deviation. Seven bins were selected (Table 3-1). The more positive the skewness of an error distribution, the more the distribution peaked in the bins of smaller error, which is an initial indicator of more accurate airflow estimation when compared to

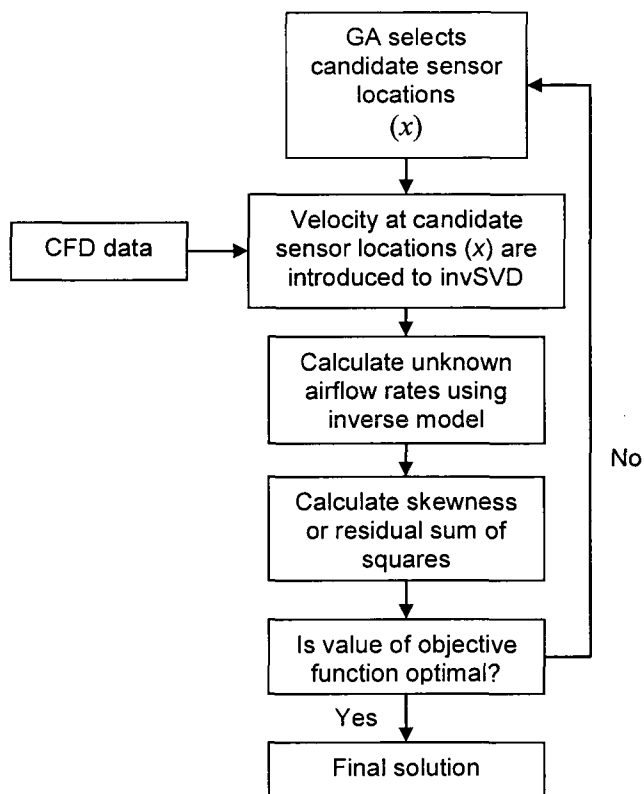


Figure 3-3. Using genetic algorithm to optimize the quantity and location of velocity data.

Table 3-1. Summary of bins used in evaluation of estimation accuracy of airflow results.

Bin	Range of absolute value of error
1	error \leq 0.05
2	0.05 < error \leq 0.10
3	0.10 < error \leq 0.15
4	0.15 < error \leq 0.20
5	0.20 < error \leq 0.25
6	0.25 < error \leq 0.30
7	error > 0.30

the CFD airflow results. Given a specific number of sensors, the objective function to be minimized was the *negative* of skewness in Eq. (19), which is also the same as maximizing skewness.

The second design objective utilized was minimizing the residual sum of squares (RSS):

$$RSS = \sum_i (y_i - f(x_i))^2 \quad (20)$$

where y_i was the airflow result from each inverse airflow model and $f(x_i)$ was the CFD model result.

3.5 Results and discussion

3.5.1 Comparing inverse models

3.5.1.1 Zone A

The estimation accuracy of invSVD, with and without considering infiltration (invSVD0 and invSVD1, respectively), was compared to that of invC for the pole configurations shown in Figure 3-2. Table 3-2 summarizes the skewness the airflow error distributions resulting from the use of each pole configuration and each inverse model for Zone A. The first row (Pole config. #0, base case) is the skewness of the error distribution with no additional sensor information provided to the inverse model. The invC has the highest skewness and lowest RSS (values of RSS not reported here for brevity. They can be found in APPENDIX D.) of the three inverse models when no additional sensor information is provided. Table 3-2 shows that in 4 out of the 18 pole configurations simulated (7, 9, 15, and 16) in Zone A, using the invSVD0 model resulted in error distributions with the highest skewness (better estimation accuracy) among the three inverse models. In 6 out of the 18 pole configurations simulated (1, 2, 4, 5, 14, and 17), using the invSVD1 model resulted in error distributions with the highest skewness

Table 3-2. Summary of skewness of error distributions resulting from use of invSVD0, invSVD1, and invC models to inversely estimate airflow for Zone A.

Pole configuration	Skewness			Model with highest skewness	% diff between invSVD models	% diff between invSVD1 and invC
	invSVD0	invSVD1	invC			
0 (base case)	0.600	0.646	0.855	invC	7.7%	32.3%
1	2.645	2.646	2.594	invSVD1	<1%	
2	2.641	2.645	2.584	invSVD1	<1%	
3	1.763	1.746	1.880	invC	<1%	7.7%
4	2.623	2.623	2.548	invSVD	<1%	
5	2.623	2.623	2.501	invSVD	<1%	
6	1.137	1.123	1.328	invC	<5%	18.3%
7	1.696	1.616	1.610	invSVD0	<5%	
8	0.951	0.998	1.281	invC	5.0%	28.3%
9	1.488	1.372	1.263	invSVD0	8.5%	
10	1.378	1.396	1.500	invC	<5%	7.5%
11	1.451	1.439	1.839	invC	<1%	27.8%
12	0.804	0.866	0.894	invC	7.7%	<5%
13	1.178	1.767	1.835	invC	<1%	<5%
14	1.539	1.713	1.710	invSVD1	11.3%	
15	1.139	1.094	0.723	invSVD0	<5%	
16	1.903	1.546	1.072	invSVD0	<1%	
17	1.546	1.625	1.531	invSVD1	5.1%	
18	1.072	1.063	1.104	invC	<1%	<5%

among the three inverse models. For the remaining pole configurations simulated (3, 6, 8, 10-13, and 18), using the invC model resulted in error distributions with the highest skewness among the three inverse models.

When using RSS as the indicator of estimation accuracy, none of the pole configurations simulated in Zone A using the invSVD0 model resulted in the lowest RSS (better estimation accuracy) among the three inverse models. In 9 out of the 18 pole configurations simulated (1-5, 13-15, and 17), using the invSVD1 model resulted in the lowest RSS among the three inverse models. For the remaining pole configurations simulated (6-12, 16, and 18), using the invC model resulted in the lowest RSS among the three inverse models. **Except for the invSVD0 model, using RSS as the indicator of**

estimation accuracy resulted in similar results to when skewness was used as the indicator of estimation accuracy.

Among the 8 pole configurations in Zone A where the skewness of the error distributions resulting from the use of the invC model were greater than those using the invSVD1 model, the difference was <5% for 3 of the pole configurations (12, 13, and 18). For the remaining 5 pole configurations (3, 6, 8, 10, and 11), plots of the error distributions and airflow results from the use of the invSVD1 and invC models showed little difference. Figure 3-4 shows the error distributions for pole configurations 8 and 11, which exhibited the greatest differences between the skewness of the error distributions resulting from the use of the invSVD1 and invC models. Among the 9 pole configurations in Zone A where the RSS resulting from the use of the invC model were less than those using the invSVD1 model, the difference was <5% for 5 of the pole configurations (6, 7, 9-10, and 16). For the remaining 4 pole configurations (8, 17, 18, and 24), the difference was <10%.

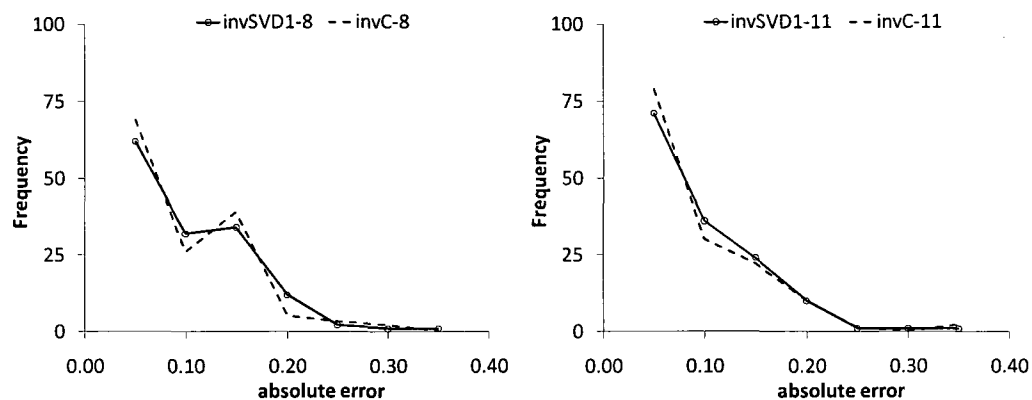


Figure 3-4. Error distribution plots for Pole Config. #8 and 11 and for invSVD1 and invC models (Zone A).

3.5.1.2 Zone B

Table 3-3 summarizes the skewness the airflow error distributions resulting from the use of each pole configuration and each inverse model for Zone B. Detailed values of RSS not reported here for brevity. They can be found in APPENDIX D.).

Table 3-3 shows that in 2 out of the 18 pole configurations simulated (7 and 8) in Zone B, using the invSVD0 model resulted in error distributions with the highest skewness (better estimation accuracy) among the three inverse models. In 7 out of the 18 pole configurations simulated (1, 3, 4, 9, 10, 13, and 15), using the invSVD1 model resulted in error distributions with the highest skewness among the three inverse models. For the remaining pole configurations simulated (2, 5, 6, 11, 12, 14, 16-18), using the invC model resulted in error distributions with the highest skewness among the three inverse models.

When using RSS as the indicator of estimation accuracy, 1 of the pole configurations simulated (6) in Zone B using the invSVD0 model resulted in the lowest RSS (better estimation accuracy) among the three inverse models. In 10 out of the 18 pole configurations simulated (1, 3-4, 9-11, and 15-18), using the invSVD1 model resulted in the lowest RSS among the three inverse models. For the remaining pole configurations simulated (2, 5, 7-8, and 12-14), using the invC model resulted in error distributions with the lowest RSS among the three inverse models. **For all three inverse models, using RSS as the indicator of estimation accuracy resulted in similar results to when skewness was used as the indicator of estimation accuracy.**

Table 3-3. Summary of skewness of error distributions resulting from use of invSVD0, invSVD1, and invC models to inversely estimate airflow for Zone B.

Pole configuration	Skewness			Model with highest skewness	% diff between invSVD models	% diff between invSVD1 and invC
	invSVD0	invSVD1	invC			
0 (base case)	1.794	1.846	2.088	invC	<5%	13.1%
1	2.615	2.619	2.503	invSVD1	<1%	
2	1.842	1.895	2.336	invC	<5%	23.3%
3	2.414	2.414	1.964	invSVD1	<1%	
4	2.508	2.524	2.459	invSVD1	<1%	
5	1.929	1.897	2.000	invC	<5%	5.4%
6	1.873	1.923	1.982	invC	<5%	<5%
7	2.450	2.443	1.331	invSVD0	<1%	
8	2.031	2.020	1.738	invSVD0	<1%	
9	2.157	2.169	1.980	invSVD1	<1%	
10	2.055	2.077	1.977	invSVD1	<5%	
11	2.083	2.083	2.087	invC	<1%	<1%
12	1.746	1.732	2.228	invC	<1%	28.7%
13	2.061	2.143	1.894	invSVD1	<5%	
14	1.564	1.564	1.985	invC	<1%	26.9%
15	2.101	2.118	2.079	invSVD1	<1%	
16	2.019	1.964	2.207	invC	<5%	12.4%
17	2.148	2.153	2.320	invC	<1%	7.8%
18	2.132	2.098	2.147	invC	<5%	2.3%

Among the 9 pole configurations in Zone B where the skewness of the error distributions resulting from the use of the invC model were greater than those using the invSVD1 model, the difference was <5% for 2 of the pole configurations (6 and 11). For the remaining 7 pole configurations (2, 5, 12, 14, 16-18), plots of the error distributions and airflow results from the use of the invSVD1 and invC models showed little difference. Figure 3-5 shows the error distributions for pole configurations 12 and 14, which exhibited the greatest differences between the skewness of the error distributions resulting from the use of the invSVD1 and invC models. Among the 10 pole configurations in Zone B where the RSS resulting from the use of the invC model were

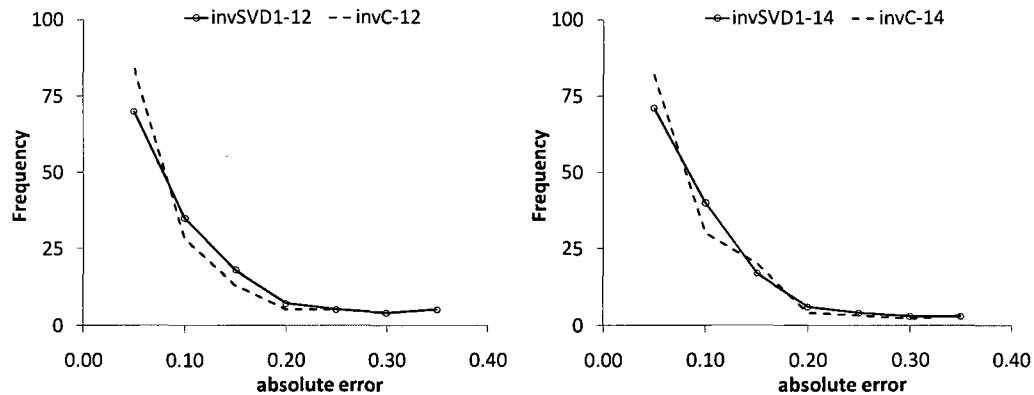


Figure 3-5. Error distribution plots for Pole Config. # 12 and 14 and for invSVD1 and invC models (Zone B).

less than those using the invSVD1 model, the difference was <5% for 1 of the pole configurations (12). For the remaining 9 pole configurations (2, 5, 7-8, and 13-14), the difference was rather large (15-85%).

3.5.1.3 Zone C

Table 3-4 summarizes the skewness the airflow error distributions resulting from the use of each pole configuration and each inverse model for Zone C. Detailed values of RSS not reported here for brevity. They can be found in APPENDIX D.).

Table 3-4 shows that in 5 out of the 18 pole configurations simulated (1, 4, 5, 6, and 8) in Zone B, using the invSVD0 model resulted in error distributions with the highest skewness (better estimation accuracy) among the three inverse models. In 7 out of the 18 pole configurations simulated (3, 10, 11, 14, and 16-18), using the invSVD1 model resulted in error distributions with the highest skewness among the three inverse models. For the remaining pole configurations simulated (2, 7, 9, 12, 13, and 15), using the invC

model resulted in error distributions with the highest skewness among the three inverse models.

When using RSS as the indicator of estimation accuracy, none of the pole configurations simulated in Zone C using the invSVD0 model resulted in the lowest RSS (better estimation accuracy) among the three inverse models. In 14 out of the 18 pole configurations simulated (1, 3-9, 12-16, and 18), using the invSVD1 model resulted in the lowest RSS among the three inverse models. For the remaining pole configurations simulated (2, 10-11, and 17), using the invC model resulted in the lowest RSS among the three inverse models. **Except for the invSVD0 model, using RSS as the indicator of estimation accuracy resulted in similar results to when skewness was used as the indicator of estimation accuracy.**

Table 3-4. Summary of skewness of error distributions resulting from use of invSVD0, invSVD1, and invC models to inversely estimate airflow for Zone C.

Pole configuration	Skewness			Model with highest skewness	% diff between invSVD models	% diff between invSVD1 and invC
	invSVD0	invSVD1	invC			
0 (base case)	1.705	1.643	1.851	invC	<5%	12.7%
1	2.597	2.597	2.344	invSVD0	<1%	
2	2.464	2.476	2.486	invC	<1%	<1%
3	2.344	2.361	1.650	invSVD1	<1%	
4	2.582	2.582	2.055	invSVD0	<1%	
5	2.390	2.381	2.374	invSVD0	<1%	
6	2.297	2.192	1.861	invSVD0	<5%	
7	1.924	1.946	1.998	invC	<5%	<5%
8	1.805	1.794	1.757	invSVD0	<1%	
9	1.790	1.829	1.957	invC	<5%	7.0%
10	2.072	2.178	2.155	invSVD1	5.12%	
11	2.178	2.223	2.159	invSVD1	<5%	
12	1.718	1.755	1.779	invC	<5%	<5%
13	2.057	2.094	2.149	invC	<5%	<5%
14	2.044	2.082	2.025	invSVD1	<5%	
15	1.819	1.864	1.886	invC	<5%	<5%
16	2.208	2.234	1.562	invSVD1	<5%	
17	2.129	2.234	1.869	invSVD1	<5%	
18	2.179	2.256	1.520	invSVD1	<5%	

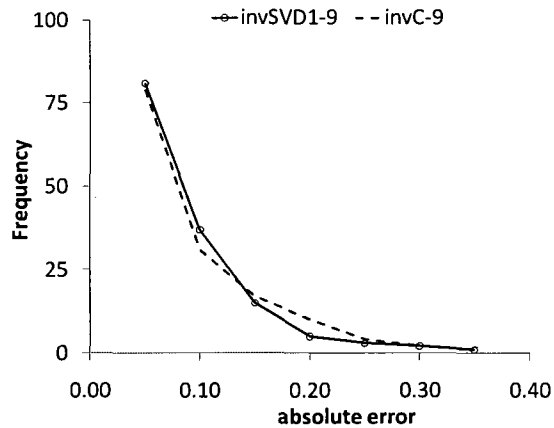


Figure 3-6. Error distribution plots for Pole Config. 9 for invSVD1 and invC models (Zone C).

Among the 6 pole configurations in Zone C where the skewness of the error distributions resulting from the use of the invC model were greater than those using the invSVD1 model, the difference was <5% for 5 of the pole configurations (2, 7, 12, 13, and 15). For the remaining pole configuration (9), the plot of the error distributions and airflow results from the use of the invSVD1 and invC models showed little difference. Figure 3-6 shows the error distributions for pole configuration 9, which exhibited the greatest differences between the skewness of the error distributions resulting from the use of the invSVD1 and invC models. Among the 4 pole configurations in Zone C where the RSS resulting from the use of the invC model were less than those using the invSVD1 model, the difference was <10% for 2 of the pole configurations (10 and 17). For the remaining 2 pole configurations (2 and 11), the difference was 27% and 13%, respectively.

Based on the airflow estimation results from three simulated zones, it was concluded that the invSVD and invC models demonstrated comparable airflow

estimation accuracy. Except for three pole configurations (9, 12, and 14), the difference between the skewness of the error distributions resulting from the use of the invSVD0 and invSVD1 models were small (<5%) for Zone A. When using RSS as the indicator of estimation accuracy, except for pole configurations 1 and 2, the difference between the RSS values resulting from the use of the invSVD0 and invSVD1 models were small (<5%) for Zone A. For all of the pole configurations, the difference between the skewness of the error distributions resulting from the use of the invSVD0 and invSVD1 models were small (<5%) for Zones B and C. When using RSS as the indicator of estimation accuracy, except for pole configuration 6, the difference between the RSS values resulting from the use of the invSVD0 and invSVD1 models were small (<5%) for Zone B. When using RSS as the indicator of estimation accuracy, except for pole configuration 6, the difference between the RSS values resulting from the use of the invSVD0 and invSVD1 models were small (<5%) for Zone B. When using RSS as the indicator of estimation accuracy, except for pole configurations 3 and 6, the difference between the RSS values resulting from the use of the invSVD0 and invSVD1 models were small (<5%) for Zone C. **Thus, it was concluded that including infiltration as a known boundary condition in the invSVD model generally neither degraded nor improved its estimation accuracy for the pole configurations tested in the simulated zones.**

3.5.2 Best sensor locations (from pre-selected configurations)

Since it was concluded in the previous section that there was little difference between the airflow estimated using the three inverse models, subsequent discussions will focus on the airflow results using the invSVD1 model. From Table 3-2, the five pole

configurations with the highest skewness values were Pole Config. #1, 2, 5, 4 and 16 for Zone A. Pole Config. #1, 2, 5, and 4 were also among the configurations with the lowest RSS values.

Pole Config. #1 and 2 are in the same "family", i.e. they have the same number of poles and only differ in the direction velocity was measured. Both configurations placed sensors in all subzones. The difference between them was that Pole Config. #1 measured velocity in both the x - and y -directions, while Pole Config. #2 only measured velocity in the y -direction. Pole Config. #4 and 5 are also in the same "family". Both configurations placed sensors in the subzones located on the perimeter of the zone. Again, the only difference between them was that Pole Config. #4 measured velocity in both directions, while Pole Config. #5 only measured velocity in the y -direction. Pole Config. #16 placed two poles near the diffuser and two poles near the exhaust, measuring velocity in both directions.

Even though there were more sensor data available for Pole Config. #1 than for Pole Config. #5, the difference between the skewness values was $<1\%$. In contrast, the RSS value for Pole Config. #1 was much less than for Pole Config. #5. Nevertheless, Figure 3-7 shows that using Pole Config. #5 (sensors around perimeter of zone), the invSVD1 model captures the general airflow pattern calculated by CFD just as well as using Pole Config. #1 (sensors in every subzone). **Thus, it was concluded that sensors placed around the perimeter subzones of Zone A provided sufficient data to estimate indoor airflow as accurately as placing sensors in every subzone.** *This offers a practical and cost effective simplification in both experimental set ups and field tests*

for future work in inverse airflow modeling. Sensors are more readily installed on walls than in the center of a room.

Not surprisingly, like for Zone A, the best pole configuration was 1 (sensors in every subzone measuring velocity in both directions) for Zones B and C when using skewness as the indicator of estimation accuracy. However, the second best pole configuration was not 2, but 4 for both Zones B and C. Using Pole Config. #4, like Pole Config. #5, the invSVD1 model captured the general airflow pattern calculated by CFD just as well as using Pole Config. #1 (sensors in every subzone) (Figure 3-8 for Zone B and Figure 3-9 for Zone C). Using RSS as the indicator of estimation accuracy, Pole Config. #8 was the best configuration for Zone B. Pole Config. #8 placed sensors in the center of the room, which was also where the diffuser was located in Zone B. Nevertheless, the pole configuration with the second best RSS in Zone B was Pole Config. #5 (as was found when using skewness to select the best configuration), and its value was <5% greater than for Pole Config. #8. Using RSS as the indicator of estimation accuracy, Pole Config. #4 was the best configuration for Zone C. **Thus, using either skewness or RSS values to evaluate estimation accuracy, similar pole configurations were selected as the best ones.**

When using skewness as the indicator of estimation accuracy, the next best three pole configurations for Zone B were 7, 3, and 9. And the next best three pole configurations for Zone C were 2, 5, and 3. Pole Config. #7 and 9 are in the same "family". Both configurations placed sensors the center of the zone. These were the next best pole configurations for Zone B since the inlet in Zone B was simulated closer to the center of the zone. The inlet in Zone A was simulated in the corner. The next best pole

configurations for Zone C were the same families as the top two configurations, like for Zone A, since the inlet location was the same. When using RSS as the indicator of estimation accuracy, other low-RSS valued pole configurations for Zone B were 13 and 14, and 16 for Zone C. Pole Configs. #13 and 14 placed sensors along the diagonal of the test space, from the inlet to the outlet. Pole Config. #16 placed sensors near the inlet in Zone C. **Thus, it was concluded that measurements below the inlet could improve the airflow estimation accuracy of the inverse models tested for all simulated zones.**

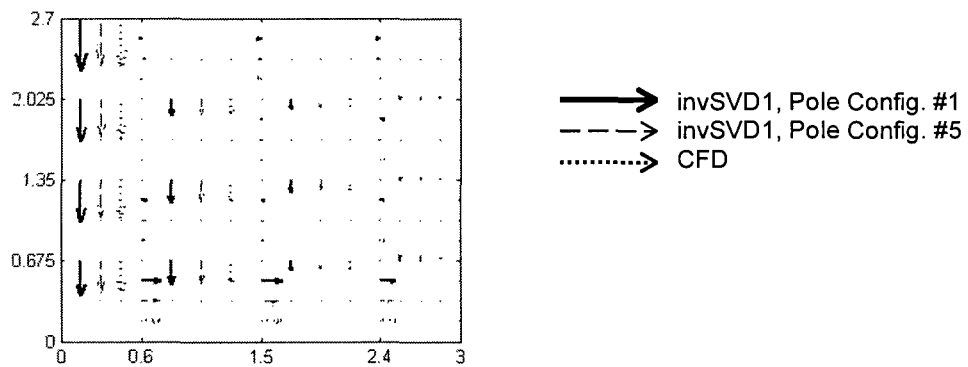


Figure 3-7. Flow pattern through diffuser in Zone A for invSVD1, Pole Config. #1 and 5, and for the CFD results.

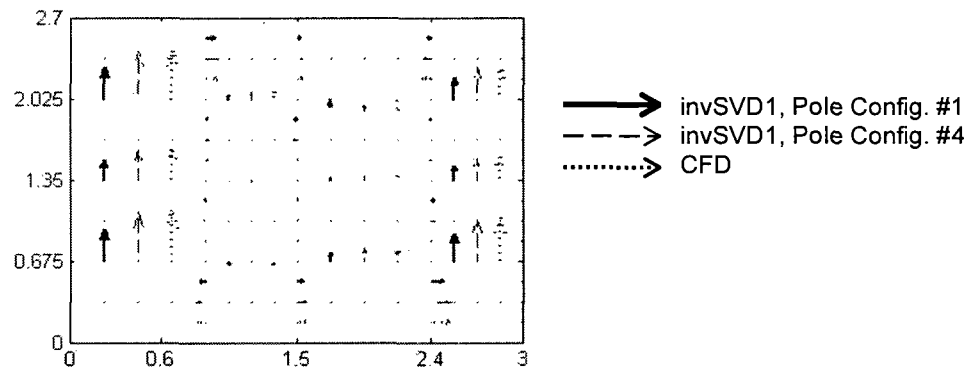


Figure 3-8. Flow pattern through diffuser in Zone B for invSVD1, Pole Config. #1 and 4, and for the CFD results.

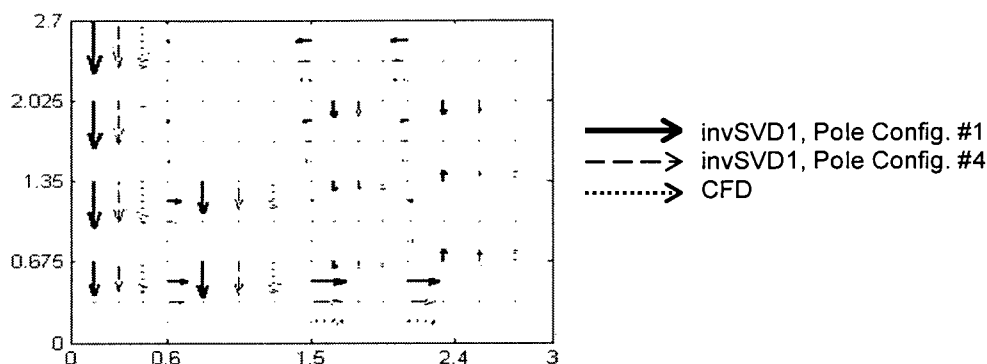


Figure 3-9. Flow pattern through diffuser in Zone C for invSVD1, Pole Config. #1 and 4, and for the CFD results.

3.5.3 Best sensor locations (from optimization)

This section discusses the optimization study using the invSVD1 model. This inverse model was chosen for the optimization process since (1) the skewness of the error distributions resulting from the use of the invSVD1 did not greatly differ from those using the invSVD0 and invC models and (2) either of the invSVD models was more easily incorporated into the optimization process than invC.

Figure 3-10 shows the skewness of the error distributions resulting from the incorporation of an increasing number of sensors for Zone A. In Trial 1, for each candidate location, only velocity measurements in one direction, either vertical or horizontal, were provided to each inverse airflow model as additional known data. In Trial 2, for each candidate location, *both* vertical and horizontal measurements were available. For both Trials 1 and 2, as the number of sensors increased, the skewness increased as well, which was to be expected. The difference between the skewness values for Trials 1 and 2 were never greater than 5% for any sensor quantity. **Thus, it could be concluded that the extra measurement (and thus the extra sensor in an experimental**

setup) would not greatly improve the estimation accuracy of the invSVD1 model.

And, for Zones B and C, only Trial 1 was conducted. **This was also found when using RSS as the indicator of estimation accuracy.**

Figure 3-10 also shows that as the number of sensors increased, the skewness stabilized. In contrast, as the number of sensors increased, the RSS values linearly decreased. For Trial 1, there is <5% improvement in skewness above nine sensors. The reason for this is with a limited number of sensors, the optimization process found locations that were more critical to the improvement of skewness. As the number of available sensors was increased, the additional measurements only provided marginal improvement to skewness. Knowing the optimal quantity of sensors for a specific test room necessary for acceptable inverse airflow estimation is important in most situations where sensor quantity is limited.

It was shown in Sec. 3.5.2 that if sensors were limited to the perimeter of the zone, the major circulation patterns predicted by CFD were well-captured (Figure 3-7). This was demonstrated during the optimization process as well. For optimal sensor configurations up to and including nine sensors, the optimization process selected a majority of the sensors (91%) to be located on the walls for Zone A when using skewness as the indicator of estimation accuracy. **This was also found when using RSS as the indicator of estimation accuracy.** It was for this reason that the difference in skewness for Trials 1 and 2 were never greater than 5%. Due to the subdivision of each zone in this study, at least one of the control faces of a subzone on a wall coincided with the wall of the zone. Thus, if a sensor was selected to be located on a wall (as was the case 91% of the time), the additional velocity measurements of Trial 2 oftentimes had values of zero

(no flow across walls), providing no additional information to improve estimation accuracy.

When using skewness as the indicator of estimation accuracy, 40% of the sensors that were found to be located on the walls were located in the z -plane closest to the outlet ($z=4$). The z -planes with the next highest percentage of sensors were $z=1$ (under the inlet) and $z=3$ (adjacent to $z=4$). For sensor configurations with ten to 18 sensors, the locations were more evenly distributed between the four z -planes with the majority still located in $z=4$. (18 sensors were tested since it was double the optimal quantity of sensors) When using RSS as the indicator of estimation accuracy, 55% of the sensors that were found to be located on the walls were located in the z -plane closest to the *inlet* ($z=1$). The z -planes with the next highest percentage of sensors were $z=2$ (adjacent to $z=1$) and then $z=3$ and $z=4$ with the same percentage. For sensor configurations with ten to 18 sensors, *again*, the locations were more evenly distributed between the four z -planes with the majority still located in $z=1$.

The majority of sensors were selected to measure velocity in the vertical direction **using either skewness or RSS as the indicator of estimation accuracy**. This is due to the fact that the inlet is delivering and the outlet is exhausting air vertically through Zone A.

As with Zone A, as the number of sensors increased, the skewness increased as well for Zones B and C when using skewness as the indicator of estimation accuracy. As the number of sensors increased, the RSS values linearly decreased. As the number of sensors increased, the skewness stabilized. However, the quantity of sensors for which

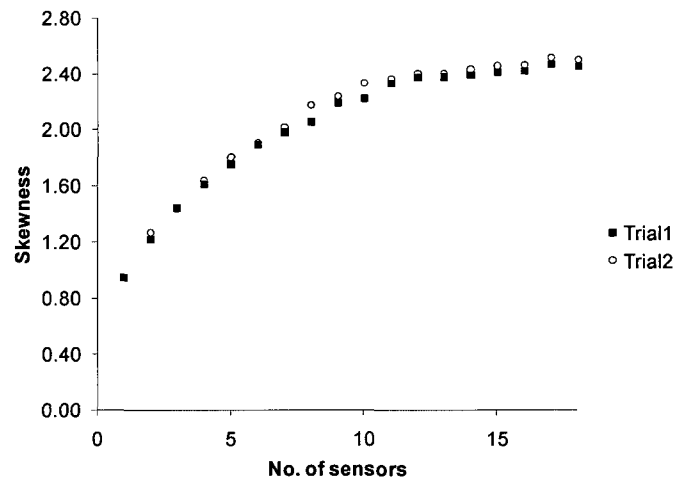


Figure 3-10. Skewness values for Trials 1 and 2 with various numbers of sensors in Zone A.

Table 3-5. Mean age of air for test cases in Chapter 3

Test Zone	Local mean age of air (LMA) (sec) Mean±Standard Deviation
A	26±10
B	55±18
C	58±23

this occurred was different for each zone. For Zone A, it was nine sensors. For both Zones B and C, it was four sensors. The mean age of air in Zones A, B, and C are reported in Table 3-5 as calculated using CFD data. See Sec. 2.10.4 on how mean age of air was calculated. Since the mean age of air for Zones B and C were similar, the optimal number of sensors for these zones was also similar when using skewness as the indicator of estimation accuracy.

In Zone B, up to four sensors, the majority of sensors were selected to be located in the z -plane closest to the outlet ($z=4$). The remaining sensors were located in the z -plane closest to the inlet ($z=2$). For sensor configurations with five to eight sensors, the

majority of sensors were selected to be located in the z -plane closest to the inlet ($z=2$). (8 sensors were tested since it was double the optimal quantity of sensors) When using RSS as the indicator of estimation accuracy, all of the sensors that were found to be located on the walls were located in the z -plane closest to the *inlet* ($z=1$). For sensor configurations with five to eight sensors, the majority were still located in $z=1$.

As with Zone A, most of the sensors were selected to be placed on the walls and measure velocity in the vertical direction **using either skewness or RSS as the indicator of estimation accuracy**. These same results were found for Zone C as well.

Since the outlet in Zones A and B were adjacent to a wall, the majority of the sensors were shown to be placed in the same z -plane as the outlet ($z=4$) when using skewness as the indicator of estimation accuracy. However, in Zone C, where the outlet was placed off the wall in $z=3$, the majority of the sensors were shown to be placed in the z -plane adjacent to the outlet ($z=4$, a wall) when using skewness as the indicator of estimation accuracy. Thus, it was concluded that, up to the optimal number of sensors for each respective test room, the majority of sensors will be placed on the wall *closest* to the outlet no matter the location of the inlet when using skewness as the indicator of estimation accuracy. When using RSS as the indicator of estimation accuracy, the majority of sensors will be placed on the wall closest to the *inlet*.

Though using skewness and RSS as the indicator of estimation accuracy resulted in different locations for the placement of sensors (i.e., using skewness, sensors should be placed near the exhaust; using RSS, sensor should be placed near the diffuser), it was found that the majority of sensors should be placed on the walls and close to a *flow element* (i.e., diffuser or exhaust). Further, the majority of the

sensors should measure velocity in direction of the bulk airflow, whether using skewness or RSS as the indicator of estimation accuracy.

3.5.4 Using synthetic temperature data

A value of $4 \text{ W/m}^2\cdot\text{K}$ for h_k was initially assumed for all subzone surfaces [111]. The temperature of the incoming air and that of the surfaces was known. Therefore, the only unknown in Eq. (18) was indoor airflow, which can be inversely solved for using invSVD. Given the sensor locations in Figure 3-2a, it was found that the skewness of the error distribution (0.708) was no better than the case when the same number of velocity data was included in the invSVD1 model (2.646). **Therefore, it was not recommended that temperature sensors be used to inversely solve for indoor airflow since the same number of velocity sensors resulted in an estimation accuracy that was better by about two-fold.** Other values for h_k were tested as well, ranging from 0.5 to $100 \text{ W/m}^2\cdot\text{K}$. It was found that the difference in skewness value was $<1\%$ up to a value of $8 \text{ W/m}^2\cdot\text{K}$. **Therefore, it was concluded that any reasonable value of h_k can be assumed when using invSVD to estimate indoor airflow from temperature measurements.**

3.5.5 Limitations of invSVD model

SVD is a method to solve an underdetermined set of *linear* equations. The invSVD model utilized a set of linear mass balance equations to inversely solve for indoor airflow. Any airflow that is better represented by a nonlinear relationship, such as infiltration, could only be included in the invSVD model if the relationship were first linearized. However, this is the solution method taken by traditional multizone models such as CONTAM. If one wanted to estimate infiltration, a multizone model simulation would be needed. If infiltration could be neglected, the invSVD model may be employed

to solve for indoor airflow, as was demonstrated by the studies on the three test zones. A research question remains as to when infiltration can be neglected.

3.6 Conclusions

Inverse modeling techniques provide opportunities to take advantage of fast-developments in sensing and communicating technologies, using sensor data for efficient and accurate estimation and prediction of indoor airflow and contaminant distribution. However, for the capabilities of inverse models to reach their full potential, proper inverse model structure and sensor system design (such as quantity and type) need to be examined. Here, (1) the feasibility of using SVD as an inverse modeling approach was studied, where indoor airflow was represented as a linear system, (2) the performances of inverse SVD models and inverse CONTAM model, where indoor airflow is represented as a non-linear system, were compared, (3) the need for including infiltration in these inverse models was evaluated, and (4) optimal sensor system design to best provide sensor measurements for inverse models was examined. It was found that for *all* zones simulated:

- (1) The inverse SVD models (invSVD0 and invSVD1) performed comparably to the inverse CONTAM model when provided with velocity data;
- (2) Infiltration data did not affect the performance of inSVD greatly;
- (3) Using data from sensors placed along the perimeter of the zone, the airflow estimated by the invSVD1 model captured the same general airflow pattern as predicted by a CFD model;
- (4) Using genetic algorithm to optimize the estimation accuracy, using either skewness or RSS as the objective function, of the invSVD1 model, most sensors

should be placed on the wall closest to the a flow element and measure velocity in the vertical direction. This was also the bulk direction of airflow since the inlet and outlets were located in the ceiling;

- (5) When using temperature data for estimating indoor airflow, it was found that the airflow estimation was better than the case when the same amount of velocity data was provided to the invSVD1. Since using temperature data to estimate indoor airflow required temperature readings from every subzone, it was not recommended that temperature sensors be used to inversely solve for indoor airflow since the same number of velocity sensors resulted in an estimation accuracy that was better by about two-fold. A similar conclusion could be drawn for other types of sensors, such as contaminant.

Hypothesis #2 was: there exists an *inverse* airflow model that is able to efficiently and accurately estimate indoor airflow patterns and contaminant transport utilizing measurements from an indoor air sensor system. In this work, it could be concluded that the invSVD model performed comparably to the invC model. The invSVD model offers several advantages to the invC model.

- (1) It is easier to set up, only requiring the size of the subzones, number/layout of subzones, and inlet conditions;
- (2) The system of equations that invSVD uses to solve for indoor airflow are linear, and thus, are easily incorporated into ventilation control systems than nonlinear systems, which invC utilizes;

The second advantage of the invSVD model is also its *limitation*. Phenomena such as infiltration and exfiltration are traditionally solved for in airflow models using

nonlinear pressure-flow relationships. Because nonlinear relationships cannot be incorporated into invSVD1 without linearization, which can introduce computational error, these nonlinear phenomena cannot be accounted for. In this work, infiltration, when included in the invSVD model, was assigned a constant value.

It is for these reasons that the invSVD model was not extended to Part 3 of this research, which is the estimation of indoor airflow for an entire building. Nevertheless, the conclusions on velocity sensor placement in this work can be beneficial for simplifying and maximizing the effectiveness of indoor airflow experiments and measurements. The resulting airflow estimation would be useful for evaluating indoor air quality and could also provide an estimate of contaminant transport.

Portions of this work were published in conference proceedings – *Indoor Air 2008* and *ANCRiSST*. The full publications can be found in APPENDIX C. Unpublished portions have been submitted for publication in *Building and Environment*.

3.7 Future work

The conclusions drawn from the work in this chapter are beneficial for simplifying and maximizing the effectiveness of indoor airflow experiments and measurements. Nevertheless, the work was *limited* in the amount of variation between test cases. Only three diffuser and exhaust layouts were tested. Therefore, additional work would include testing whether or not the sensor placement guidelines for the zones tested in this work can be extended to other diffuser/exhaust layouts (such as wall-mounted). The airflow estimated from the invSVD model should be further validated against real sensor data. One could compare airflow and contaminant measurements.

3.8 Plans for publication

Unpublished portions of this work has been submitted to *Building and Environment*, which has an impact factor of 1.192. Another possible publication is *Journal of Environmental Monitoring*, which has an impact factor of 2.0.

4. CHAPTER 4: TESTING HYPOTHESIS #3 – DEVELOPING AND UTILIZING INVERSE MODEL FOR WHOLE BUILDING

As discussed in the Sec. 1.4, determining the airflow pattern throughout a whole building is useful for predicting contaminant distribution, determining building envelope airtightness, pressure distribution within a building, for decontamination, building commissioning, and retrofitting. The current methods for determining a building airflow network and the proposed framework for developing a building airflow network inverse model are discussed below and shown in Figure 4-2.

4.1 Current methods and limitations for determining a building airflow network

There are currently two methods for determining the airflow pattern within a building, which will now be referred to as the *building airflow network*. The first is using a forward airflow model (see Sec. 1.3.1) and the second is by specialized experiments, such as fan pressurization and tracer gas tests. Forward airflow models require detailed information about a building in order to simulate airflow patterns. Depending on the forward airflow model, they require time and sometimes specialized knowledge in order to obtain an accurate result (Sec. 1.3.1.1 to 1.3.1.3).

Air exchange is the exchange of outdoor air and the air inside a building. It can be intentional or unintentional. Outdoor air is *intentionally* delivered to a building through the ventilation system in order to maintain IAQ. Outdoor air is *unintentionally* delivered to a building (or indoor air is *unintentionally* leaving a building) through the openings in the building envelope or other leakage paths. Fan pressurization tests determine the airtightness of these leakage paths.

A fan pressurization test can be used to determine the parameters K and n in the following relationship:

$$Q = K(\Delta P)^n \quad (21)$$

The volume of air supplied by a fan, Q , is recorded along with the indoor-outdoor pressure difference, ΔP , generated by Q (Figure 4-1). The parameters K and n are characteristic of the building envelope and do not change when ΔP changes. Thus, theoretically for any other ΔP measured, the airflow rate (*infiltration*) through the building envelope and other leakage paths can be determined.

ASTM Standard E779 specifies test conditions for fan pressurization (or blower-door) tests. The standard is intended for *single-zone* buildings or multi-zone buildings that can be considered a single-zone [112]. Canadian Standard CGSB149.15 specifies test conditions for a fan pressurization test using a building's own air handling system [113]. It was applied to commercial buildings with limitations [114]. Bahnfleth et al. [115]

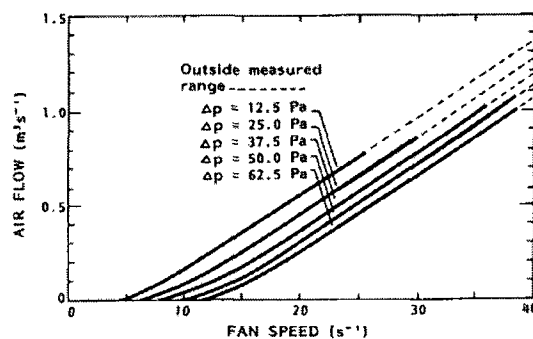


Figure 4-1. Example of blower-door test results.
Source: [116].

compared these two test standards in two multi-zone, multi-story buildings. The researchers found that *neither* method was easy to implement. Wind and stack effects were difficult to control in multi-story buildings. Further, the sealing of leakage paths between floors, such as shaft penetrations, was also challenging. The results of the fan pressurization tests may be inaccurate in this case. **Therefore, a method is needed to accurately determine the building envelope airtightness of multi-zone buildings, in order to be useful in determining infiltration.**

A *tracer gas* test is used to determine infiltration rates under specific test conditions, e.g., outdoor weather condition, ventilation system operation, etc. A known amount of a tracer, or substance that does not affect indoor airflow, is released and measured in a zone (or multiple zones). Knowing the amount of tracer released and how its concentration inside a zone changes with time, the air exchange rate can be calculated. Tracer gas tests can be categorized in many ways: single-zone or multi-zone methods, injection technique, and sampling technique. McWilliams [117] provided a detailed summary of current tracer gas test techniques.

ASTM Standard E741 specifies test conditions for tracer gas tests, as well as how to calculate air exchange rates [118]. Traditional tracer gas tests require specialized equipment to inject and sample specialized tracers, such as SF₆ or NO₂. They are mostly performed for *single-zone or small multi-zone* buildings. Studies in the literature have also used CO₂ as a tracer for single zones [41, 119-124]. Most of these tests determined overall air exchange rates with the outdoors and not the specific airflow rate through the building envelope or between zones (*interzonal* airflow). In order to estimate interzonal

airflow rates, either multiple tracers were needed [40] or multiple tracer tests needed to be performed [125].

Results from tracer gas tests are limited because their results are obtained under *specific* indoor and outdoor test conditions. If any of the test conditions changes significantly, the tracer test would need to be repeated in order to obtain a new infiltration (air exchange) rate. Also, the need for special injection and sampling equipment limits the use of tracer gas tests for continuous or regular measuring of infiltration rates. Lastly, to determine interzonal airflow rates, one would need multiple tracers or repeat a single tracer test as many times as there are zones. **Therefore, a method is needed to accurately determine the building infiltration rate, especially a method to continuously determine the infiltration rate under changing indoor and outdoor conditions.**

These specialized tests are used to determine *building air exchange rates*, and not the relatively more detailed airflow patterns that are simulated by forward airflow models. **Thus, an effective method for determining interzonal airflow rates is also needed.**

4.2 Framework for developing a building airflow network inverse model

Figure 4-2 shows the information needed to completely describe a *building airflow network*, as defined in this research. They are: building envelope leakage, building air exchange rates, interzonal airflow rates, and ventilation system operation. As discussed in the previous section, this information can be obtained through simulation or measurements. However, the major shortcomings of the current methods for determining a building airflow network is that they are neither fast nor simple to perform, they

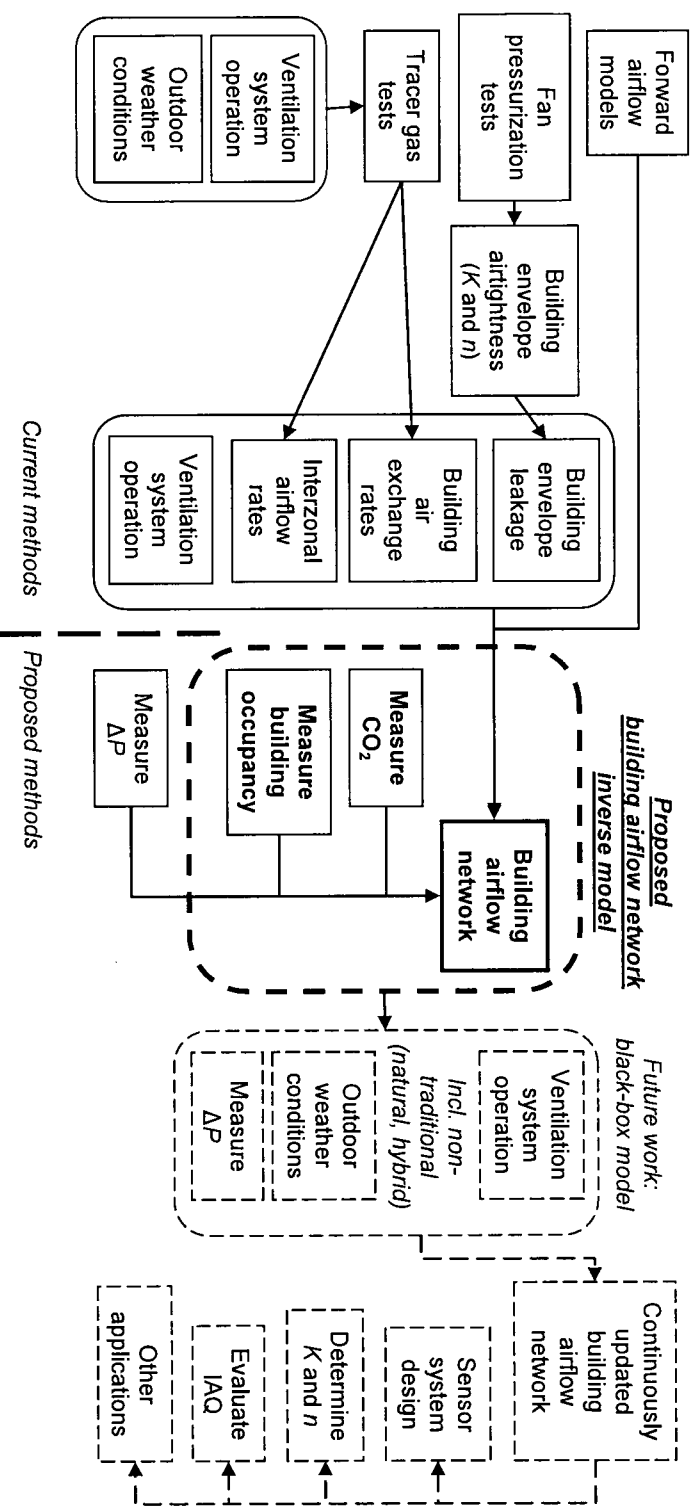


Figure 4-2. Framework for developing building airflow network inverse model.

are not standardized for multi-zone buildings, and they cannot give a real-time estimate of a building airflow network. A real-time estimate is needed since changes are always occurring in ventilation operation, weather conditions, etc. Even building envelope airtightness, which is characteristic of the envelope construction, will change over time as a building ages. These shortcomings can be potentially overcome by the development and utilization of the *building airflow network inverse model* proposed in this research.

The proposed building airflow network inverse model utilizes information that is easily obtained from commonly installed sensor systems, e.g. CO₂ measurements and occupancy. The use of pressure measurements was considered. They were not included in the proposed building airflow network inverse model because pressure sensors are sensitive to error when ΔP is low, e.g., under normal operating/airflow conditions inside a building [33].

The building airflow network inverse model developed in this research was able to determine all the information that completely describes a building airflow network, as defined in this research. Specifically, it was able to estimate airflow rates through the building envelope, interzonal airflow rates, and exhaust rates from zones. The building airflow network inverse model developed in this research was also easily implemented for a multi-zone building and provided a quick estimate of the building airflow network.

The building airflow network inverse model in this research was tested using a *single* set of ventilation system operation, outdoor weather conditions, and occupancy information. Since changes are always occurring in ventilation operation, weather conditions, etc., real-time estimates of the *changing* building airflow network is ultimately needed.

Figure 4-2 shows that future work can utilize the building airflow network inverse model proposed in this research, along with a black-box model (or pattern recognition technique, etc.), to update the building airflow network.

The proposed building airflow network inverse model could provide multiple "point" estimates of a building airflow network. Other information, such as ventilation operation, outdoor weather conditions, and pressure measurements, could be collected each time a point estimate was made. All of this information would then be used to "train" a black-box model to draw relationships between each point estimate and the information collected. Then, in the future, as ventilation operation, outdoor weather conditions, and pressure measurements change, the black-box model could easily provide an updated building airflow network. Important to note as well is the potential to use a well-developed black-box model to estimate the building airflow network when non-traditional ventilation systems, such as natural ventilation and hybrid systems, are in use. Non-traditional ventilation systems are more greatly affected by continuously-changing and uncertain outdoor weather conditions. Thus, they are more difficult to correctly mathematically model than traditional ventilation systems.

The updated building airflow network would have many applications. Some are shown in Figure 4-2. They are: for sensor system design, providing real-time IAQ evaluation, quickly and easily determining K and n (which would traditionally require a fan pressurization test), and others.

4.3 Chapter 4 outline

The following section describes the proposed building airflow network inverse model. Sec. 4.5 describes the study methods to test the proposed building airflow network

inverse model. Sec. 4.6 describes the test cases used to test the proposed building airflow network inverse model and the results. Conclusions are discussed in Sec. 4.7 and future work in Sec. 4.8.

4.4 Proposed building airflow network inverse model

The *building airflow network inverse model* presented here determines the airflow pattern within a whole building using measurements from a distributed sensor network. Two methods were used to mathematically represent the building airflow network: deterministic and stochastic.

4.4.1 Deterministic inverse model

The building airflow network was represented by the general contaminant mass balance equation:

$$V_i \frac{dC_i}{dt} = \sum_{j \neq i} Q_{ji} C_j - \sum_{j \neq i} Q_{ij} C_i + M_i S \quad (22)$$

where V_i is the volume of each zone, Q_{ji} is the airflow rate from zone j to zone i (m^3/s), Q_{ij} is the airflow rate from zone i to zone j (m^3/s), C_j is the CO_2 concentration in zone j (kg/m^3), C_i is the CO_2 concentration in zone i (kg/m^3), M_i is the number of occupants in a zone, and S is the CO_2 generation rate (kg/s) for each occupant. S was assumed to be the same for every occupant. It was assumed that the occupants were the only source of CO_2 in addition to the ambient (outdoor) CO_2 concentration. Other possible sources of CO_2 would be combustion appliances that burn fuel for heating and cooking, such as stoves, space heaters, and furnaces. However, these were not present in this research. It was also assumed that no CO_2 sinks were present. Lastly, it was assumed that each airflow rate, Q , remained constant.

The use of CO₂ was advantageous because it is a naturally present tracer. CO₂ sensors are also more readily available and relatively inexpensive compared to the equipment needed to measure a traditional tracer gas such as SF₆.

For N zones, the system of *steady-state* contaminant mass balance equations was:

$$\mathbf{QC} = -\mathbf{G} \quad (23)$$

where \mathbf{Q} is the parameter matrix to be estimated (the unknown building airflow network). \mathbf{C} is the concentration matrix representing CO₂ measurements in each of the N zones, the supply concentration, C_s , and the ambient concentration, C_θ . \mathbf{G} is the source matrix representing the total source of CO₂ in each of the N zones. Equation (23) was expanded as:

$$\begin{bmatrix} -\sum_j Q_{1-j} & Q_{2-1} & \dots & Q_{N-1} \\ Q_{1-2} & -\sum_j Q_{2-j} & & Q_{N-2} \\ \dots & \dots & \dots & \dots \\ Q_{1-N} & Q_{2-N} & \dots & -\sum_j Q_{N-j} \end{bmatrix} \begin{bmatrix} C_1 \\ C_2 \\ \dots \\ C_N \\ C_s \\ C_\theta \end{bmatrix} = - \begin{bmatrix} G_1 \\ G_2 \\ \dots \\ G_N \end{bmatrix} \quad (24)$$

where $G_i = M_i S$, which is the number of occupants in each zone multiplied by the rate at which the occupant generated CO₂.

For a *transient system*, the time change of C_i in Eq. (22) was represented using a first-order backward approximation. Thus, Eq. (22) was rewritten as:

$$V_i \frac{-C_i(t-1) + C_i(t)}{\Delta t} = \sum_{j \neq i} Q_{ji} C_j(t-1) - \sum_{j \neq i} Q_{ij} C_i(t-1) + G_i(t-1) \quad (25)$$

where t is the current time step, $t-1$ is the previous time step, and Δt is the time between time steps (sec). A higher-order approximation was also tested in this research. It was

found that a higher-order approximation introduced more noise into the calculation of $\mathbf{C}(t)$.

An analytical method to solve for $\mathbf{C}(t)$ also could have been used. In [126], the researchers utilized eigenvalues. This method was also employed by [40]. However, the researchers reported that as the number of zones increased (and thus also the number of unknowns in \mathbf{Q}), the eigenvalue method would be mathematically unstable. Therefore, a numerical approach was utilized for the building airflow network inverse model proposed in this research so that the framework and results could be extended to buildings of any size.

For N zones, the system of *transient* contaminant mass balance equations was:

$$\hat{\mathbf{C}}(t) = [\mathbf{Q}\hat{\mathbf{C}}(t-1) + \mathbf{G}(t-1)]\frac{\Delta t}{\mathbf{V}} + \hat{\mathbf{C}}(t-1) \quad (26)$$

which was expanded as:

$$\begin{bmatrix} \hat{C}_1 \\ \hat{C}_2 \\ \dots \\ \hat{C}_N \end{bmatrix}_t = \begin{bmatrix} \frac{1}{V_1} & 0 & \dots & 0 \\ 0 & \frac{1}{V_2} & \dots & 0 \\ \dots & \dots & \dots & \dots \\ 0 & 0 & \dots & \frac{1}{V_N} \end{bmatrix} \left\{ \begin{bmatrix} -\sum_j Q_{1-j} & Q_{2-1} & \dots & Q_{N-1} \\ Q_{1-2} & -\sum_j Q_{2-j} & \dots & Q_{N-2} \\ \dots & \dots & \dots & \dots \\ Q_{1-N} & Q_{2-N} & \dots & -\sum_j Q_{N-j} \end{bmatrix} \begin{bmatrix} \hat{C}_1 \\ \hat{C}_2 \\ \dots \\ \hat{C}_N \\ C_S \\ C_0 \end{bmatrix}_{t-1} + \dots \right. \\ \left. \dots \begin{bmatrix} G_1 \\ G_2 \\ \dots \\ G_N \end{bmatrix}_{t-1} \right\} \Delta t + \begin{bmatrix} \hat{C}_1 \\ \hat{C}_2 \\ \dots \\ \hat{C}_N \end{bmatrix}_{t-1} \quad (27)$$

where the " $\hat{}$ " represented the CO_2 concentration calculated using the building airflow network estimated by the building airflow network inverse model. The solution of Eq.

(27) was initiated knowing $C_i(t=0)$ for $i = 1 \dots N$. The quantities C_S (CO₂ concentration from supply diffusers) and C_0 (outdoor CO₂ concentration, were known.

4.4.2 Stochastic inverse model

Many of the terms in Eq. (22) are inherently random (or uncertain), or can be described in a statistical (probabilistic) sense. There are uncertainties in airflow measurements, Q , such as the airflow rate through an open window or how an occupant moving past an open doorway affects the airflow rate. There are uncertainties in contaminant measurements, C , due to sensor errors. There are also uncertainties in CO₂ generation rates, G . Even if the number of occupants in a space can be accurately determined, the rate at which CO₂ is generated will vary from occupant to occupant depending on physical factors such as gender, activity level, and metabolic rate.

In addition to the uncertainties in Q , C , and G , there is also variability in the system, which can be represented by a stochastic model. Variability includes those that factors that affect indoor airflow and thus contaminant distribution in Eq. (22). Examples include occupant movement, furniture being moved, and door openings and closings.

Therefore, a stochastic model was used to represent the building airflow network in this research. A stochastic term was added to Eq. (22) to account for CO₂ sensor error and variability in the system only. Stochastic terms can also be added to account for uncertainty in other terms, like Q and G . This is saved for future work.

A *stochastic differential equation* (SDE) is one in which some of the coefficients of a deterministic differential equation are random [127]. Consider a simple population growth model:

$$\frac{dN}{dt} = a(t)N(t), \quad N(0) = N_0 \quad (28)$$

where $N(t)$ is the size of the population at time t , and $a(t)$ is the relative rate of growth at time t . If $a(t)$ is random, then:

$$a(t) = r(t) + \text{"noise"} \quad (29)$$

and

$$\frac{dN}{dt} = [r(t) + \text{"noise"}]N(t) \quad (30)$$

The function $r(t)$ is assumed to be known and not random. More generally:

$$\frac{dX}{dt} = f(t, X) + g(t, X) \text{"noise"} \quad (31)$$

where f and g are given functions. The "noise" term is represented as W in the literature and is a white noise process. The solution of Eq. (31) can be solved using either Ito or Stratonovich integrals. The reader is directed to [127] for a detailed explanation of the two methods. In this research, Eq. (31) was solved using the Ito integral method, which has been used in studies of other stochastic engineering applications [128-129]. The Ito stochastic differential form of Eq. (31) is:

$$dX = f(t, X)dt + g(t, X)dW \quad (32)$$

where f is the deterministic *drift coefficient* and g is the continuous random *diffusion coefficient*. The simplest discrete approximation of Eq. (32) is the Euler-Maruyama (EM) approximation [130] and is the one employed in this research:

$$X_n = X_{n-1} + f(X_{n-1})\Delta t_{n-1} + g(X_{n-1})\Delta W_{n-1} \quad (33)$$

The random variables ΔW_{n-1} are independent, normally distributed random variables with mean 0 and variance Δt_n . This scheme has a "strong" order of accuracy of $\gamma=0.5$. The "strong" convergence criterion is merely how good the approximation (X_n) is to the exact solution (Y_n) (see [130] for a formal description of the strong convergence

criterion as well as the weak convergence criterion). For this research, the CO₂ measurements were subject to sensor error. Eq. (26) was rewritten in Ito stochastic differential form as:

$$d\hat{C} = \frac{1}{V} (Q\hat{C} + G)dt + \frac{1}{V} (Q\hat{C})\sigma dW \quad (34)$$

where C was replaced by $C+C\sigma W$, and σ is the sensor error (%) of each sensor. The EM approximation was thus:

$$\hat{C}(t) = \frac{1}{V} (Q\hat{C}(t-1) + G(t-1))\Delta t + \frac{1}{V} (Q\hat{C}(t-1))\sigma\Delta W \quad (35)$$

4.4.3 Additional relationships

In addition to the mass balance equations just presented, additional relationships were established:

- (1) All values of Q (the unknown *building airflow network*) must be non-negative.
- (2) The total airflow rate leaving a zone must equal to the total airflow rate entering a zone. This was applied to all physical zones as well as to the "ventilation" and "outdoors" zones. The "ventilation" zone referred to the air entering the ventilation system via the OA intake and return vents in each physical zone. It also referred to the air leaving the ventilation system via the EA exhaust vent and supply diffusers in each physical zone. The "outdoors" zone referred to air entering the outdoors via the EA exhaust vent and any exfiltration from each physical zone. It also referred to the air leaving the outdoors via the OA intake and any infiltration to each physical zone.

- (3) The supply airflow rates into each zone were known. This information can often be obtained by on-site measuring or from sensors used to control the ventilation system.
- (4) Other known conditions were: total outdoor air supplied to the building through the ventilation system; and total air exhausted from the building by the ventilation system.
- (5) Flow between non-adjacent zones was zero.

4.4.4 Summary of equations

Deterministic, steady-state inverse model: $\mathbf{QC} = -\mathbf{G}$ (23)

Deterministic, transient inverse model: $\hat{\mathbf{C}}(t) = [\mathbf{QC}(t-1) + \mathbf{G}(t-1)] \frac{\Delta t}{V} + \hat{\mathbf{C}}(t-1)$ (26)

Stochastic, transient inverse model:

$$\hat{\mathbf{C}}(t) = \frac{1}{V} (\mathbf{QC}(t-1) + \mathbf{G}(t-1)) \Delta t + \frac{1}{V} (\mathbf{QC}(t-1)) \sigma \Delta W$$
 (35)

Additional relationships:

(1) $\mathbf{Q} \geq \mathbf{0}$ (36)

(2) $\sum_{j \neq i} Q_{ij} = \sum_{j \neq i} Q_{ji}$ (37)

(3) $Q_{\text{supplyzone } i} = Q_{S_i} = \text{known for } i = 1 \dots N$ (38)

(4) $Q_{O_A} = \text{known}, Q_{E_A} = \text{known}$ (39)

(5) If zone i non-adjacent to zone j , then $Q_{ij} = Q_{ji} = 0$ (40)

Thus, the unknown airflow rates in the building airflow network were the interzonal airflow rates, the infiltration (or exfiltration) rates, and the return airflow rates from each physical zone. These were the unknown *parameters* that need to be estimated.

The following section describes the proposed parameter estimation techniques for the proposed building airflow network inverse model.

4.4.5 Solving the mathematical models (parameter estimation)

This section presents the *parameter estimation* techniques used in the building airflow network inverse model to determine the unknown airflow rates. The techniques tested were: linear least squares (Sec. 4.4.5.1), recursive least squares (Sec. 4.4.5.2), and nonlinear parameter optimization (Sec. 4.4.5.3 and 4.4.5.4). Nonlinear parameter optimization for the *deterministic* model is described in Sec. 4.4.5.3 and for the *stochastic* model in Sec. 4.4.5.4.

4.4.5.1 Linear least squares (LSQ model)

Linear least squares (now referred to as the LSQ model) is a popular method for parameter estimation of linear systems. The method minimizes the squared distances between an observed (actual) value and one estimated by the method. For the *deterministic steady-state system*, the Matlab [131] function LSQLIN was used to estimate \mathbf{Q} from Eq. (23) given \mathbf{C} and \mathbf{G} . For the *deterministic transient system*, the function LSQLIN was used to estimate \mathbf{Q} from Eq. (26) given $C_i(t=0)$ for $i = 1 \dots N$ and $\mathbf{G}(t)$.

4.4.5.2 Recursive least squares (RLS model)

Recursive least squares (now referred to as the RLS model) offers an advantage over the LSQ model, especially when data is available in a time-series. Thus, it was applied to the *deterministic transient system*. Its recursive nature eliminates the need for

matrix inversion, which saves computational time. It is arranged such that the least squares estimate from time $t-1$ is used to obtain estimates for time t .

The general form a linear system is:

$$y(i) = \varphi_1(i)\theta_1 + \varphi_2(i)\theta_2 + \dots + \varphi_n(i)\theta_n = \varphi^T \theta \quad (41)$$

where $y(i)$ is the observed variable, θ_i are the parameters of the model to be determined, and φ_i are the known functions. In this research, φ^T was represented by $C_i(t-1)$ for $i=1 \dots N$, and θ was represented by \mathbf{Q} . The recursive equations for solving θ (or \mathbf{Q}) were [132]:

$$\hat{\theta}(t) = \hat{\theta}(t-1) + K(t)(y(t) - \varphi^T(t)\hat{\theta}(t-1)) \quad (42)$$

$$K(t) = P(t-1)\varphi(t)(I + \varphi^T(t)P(t-1)\varphi(t))^{-1} \quad (43)$$

$$P(t) = P(t-1)(I - K(t)\varphi^T(t)) \quad (44)$$

and were coded into Matlab (APPENDIX A). The recursive algorithm was initiated at time $t=0$ with an initial guess of the parameters, $\hat{\theta}(t=0)$, and a sufficiently large value for $P(t=0)$ to avoid computational difficulty [132].

In order to impose any constraints on the RLS model, a method called constrained recursive identification (CRI) was employed [133]. It was developed for the prediction of traffic patterns through an intersection. It utilized an equality-constrained optimization and then Bell's correction [134] to adjust the estimate for the inequality constraints. The method was shown numerically to obtain the same accuracy as the optimal solution based on both equality- and inequality-constrained optimization. The steps in the CRI algorithm were:

- (1) Compute the RLS estimate, $\hat{\theta}(t)$.
- (2) Compute the equality-constrained least squares estimate using:

$\hat{\theta}(t) = \hat{\theta}(t-1) - PR^T W [R\hat{\theta}(t) - b]$ where $R\theta = b$ were the equality constraints.

$$W = [RPR^T]^{-1}$$

$$\bar{\theta}(t) = \hat{\theta}(t)$$

- (3) Compute Bell's correction for the inequality-constraints (non-negativity).

$$H = P - PR^T WRP$$

$$D = \text{diag}\{1/h_{ii}\}$$

$\mu^* = T[-D\bar{\theta}(t)]$ where $T[\cdot]$ truncates the negative elements of $[\cdot]$ to zero.

$$\theta'(t) = \bar{\theta}(t) + H\mu^*$$

- (4) If not all elements of $\theta'(t) \geq 0$, then truncate once more to obtain $\theta''(t)$ and normalize by $R\theta''(t)$.

- (5) $\hat{\theta}(t) = \theta''(t)$ and the algorithm returns to Step 2.

4.4.5.3 Nonlinear parameter optimization (NONLINOPTIM model)

The nonlinear parameter optimization method (now referred to as the NONLINOPTIM model) used to estimate the unknown parameters was a gradient-based method (see Sec. 1.3.2). It was applied to the *deterministic transient system*. The Matlab function FMINCON, which is a constrained optimization function, was used. The NONLINOPTIM model found the values of the unknown parameters that minimized the difference between $\sum_{t=1}^{t=T} |\hat{C}(t) - C(t)|^2$, where $\hat{C}(t)$ was calculated according to Eq. (26) and T was the time period for which CO₂ measurements were available. The reader is referred to [131] for details on FMINCON and APPENDIX A for the Matlab code.

4.4.5.4 Nonlinear parameter optimization with stochastic term (SDE model)

The only difference between the nonlinear parameter optimization model with stochastic term (now referred to as the SDE model) and the NONLINOPTIM model from the previous section was the inclusion of the random term, $\Delta\mathbf{W}$, in Eq. (35). As discussed in Sec. 4.4.2, the random term $\Delta\mathbf{W}$ was modeled as independent, normally distributed random variables with mean 0 and variance Δt_n . In Matlab, this was modeled using the following functions: $\text{SQRT}(\Delta t_n) \times \text{RANDN}$, where $\text{SQRT}(\Delta t_n)$ is the square root of the time step and RANDN randomly selects a number from the normal distribution.

4.4.6 Solution condition

A mathematical model (Eq. (23), (26), or (35)) was combined with the additional relationships (Eqs. (37) to (40)) in order to determine the *rank* of the *known-information matrix*. The rank of the *known-information matrix* must be equal to or greater than the number of unknown airflow rates in \mathbf{Q} in order to solve for \mathbf{Q} using the proposed mathematical models.

In general, the number of interzonal airflows in a building with N physical zones was $N(N-1)$. Two other "zones" exchanged air with the physical zones: the outdoors and the ventilation system, which added $4N$ more unknown airflow rates (two paths for air exchange between each physical zone and the outdoors plus two paths for air exchange between each physical zone and the ventilation system). The ventilation system also exchanged air with the outdoors, which added 2 more unknown airflow rates. The additional relationships listed in Sec. 4.4.3 served to reduce the number of unknown airflow rates in \mathbf{Q} . Thus, the rank of the known-information matrix must be $\geq [N(N-1)+4N+2$ -any additional relationships].

As an example, take a 3-zone building where $N=3$. The number of unknown airflow rates in \mathbf{Q} would be initially calculated as $N(N-1)+4N+2=3(3-1)+4(3)+2 = 20$. Using the additional relationships in Sec. 4.4.3, $N=3$ can be subtracted from this number $N=3$ supply airflow rates into each physical zone are known. The total outdoor air supplied to the building through the ventilation system and total air exhausted from the building by the ventilation system are also known, which reduces the number of unknown airflow rates by another 2. This gives $20-3-2=15$ unknowns. Thus, the rank of known-information matrix must be ≥ 15 in the case of a 3-zone building.

4.4.7 Uncertainty in building airflow network inverse model

Uncertainty analysis for the *deterministic* inverse models can be performed using one-way or two-way sensitivity analyses, first-order uncertainty analysis, or Monte Carlo analysis. The sensitivity analyses required that the upper and lower bound on the inputs were known. In this research, that would mean knowing the upper and lower bounds on CO₂ measurements. These bounds *could not* be generalized to *all* buildings under *all* conditions. A first-order uncertainty analysis required using the variance of each input (i.e., CO₂ measurements), which *could not* be generalized to *all* CO₂ sensors. Each sensor would have exhibited individual characteristics, such as in accuracy, precision, false detection rate, etc. Thus, a Monte Carlo analysis was selected. The parameter estimation was repeated a sufficiently large number of times (X), each time applying a random error to each input from a known variance, or in this research, a known sensor error. Random error was applied to the CO₂ concentration using the sensor models to be described in Sec. 4.5.1. Monte Carlo analysis resulted in X discrete values for each of the unknown parameters. Together, they approximated the true distribution of the unknown parameters.

In essence, each parameter was described by a mean value and a standard deviation. The uncertainty in the *stochastic* inverse model was performed by repeating the parameter estimation X number of times, each time randomly selecting a different value for the random term, ΔW . Only one set of CO₂ measurements was needed.

In this research, X was selected as 1,000, which is commonly selected for Monte Carlo analyses. Parameter estimation was also performed with $X=1$ for comparison.

4.5 Study methods

Figure 4-3 summarizes the study process. In lieu of experimental data, the first step was to develop a synthetic test building using CONTAM (Step 1). The developed CONTAM model determined the pressure distribution, the airflow rate through each leakage path and the ventilation system (Step 2), and CO₂ concentration (Step 3). Simulated CO₂ concentrations from the synthetic test building were then fed into a sensor model (Step 3a, Sec. 4.5.1). Two types of sensor models were used, namely, a perfect sensor model, where synthetic CO₂ concentrations were directly used to simulate *synthetic perfect measurements*; and a "real-world" sensor model, where *synthetic imperfect measurements* were generated by adding random bias and/or precision sensor errors to the simulated CO₂ concentrations. The building airflow network inverse model was then developed using the mathematical models described in Sec. 4.4.5 and the synthetic CO₂ measurements (perfect and imperfect) (Step 4).

The developed building airflow network inverse model from Step 4 was used to estimate a building airflow pattern. This was then compared to the one that was simulated by the CONTAM model (Step 5). Keep in mind that CONTAM utilized nonlinear relationships between pressure and airflow to calculate airflow rates, whereas in this

research, linear relationships between contaminant concentration and airflows were utilized to develop a simplified inverse model. The developed building airflow network inverse model was *also* used to predict CO₂ concentrations based on known occupancy schedule information (Step 6). The predicted CO₂ concentrations were then compared to the synthetic CO₂ measurements (perfect or imperfect) (Step 7). When comparing CO₂ concentrations (Step 7), two simulated CO₂ concentration datasets were used. One dataset was the one used to develop the inverse model, and was labeled as "training data". The other dataset was also simulated by the CONTAM model but was *not* used to develop the inverse model. It was labeled as "testing data". Thus, the accuracy of the developed building airflow network inverse model was evaluated based on differences with the airflow rates *and* CO₂ concentrations simulated by the CONTAM model.

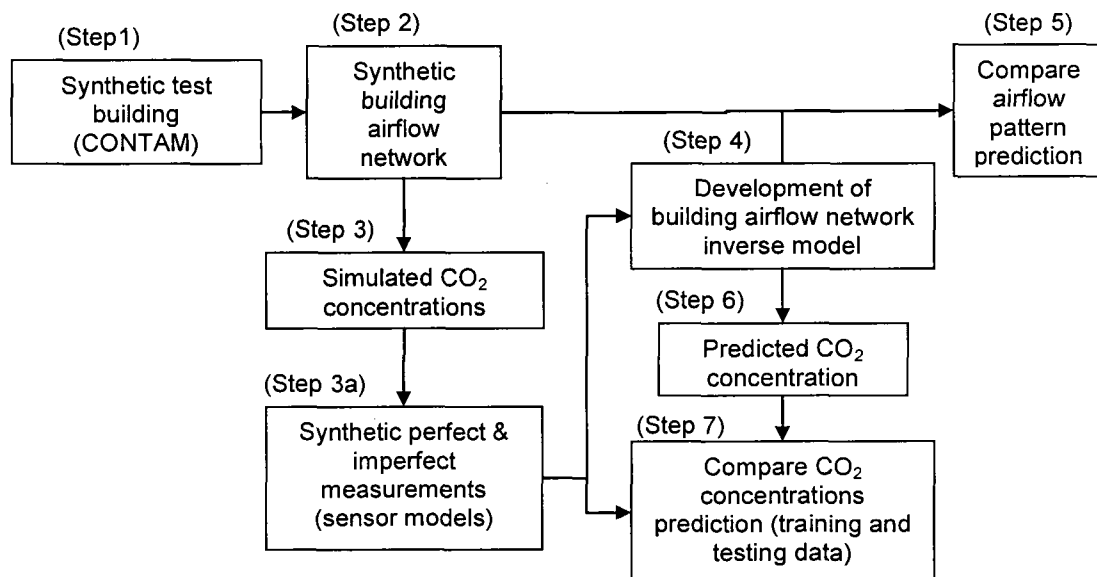


Figure 4-3. Flow diagram of study process.

4.5.1 Sensor models

As mentioned above, two types of sensor models were used: a *perfect sensor model*, where synthetic CO₂ concentrations from CONTAM were directly used to represent *synthetic perfect measurements*; and a *"real-world" sensor model*, where *synthetic imperfect measurements* were generated. In the real-world sensor model, simulated CO₂ concentrations from CONTAM were perturbed by (1) precision error and (2) precision error and a bias. The total error was thus $\sqrt{\text{precision error}^2 + \text{bias}^2}$ % of the simulated concentration. The precision error was randomly selected for every time step that CO₂ concentrations were simulated. When using steady-state CO₂ data, the precision error was randomly selected once. The bias, on the other hand, was randomly selected for every sensor which "measured" concentration for each simulated zone, i.e., for each physical zone, the ventilation zone, and outdoors zone (see Sec. 4.4.3). The bias then remained constant for that particular sensor for every time step. The synthetic imperfect measurements were filtered in order to reduce noise. Filtering was performed by taking a 30-min moving average. An example of the different types of synthetic measurements used to test the building inverse models in this research is shown Figure 4-4.

4.5.2 Reporting uncertainty

To express the uncertainty in the building airflow network estimated by the building airflow network inverse model, a minimum and maximum value for each of the *unknown* airflow rates was reported. This was also referred to as the *range* of the estimated airflow rate. The minimum and maximum values were calculated using the

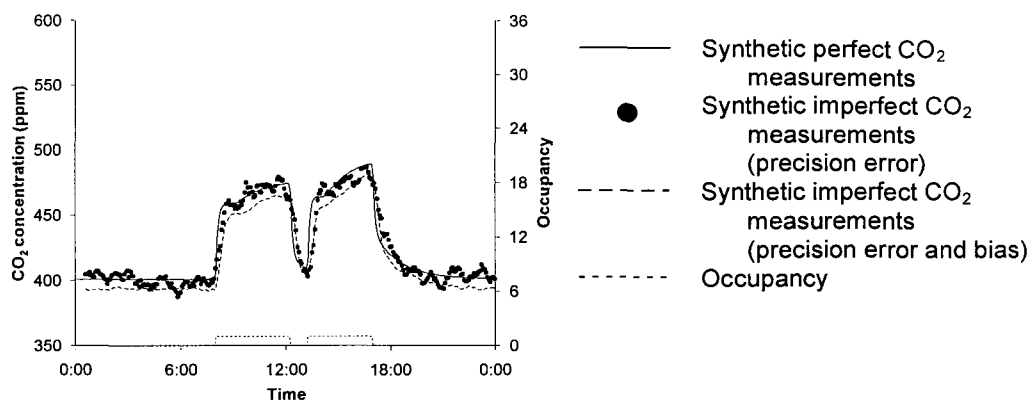


Figure 4-4. Example of synthetic perfect and imperfect CO₂ measurements.

estimated mean value \pm the standard deviation of the estimate. These were obtained when *either* multiples sets of synthetic imperfect CO₂ measurements were used (in the case of the deterministic inverse models) or the stochastic inverse model was used (Sec. 4.4.7).

If the synthetic airflow rate from CONTAM fell within the range of the estimated airflow rate, then the difference between the two was reported as zero. On the other hand, if the synthetic airflow rate from CONTAM *did not* fall within the range of the estimated airflow rate, two quantities were reported: *mean percentage error in Q* and *mean absolute error in Q*. Using these reporting scheme, the average of the *best* estimate from the building airflow network inverse model was used to determine its estimation accuracy. The *percentage error in Q* was:

$$|\text{Synthetic airflow rate} - \text{Min or Max airflow rate}| / \text{Synthetic airflow rate} \times 100 \quad (45)$$

where $|\cdot|$ was the absolute value, and "Min or Max" were the lower or upper values in the range of the estimated airflow rate. The *mean percentage error in Q* was then the average of these errors for all unknown airflow rates.

For example, if the synthetic airflow rate for Q_1 was 5 cfm, and the range of the estimated airflow rate was 0-10 cfm, then the difference between the two would be 0% since the estimated range included the synthetic value. On the other hand, if the synthetic airflow rate for Q_2 was 10 cfm, and the estimated range was 0-5 cfm, then the difference between the two would be $|10 \text{ cfm} - 0 \text{ cfm}|/10 \text{ cfm} \times 100 = 100\%$ and $|10 \text{ cfm} - 5 \text{ cfm}|/10 \text{ cfm} \times 100 = 50\%$. If Q_1 and Q_2 were the only two unknown airflow rates, then the *mean percentage error in Q* would be $mean(0\%, 50-100\%)=25-50\%$ for this example building airflow network.

It should be noted that if a synthetic airflow rate were zero, then the percentage difference between that synthetic airflow rate and an estimated value was reported as 100%, no matter the magnitude of the difference. This avoided division by zero in Eq. (45).

The *mean absolute error in Q* was calculated as the average of the *absolute error in Q* for all unknown airflow rates. The *absolute error in Q* was:

$$|\text{Synthetic airflow rate} - \text{Min or Max airflow rate}| \quad (46)$$

Thus, for the example building airflow network, the *absolute error in Q* would be 0 cfm for Q_1 and 5-10 cfm for Q_2 . The *mean absolute error in Q* would be $mean(0 \text{ cfm}, 5-10 \text{ cfm})=2.5-5 \text{ cfm}$.

4.5.3 Reporting building airflow network inverse model performance

To express the performance of the building airflow network inverse model, the estimated building airflow network was used to predict CO₂ concentrations. As discussed in the beginning Sec. 4.5, two predictions were made. The first prediction was made using the occupancy schedule used by CONTAM model to simulate the *training* data.

The training data was used to develop the inverse model. The second prediction was made using a different occupancy schedule used by CONTAM model to simulate the *testing* data. The testing data were *not used* to develop the inverse model. Both the training and testing data were fed into the sensor models before being respectively used to develop the building airflow network inverse model and test the ability of the building airflow network inverse model to predict CO₂ concentrations that were not part of the training data.

The accuracy of the CO₂ concentration predictions was reported using the *RSME in C* for each physical zone (the "^" above *C* was dropped for clarity). It was expressed in ppm and calculated using the testing and training data. The *RSME in C* was the root-mean-squared-error (RSME). RSME is the square root of the mean-squared-error (MSE), defined as:

$$MSE(\hat{C}_i) = E\left[(\hat{C}_i - C_i)^2\right] \quad (47)$$

where \hat{C}_i is the predicted concentration, C_i is the synthetic (perfect or imperfect) measurement, and $E[\cdot]$ is the expected value (i.e., mean). The average of the *RSME in C* for all physical zones was also reported. Mean and standard deviation values for the *RSME in C* were also reported when the building airflow network was estimated using imperfect measurements and/or the stochastic inverse model.

The accuracy of the CO₂ concentration predictions was reported by an additional *R² value* for each physical zone when the *transient inverse model* was tested. The *R² value* was the fit between the predicted concentration and synthetic measurements. The

closer the value was to 1.0, the better the fit. It was unitless and calculated using the testing and training data. It was defined as the square of the correlation coefficient:

$$R^2 = \left[\frac{E[(\hat{C}_i - \mu_{\hat{C}_i})(C_i - \mu_{C_i})]}{\sigma_{\hat{C}_i} \sigma_{C_i}} \right]^2 \quad (48)$$

where $\mu_{\hat{C}_i}$ is the average of the predicted concentrations, μ_{C_i} is the average of the synthetic (perfect or imperfect) measurements, $\sigma_{\hat{C}_i}$ is the standard deviation of the predicted concentrations, and σ_{C_i} is the standard deviation of the synthetic (perfect or imperfect) measurements. The average of the R^2 values for all physical zones was also reported. Mean and standard deviation values for the R^2 value were also reported when the estimated building airflow network was estimated using imperfect measurements and/or the stochastic inverse model.

4.6 Test cases

The performance of the proposed building airflow network inverse model was tested using two test cases – one for the *steady-state* system and the other for the *transient* system. Both test cases compared the performance of the proposed building airflow network inverse model using synthetic perfect and imperfect CO₂ measurements.

The developed building airflow network inverse model offered several advantages over the traditional blower-door and tracer gas tests discussed in Sec. 4.1. First, the inverse model was implemented on a multi-zone building, for which the use of traditional blower-door and tracer gas tests to determine air exchange rates is challenging. Second, the inverse model was able to determine airflow rates across the building envelope in each zone and also *between* zones. Third, the use of CO₂ was advantageous as it would be

a naturally present tracer. CO₂ sensors would be readily available and relatively inexpensive compared to the equipment needed to measure a traditional tracer gas such as SF₆. And lastly, the inverse model provided a fast estimate of the building airflow network. It required less time to set-up than a traditional blower-door or tracer gas test and has the potential to determine a building airflow network in real-time.

4.6.1 Test case 1 – steady-state system

4.6.1.1 Building airflow network inverse model (steady-state)

A deterministic inverse model was used for the steady-state system. From Sec. 4.4.1, the mathematical model for the building airflow network was:

$$\mathbf{QC} = -\mathbf{G} \quad (23)$$

From Sec. 4.4.5.1, the LSQ model was selected to solve \mathbf{Q} , given this steady-state system.

4.6.1.2 Synthetic test building

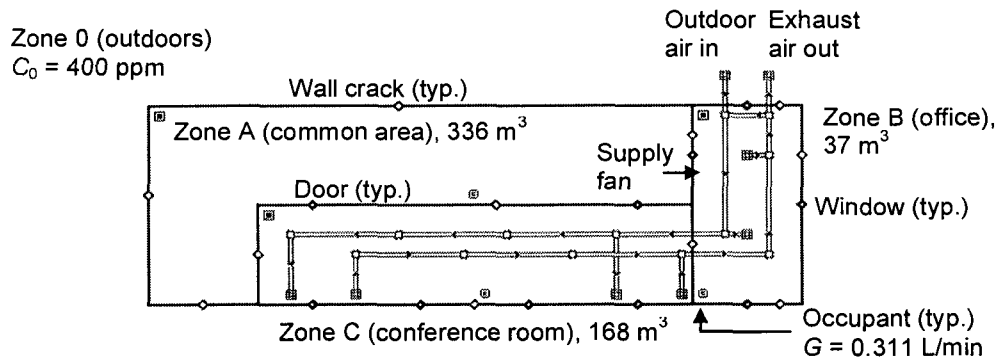
A three-zone synthetic test building was modeled in CONTAM [5]. Figure 4-5 shows the location of Zones A (common area), B (office), and C (conference room), along with their respective volumes. The exterior wall was modeled as brick veneer with a leakage property of 1.14 cm²/m². The interior walls were modeled with leakage of 1.12 cm²/m². The inoperable closed windows were modeled with leakage of 0.86 cm²/m of sash. The interior open doors were modeled as 2.1 m² openings. One-way flow through each of these leakage paths was governed by a power-law equation of the form $F = K(\Delta P)^n$, where F is the airflow rate (kg/s), ΔP is the pressure difference calculated by CONTAM (Pa), and K and n are empirical constants. For this synthetic test building, $K=1$

and $n=0.65$ for all of the leakage paths. All leakage properties were selected from data collected for commercial or other high-rise buildings [135].

A recirculation ventilation system was modeled with 20% outdoor air. The location of the outdoor air intake and total exhaust are shown in Figure 4-5. The supply fan delivered $4 \text{ m}^3/\text{h}$ (145 cfm) to Zone B and $20 \text{ m}^3/\text{h}$ (690 cfm) to Zone C, which were approximately 7 air changes per hour (ACH). Because Zone A was not mechanically ventilated and had a relatively large volume, the whole building air exchange rate was about 1 ACH. The figure shows the location of ductwork, diffusers, and exhausts. CO_2 was present in the outdoors (Zone 0) with a constant concentration of 400 ppm [136]. CO_2 was generated by occupants in each zone at a rate of $G = 0.311 \text{ L}/\text{min}$ [137].

The maximum number of unknown airflow rates in this synthetic 3-zone test building was calculated to be 20 (see Sec. 4.4.6 for detailed calculation). The known airflow rates included the supply airflow rates to each zone (Q_{SA} , Q_{SB} , Q_{SC}), the total outdoor air supplied to the building through the ventilation system (Q_{OA}); and total air exhausted from the building by the ventilation system (Q_{EA}). Because Zone A was not mechanically ventilated, an additional known airflow rate was $Q_{RA}=0$. Thus, the number of unknown airflow rates in this synthetic 3-zone test building was $20-6=14$.

Figure 4-6 graphically shows the location of these unknown airflow rates in the synthetic 3-zone test building. There were two exhausts modeled in Zone C (Q_{RC1} and Q_{RC2}) as shown, but only the *total* exhaust rate, Q_{RC} , was estimated. The airflow rate estimated between two zones, including the outdoors, was the *total* airflow rate through all of the leakage paths between them. For example, there were two open doors and one



Notes: "typ." means typical. For leakage paths, such as wall crack, "typ." indicates that all wall cracks in the figure are represented by a similar icon ($\text{$). Also, all occupants are represented by $\text{$.

Figure 4-5. CONTAM model of synthetic 3-zone test building.

interior wall leakage paths modeled between Zones A and C. However, the airflow rate that was estimated between them was represented by Q_{AC} and Q_{CA} for the inverse model developed in this research. A non-negativity relationship was established (see Sec. 4.4.3) so that, in the example above, both Q_{AC} and Q_{CA} must be non-negative.

In the example above, each of the two open doors and one interior wall leakage paths between Zones A and C was modeled as a separate one-way flow element. CONTAM then calculated the direction and magnitude of the flow across each leakage path. The *net* flow, either from Zone A to Zone C ($Q_{AC} \geq 0$) or from Zone C to Zone A ($Q_{CA} \geq 0$), was calculated and used in defining the synthetic building airflow network. CONTAM also had the ability to model leakage paths with two-way flow, which is used when modeling open doors or windows. Two-way flow is driven by a temperature (or more precisely, air density) difference across the opening [5]. Since in this research, all zones were maintained at the same temperature, there was no need to model two-way flow in CONTAM.

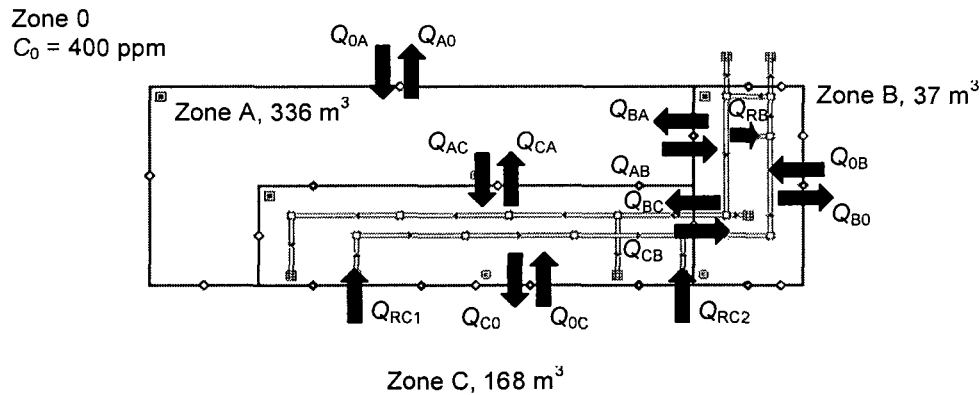


Figure 4-6. Building airflow network to be estimated for synthetic 3-zone test building.

4.6.1.3 Synthetic perfect and imperfect steady-state measurements

The rank of the known-information matrix was calculated for up to 9 sets of CO_2 concentrations simulated by the CONTAM model for training. The datasets were simulated based on the occupancy information in Table 4-1. It was assumed that each occupant generated CO_2 at a rate of 0.311 L/min . The resulting steady-state CO_2 concentrations simulated by CONTAM are given in Table 4-2. Since the number of unknown airflow rates in this synthetic 3-zone test building was 14, Table 4-3 shows that 6 sets of CO_2 concentrations were needed in order for the building airflow network inverse model to estimate the unknown airflow rates. Future work includes examining the effect of using more datasets (rank much greater than the number of unknown airflow rates) on the performance of the building airflow network inverse model.

Table 4-1. Number of occupants modeled in CONTAM for 3-zone synthetic test building (training data).

	Dataset 1	Dataset 2	Dataset 3	Dataset 4	Dataset 5	Dataset 6	Dataset 7	Dataset 8	Dataset 9
Zone A	1	1	1	1	1	1	1	1	1
Zone B	1	1	1	1	1	1	2	3	4
Zone C	5	4	3	2	1	0	1	2	3
Total	7	6	5	4	3	2	4	6	8

Table 4-2. Steady-state CO₂ concentrations (ppm) simulated by CONTAM for 3-zone synthetic test building (training data).

	Dataset 1	Dataset 2	Dataset 3	Dataset 4	Dataset 5	Dataset 6	Dataset 7	Dataset 8	Dataset 9
Zone A	786	741	695	650	604	558	627	696	765
Zone B	720	687	653	620	588	554	669	784	900
Zone C	698	653	607	562	516	471	539	608	677
Supply	611	583	555	527	499	471	522	573	625

Table 4-3. Rank of CO₂ training data datasets (steady-state).

Number of datasets	Rank
1	7
2	10
3	13
4	13
5	13
6	16
7	16
8	16
9	16

As discussed in Sec. 4.5.1, the simulated CO₂ concentrations were directly used as *synthetic perfect measurements*. The simulated CO₂ concentrations were perturbed to generate *synthetic imperfect measurements*. Two types of synthetic imperfect measurements were generated: one with precision error ($\pm 5.0\%$ of the synthetic perfect measurement) and the other with precision error ($\pm 2.5\%$ of the synthetic perfect measurement) and bias ($\pm 2.5\%$ of the synthetic perfect measurement). To determine the uncertainty of the building airflow network inverse model, 1,000 randomly generated sets

of synthetic imperfect CO₂ measurements were used to determine a mean value and standard deviation of the unknown airflow rates. For comparison, just *one* randomly generated set of synthetic imperfect CO₂ measurements was also used to estimate the unknown airflow rates.

One set of testing data was generated in CONTAM (Table 4-4). This was also fed into the sensor models to generate synthetic perfect and imperfect measurements. The testing data was used to assess the ability of the estimated building airflow network (the one estimated using the *training* data) to predict contaminant concentrations that were not included in the training data.

4.6.1.4 Results – synthetic perfect steady-state measurements

Table 4-5 shows that a majority of the estimated airflow rates were in good agreement with the synthetic airflow rates when using synthetic perfect steady-state CO₂ measurements. The estimated building airflow network met all of the required constraints. For example, they (a) satisfied air mass balance in each zone (last six rows of Table 4-5) and (b) were all non-negative.

The *mean error in Q* was 25% and 30 m³/h (18 cfm). This error was <0.5 ACH in any zone, where ACH (air change rate per hour) was defined as the airflow rate divided by the volume of a zone. The supply airflow rates to Zones B and C were 7 ACH; thus, a 0.5 ACH error could be considered insignificant. A *mean error in Q* of 30 m³/h (18 cfm) also translated to 3% of the maximum value in *Q*. No tracer studies in the literature, whether synthetic or experimental, utilized *steady-state* CO₂ measurements to estimate airflow rates.

Table 4-4. Testing data for 3-zone synthetic test building.

	Occupancy	CO ₂ concentrations from CONTAM (ppm)
Zone A	2	747
Zone B	1	655
Zone C	2	571
Supply	N/A	537

Table 4-5. Estimated building airflow network using synthetic perfect CO₂ measurements (steady-state, LSQ model).

	Synthetic airflow rate, m ³ /h (cfm)	Estimated airflow rate, m ³ /h (cfm)	Percentage error in Q
Q _{0A}	0	0	0%
Q _{A0}	135 (79)	134 (78)	1%
Q _{0B}	0	0	0%
Q _{B0}	129 (75)	234 (137)	82%
Q _{0C}	0	0	0%
Q _{C0}	104 (61)	0	100%
Q _{AB}	97 (57)	99 (58)	2%
Q _{BA}	0	0	0%
Q _{AC}	0	0	0%
Q _{CA}	233 (136)	233 (136)	0%
Q _{BC}	0	0	0%
Q _{CB}	0	1 (1)	100%
Q _{RB}	218 (128)	115 (67)	47%
Q _{RC}	841 (493)	943 (553)	12%
ΣQ _{jA}	233 (136)	233 (136)	0%
ΣQ _{Aj}	233 (136)	233 (136)	0%
ΣQ _{jB}	346 (203)	349 (205)	1%
ΣQ _{Bj}	346 (203)	349 (205)	1%
ΣQ _{jC}	1177 (690)	1177 (690)	0%
ΣQ _{Cj}	1177 (690)	1177 (690)	0%

4.6.1.5 Results – synthetic imperfect steady-state measurements

Minimum and maximum values of each of the estimated airflow rates are listed in Table 4-6 and Table 4-7. Whether using measurements with only precision error or with precision error and bias, a majority of the synthetic airflow rates fell within the range of the estimated airflow rates. In both cases, the estimated airflow rates satisfied the constraints for mass balance and non-negativity.

The *mean error in Q* was 21-27% and 39-49 m³/h (23-29 cfm) (3-4% max *Q*) when using synthetic imperfect measurements with only precision error. The *mean error in Q* was 22-25% and 32-36 m³/h (19-21 cfm) (3% max *Q*) when using synthetic imperfect measurements with precision error and bias. As was the case when using synthetic perfect measurements, these errors were <0.5 ACH in any zone.

4.6.1.6 Performance of building airflow network inverse model

Using the estimated building airflow network inverse model developed with synthetic *perfect* measurements, the *RSME in C* was calculated as <1 ppm (for both the training and testing data) (Table 4-8). This was <1% of the maximum concentration in any zone. Using the estimated building airflow network inverse model developed with synthetic *imperfect* measurements, the *RSME in C* was again calculated as <1 ppm (<1% of the maximum concentration in any zone) for each zone (for both the training and testing data) (Table 4-8).

Table 4-8 shows that, as expected, the best estimate, both in terms of estimated airflow rates and contaminant prediction, was made using synthetic perfect CO₂ measurements. The next best estimate was made using synthetic measurements with precision error and bias. And the worst estimate was made using synthetic measurements with only precision error. The *RSME in C* and its uncertainty (i.e., standard deviation) were lower when using synthetic measurements with precision error and bias than when using synthetic measurements with precision error only to develop the inverse model. This was due to the values of the sensor errors selected (Sec. 4.6.1.3). **Thus, it could be**

Table 4-6. Estimated building airflow network using 1,000 sets of synthetic imperfect CO₂ measurements with precision error (steady-state, LSQ model).

	Synthetic airflow rate, m ³ /h (cfm)	Estimated airflow rate, m ³ /h (cfm)		Synthetic value within estimated range? (If N, percentage difference)
		Min	Max	
Q _{0A}	0	8 (4)	40 (23)	N (100%)
Q _{A0}	135 (79)	27 (16)	167 (98)	Y
Q _{0B}	0	0	3 (1)	Y
Q _{B0}	129 (75)	158 (93)	338 (198)	N (23-163%)
Q _{0C}	0	0	95 (56)	Y
Q _{C0}	104 (61)	0	205 (120)	Y
Q _{AB}	97 (57)	0	106 (62)	Y
Q _{BA}	0	0	46 (27)	Y
Q _{AC}	0	0	115 (67)	Y
Q _{CA}	233 (136)	114 (67)	201 (118)	N (14-51%)
Q _{BC}	0	0	118 (69)	Y
Q _{CB}	0	0	19 (11)	Y
Q _{RB}	218 (128)	0	44 (26)	N (80-100%)
Q _{RC}	841 (493)	1014 (594)	1077 (631)	N (21-28%)
ΣQ _{iA}	233 (136)	122 (71)	287 (168)	Y
ΣQ _{Aj}	233 (136)	27 (16)	388 (227)	Y
ΣQ _{jB}	346 (203)	249 (146)	377 (221)	Y
ΣQ _{Bj}	346 (203)	158 (93)	546 (320)	Y
ΣQ _{jC}	1177 (690)	1177 (690)	1505 (882)	Y
ΣQ _{ci}	1177 (690)	1128 (661)	1502 (880)	Y

Table 4-7. Estimated building airflow network using 1,000 sets of synthetic imperfect CO₂ measurements with precision error and bias (steady-state, LSQ model).

	Synthetic airflow rate, m ³ /h (cfm)	Estimated airflow rate, m ³ /h (cfm)		Synthetic value within estimated range? (If N, percentage difference)
		Min	Max	
Q _{0A}	0	0	4 (2)	Y
Q _{A0}	135 (79)	102 (60)	142 (83)	Y
Q _{0B}	0	0	3 (1)	Y
Q _{B0}	129 (75)	175 (103)	333 (195)	N (36-159%)
Q _{0C}	0	18 (11)	42 (25)	N (100%)
Q _{C0}	104 (61)	0	102 (60)	N (2-100%)
Q _{AB}	97 (57)	74 (43)	111 (65)	Y
Q _{BA}	0	0	1 (1)	Y
Q _{AC}	0	0	10 (6)	Y
Q _{CA}	233 (136)	208 (122)	222 (130)	N (4-11%)
Q _{BC}	0	0	9 (5)	Y
Q _{CB}	0	0	15 (9)	Y
Q _{RB}	218 (128)	10 (6)	175 (103)	N (20-95%)
Q _{RC}	841 (493)	883 (518)	1048 (614)	N (5-25%)
ΣQ _{iA}	233 (136)	208 (122)	227 (133)	N (2-11%)
ΣQ _{Aj}	233 (136)	176 (103)	263 (154)	Y
ΣQ _{jB}	346 (203)	323 (189)	377 (221)	Y
ΣQ _{Bj}	346 (203)	185 (108)	518 (304)	Y
ΣQ _{jC}	1177 (690)	1196 (701)	1239 (726)	N (2-5%)
ΣQ _{ci}	1177 (690)	1091 (639)	1388 (813)	Y

concluded that there was a direct relationship between the performance of the deterministic building airflow network inverse model and the sensor error when synthetic steady-state measurements were used.

It should be noted that the uncertainty in the *RSME in C* was almost equal to the mean value, i.e., the uncertainty was quite large, for both the training and testing data. Nevertheless, both the mean and uncertainty was <1 ppm. As expected, the *RSME in C* was slightly higher for the testing data than it was for the training data since the training data was used to develop the building airflow network inverse model.

The difference between the performances of the building airflow network inverse models developed using synthetic perfect and imperfect CO₂ measurements was 3-4% in terms of *mean error in Q*, which was 2-19 m³/h (1-11 cfm). The differences in terms of *RSME in C* was 1.2E-05 to 1.5E-03 ppm. **Thus, it could be concluded that the use of synthetic imperfect measurements did not greatly affect the performance of the building airflow network inverse model developed for the steady-state system.**

Even if only one set of synthetic imperfect measurements were used to develop the building airflow network inverse, the *mean error in Q* was still <0.5 ACH in any zone, and the *RSME in C* <1 ppm (Table 4-8). **Thus, the proposed building airflow network inverse model shows potential to be used in real-life with only one set of actual measurements.** Nevertheless, the proposed building airflow network inverse model could be implemented offline, where 1,000 sets of *synthetic* imperfect measurements could be randomly generated from one set of *actual* measurements in order to determine the uncertainty in the estimated building airflow network. The computational time for this would be minimal.

Table 4-8. Summary of uncertainty and performance of building airflow network inverse model (steady-state, LSQ).

	Using synthetic perfect meas.	Using 1,000 sets of synthetic measurements		Using 1 set of synthetic measurements	
		With precision error	With precision error and bias	With precision error	With precision error and bias
Mean error in Q					
Percentage	25%	21-27%	22-25%	38%	29%
m ³ /h	30	39-49	32-36	70	45
cfm	18	23-29	19-21	41	26
RSME in C (ppm), training					
Zone A	7.6e-08	1.1e-3±7.6e-04	3.8e-5±1.9e-05	9.0e-04	4.0e-05
Zone B	4.1e-08	9.0e-4±5.2e-04	1.7e-5±1.0e-05	8.0e-04	1.4e-05
Zone C	0	6.0e-4±3.9e-04	1.4e-5±7.9e-06	1.8e-03	2.7e-06
Mean	3.9e-08	8.7e-4±5.6e-04	2.3e-5±1.3e-05	1.2e-03	1.9e-05
RSME in C (ppm), testing					
Zone A	6.0e-08	2.2e-3±2.4E-03	1.6e-4±1.5e-04	5.2e-06	6.0e-05
Zone B	9.4e-08	1.0e-3±1.3E-03	2.3e-5±2.8e-05	6.9e-05	2.6e-06
Zone C	0	8.0e-3±9.0E-04	1.6e-5±1.9e-05	2.8e-04	8.9e-06
Mean	5.1e-08	1.3e-3±1.5E-03	6.7e-5±6.7e-05	1.2e-04	2.4e-05

Note: Both 1,000 and 1 sets of synthetic CO₂ measurements were used to develop the building airflow network inverse model. The "1 set" of synthetic measurements was generated by feeding the simulated CO₂ concentrations from CONTAM into sensor models (Sec. 4.5.1). The "1,000 sets" of synthetic measurements were generated by applying the sensor model 1,000 times in order to determine the uncertainty in the estimated building airflow network (Sec. 4.4.7). The table demonstrates that the proposed building airflow network inverse model has the potential to be used in real-life with only one set of actual measurements.

The performance of the building airflow network inverse model can also be evaluated in terms of estimated infiltration rates through the building envelope in each zone. Table 4-9 indicates the *mean* difference in infiltration rates was about the same whether using synthetic perfect or imperfect CO₂ measurements. How these differences may affect predicted IAQ or energy use is saved for future work.

The leakiest zone simulated by CONTAM was Zone B (-0.94 ACH), which was also estimated by the building airflow network inverse model (-1.15 to -2.47 ACH). The negative sign indicated exfiltration rather than infiltration. One could reasonably use the

Table 4-9. Summary of error in infiltration rates.

Zone	Using synthetic perfect meas., % (cfm)	Using 1,000 sets of synthetic measurements	
		With precision error, % (cfm)	With precision error and bias, % (cfm)
A	1% (1)	100% (4-23)	0%
B	82% (62)	23-163% (17-123)	36-159% (27-120)
C	100% (61)	0%	1-100% (1-61)
<i>Mean</i>	31% (21)	20-44% (4-24)	39-44% (16-24)

results of the building airflow network inverse model to improve the airtightness at specific locations in a building to reduce the amount of energy wasted through exfiltration.

Lastly, the performance of the building airflow network inverse model can also be evaluated in terms of a qualitative assessment of pressure distribution in the synthetic test building. The CONTAM simulated $P_A \approx P_B < P_C$. This pressure distribution that would also result from the building airflow network estimated using synthetic CO₂ measurements with precision error and bias, but not from the one using synthetic CO₂ measurements with only precision error.

4.6.1.7 Conclusions for test case 1 – steady-state system

- (1) The proposed building airflow network inverse model performed similarly whether using synthetic perfect or imperfect CO₂ measurements. The *mean error in Q* was <1 ACH, the *RSME in C* was <1 ppm, and the error in estimated infiltration rates was similar;
- (2) The proposed building airflow network inverse model has the potential to make good predictions for other gaseous contaminants;

- (3) In terms of a qualitative assessment of pressure distribution, the proposed building inverse airflow model performed similarly whether using synthetic perfect or imperfect steady-state CO₂ measurements with precision error and bias.

4.6.2 Test case 2 – transient system

In reality, steady-state CO₂ measurements may be difficult to obtain. Therefore, test case 2 utilized perfect and imperfect *transient* CO₂ measurements to develop a building airflow network inverse model.

4.6.2.1 Building airflow network inverse models (transient)

Both the deterministic and stochastic inverse models were used for the transient system. From Sec. 4.4.1, the deterministic mathematical model for the building airflow network was:

$$\hat{C}(t) = \left[\mathbf{Q}\hat{C}(t-1) + \mathbf{G}(t-1) \right] \frac{\Delta t}{V} + \hat{C}(t-1) \quad (26)$$

The stochastic mathematical model for the building airflow network was:

$$\hat{C}(t) = \frac{1}{V} \left(\mathbf{Q}\hat{C}(t-1) + \mathbf{G}(t-1) \right) \Delta t + \frac{1}{V} \left(\mathbf{Q}\hat{C}(t-1) \right) \sigma \Delta W \quad (35)$$

From Sec. 4.4.5, the LSQ, RLS, and NONLINOPTIM models were proposed to solve for \mathbf{Q} in the *transient system* in Eq. (26). The SDE model was proposed to solve for \mathbf{Q} in the *transient system* in Eq. (35).

The RLS model used the difference between $y(t)$ (actual/synthetic) and $\varphi^T(t)\hat{\theta}(t-1)$ (calculated) to update the parameters at the current time step, as seen in the equation below (repeated from Sec. 4.4.5.2).

$$\hat{\theta}(t) = \hat{\theta}(t-1) + K(t) \left(y(t) - \varphi^T(t)\hat{\theta}(t-1) \right) \quad (42)$$

The initial value of all parameters was set to 0.01, except for the known airflow rates (Sec. 4.4.3) which were given their synthetic values from CONTAM as initial values. The initial value of P was $1e+05$. The RLS model quickly converged to a solution that was no better than the LSQ or NONLINOPTIM models. In fact, even though non-negativity and mass balance constraints were satisfied, the constraints on the known airflow rates were *not* satisfied. Figure 4-7 shows that the final parameter values for Q_{SC} and Q_{SB} were less than their actual values. Q_{RA} should be zero since Zone A was not mechanically ventilated, but the RLS model estimated it to be a non-zero value. The correct values for the known airflow rates *were* all estimated using the other models.

The initial value of all parameters was then set to 0.1, except for the known airflow rates. The RLS model once again quickly converged to a solution but it was even worse than the one made when the initial value of the parameters was set to 0.01. Finally, the initial value of *all* parameters was set to their respective synthetic values from CONTAM. The RLS model *did not* adjust the values as each synthetic measurement became available. Thus, the RLS model had the capability to estimate the correct parameter values but did not when the initial values of the parameters were set to values other than the synthetic ones.

This led to the conclusion that the difference between the synthetic measurements and calculated concentrations was not sensitive enough to changes or errors in the parameter values. Thus, $\hat{\theta}(t)$ was not properly updated as each synthetic measurement became available. In order to improve the performance of the RLS model, methods need to be employed to make the parameters more sensitive to the difference between $y(t)$

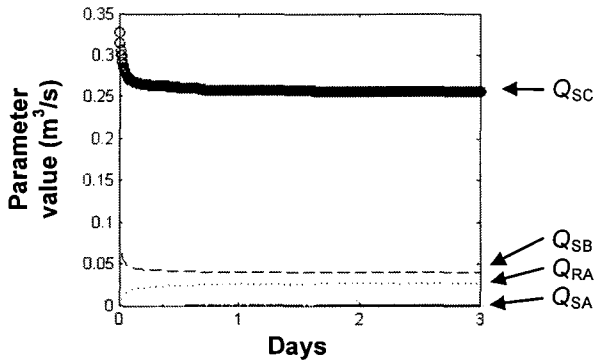


Figure 4-7. Parameter values for known airflow rates over time (RLS model).

(synthetic measurements) and $\varphi^T(t)\hat{\theta}(t-1)$ (calculated concentration). One possibility is manually injecting CO₂, as in a traditional tracer gas test, which may excite/perturb the system to be more sensitive to changes in the measurement matrix. This is saved for future work. Nevertheless, a *recursive* parameter estimation method may not be necessary as data collection and parameter estimation can be performed offline, as was demonstrated by the steady-state test case and the testing of non-recursive parameter estimation methods in this section.

4.6.2.2 Synthetic test building

The synthetic 3-zone test building used to test the building airflow network inverse model for the *steady-state system* was also employed to test the building airflow network inverse model for the *transient system*. The only difference here was that the mechanical ventilation system supplied 100% outdoor air. The results of this test case would not be affected if transient CO₂ measurements from supply diffusers were available.

4.6.2.3 Synthetic perfect and imperfect transient measurements

The rank of the known-information matrix was calculated for 1 day of CO₂ concentrations simulated every 5 min (300 sec) by the CONTAM model for training. Thus $\Delta t = 300$ sec in Eqs. (26) and (35). One day of CO₂ concentrations was then 288 datasets. The datasets were simulated based on the occupancy information in Figure 4-8(a). There were zero occupants modeled in Zone A (common area). The resulting transient CO₂ concentrations simulated by CONTAM are also shown in Figure 4-8(b) for each of the three simulated physical zones. Since the number of unknown airflow rates in this synthetic 3-zone test building was 14, Table 4-10 shows that 108 sets (9 hrs) of CO₂ concentrations were needed in order for the building airflow network inverse model to estimate the unknown airflow rates. However, because the first nine hours of data included eight hours where there were no occupants, and thus no sources of CO₂ (other than the outdoors), the entire day's data was used as training data.

As discussed in Sec. 4.5.1, the simulated CO₂ concentrations were directly used as *synthetic perfect measurements*. The simulated CO₂ concentrations were perturbed to generate *synthetic imperfect measurements*. The precision error and bias used for the steady-state test case were also used for the transient test case. To determine the uncertainty of the deterministic building airflow network inverse models (LSQ and NONLINOPTIM models), 1,000 randomly generated sets of synthetic imperfect CO₂ measurements were used to determine a mean value and standard deviation of the unknown airflow rates. To determine the uncertainty of the stochastic building airflow network inverse model (SDE model), 1,000 values of the random term were used to determine a mean value and standard deviation of the unknown airflow rates. For

comparison, just *one* randomly generated set of synthetic imperfect CO₂ measurements and *one* value of the random term were also used to estimate the unknown airflow rates.

Two days of CO₂ concentrations (or 576 sets) of testing data were generated in CONTAM . These were also fed into the sensor models to generate synthetic perfect and imperfect measurements. An example of the testing data in Zone B is shown in Figure 4-9. The testing data used to assess the ability of the estimated building airflow network to predict contaminant concentrations that were not included in the training data.

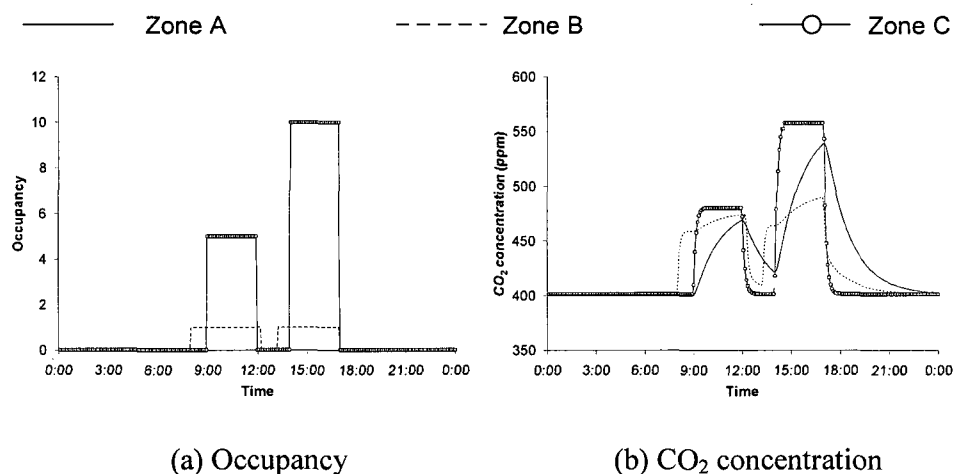


Figure 4-8. (a) Occupancy and (b) simulated CO₂ concentrations in each simulated physical zone for 3-zone test building (training data).

Table 4-10. Rank of CO₂ training data datasets (transient).

Number of datasets	Rank
1-95	8
96-107	11
108-288	14

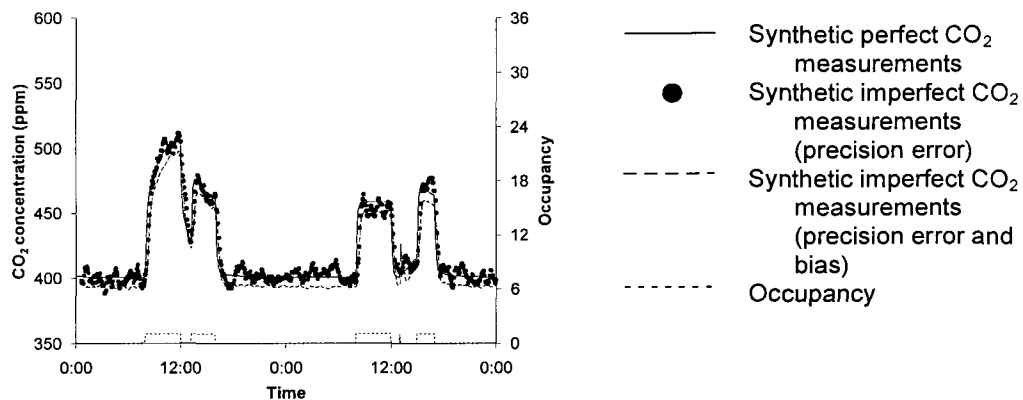


Figure 4-9. Example of testing data in Zone B.

4.6.2.4 Results – synthetic perfect transient measurements

The *mean error in Q* was 35.5-48.2% and 39-90 m³/h (23-53 cfm) (3-8% of max Q), depending on the transient inverse model used (Figure 4-10). Detailed tables comparing each estimated airflow rate with the synthetic value (such as Table 4-5 to Table 4-7 for the steady-state case) were not shown here for brevity. They can be found in APPENDIX F. This error was at most 2.4 ACH in Zone B. The supply airflow rate to Zone B was 7 ACH; thus, a 2.4 ACH error was about 30%.

The *mean error in Q* published in a similar synthetic tracer study [43] was 30% and 17.5 m³/h (10 cfm) (16% of max Q) using simulated annealing as the parameter estimation method. This result was for a test case when synthetic measurements were simulated every 50 sec and relatively precise (coefficient of variation=0.1). This result was 0.3-0.9 ACH, based on zone sizes simulated in their study. The zones they simulated were *not* mechanically ventilated.

In relation to the maximum value of Q , all three inverse models developed in this research performed *better* than the method described in the published synthetic tracer study [43]. The building airflow network inverse models developed in this research offered several advantages over the one reported in the published synthetic study. First, in the published synthetic study [43], *multiple* tracers were used to estimate unknown airflow rates. In contrast, *one* tracer was sufficient in this research to estimate unknown airflow rates as long as the rank of the known-information matrix was greater than or equal to the number of unknown airflow rates (Sec. 4.4.6). Second, no such condition(s) was discussed in [43] in regards to its method being generalized to a building/space of any size.

Lastly, each building airflow network inverse model developed in this research offered an advantage over the simulated annealing method used in the published synthetic tracer study. The LSQ model also guaranteed a global minimum, whereas the simulated annealing method used in the published synthetic tracer study could not [43]. The simulated annealing parameter estimation method would be useful in cases where the rank of the known-information matrix is *less* than the number of unknown airflow rates (Sec. 4.4.6). Neither the NONLINOPTIM nor SDE model may not offer any computational advantages over the simulating annealing method used in the literature, though the error in the estimated building airflow network was less. The SDE model offers an advantage over the estimation method presented in the literature by including uncertainty in both the concentration measurement *and* perturbations to the system (see Sec. 4.4.2). Results – synthetic imperfect transient measurements

The *mean error in Q* was $8.5 \pm 0.5\%$ and $8 \pm 0.4 \text{ m}^3/\text{h}$ ($5 \pm 0 \text{ cfm}$) ($<1\%$ of max **Q**) when using synthetic imperfect measurements with precision error only and the LSQ model. These values were calculated according to the discussion in Sec. 4.5.2. They were *lower* than those calculated when using synthetic perfect measurements (Figure 4-10) because many of the synthetic airflow rates fell within the range of the estimated airflow rates. Thus, more "0% error" resulted in a lower *mean error in Q*. The *mean error in Q* increased when using synthetic imperfect measurements with precision error and bias, but it was still lower than when using synthetic perfect measurements. The values were $26.4 \pm 2.2\%$ and $26 \pm 2 \text{ m}^3/\text{h}$ ($15 \pm 1 \text{ cfm}$) (2% of max **Q**).

In contrast, the use of **synthetic imperfect measurements did not affect the mean error in Q** for building airflow network estimates made by the NONLINOPTIM and SDE inverse models (Figure 4-10). The *mean error in Q* was $44.8 \pm 0.0\%$ and $82 \pm 0 \text{ m}^3/\text{h}$ ($48 \pm 0 \text{ cfm}$) (7% of max **Q**) using either set of synthetic imperfect measurements to develop the NONLINOPTIM inverse model. The *mean error in Q* was $40.1 \pm 8.7\%$ and $77 \pm 16 \text{ m}^3/\text{h}$ ($45 \pm 9 \text{ cfm}$) (7% of max **Q**) using synthetic imperfect measurements with precision error only to develop the SDE inverse model. It was $39.6 \pm 6.5\%$ and $76 \pm 12 \text{ m}^3/\text{h}$ ($45 \pm 7 \text{ cfm}$) (7% of max **Q**) using synthetic imperfect measurements with precision error and bias to develop the SDE inverse model. **There was larger uncertainty in terms of Q using the SDE inverse model than using the LSQ or NONLINOPTIM inverse model.**

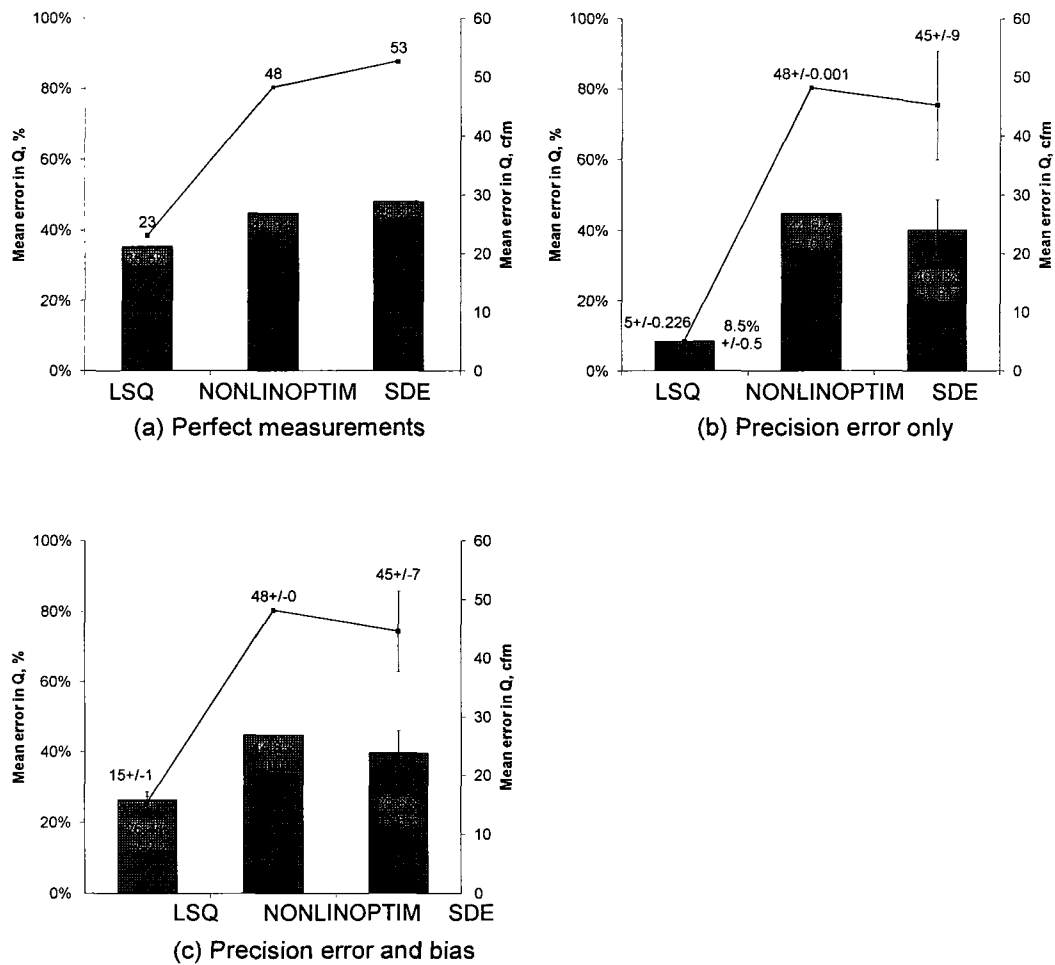


Figure 4-10. Comparing *mean error in Q* for three transient inverse models.

Similar to the case when using synthetic perfect measurements, the *mean error in Q* was at most 2.2 ACH in Zone B using synthetic imperfect measurements. The *mean error in Q* reported in the literature [43] was 81% and $36.9 \text{ m}^3/\text{h}$ (22 cfm) (34% of max Q) when using synthetic imperfect measurements (coefficient of variation=0.5) and simulated annealing as the parameter estimation method. This error was 0.6-1.8 ACH, depending on zone size. In a published experimental tracer study [40], the *mean error in*

Q was 8% and 5.0 m³/h (3 cfm) (3% of max Q) using nonlinear least squares as the parameter estimation method.

In relation to the maximum value of Q , the LSQ inverse model developed in this research performed *similarly* to the method described in the published experimental tracer study [40]. The LSQ inverse model developed in this research offered computational savings over the *nonlinear* least squares parameter estimation method used in [40] to estimate airflow rates from tracer measurements. As was the case when using synthetic perfect measurements (previous section), in relation to the maximum value of Q , all three inverse models developed in this research performed *better* than the method described in the published synthetic tracer study [43]. Advantages of the building airflow network inverse models developed in this research over the one published in the synthetic tracer study were already discussed in the previous section and will not be repeated.

4.6.2.5 Performance of building airflow network inverse model

Using the estimated building airflow network inverse models developed with synthetic *perfect* measurements, the *RSME in C* (Figure 4-11 and Figure 4-12) was calculated as 1.7-6.5 ppm using the training data (0.2-1.1% of the maximum concentration in any zone) and 2.3-8.0 ppm using the testing data (0.3-1.1% of the maximum concentration in any zone), depending on the transient inverse model used. The *RSME in C* published in a synthetic tracer study was 0-33 ppm [43] (0-5% of the maximum concentration, depending on the zone). In another published synthetic tracer study, which also used CO₂ as the tracer, the *RSME in C* was 1.7-48.3 ppm [42] (2-11% of the maximum concentration depending on the zone). The fit between the synthetic measurements and predicted concentrations (*R² value*) was calculated as 0.932-0.997

using training data and 0.905-0.995 using testing data, depending on the transient inverse model used.

Using *training* data, the *RSME in C* was about the same (an average of 14.6 ± 0.5 ppm) for all three inverse models (Figure 4-11), using synthetic imperfect measurements with precision error only. Using synthetic imperfect measurements with precision error and bias, the *RSME in C* was on average 10.3 ± 0.4 ppm for all three inverse models.

Using *testing* data with precision error only, the *RSME in C* was about the same using the LSQ and NONLINOPTIM inverse models (16.4 ± 0.2 ppm). The *RSME in C* was higher for the SDE inverse model (20.4 ± 0.0 ppm). Using *testing* data with precision error and bias, the models performed differently, with the LSQ inverse model performing the best and SDE inverse model performing the worst.

In relation to the maximum value of *C*, the inverse models developed in this research performed *better* than the methods described in the published synthetic tracer study [42]. Advantages of the building airflow network inverse models developed in this research over the one published in the synthetic tracer study were already discussed in the previous section and will not be repeated.

The R^2 value (also shown in Figure 4-11 and Figure 4-12) was lower (indicating a worse fit) when using synthetic measurements with error when compared to the values when using synthetic perfect measurements, which was to be expected.

Using *training* data, the R^2 value was about the same (an average of 0.827 ± 0.014) for all three inverse models (Figure 4-11), using synthetic imperfect measurements with precision error only. Using synthetic imperfect measurements with precision error and bias, the R^2 value was on average 0.908 ± 0.007 for all three inverse models.

Using *testing* data with precision error only, the R^2 value was about the same (an average of 0.816 ± 0.005) for all three inverse models (Figure 4-12), using synthetic imperfect measurements with precision error only. Using *testing* data with precision error and bias, the models performed differently, with the LSQ inverse model performing the best (0.919 ± 0.001) and the NONLINOPTIM and SDE inverse models performing worse (but about the same, an average of 0.876 ± 0.001).

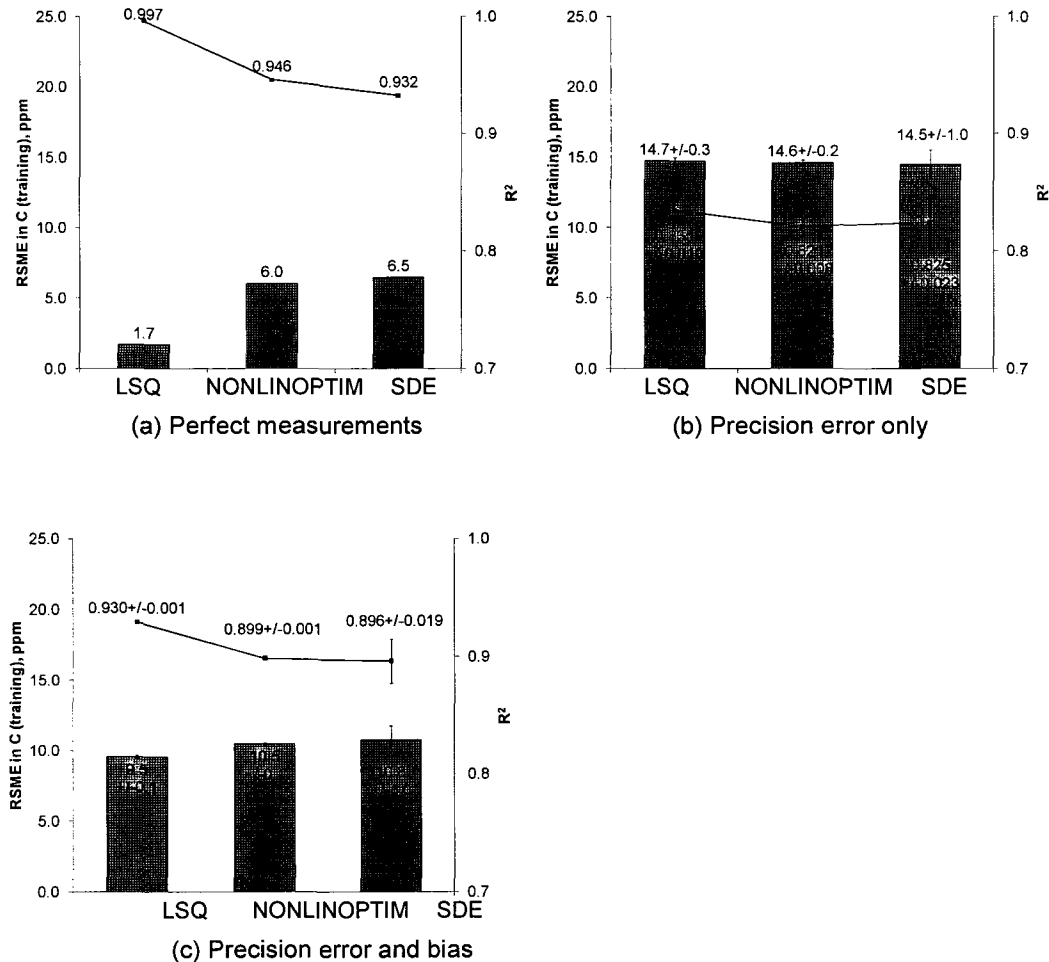


Figure 4-11. Comparing $RSME$ in C and R^2 values for three transient inverse models (training data).

It could also be concluded that the proposed building airflow network inverse model has the potential to make good predictions for other gaseous contaminants as well.

The uncertainty in the *RSME in C* was significantly *less* when using synthetic *transient* measurements compared to using synthetic *steady-state* measurements. **Thus, the proposed building airflow network inverse model can be implemented in real buildings where transient measurements would be more easily obtained than steady-state measurements.** As expected, the *RSME in C* was slightly higher for the testing data than it was for the training data since the training data was used to develop the building airflow network inverse model.

The difference between the performances of the building airflow network inverse models developed using synthetic perfect and imperfect CO₂ measurements was larger for the LSQ inverse model than it was for the NONLINOPTIM and SDE inverse models in terms of *mean error in Q* (Figure 4-10). The difference in LSQ inverse model performance was 26-28% and 31 m³/h (18 cfm), which was *greater* than the difference found in the steady-state test case also using the LSQ inverse model. The difference in NONLINOPTIM inverse model performance was 0% in terms of *mean error in Q*, whether using synthetic perfect or imperfect CO₂ measurements. The difference in SDE inverse model performance was 2-17% and 2-28 m³/h (1-17 cfm), which was *greater* to the differences found in the steady-state case. **It could be concluded that the use of synthetic imperfect measurements affected the performance of the LSQ and SDE building airflow network inverse models, but not the NONLINOPTIM model, in**

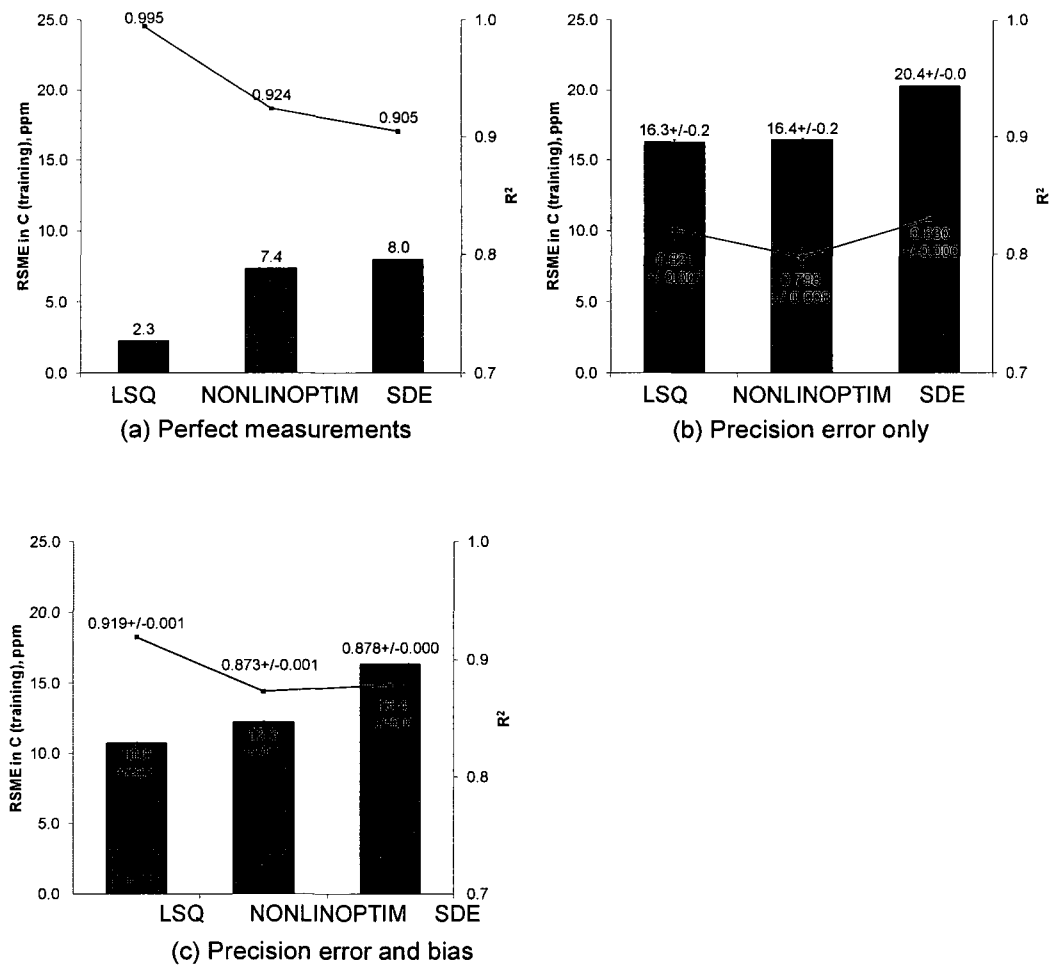


Figure 4-12. Comparing $RSME$ in C and R^2 values for three transient inverse models (testing data).

terms of the building airflow network only. In terms of $RSME$ in C and R^2 values, the use of synthetic measurements affected the performance of all the tested building airflow network inverse models.

Even if only one set of synthetic imperfect measurements were used to develop each of building airflow network inverse models tested (or only one iteration of the random term in the SDE inverse model used), the *mean error in Q* was still at most 2.2

ACH in Zone B (30% of the supply ACH). The *RSME in C* and *R² values* (training) were about the same as when multiple sets of synthetic imperfect measurements were used.

Thus, the proposed building airflow network inverse model shows potential to be used in real-life with only one set of actual measurements. Nevertheless, the proposed building airflow network inverse model could be implemented offline, where 1,000 sets of *synthetic* imperfect measurements could be randomly generated from one set of *actual* measurements.

The SDE inverse model required much more computational time (3 hours) than the LSQ and NONLINOPTIM models (~7 min.). In terms of inverse model performance, the SDE inverse model did not estimate a more accurate building airflow network nor was its estimate able to predict concentration more accurately than the other two inverse models. Nevertheless, only error in the CO₂ measurements was considered in this research. Future work includes studying the effects of error in the CO₂ generation rate and in the measurements of **Q** on the performance of the proposed building airflow network inverse models.

The performance of the building airflow network inverse model can also be evaluated in terms of estimated infiltration rates through the building envelope in each zone. Table 4-11, Table 4-12, and Table 4-13 summarize the results for the LSQ, NONLINOPTIM, and SDE inverse models, respectively. These tables indicate the *mean* difference in infiltration rates was about the same whether using synthetic perfect or imperfect CO₂ measurements. The best estimate was provided by the LSQ inverse model.

Table 4-11. Summary of error in infiltration rates (LSQ, transient).

Zone	Using synthetic perfect meas., % (cfm)	Using 1,000 sets of synthetic measurements	
		With precision error, % (cfm)	With precision error and bias, % (cfm)
A	6% (5)	17-37% (15-33)	29-34% (26-30)
B	100% (85)	69-84% (58-71)	29-117% (25-99)
C	104% (80)	40-100% (30-77)	72-127% (55-98)
<i>Mean</i>	70% (57)	53-62% (45-50)	62-74% (50-62)

Table 4-12. Summary of error in infiltration rates (NONLINOPTIM, transient).

Zone	Using synthetic perfect meas., % (cfm)	Using 1,000 sets of synthetic measurements	
		With precision error, % (cfm)	With precision error and bias, % (cfm)
A	38% (34)	38% (34)	38% (34)
B	51% (43)	51% (43)	51% (43)
C	201% (154)	201% (154)	201% (154)
<i>Mean</i>	97% (77)	97% (77)	97% (77)

Table 4-13. Summary of error in infiltration rates (SDE, transient).

Zone	Using synthetic perfect meas., % (cfm)	Using 1,000 sets of synthetic measurements	
		With precision error, % (cfm)	With precision error and bias, % (cfm)
A	40% (36)	5-61% (5-55)	13-54% (11-49)
B	62% (53)	9-66% (7-56)	21-58% (18-50)
C	182% (140)	167-236% (128-181)	172-223% (132-172)
<i>Mean</i>	95% (76)	60-121% (47-97)	69-112% (54-90)

The uncertainty in the error was greatest when using the SDE inverse model, and least when using the NONLINOPTIM model. How these differences may affect predicted IAQ or energy use is saved for future work.

The leakiest zone simulated by CONTAM was Zone B (-1.05 ACH), which was *not* always the case using the building airflow network estimates provided by each inverse model. In most cases, the inverse models estimated Zone C to be the leakiest. The maximum difference among the inverse models, whether using synthetic perfect or imperfect measurements, was 55 cfm in Zone A, 103 cfm in Zone B, and 182 cfm in Zone C.

Lastly, the performance of the building airflow network inverse model can also be evaluated in terms of a qualitative assessment of pressure distribution in the synthetic test building. The building airflow network estimate from the LSQ and NONLINOPTIM inverse models agreed the most with the synthetic pressure distribution from CONTAM. The building airflow network estimate from the SDE inverse model contained larger uncertainty.

4.6.2.6 Conclusions for test case 2 – transient system

- (1) The uncertainty in Q and in $RSME$ in C , i.e., the standard deviation, was much *less* in the case of using synthetic transient measurements than when using synthetic steady-state measurements to develop the transient inverse models;
- (2) The use of synthetic imperfect measurements affected the performance of the LSQ and SDE building airflow network inverse models, but not the NONLINOPTIM model, in terms of the building airflow network only. In terms of $RSME$ in C and R^2 values, the use of synthetic measurements affected the performance of all the tested building airflow network inverse models;
- (3) The building airflow network inverse models developed in this research offered several advantages over the one reported in the published synthetic study [42]:

- a. *One* tracer was sufficient in this research to estimate unknown airflow rates as long as the rank of the known-information matrix was greater than or equal to the number of unknown airflow rates.
 - b. No such condition(s) was discussed in the literature in regards to the published methods being generalized to a building/space of any size.
 - c. Each building airflow network inverse model developed in this research offered an advantage over the methods used in the literature.
 - i. The LSQ model guaranteed a global minimum, whereas the simulated annealing method used in the published synthetic tracer study could not.
 - ii. Neither the NONLINOPTIM nor SDE model may not offer any computational advantages over the simulating annealing method used in the literature, though the error in the estimated building airflow network was less.
 - iii. The SDE model offers an advantage over the estimation method presented in the literature by including uncertainty in both the concentration measurement *and* perturbations to the system (see Sec. 4.4.2).
- (4) The proposed building airflow network inverse model has the potential to make good predictions for other gaseous contaminants;
- (5) In terms of a qualitative assessment of pressure distribution, the proposed LSQ and NONLINOPTIM building inverse airflow models performed similarly

whether using synthetic perfect or imperfect CO₂ measurements. There was greater uncertainty in the pressure distribution when using the SDE inverse model.

4.7 Conclusions

Synthetic steady-state and transient CO₂ measurements, without and with two types of sensor error, were used to estimate the building airflow network of a synthetic 3-zone test building. Minimizing least squares (LSQ) was used to estimate the building airflow network using synthetic steady-state and transient measurements. Nonlinear parameter optimization was used for both a deterministic (NONLINOPTIM) and stochastic (SDE) inverse model of the building airflow network. It was found that:

- (1) The building airflow network inverse model tested in this research could be applied to a building of any number of zones as long as the rank of the known-information matrix was equal to or greater than the number of unknown airflows in the building airflow network;
- (2) The building airflow network inverse model could be implemented offline. The computational time for the LSQ and NONLINOPTIM model was about 7 min when using one days of synthetic CO₂ measurements;
- (3) The estimated building airflow network could be used for: determining the building airtightness at specific parts of a building; provide a quick estimate of the transport of other unmeasured contaminants; and provide insight into the pressure distribution of a building.
- (4) The proposed building airflow network inverse models performed similarly, if not better, than ones published in the literature. They also offered computational advantages over the ones published in the literature.

Hypothesis #3: there exists a framework for easily and effectively determining the airflow pattern within a whole building using a distributed sensor network. The proposed building airflow network was fast and easy to set up. It proved computationally effective in estimating the building airflow network comparably to studies found in the literature.

Portions of this work will be presented at the 1st International High Performance Buildings Conference later this month [138]. The full publication can be found in APPENDIX G.

4.8 Future work

A fast and robust method was developed to estimate a building airflow network that has potential to be used for applications such as determining building infiltration, contaminant transport, pressure distribution, and for building commissioning. Many other unidentified applications exist. Future work involves exploring the full potential of the estimation method proposed in this work.

First, the distributed CO₂ sensor system could be optimized in order to provide the information for an airflow estimate that is accurate, precise and reliable. This process could optimize the number of sensors and other sensor system performance metrics used in other industries (see Sec. 1.3.3.1 for those used in municipal water networks and Sec. 1.3.3.2 for those used in chemical process plants).

Second, pressure measurements can be made to further verify or enhance the estimated building airflow network. Pressure measurements across the building envelope at varying levels of estimated infiltration could be used to quickly determine the building envelope airtightness. The level of infiltration could be varied by manually adjusting the supply and return airflow rates from a particular zone. Pressure measurements between

the zone and the exhaust vent were used in calculate changes in air exchange rates due to the operation of a variable-air-volume (VAV) system [41].

Third, the building airflow network was assumed to remain constant in this research, which may not reflect actual operating conditions. VAV systems and operation during nighttime or weekend schedules introduce changes to the building airflow network. If a natural or hybrid ventilation system is in use, changes in outdoor (wind, temperature) and indoor conditions (occupant behavior) will also affect the building airflow network. The feasibility of including open windows, trickle vents, and other non-mechanical devices that are used in natural and hybrid ventilation systems should be explored in future work. This would be part of the proposed framework for the building airflow network inverse model discussed in Sec. 4.2.

Fourth, when natural or hybrid ventilation systems are in use, then the effects of buoyancy and diffusion may play more of an important role in contaminant transport than when mechanical ventilation systems are in use. Thus, the feasibility of including these effects should be explored in future work.

Fifth, other leakage paths exist in real buildings that were not accounted for in this research. They include air exchange between a zone and a ceiling plenum, and between zones through the ceiling plenum. The importance of understanding the pressure field, and thus airflow through these and other interstitial spaces is discussed in [139].

Sixth, formal metrics could be applied to the proposed estimation methods using ASTM D5157, as they were used to evaluate the tuned multizone models in Sec. 1.3.1.4.

Lastly, as mentioned in the text:

- (1) This method should be extended to multi-story buildings or building with spaces of non-uniform (not well-mixed) conditions, such as atria or gymnasiums. The method should also be extended to spaces with much smaller or much larger air change rates.
- (2) The RLS model was not successful in estimating the building airflow network because the difference between the actual and calculated concentration was not sensitive enough to changes or errors in the parameter (airflow) values. Methods need to be employed to make the parameters more sensitive to these differences in order to utilize RLS for building airflow network estimation.
- (3) The inclusion of uncertainty in other coefficients of the governing equation, such as in \mathbf{Q} , to account for uncertainty in airflow through an open door caused by occupant movement or window caused by wind, and in \mathbf{G} , to account for uncertainty in the respiration rates of multiple occupants in a zone, should be performed for the SDE model.
- (4) The method proposed for estimating a building airflow network should be validated with experimental data (see following section for possible datasets).
- (5) The differences in the actual and estimated building airflow network should be examined in terms of predicted IAQ or energy use.
- (6) Application-specific criteria for selecting the most appropriate model for estimating a building airflow network should be developed. For instance, one could use the sensor system design methods and performance metrics in Sec. 1.3.3.2 to improve the design of a distributed CO₂ sensor system in order to meet specific levels of reliability, redundancy, observability, and robustness for each

application. Applications which may require different levels of these performance metrics are those for energy evaluation, decontamination, clean room (laboratories, hospitals), determining building envelope airtightness and infiltration, and many more.

4.8.1 Validation

Validation studies of the building airflow network estimation method presented in this research could verify whether in real buildings, the rank of the known-information matrix will be greater than the number of unknown airflow rates. Validation studies could also verify whether real-time CO₂ measurements, subject to both sensor error and system variability, can be used to efficiently and accurately estimate the building airflow network. The following published studies are possible sources of experimental data for validating the building airflow network estimation method presented in this work.

Validation is saved for future work.

The National Center for Energy Management and Building Technologies has organized several projects in order to better understand and improve the performance of mechanical ventilation systems in the U.S. building stock. Their website lists over 25 tasks in order to do so [140]. The first task was the "Measurement and Verification of Building Performance Characteristics" [141]. The objective of the study was to develop a protocol for assessing indoor air quality (IAQ). Measurements were taken at 10 U.S. office buildings located in various parts of the country. The buildings varied in size, occupancy, and year of construction. Air velocity and CO₂ were measured in six locations in each building, each location representing a pre-determined zone. A similar

study was also performed for educational buildings (Task 13), which may also provide additional experimental data.

One study discussed in Sec. 1.3.1.4 described the tuning of CONTAM with experimental data from a real building. In that study, CO₂ was released as a tracer at the air handling unit (AHU) supply duct and measured at the AHU return duct. This measurement was then compared to one calculated by the tuned CONTAM model. The number of CO₂ measurements was limited and thus, the agreement was not very good. However, this study is currently being extended in a project funded by the Department of Homeland Security (DHS) [142-143].

4.9 Plans for publication

Possible publications:

- Review of tracer gas studies conducted using CO₂
- Development of deterministic and stochastic building airflow network inverse models utilizing CO₂ measurements

Possible journals:

- *Building and Environment*, which has an impact factor of 1.192.
- *Journal of Environmental Monitoring*, which has an impact factor of 2.0.
- *Indoor Air*, impact factor of 1.59

5. CONCLUSIONS AND RECOMMENDATIONS

In Part 1, a framework was presented for utilizing forward airflow models in systematic sensor system design. Specifically, how to select the simplest and most appropriate airflow model for sensor system design. It was found that for the zones tested and for sensor systems with *more than one* sensor, the simplest airflow model for sensor system design was either the multizone or zonal model. Also, none of the zone characteristics tested affected the selection of either the multizone or zonal model for sensor system design when the number of sensors was *greater than one*.

In Part 2, a framework was presented for utilizing inverse airflow models to estimate airflow patterns within a single zone, which could then be used in systematic sensor system design. It was found for the developed inverse airflow model, *inverse singular value decomposition*, that velocity sensors placed on the *wall closest to the outlet* and that measured velocity in direction of *bulk airflow* most improved airflow estimation accuracy. Also, the use of temperature sensors systems was not recommended since a large number of sensors would be needed and, airflow pattern estimation was no better than using fewer velocity sensors.

Lastly, in Part 3, a framework was presented for utilizing inverse airflow models to estimate airflow patterns within a whole building, which could then be used in systematic sensor system design, among other applications. It was found that utilizing synthetic imperfect measurements for training, all tested building airflow network inverse models performed similarly in terms of the accuracy of the estimated building airflow network. In terms of CO₂ prediction (using the testing data), performance varied among the tested inverse models, but the difference was <5 ppm. In addition, utilizing synthetic

transient measurements for training, the uncertainty in CO₂ prediction was much less than utilizing steady-state measurements. The performance of the tested building airflow network inverse models were comparable to (if not better than) those for similar studies in the literature. Lastly, it was shown that the tested building airflow network inverse models could be extended to 1-story buildings of any size under certain conditions.

Recommendations for future work include testing more zone types in Parts 1 and 2. The results of this research could have a larger impact on the building industry with future development of the black-box model shown in the framework for developing a building airflow network inverse model (Part 3). Validation with experimental data is needed for all three parts of this research.

6. LONG TERM RESEARCH GOALS AND ENGINEERING IMPACT

One long-term goal of this research is the protection building occupants in terms of their health, productivity, and safety. Adequately designed indoor air sensor systems will help to ensure this by continuously monitoring IAQ, which includes the presence of foreign/dangerous contaminants. The second long-term goal of this research is to be able to utilize the information gathered from indoor air sensor systems to further improve IAQ, ventilation performance, and reduce energy consumption.

The results of Part 1 of this research (Chapter 2) demonstrated that sensor systems designed using data from simpler airflow models could perform just as well as those designed using more complex airflow models even in instances where the indoor space was not actually well-mixed. This offers computational savings for design engineers while not compromising sensor system performance.

7. LIST OF REFERENCES

1. EPA, *Indoor Air Pollution: An Introduction for Health Professionals*, E.P. Agency, Editor. 1994.
2. Brown, S.K., *Indoor air quality*, in *Australia: State of the Environment Technical Paper Series (Atmosphere)*. 1997.
3. Fisk, W.J., Anibal T. De Almeida, *Sensor-based demand-controlled ventilation: a review*. Energy and Buildings, 1998. 29(1): p. 35-45.
4. Dubberley, M., A.M. Agogino, and A. Horvath. *Life-cycle Assessment of an Intelligent Lighting System Using a Distributed Wireless Mote Network*. in *Proceedings of IEEE International Symposium 2004*. 2004. p. 122-7.
5. Walton, G.N. and W.S. Dols, *CONTAM 2.4 User Guide and Program Documentation*. 2005, National Institute of Standards and Technology: Gaithersburg, MD. p. 313.
6. Feustal, H.E. and B.V. Smith, *COMIS 3.0 - User's Guide*. 1997, Lawrence Berkeley National Laboratory.
7. McDowell, T.P., et al., *Integration of Airflow and Energy Simulation Using CONTAM and TRNSYS*. 2003 ASHRAE Transactions, 2003. 109(2).
8. Haghigat, F. and A.C. Megri, *A Comprehensive Validation of Two Airflow Models - COMIS and CONTAM*. Indoor Air, 1996. 6(4): p. 278-288.
9. Chung, K.C., *Development and validation of a multizone model for overall indoor air environment prediction*. HVAC&R Research, 1996. 2(4): p. 376-385.
10. Emmerich, S.J., et al., *Validation of multizone IAQ model predictions for tracer gas in a townhouse*. Building Services Engineering Research and Technology, 2004. 25(4): p. 305-316.
11. Emmerich, S.J., *Validation of Multizone IAQ Modeling of Residential-Scale Buildings: A Review*. ASHRAE Transactions, 2001. 107(2).
12. Wang, L. and Q. Chen, *Evaluation of some assumptions used in multizone airflow network models*. Building and Environment, 2008. 43(10): p. 1671-1677.
13. Wurtz, E., J.-M. Nataf, and F. Winkelmann, *Two- and three-dimensional natural and mixed convection simulation using modular zonal models in buildings*. International Journal of Heat and Mass Transfer, 1999. 42(5): p. 923.
14. Inard, C., H. Bouia, and P. Dalicieux, *Prediction of air temperature distribution in buildings with a zonal model*. Energy and Buildings, 1996. 24(2): p. 125.
15. Laporte, S., J. Virgone, and S. Castanet, *A comparative study of two tracer gases: SF₆ and N₂O*. Building and Environment, 2001. 36(3): p. 313-320.
16. Musy, M., et al., *Generation of a zonal model to simulate natural convection in a room with a radiative/convective heater*. Building and Environment, 2001. 36(5): p. 589-596.

17. Mora, L., A.J. Gadgil, and E. Wurtz, *Comparing zonal and CFD model predictions of isothermal indoor airflows to experimental data*. Indoor Air, 2003. 13(2): p. 77-85.
18. Axley, J.W., *Surface-drag flow relations for zonal modeling*. Building and Environment, 2001. 36(7): p. 843.
19. Jiru, T.E. and F. Haghghat, *A new generation of zonal models*. ASHRAE Transactions, 2006. 112(2): p. 163-174.
20. Ren, Z. and J. Stewart, *COwZ User's Guide: Zonal indoor source emission and dispersion model, Version 1*. 2003, The School of Computer Science and QUESTOR Centre.
21. Ren, Z., *Enhanced modelling of indoor air flows, temperatures, pollutant emission and dispersion by nesting sub-zones within a multizone model*. 2002, Queen's University: The United Kingdom. p. 269.
22. Ren, Z. and J. Stewart, *Simulating air flow and temperature distribution inside buildings using a modified version of COMIS with sub-zonal divisions*. Energy and Buildings, 2003. 35(3): p. 257-271.
23. Zhai, Z., et al., *Evaluation of various turbulence models in predicting airflow and turbulence in enclosed environments by CFD: Part-1: Summary of prevalent turbulence models*. HVAC&R Research, 2007. 13(6).
24. Zhang, Z., et al., *Evaluation of various turbulence models in predicting airflow and turbulence in enclosed environments by CFD: Part-2: Comparison with experimental data from literature*. HVAC&R Research, 2007. 13(6).
25. Chen, Q., *Comparison of different $k-\epsilon$ models for indoor air flow computations*. Numerical Heat Transfer, Part B: Fundamentals, 1995. 28(3): p. 353-369.
26. Chen, Q., *Prediction of Room Air Motion by Reynolds-Stress Models*. Building and Environment, 1996. 31: p. 233-244.
27. Stamou, A. and I. Katsiris, *Verification of a CFD model for indoor airflow and heat transfer*. Building and Environment, 2006. 41(9): p. 1171.
28. Chen, Q. and W. Xu, *A zero-equation turbulence model for indoor airflow simulation*. Energy and Buildings, 1998. 28(2): p. 137-144.
29. Musser, A., O. Schwabe, and S. Nabinger. *Validation and calibration of a multizone network airflow model with experimental data*. in *Proceedings of eSim Canada conference*. 2001. Canada. p. 228-235.
30. ASTM, *ASTM D5157-97 Standard Guide for Statistical Evaluation of Indoor Air Quality Models*. 2003, American Society of Testing and Materials.
31. Firrantello, J., *Development of a Rapid, Data Driven Method for Tuning Multizone Airflow Models*, in *Architectural Engineering*. 2007, Pennsylvania State University: University Park. p. 161.
32. Firrantello, J., et al., *Use of factorial sensitivity analysis in multizone airflow model tuning*. ASHRAE Transactions, 2007. 113(1): p. 642-651.
33. Jeong, J.-W., et al., *Feasibility of wireless measurements for semi-empirical multizone airflow model tuning*. Building and Environment, 2008. 43(9): p. 1507-1520.
34. Price, P.N., S.C. Chang, and M.D. Sohn, *Characterizing buildings for airflow models - what should we measure?* 2004, Indoor Environment Department: Lawrence Berkeley National Laboratory: Berkeley, CA.

35. Zhang, Z. and Q. Chen, *Comparison of the Eulerian and Lagrangian methods for predicting particle transport in enclosed spaces*. Atmospheric Environment, 2007. 41(25): p. 5236-5248.
36. Wang, L. and Q. Chen, *Validation of a coupled multizone and CFD program for building airflow and contaminant transport simulations*. HVAC&R Research, 2007. 13(2): p. 267-281.
37. Tan, G. and L.R. Glicksman, *Application of integrating multi-zone model with CFD simulation to natural ventilation prediction*. Energy and Buildings, 2005. 37(10): p. 1049-1057.
38. Jayaraman, B., D. Lorenzetti, and A. Gadgil, *Coupled model for simulation of indoor airflow and pollutant transport*. 2004, Lawrence Berkeley National Laboratory.
39. Wang, L. and Q. Chen, *Theoretical and numerical studies of coupling multizone and CFD models for building air distribution simulations*. Indoor Air, 2007. 17(5): p. 348-361.
40. Miller, S.L., K. Leiserson, and W.W. Nazaroff, *Nonlinear Least-Squares Minimization Applied to Tracer Gas Decay for Determining Airflow Rates in a Two-Zone Building*. Indoor Air, 1997. 7(1): p. 64-75.
41. Lu, T., et al., *A novel methodology for estimating space air change rates and occupant CO₂ generation rates from measurements in mechanically-ventilated buildings*. Building and Environment, 2010. 45(5): p. 1161-1172.
42. Lawrence, T.M. and J.E. Braun, *Evaluation of simplified models for predicting CO₂ concentrations in small commercial buildings*. Building and Environment, 2006. 41(2): p. 184-194.
43. Sohn, M.D. and M.J. Small, *Parameter estimation of unknown air exchange rates and effective mixing volumes from tracer gas measurements for complex multi-zone indoor air models*. Building and Environment, 1999. 34(3): p. 293-303.
44. Hasham, F.A., W.B. Kindzierski, and S.J. Stanley, *Modeling of hourly NO_x concentrations using artificial neural networks*. Journal of Environmental Engineering and Science, 2004. 3(S): p. S111-S119.
45. Goldberg, D.E., *Genetic Algorithm in Search, Optimization and Machine Learning*. 1989, Reading, Massachusetts: Addison-Wesley Pub. Co.
46. Ali, M.M., C. Storey, and A. Törn, *Application of Stochastic Global Optimization Algorithms to Practical Problems*. Journal of Optimization Theory and Applications, 1997. 95(3): p. 545-563.
47. Arvelo, J., et al., *An Enhanced Multizone Model and Its Application to Optimum Placement of CBW Sensors*. ASHRAE Transactions, 2002. 108(2): p. 818-825.
48. Arora, J.S., M.W. Huang, and C.C. Hsieh, *Methods for optimization of nonlinear problems with discrete variables: A review*. Structural and Multidisciplinary Optimization, 1994. 8(2): p. 69-85.
49. Carrano, J., *Chemical and Biological Standards Study*, DARPA, Editor. 2004, MicroSystems Technology Office.
50. Berry, J., et al., *Sensor Placement in Municipal Water Networks with Temporal Integer Programming Models*. Journal of Water Resources Planning and Management, 2006. 132(4): p. 218-224.

51. Watson, J.-P., R. Murray, and W.E. Hart, *Formulation and optimization of robust sensor placement problems for drinking water contamination warning systems*. Journal of Infrastructure Systems, 2009. 15(4): p. 330-339.
52. Krause, A., et al., *Efficient Sensor Placement Optimization for Securing Large Water Distribution Networks*. Journal of Water Resources Planning and Management, 2008. 134(6): p. 516-526.
53. Berry, J., et al., *Designing contamination warning systems for municipal water networks using imperfect sensors*. Journal of Water Resources Planning and Management, 2009. 135(4): p. 253-263.
54. Lansey, K., et al., *Locating Satellite Booster Disinfectant Stations*. Journal of Water Resources Planning and Management, 2007. 133(4): p. 372-376.
55. Tryby, M.E., et al., *Facility Location Model for Booster Disinfection of Water Supply Networks*. Journal of Water Resources Planning and Management, 2002. 128(5): p. 322-333.
56. Prasad, T.D., G.A. Walters, and D.A. Savic, *Booster Disinfection of Water Supply Networks: Multiobjective Approach*. Journal of Water Resources Planning and Management, 2004. 130(5): p. 367-376.
57. Bagajewicz, M., *A review of techniques for instrumentation design and upgrade in process plants*. Canadian Journal of Chemical Engineering, 2002. 80(1): p. 3-16.
58. *Airflow through large openings in buildings*, in *Airflow patterns within buildings*, J. van der Maas, Editor. 1992, International Energy Agency: Switzerland. p. 168.
59. Bhushan, M., S. Narasimhan, and R. Rengaswamy, *Robust sensor network design for fault diagnosis*. Computers and Chemical Engineering, 2008. 32(4-5): p. 1067-84.
60. Ali, Y. and S. Narasimhan, *Sensor network design for maximizing reliability of bilinear processes*. AIChE Journal, 1996. 42(9): p. 2563-2575.
61. Bagajewicz, M.J. and M.C. Sánchez, *Design and upgrade of nonredundant and redundant linear sensor networks*. AIChE Journal, 1999. 45(9): p. 1927-1938.
62. Dhillon, S.S., K. Chakrabarty, and S.S. Iyengar. *Sensor placement for grid coverage under imprecise detections*. in *Information Fusion, 2002. Proceedings of the Fifth International Conference on*. 2002. p. 1581-1587 vol.2.
63. Chiu, P.L. and F.Y.S. Lin. *A simulated annealing algorithm to support the sensor placement for target location*. in *Electrical and Computer Engineering, 2004. Canadian Conference on*. 2004. p. 867-870 Vol.2.
64. Hamel, D., et al. *A Computational Fluid Dynamics Approach for Optimization of a Sensor Network*. in *Measurement Systems for Homeland Security, Contraband Detection and Personal Safety, Proceedings of the 2006 IEEE International Workshop on*. 2006. p. 38-42.
65. Lohner, R. and F. Camelli, *Optimal placement of sensors for contaminant detection based on detailed 3D CFD simulations*. Engineering Computations, 2005. 22(3): p. 260-73.
66. Tsujita, W., et al., *Gas sensor network for air-pollution monitoring*. Sensors and Actuators, 2005. B(110): p. 304-311.

67. Seppänen, O.A., W.J. Fisk, and M.J. Mendell, *Association of Ventilation Rates and CO₂ Concentrations with Health and Other Responses in Commercial and Institutional Buildings*. *Indoor Air*, 1999. 9(4): p. 226-252.
68. Schell, M.B., Stephen C. Turner, R. Omar Shim, *Application of CO₂-Based Controlled Ventilation Using ASHRAE Standard 62: Optimizing Energy Use and Ventilation*. *ASHRAE Transactions*, 1998. 104: p. 1213-1225.
69. Schell, M. and D. Int-Hout, *Demand Control Ventilation Using CO₂*. *ASHRAE Journal*, 2001. February(2001): p. 18-29.
70. Zhai, Z., J. Srebric, Q. Chen, *Application of CFD to Predict and Control Chemical and Biological Agent Dispersion in Buildings*. *International Journal of Ventilation*, 2003. 2(3): p. 251-264.
71. Zhang, T.F., Q. Chen, and C.-H. Lin, *Optimal sensor placement for airborne contaminant detection in an aircraft cabin*. *HVAC&R Research*, 2007. 13(5): p. 683-696.
72. Mazumdar, S. and Q. Chen, *Influence of cabin conditions on placement and response of contaminant detection sensors in a commercial aircraft*. *Journal of Environmental Monitoring*, 2008. 2008(10): p. 71-81.
73. Brand, K.P. and M.J. Small, *Updating Uncertainty in an Integrated Risk Assessment: Conceptual Framework and Methods*. *Insurance: Mathematics and Economics*, 1996. 18: p. 147-147.
74. Haupt, S.E., *A demonstration of coupled receptor/dispersion modeling with a genetic algorithm*. *Atmospheric Environment*, 2005. 39: p. 7181-7189.
75. Haupt, S.E., G.S. Young, and C.T. Allen, *Validation of a Receptor/Dispersion Model Coupled with a Genetic Algorithm Using Synthetic Data*. *Journal of Applied Meteorology and Climatology*, 2006. 45(3): p. 476-490.
76. Allen, C.T., G.S. Young, and S.E. Haupt, *Improving pollutant source characterization by better estimating wind direction with a genetic algorithm*. *Atmospheric Environment*, 2007. 41(11): p. 2283-2289.
77. Mathur, R., S.G. Advani, and B.K. Fink, *A real-coded hybrid genetic algorithm to determine optimal resin injection locations in the resin transfer molding process*. *Computer Modeling in Engineering and Sciences*, 2003. 4(5): p. 587-601.
78. Sohn, M.D., et al., *Rapidly locating and characterizing pollutant releases in buildings*. *Journal of the Air and Waste Management Association*, 2002. 52(12): p. 1422-1432.
79. Sreedharan, P., et al., *Systems approach to evaluating sensor characteristics for real-time monitoring of high-risk indoor contaminant releases*. *Atmospheric Environment*, 2006. 40(19): p. 3490-3502.
80. Vukovic, V. and J. Srebric, *Application of neural networks trained with multizone models for fast detection of contaminant source position in buildings*. *ASHRAE Transactions*, 2007. 113(2).
81. Federspiel, C.C., *Estimating the Inputs of Gas Transport Processes in Buildings*. *IEEE Transactions on Control Systems Technology*, 1997. 5(5): p. 480-489.
82. Zhang, T.F. and Q. Chen, *Identification of contaminant sources in enclosed environments by inverse CFD modeling*. *Indoor Air*, 2007. 17(3): p. 167-177.
83. Zhang, T.F. and Q. Chen, *Identification of contaminant sources in enclosed spaces by a single sensor*. *Indoor Air*, 2007. 17(6): p. 439-449.

84. Liu, X. and Z.J. Zhai, *Inverse modeling methods for indoor airborne pollutant tracking: literature review and fundamentals*. *Indoor Air*, 2007. 17(6): p. 419-438.
85. Liu, X. and Z.J. Zhai, *Location identification for indoor instantaneous point contaminant source by probability-based inverse Computational Fluid Dynamics modeling*. *Indoor Air*, 2008. 18(1): p. 2-11.
86. Liu, X. and Z.J. Zhai, *Prompt tracking of indoor airborne contaminant source location with probability-based inverse multi-zone modeling*. *Building and Environment*, 2009. 44(6): p. 1135-1143.
87. Nofsinger, G. and G. Cybenko. *Distributed chemical plume process detection: MILCOM 2005 #1644*. in *Military Communications Conference, 2005. MILCOM 2005. IEEE*. 2005. p. 1076-1082 Vol. 2.
88. Rosen, G.L. *ULA Delay-and-Sum Beamforming for Plume Source Localization*. in *Signal Processing Applications for Public Security and Forensics, 2007. SAFE '07. IEEE Workshop on*. 2007. p. 1-4.
89. Underwood, D., *HVAC Controls After an Outside Contaminant Release*. *ASHRAE Journal*, 2007. 49(4): p. 36-41.
90. Chen, Y.L. and J. Wen, *Sensor system design for building indoor air protection*. *Building and Environment*, 2008. 43(7): p. 1278-1285.
91. Chen, Y.L. and J. Wen, *Comparison of sensor systems designed using multizone, zonal, and CFD data for protection of indoor environments*. *Building and Environment*, 2010. 45(4): p. 1061-1071.
92. Chen, Y.L. and J. Wen. *Application of zonal model on indoor air sensor network design*. in *Proceedings of Sensors and Smart Structures Technologies for Civil, Mechanical, and Aerospace Systems 2007*. 2007. San Diego, CA: SPIE 6529.
93. De Chiara, J. and M.J. Crosbie, eds. *Time-saver standards for building types*. 4th ed. 2001.
94. Wallace, L.A., S.J. Emmerich, and C. Howard-Reed, *Continuous measurements of air change rates in an occupied house for 1 year: The effect of temperature, wind, fans, and windows*. *Journal of Exposure Analysis and Environmental Epidemiology*, 2002. 12: p. 296-306.
95. Haghghat, F., et al., *The Influence of Office Furniture, Workstation Layouts, Diffuser Types and Location on Indoor Air Quality and Thermal Comfort Conditions at Workstations*. *Indoor Air*, 1996. 6(3): p. 188-203.
96. Sherman, M.H. and R. Chan, *Building airtightness: research and practice*. 2004, LBNL-53356.
97. Srebric, J. and Q. Chen, *A method of test to obtain diffuser data for CFD modeling of room airflow*. *ASHRAE Transactions*, 2001. 107(2).
98. Djunaedy, E. and K.W.D. Cheong, *Development of a simplified technique of modelling four-way ceiling air supply diffuser*. *Building and Environment*, 2002. 37(4): p. 393.
99. Huo, Y., et al., *Systematic approach to describe the air terminal device in CFD simulation for room air distribution analysis*. *Building and Environment*, 2000. 35(6): p. 563.
100. FLUENT, *Airpak 2.1 User's Guide*. 2002, Fluent Inc.: Lebanon, NH.
101. ASHRAE, *1995 ASHRAE Handbook HVAC Applications*. 1995, American Society of Heating, Refrigerating and Air-Conditioning Engineers.

102. Nielsen, J.R., P.V. Nielsen, and K. Svidt. *The influence of furniture on air velocity in a room - an isothermal case*. in *ROOMVENT '98: 6th International Conference on Air Distribution in Rooms*. 1998. Stockholm, Sweden. p. 281-286.
103. Persily, A.K. *Airtightness of commercial and institutional buildings: blowing holes in the myth of tight buildings*. in *Thermal Envelopes VII Conference*. 1998. Clearwater, Florida: ASHRAE.
104. Persily, A.K., A. Musser, and D. Leber, *A Collection of Homes to Represent the U.S. Housing Stock*. 2006, National Institute of Standards and Technology: Gaithersburg, MD.
105. Koestel, A., *Computing Temperatures and Velocities in Vertical Jets of Hot or Cold Air*. Heating, Piping & Air Conditioning, 1954(June): p. 110-148.
106. Mathworks, *Genetic Algorithm and Direct Search Toolbox*. 2004, The Mathworks Inc.: Natick, MA.
107. Institute, o.M., *Chemical and Biological Terrorism - Research and Development to Improve Civilian Medical Response*, I.o.M.a.M.R. Council, Editor. 1999, National Academies Press: Washington, D.C.
108. Aubin, D., et al. *Preliminary comparison of air change rates measured in Quebec City homes using SF₆*. Syracuse, New York. p. 1-4.
109. Golub, G. and W. Kahan, *Calculating the Singular Values and Pseudo-Inverse of a Matrix*. Journal of the Society for Industrial and Applied Mathematics: Series B, Numerical Analysis, 1965. 2(2): p. 205-224.
110. Murakami, S. and S. Kato, *Numerical and experimental study on room airflow - 3-D predictions using the k- ϵ turbulence model*. Building and Environment, 1989. 24(1): p. 85-97.
111. El Mankibi, M., et al., *Prediction of hybrid ventilation performance using two simulation tools*. Solar Energy, 2006. 80(8): p. 908-926.
112. ASTM, *ASTM E779-03 Standard Test Method for Determining Air Leakage Rate by Fan Pressurization*. 2003, American Society of Testing and Materials.
113. CGSB, *Determination of the Overall Envelope Airtightness of Buildings by the Fan Pressurization Method Using the Building's Air Handling Systems*. 1999, Canadian General Standards Board.
114. Jeong, J., et al., *Case studies of building envelope leakage measurement using an air-handler fan pressurisation approach*. Building Service Engineering, 2008. 29(2): p. 137-155.
115. Bahnfleth, W.P., G.K. Yuill, and B.W. Lee, *Protocol for field testing of tall buildings to determine envelope air leakage rate*. ASHRAE Transactions, 1999. 105(2): p. 27-38.
116. Roulet, C.A. and L. Vandeale, *Air flow patterns within buildings: measurement techniques*. 1991, AIVC. p. 265.
117. McWilliams, J., *Review of Airflow Measurement Techniques*. 2002, Lawrence Berkeley National Laboratory. p. 116.
118. ASTM, *ASTM E741-00 Standard Test Method for Determining Air Change in a Single Zone by Means of a Tracer Gas Dilution*. 2000, American Society for Testing and Materials.
119. Aglan, H.A., *Predictive model for CO₂ generation and decay in building envelopes*. Journal of Applied Physics, 2003. 93(2): p. 1287-90.

120. Roulet, C.A. and F. Foradini, *Simple and Cheap Air Change Rate Measurement Using CO₂ Concentration Decays*. International Journal of Ventilation, 2002. 1(1): p. 39-44.
121. Penman, J.M., *An experimental determination of ventilation rate in occupied rooms using atmospheric carbon dioxide concentration*. Building and Environment, 1980. 15(1): p. 45-47.
122. Penman, J.M. and A.A.M. Rashid, *Experimental determination of air-flow in a naturally ventilated room using metabolic carbon dioxide*. Building and Environment, 1982. 17(4): p. 253-256.
123. Smith, P.N., *Determination of ventilation rates in occupied buildings from metabolic CO₂ concentrations and production rates*. Building and Environment, 1988. 23(2): p. 95-102.
124. Yan, Y., et al. *Measuring air exchanges rates using continuous CO₂ sensors*. in *Symposium on Air Quality Measurement Methods and Technology 2007, April 30, 2007 - May 3, 2007*. 2007. San Francisco, CA, United states: Air and Waste Management Association. p. 101-108.
125. Afonso, C.F.A., E.A.B. Maldonado, and E. Skåret, *A single tracer-gas method to characterize multi-room air exchanges*. Energy and Buildings, 1986. 9(4): p. 273-280.
126. Sinden, F.W., *Multi-chamber theory of air infiltration*. Building and Environment, 1978. 13(1): p. 21-28.
127. Oksendal, B., *Stochastic differential equations*. 6th ed. 2003, New York: Springer-Verlag.
128. Carletti, M., *Numerical solution of stochastic differential problems in the biosciences*. Journal of Computational and Applied Mathematics, 2006. 185(Copyright 2006, IEE): p. 422-40.
129. Siurna, L., G.M. Bragg, and G. Reusing, *Transient solutions to a stochastic model of ventilation*. Building and Environment, 1989. 24(3): p. 265-277.
130. Kloeden, P.E. and E. Platen, *Numerical solution of stochastic differential equations*. 1992, New York: Springer-Verlag.
131. Mathworks, *Matlab 7.9.0 (R2009b)*. 2009, The Mathworks Inc.: Natick, MA.
132. Astrom, K.J. and B. Wittenmark, *Adaptive Control*. 1995, Addison-Wesley Publishing Company, Inc.: New York.
133. Li, B. and B. De Moor, *Recursive estimation based on the equality-constrained optimization for intersection origin-destination matrices*. Transportation Research Part B: Methodological, 1999. 33(3): p. 203-214.
134. Bell, M.G.H., *The estimation of origin-destination matrices by constrained generalised least squares*. Transportation Research Part B: Methodological, 1991. 25B(1): p. 13-22.
135. Persily, A.K. and E.M. Ivy, *Input Data for Multizone Airflow and IAQ Analysis*. 2001, National Institute of Standards and Technology: Gaithersburg, MD.
136. DOC. *Trends in Atmospheric Carbon Dioxide*. 2010; Available from: <http://www.esrl.noaa.gov/gmd/ccgg/trends/>.
137. ASHRAE, *ANSI/ASHRAE Standard 62-1989: Ventilation for acceptable indoor air quality*. 1990, American Society of Heating, Refrigerating and Air-Conditioning Engineers.

138. Chen, Y.L. and J. Wen. *Estimating a Building Airflow Network using CO₂ Measurements from a Distributed Sensor Network*. in *1st International High Performance Buildings Conference*. 2010. Purdue University, West Lafayette, IN: Accepted.
139. Lstiburek, J.W., K. Pressnail, and J. Timusk, *Transient Interaction of Buildings with HVAC Systems-- Updating the State of the Art*. *Journal of Building Physics*, 2000. 24(2): p. 111-131.
140. NCEMBT. *Current NCEMBT Tasks*. 1999; Available from: http://www.ncembt.org/our_work/index.html.
141. Stetzenbach, L.D., et al., *National Center for Energy Management and Building Technologies, Task 1: Measurement and Verification of Building Performance Characteristics*. 2008, National Center for Energy Management and Building Technologies: Alexandria, VA.
142. Bahnfleth, W., *Rapid semi-empirical tool for estimating air flow in facilities*. In progress, Department of Homeland Security.
143. Reddy, T.A., *Rapid Semi-Empirical Tool for Estimating Air Flow in Facilities TSWG Task T-PR-1984; Task 16: Investigation of CO₂ tracer gas-based calibration*. In progress, Department of Defense.

**Framework for the Utilization of Forward and Inverse Airflow Models in
Systematic Sensor System Design for Indoor Air**

A Thesis

Submitted to the Faculty

of

Drexel University

by

Lisa (Yung Hua) Chen Ng

in partial fulfillment of the
requirements for the degree

of

Doctor of Philosophy

August 2010

VOLUME 2 of 2 (Appendices)

APPENDIX A Preliminary sensor system studies

Sensor system design for building indoor air protection

Y. Lisa Chen, Jin Wen*

Civil, Architectural, and Environmental Engineering Department, Drexel University, Philadelphia, PA, 19104, USA

Received 10 October 2006; received in revised form 13 January 2007; accepted 16 March 2007

Abstract

Many new biological and chemical sensors have been or are continuously being developed for infrastructure and environmental protection, e.g., for protecting the quality of water and indoor and outdoor air. However, there is a lack of fundamental system-level research leading to the development of sensor networks that both maximize protection and minimize the system cost for indoor air protection. Four key parameters are usually used to evaluate sensor performance: sensor sensitivity, probability of correct detection, false positive rate, and response time. The optimal design of a sensor system is affected by the above sensor performance parameters. This paper describes a preliminary study to: (1) identify simplified simulation and optimization strategies that can be used for sensor system design; (2) examine the relationships between sensor location, sensitivity, and quantity, and (3) use both detection time and total occupant exposure as optimization objective functions for sensor system design. Common building attack scenarios, using a typical chemical and biological warfare (CBW) agent, are simulated for a small commercial building. Genetic algorithm (GA) is then applied to optimize the sensor sensitivity, location, and quantity, thus achieving the best system behavior while also reducing the total system cost. Assuming that each attack scenario has the same probability for occurrence, optimal system designs that account for the simulated possible attack scenarios are obtained.

© 2007 Elsevier Ltd. All rights reserved.

Keywords: Indoor air quality; Chemical and biological warfare (CBW) agent; Sensor system design

1. Introduction

During the last few decades, significant effort has been made to ensure that buildings become safer, more energy efficient, and more cost effective than in the past. However, the public now expects the built environment to provide even more protection, especially against natural or man-made extraordinary incidents since the tragic events of September 11th and the subsequent anthrax attacks. Buildings are especially vulnerable to chemical and biological warfare (CBW) agent contamination because the central air conditioning and ventilation system serves as a natural carrier for spreading the released agent from a single release location to the entire indoor environment and within a short period of time. CBW agents are normally highly lethal. It is reported that a person may suffer mild injury, serious injury, or even death, respectively, if as little

as 0.9, 10, or 15 mg VX gas (a nerve agent) is inhaled [1]. Moreover, airborne CBW agents are usually colorless and odorless, exhibiting surprisingly rapid dispersion rates. Therefore, early detection and warning of airborne CBW agents play important roles in protecting the occupants and in minimizing the consequences of such extraordinary incidents. However, current built environments generally lack the ability to detect hazardous chemical and biological components in the indoor air [2].

Rapid advancements in sensing technology are making a variety of sensors that are able to detect indoor pollutants available, including those that can detect chemical and biological agents. It is envisioned that a baseline detect-to-warn system will be available in the next one to 2 years, and a distributed low-cost sensor system will be available in the next 10 years [2].

In order to realize such visions, system-level analysis is needed along with developing sensing technology. Different sensing mechanisms offer different sensor characteristics. For example, structure-based detection (such as

*Corresponding author. Tel.: +12158954911; fax: +12158951363.
E-mail address: jinwen@drexel.edu (J. Wen).

immunoassays) offers the greatest potential for identification in less than 2 min with very low false alarm rates. On the other hand, nucleic acid sequence-based assays (such as polymerase chain reaction-based sensors) provide definitive confirmation of a specific agent. In general, sensors with a high detection threshold (i.e., low sensitivity) have lower false alarm rates, while sensors with a high sensitivity have higher false alarm rates. There is an opportunity to design a distributed sensor system composed of sensors with different characteristics in order to achieve the best system-level protection.

To achieve maximum protection, sensor locations also need to be carefully selected. It is not desirable to place sensors in locations where contaminant concentration is normally low at the beginning of an attack. For locations where a contaminant generally disperses rapidly, a fast response sensor is needed. Indoor air flow patterns and contaminant movement is non-linear and complicated; therefore, predicting the contaminant dispersion path is not a trivial task, especially when different attack scenarios and interior arrangement of partitions and furniture exist.

Sensor types, locations, quantities, and characteristics affect system costs, system-level detection probabilities, and system-level false positive rates. It is hypothesized that an optimized sensor system design does exist for a specific building. The focus of this project is to determine how to optimally design such a sensor system to ensure the safety of an indoor environment.

Many characteristics can be used to evaluate a CBW sensor, among which sensitivity, probability of correct detection, false positive rate, and response time are four key parameters. Moreover, these parameters are interrelated. For example, when the sensor sensitivity is increased, the false positive rate is increased as well. The Receiver Operating Characteristics curve can be used to describe the inter-relationship among the four key characteristics. A graphical technique called the spider chart (Fig. 1) includes 12 characteristics and is the recommended method to capture the overall performance of a CBW sensor [3].

It is difficult to establish a certain sensitivity threshold because an extremely large uncertainty exists when attempting to relate an inhalation exposure level to the agent concentration in the air [3]. The ambiguity in the threat also suggests that the sensors need to have different modes of operation with different sensitivities/false positive rates for different threat probabilities. It is anticipated that a well-designed CBW sensor system, which is composed of sensors having different characteristics and operating modes, can reduce the system-level false positive rate and thus increase the system-level detection confidence, leading to better system-level protection. However, very few studies exist in the open literature that examine indoor air-sensor system design issues for protecting a building against CBW agent dispersion.

Arvelo et al. [4] studied the possibility of using an enhanced multi-zone flow model, CONTAM [5], for CBW sensor location design. Only average mass flow and

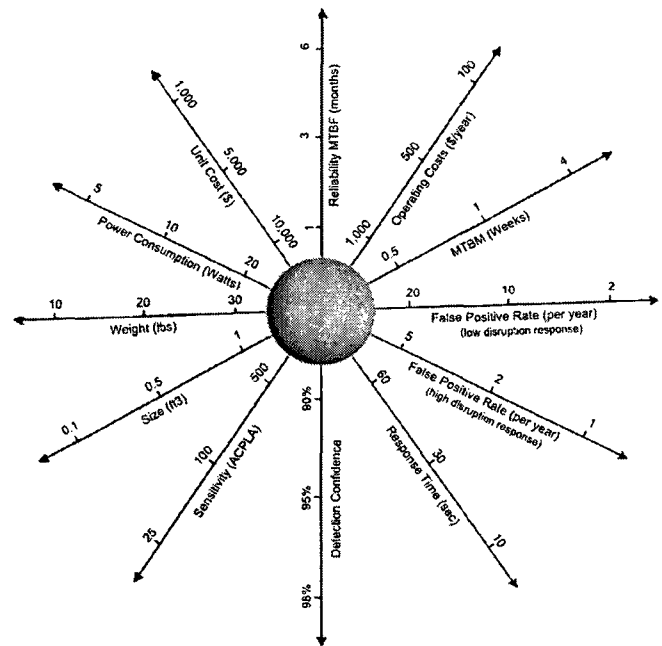


Fig. 1. Overall performance of a CBW sensor (reproduced from [3]).

contaminant concentration are provided by CONTAM for each building zone, which limits its stand-alone application in CBW sensor design. Hence, the authors adopted a computational fluid dynamics (CFD) model to provide contaminant concentration information inside a zone, which is based on the average mass flow and contaminant concentration supplied by CONTAM. The authors simulated a Sarin attack for one floor of a two-floor office building. Multiple releasing locations, each associated with an attacking probability, were generated. Genetic algorithm (GA) with a dynamic objective function, which accounts for varying releasing locations, was adopted. The optimal detection time were selected. Although no internal partitions or furniture were considered in the building zones or the hallway, the study demonstrated the effect of the opening of office doors on the contamination concentration.

Zhai et al. [1] adopted commercial CFD software to predict a gas-phase CBW agent dispersion in a section of a typical office building, which consisted of two identical offices separated by a corridor. Three agent-releasing locations were considered. The CBW agent dispersion information was then used to evaluate different sensor locations. This study demonstrated that the spreading rate of a CBW agent is very fast and will affect the occupants in 5–10 min. No methodology on how to optimally select sensor locations was provided.

The above studies demonstrate: (1) the effect that different sensor locations have on protecting the building against CBW terrorism; and (2) the feasibility of using fluid simulation software, especially CFD models, to select the indoor air sensor location(s). However, to design an indoor

air sensor system for a real building, the following challenges need to be overcome: (1) modeling a real building using CFD or other fluid simulation software is not an easy task; it requires detailed information about the building as well as a user with adequate knowledge of fluid physics and numerical techniques; (2) the computing time for a CFD model is very high, especially when the building is complex; (3) besides minimizing the time of detection, other design objectives, such as minimizing the population exposed, the air volume contaminated, and the total sensor system cost, need to be considered concurrently; (4) identifying the effect of different internal objects, such as furniture, partitions, appliances, and occupants, on the CBW agent dispersion and sensor system design is not a trivial task; (5) the impact of indoor pollutant type on sensor system design needs further investigation; (6) a methodology to combine sensors of different characteristics into a single system in order to achieve optimal system-level protection is still lacking; and (7) a methodology to evaluate a sensor system as a whole is also lacking.

The objectives of this project, which is to respond to some of the challenges above, are to: (1) identify simplified simulation and optimization strategies that can be used for sensor system design; (2) examine the relationships between sensor location, sensitivity, and quantity, and; (3) use both detection time and total occupant exposure as optimization objective functions for sensor system design.

2. Simulation model

The air flow pattern and pollutant dispersion for a typical small office building after the release of a chemical weapon agent is modeled in this project using a multi-zone model, CONTAM [5]. GA is then adopted as the optimization approach for sensor system design (introduced in Section 3.1). CONTAM is introduced first in Section 2.1. Section 2.3 introduces the office building that is modeled in this study.

2.1. Simulation software

To design an indoor air sensor system, information about indoor pollutant distribution needs to be available. Various numerical models used to simulate the indoor pollutant dispersion in a built environment have been developed and reported in the literature. Sohn et al. [6] identified and reviewed currently available simulation models for determining the dispersion of CBW agents in and around buildings and serves as the basis for this discussion. For indoor air simulation, there are three categories of simulation models: CFD, multi-zone, and zonal models.

CFD modeling has been continually validated ever since the early 1970s. However, the degree of accuracy of a CFD model depends on the correct representation of boundary conditions, the solution grid, and the level of transient characteristics. One of the biggest obstacles of using a CFD

model is its high computational overhead. It would take an estimated 8–10 work weeks to completely model and analyze the air flow within a 60,000 sq ft. four-story office building using a commercial CFD package [6].

In contrast, multi-zone models represent a building as a network of well-mixed zones (i.e., conditions such as temperature, humidity, air velocity, and pollutant concentration are uniform within one zone), which are connected by discrete flow paths such as doors, windows, wall cracks, ducts, and hallways. The model then predicts the flow parameters based on mass conservation and component interaction. The major shortcomings of multi-zone models include: (1) they cannot determine detailed air flow within a zone and (2) they cannot model bi-directional floor-to-floor flows, duct junctions, and transport delays. However, the most recent release of CONTAMW, version 2.4 [5], is able to account for transport delays using a “one-dimensional convection/diffusion” model. This model creates contaminant concentration gradients along a specified axis in a zone and through an entire duct system. Despite the shortcomings in multi-zone models, compared with CFD modeling, multi-zone models are computationally efficient and are able to consider numerous transient effects such as occupants coming and going, air handling units turning on and off, and wind directions, etc.

When physical zones are large, the well-mixed condition assumed by multi-zone models would be unrealistic and inaccurate. A modeling approach called “zonal model”, which aims at overcoming the simplicity of multi-zone model and the calculation complexity of CFD, has also been developed in the literature. In a zonal model, each physical zone is divided into a small number of sub-zones. Sub-zones can be further divided into standard flow zones and specific flow zones (including jets, plumes, heaters, and boundary layer zones) [7]. A challenge for a zonal model approach is to model the airflow pattern between zones. Many studies in the open literature have validated the use of zonal models to simulate indoor air flow and contaminant dispersion. A study by Mora et al. [7] compared zonal and CFD models to experimental measurements. The results showed that the CFD model was able to model air flow much more accurately than the zonal models employed.

As a preliminary study, the authors have chosen to utilize the multi-zone model, CONTAMW2.4 [5] developed by the National Institute of Standards and Technology, in simulating the building air flow and contaminant dispersion process. The physical rooms are further divided into smaller zones in the simulation to justify the non-ideal mixing condition, which normally exists in a physical room.

2.2. Building model

A small office building, which is similar to Iowa Energy Center Energy Resource Station [5], is selected as the prototype building for this study. A schematic floor plan is shown in Fig. 2. The building is divided into three major

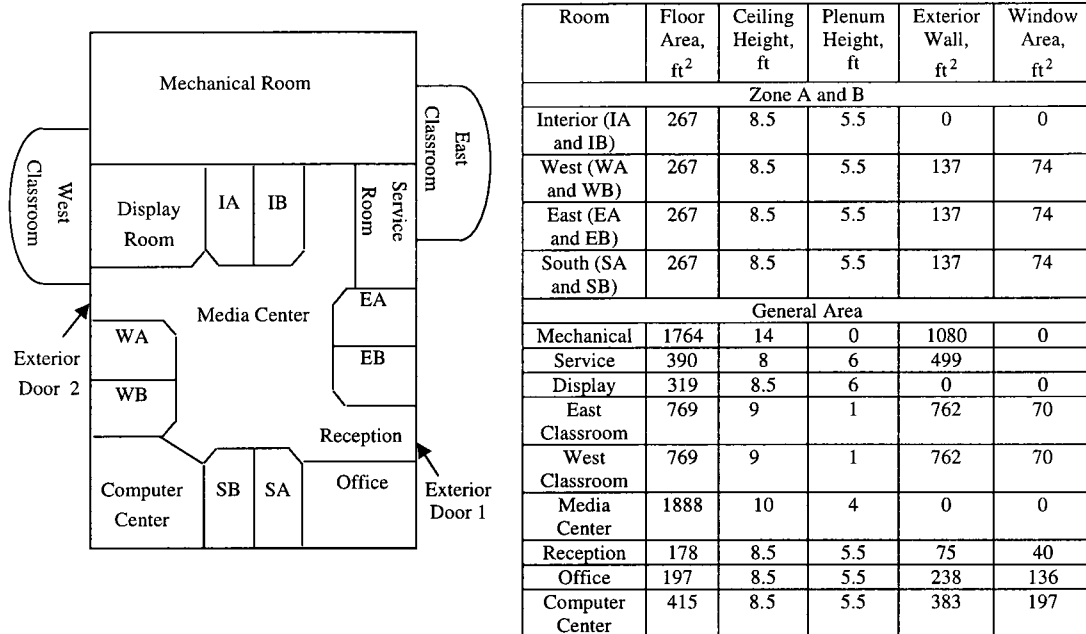


Fig. 2. Simulated building: Iowa Energy Center Energy Resource Station [12].

areas: the common area and two sets of zones, designated A and B. Each set of zones is comprised of an east, south, west, and interior zone. The common areas consist of office space, a display room, a computer center, two classrooms (not simulated), service rooms, a media center, a reception space, and a mechanical room. The actual building is served by three small air-handling units. In this study, however, only one larger air-handling unit is assumed to serve the entire building. The mechanical room is not air conditioned and is thus not included in the simulation model. Detailed dimensions of the floor area, doors, and windows are also included in Fig. 2.

If each physically enclosed space in the building described above is considered as one zone, the building can be modeled in CONTAM as shown in Fig. 3a. To consider the non-ideal mixing condition, each enclosed space is further divided into smaller sub-zones. The scope of this study is to identify simplified sensor design strategy and to examine relationships among sensor characteristics and design objectives. Therefore, the size for sub-zones is only selected to be small enough to separate spaces that enclose major flow disturbing devices, such as diffusers and return grills. For example, a test room is divided into four sub-zones: one contains a diffuser one contains a return grill, one that does not contain any major flow disturbing devices but is next to the diffuser zone, and one that does not contain any major flow disturbing devices but is next to the return zone. The average zone size in the sub-zone model is about $6.5 \text{ m}^2 \times 2.6 \text{ m}$ high. The sub-zone model (Fig. 3b) increases the total number of zones from 13 to 77. For brevity, the sub-zones created and shown in Fig. 3b will be further referred to as simply “zones”. In a follow-up study, the effect of zone sizes as well as different

air flow modeling approaches (multi-zone model, zonal model, and CFD model) on sensor system design will be further discussed.

Air flow between zones is modeled by a two-way flow model used for large openings [5]. The discharge coefficient is 0.78 and the minimum temperature difference is $0.01 \text{ }^\circ\text{C}$, provided by CONTAM [5]. The openings are modeled with dimensions of $2.7 \times 2.4 \text{ m}$. The doors are modeled using the same flow parameters, except with dimensions of $2.1 \times 0.9 \text{ m}$ for interior doors and $2.2 \times 1.5 \text{ m}$ for exterior doors. The windows are modeled using the WNI06AA-CAV model supplied by the CONTAM library (typical inoperable window for building AA [8]). Seven occupant exposure models are placed in the building model (Fig. 3a). Each is modeled as a person weighing 70 kg and inhaling at a peak rate of 12 L/min. Steady-state weather conditions ($20 \text{ }^\circ\text{C}$, 1 atm, 0 m/s wind speed) are used to simplify the simulation. The air handling unit that serves the building is the “simple air handling unit” model ([8]) with $4.7 \text{ m}^3/\text{s}$ supply air flow rate and $0.47 \text{ m}^3/\text{s}$ outdoor air flow rate. A transient air flow simulation model is chosen.

2.3. Contaminant releasing scenarios

Sarin gas, a highly toxic nerve agent of high volatility, is selected as a typical chemical weapon agent to be simulated in this study. The source release rate is simulated using the cutoff concentration model [4],

$$S = G \left(1 - \frac{C}{C_{\text{cut}}} \right), \quad (1)$$

where S is the source strength, C is the current ambient Sarin concentration inside the zone where the source is

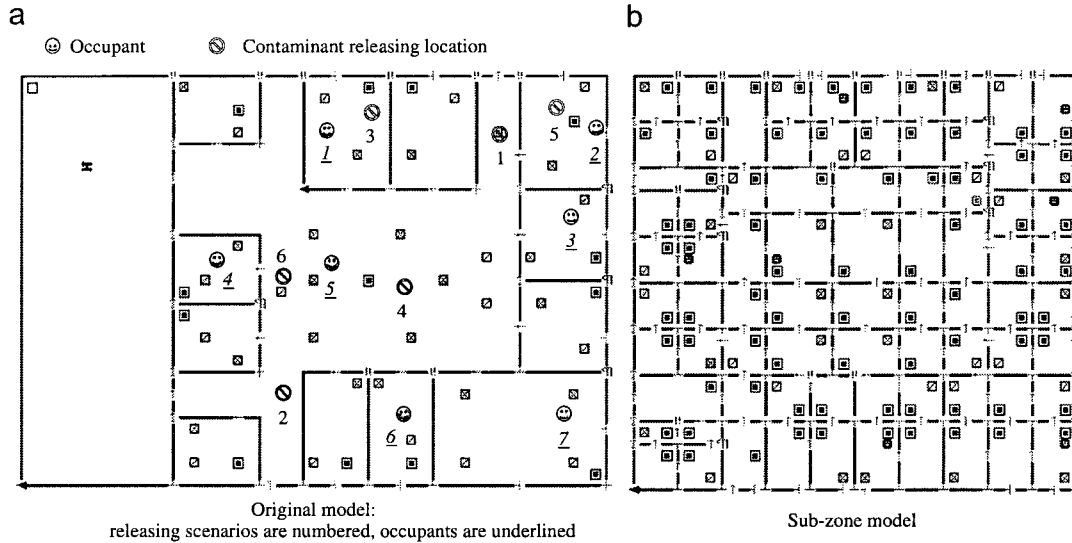


Fig. 3. Building model in CONTAM.

located, G is the generation rate coefficient (5 mg/s), and C_{cut} is the cutoff concentration (0.1 kg/kg-air). Six releasing scenarios, including release around doorways, in the open office, and in enclosed offices, are assumed and simulated in this study (Fig. 3a). Each releasing location is given the same probability for occurrence.

3. Sensor system optimization

3.1. Optimization approach

The contaminant dispersion process is a complicated non-linear process. Hence GA, a stochastic search algorithm [9], is selected as the optimization approach because of its ability to handle complicated non-linear problems. Compared with other stochastic search methods, GA has the following features [9]: (1) GA works with a coding of the parameter set, not the parameters themselves; (2) GA searches for the optimized value from a population of points (multiple points) to another population instead of from a single point to another single point; (3) GA uses the objective function information rather than the derivatives or other auxiliary knowledge; and (4) GA uses probabilistic transition rules, not deterministic rules.

Fig. 4 shows the basic process of a GA optimization. The user supplies n initial guesses for the design variables, which serves as the initial population. For each vector of n initial guesses, the objective function is calculated and compared. The vector that generates the optimal value of the objective function, whether the minimum or the maximum value depending on the definition of the problem, is called a best “parent”. A second population is generated based on the information of the objective functions corresponding to each design variable. The goal is to generate a new population so that the “features” that make one vector yield better values of the objective

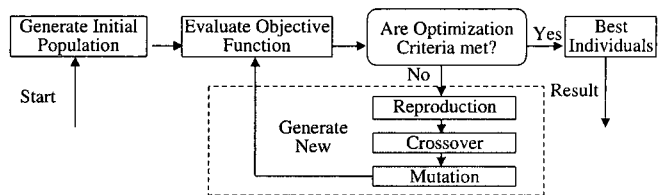


Fig. 4. GA flow chart.

function remain in the new population. Once a new population is generated, the values of the objective function are calculated and compared again. Thus, the third population is generated mainly by the best “parents” that yielded better values of the objective function in previous generations. This process is repeated until certain optimization criteria are satisfied. The terms “reproduction” and “crossover” (Fig. 4) represent processes that generate a new population from a previous population, guided by the information of the objective function for each vector. To prevent premature converging to a local optimal solution, a process called “mutation”, which generates a new vector randomly, is involved in the process.

3.2. Objective functions

Two objectives, to minimize detection time and minimize occupant exposure, are considered in this study. The detection time of one sensor is defined as the earliest time when the sub-zone contaminant concentration, where a sensor is placed, is higher than the sensor sensitivity. The detection time of the k th releasing scenario, t_{det-k} , is defined as the shortest detection time among all the distributed sensors during the k th scenario. For all six releasing scenarios, the objective function based on detection time,

J_{det} , is thus defined by

$$J_{det} = \sum_{k=1}^6 p_k \times t_{det-k}, \quad (2)$$

where p_k is the probability for the k th releasing scenario to occur. Besides detection time, total exposure for an occupant, which is also related to detection time, is another design criterion. The total exposure of all seven occupants, E_k , for the k th releasing scenario is defined as

$$E_k = \sum_{m=1}^7 \sum_{t=0}^{t_{det-k}} \text{Exp}(m, t), \quad (3)$$

where $\text{Exp}(m, t)$ is the occupant exposure for the m th occupant at time t , which is obtained by the CONTAM simulation. Thus, for all six releasing scenarios, the objective function based on total occupant exposure, J_{exp} , is defined by

$$J_{exp} = \sum_{k=1}^6 p_k \times E_k. \quad (4)$$

Cost is a constraint in this study because of the high expense of CBW sensors. The total cost of the sensor system, M , is determined by the single sensor price and total sensor quantity. Since the sensors chosen for this study have the same characteristics and thus the same unit price, the constraint, M , will be discussed based on sensor quantity alone.

4. Results and discussion

4.1. Simulation results

The air flow rate through each air flow path after the contaminant is released is basically steady during our study and is not affected when changing the contaminant releasing location. Fig. 5 shows the direction and magnitude of the simulated air flow rates for each air flow path by CONTAM under the procedure described in Section 2.2. The length of each line represents the magnitude and direction of the air flow. It is observed that the air flow rate through diffusers, returns, and exterior doors are generally larger than the air flow rates through interior doors and between zones. The latter is due to the modeling of free air movement between zones when a physical wall is not present.

The contaminant concentration for each zone varies with the contaminant releasing location. Fig. 6 shows the contaminant concentration in zones 18, 24, 28, 30, and 36 when the contaminant is released from location 1 (refer to Fig. 3 for release location and Fig. 7 for location of zones). Fig. 6a shows that the contaminant concentration in these zones peaks within 15 min and gradually reduces to zero due to the ventilation dilution effect. Both the rate of the concentration variation and the peak value of the concentration vary from zone to zone, which verifies the

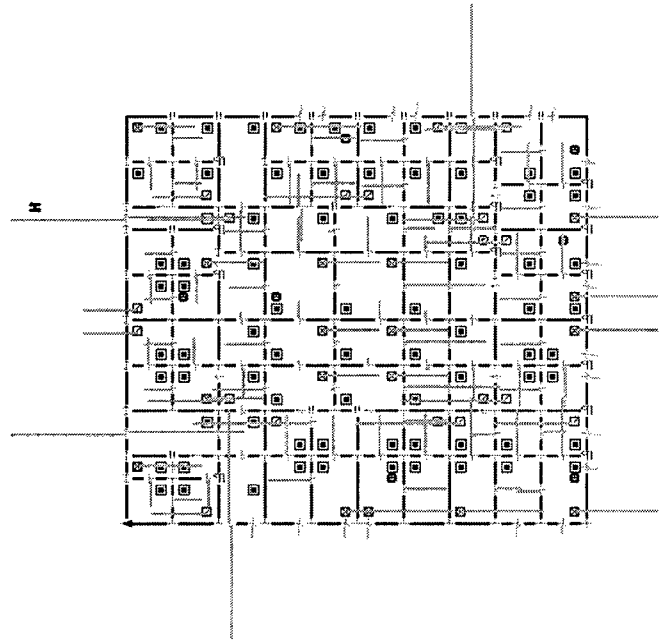


Fig. 5. Air flow rates through airflow paths.

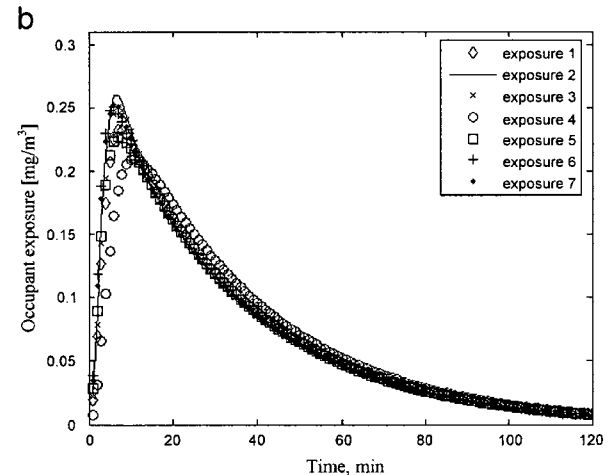
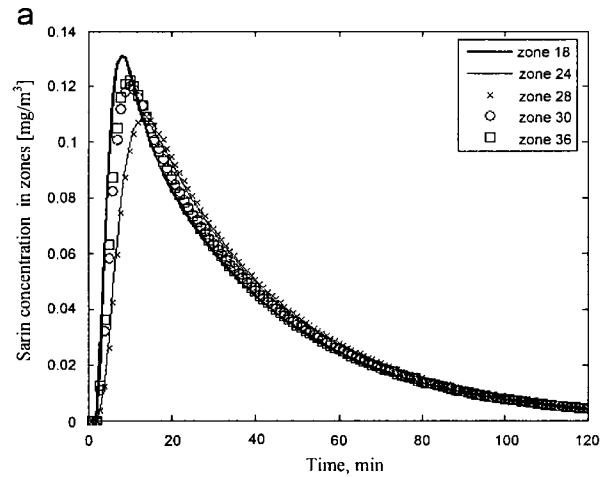


Fig. 6. Contaminant concentration and occupant exposure for releasing location 1.

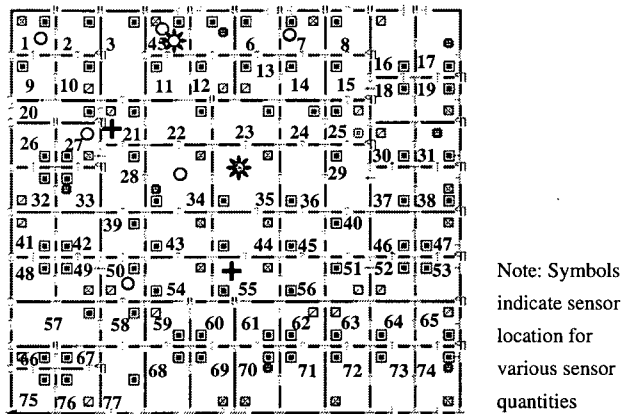


Fig. 7. Sensor location design.

assumption that the sensor(s) location will affect the system-level detection time. Fig. 6b shows the occupant exposure when the contaminant is released at location 1. Contaminant concentration and occupant exposure under the other five releasing locations exhibit behaviors similar to those in Fig. 6 and are thus not provided.

4.2. System design results

The air flow rates, contaminant concentration, and occupant exposure are simulated for the six releasing scenarios. A sensor system is designed using the Matlab GA optimization toolkit [10] after the simulation. The selection of sensor quantities and location(s) for a fixed sensitivity are discussed in Section 4.2.1. For other sensitivities, the selection of sensor quantities and location(s) are discussed in Section 4.2.2.

4.2.1. Sensitivity = 0.03 mg/m³

The first case discussed here is when the sensor sensitivity is a fixed value, such as 0.03 mg/m³ (portable sensor, \$7500 each [11]). Because there are many locations where the contaminant concentration is higher than the sensitivity after 1 min, the minimum detection time is 1 min when the sensor quantity is large enough. The sensor quantity is originally set at six because six releasing scenarios are considered. When the sensor quantity is six, many sensor location design exist that will provide a minimum detection time of 1 min for all six releasing scenarios. Table 1 summarizes some location combinations (refer to Fig. 7 for zone number). The total number of sensors can be reduced to two while still ensuring the detection time to be under 1 min (Table 1). When the total number of sensors is larger than one, using minimum detection time or minimum occupant exposure as the objective function yields similar results. When the sensor quantity is reduced to two, the sensor arrangement is unique in order to achieve a detection time of 1 min. If the sensor quantity is further reduced to one, there would be at least one releasing scenario when the minimum detection time is 2 min, no

Table 1
Sensor design for sensor with 0.03 mg/m³ sensitivity

Quantity	Detection time	Objective	Location
6	1 min	D or E	1, 4, 7, 27, 34, 50
6	1 min	D or E	8, 21, 29, 41, 62, 70
6	1 min	D or E	16, 21, 35, 39, 59, 69
2	1 min	D or E	21, 35
1	2 min	D	35
1	2 min	E	4

Note: D is detection time; E is occupant exposure.

matter which location is selected. However, at this time, using occupant exposure would yield a design that provides a minimum occupant total exposure. In order to maximize building protection, a specified detection time, such as 2 min, may be required. Therefore, in the case of only one sensor, using occupant exposure as the objective function yields a better sensor system design because it minimizes the total occupant exposure and total detection time for all six releasing scenarios.

4.2.2. Other sensitivities

When the sensitivity of the sensor is lowered, i.e., the detection threshold is higher, not only the false positive rate decreases but also the cost of the sensor decreases as well. Therefore, sensors with lower sensitivities are examined in this study in order to observe the effect of this parameter on the design of the optimal sensor system. In general, lowering the sensitivity increases the minimum number of sensors that are needed to guarantee a specified detection time. Thus, in this study where there are a total of six possible releasing scenarios, a minimum of six sensors is needed to guarantee a detection time of 1 min, when the sensor sensitivity is less than 0.03 mg/m³. The sensor location design using a total of six sensors is not unique. However, as sensor sensitivity decreases further, the possible locations where the sensors can be optimally located are also reduced until an extreme case is met when the sensor sensitivity is the same as the initial contaminant releasing strength. For this extreme case, the sensor has to be placed in the same zone as the releasing location. Hence, six would be the maximum sensor quantity for this study since six releasing scenarios are simulated.

Both sensor quantity and sensitivity affect detection time and occupant exposure. Likewise, the relationship among sensor quantity, sensitivity, and the cost of a sensor system is most likely non-linear and is thus currently not well defined. If this relationship were known, the sensor system that both maximizes protection and minimizes the system cost could be chosen.

5. Conclusion

Indoor contaminant sensor system design to protect a building from CBW attack is discussed in this study. Contaminant concentration and occupant exposure are

simulated using a multi-zone air flow model, for six contaminant releasing scenarios. GA is used to optimize the sensor system using either minimum detection time or minimum occupant exposure as the objective function. Sensor sensitivity, quantity, and location are considered when optimizing the sensor system with cost constrictions. In this study, six sensors guarantee a detection of 1 min under six releasing scenarios. However, the sensor quantity could also be lowered to two while still maintaining a detection time of 1 min, when sensor sensitivity is 0.03 mg/m^3 . For any given sensitivity, a minimum sensor quantity that achieves the same minimum detection as using more sensors does in fact exist. Lowering the sensor sensitivity increases the minimum number of sensors needed throughout the building. If the total sensor quantity chosen is less than this minimum sensor quantity, the desired detection time cannot be guaranteed because lowering the sensitivity raises the threshold at which the sensor begins to detect. It is also found that occupant exposure is a better objective function used to identify the locations that will minimize both detection time and total occupant exposure.

6. Future work

The selection of sensor quantity and location in this study were based on the air flow and contaminant dispersion results from a multi-zone model. It is desired to compare the sensor system designs when using multi-zone model, zonal model, and CFD model approaches in the future.

Design of a sensor system in this study was comprised of sensors that exhibited identical characteristics, such as type and sensor sensitivity. The possible benefit of incorporating sensors with varying characteristics into a single sensor system is another area for future research. Furthermore, the overall performance of a CBW sensor, as mentioned in Introduction, includes twelve characteristics, and all of them should be considered when embarking on sensor system design.

While the authors chose two objectives for the sensor system design, to minimize detection and occupant exposure, other objectives for other building types exist,

such as after CBW agent release, at what point is the building safe to allow occupants to re-enter. Establishing design objectives leads to future work in developing strategies to evaluate the performance of sensor systems.

References

- [1] Zhai Z, Srebric J, Chen Q. Application of CFD to predict and control chemical and biological agent dispersion in buildings. *International Journal of Ventilation* 2003;2(3):251–64.
- [2] NRCa. Sensor systems for biological agent attacks: protecting buildings and military bases. Washington, DC: National Research Council of the National Academies, National Academies Press; 2004.
- [3] Carrano J. Chemical and biological standards study. MicroSystems Technology Office, Defense Advanced Research Projects Agency, 2004. (http://www.darpa.mil/mto/publications/briefings/CBS3_final_report.pdf).
- [4] Arvelo J, Brandt A, Roger RP, Saksena A. An enhanced multizone model and its application to optimum placement of CBW sensors. *ASHRAE Transactions* 2002;108(2):818–25.
- [5] NIST. CONTAM Description. National Institute of Standards and Technology, Gaithersburg, MD, 2003. (<http://www.bfrl.nist.gov/IAQanalysis/CONTAMWdesc.htm>).
- [6] Sohn CW, Solberg A, Gonsoulin T. Analysis of numerical models for dispersion of chemical/biological agents in complex building environments. Construction Engineering Research Laboratory, ERDC/CERL TR-04-25, US Army Corps of Engineers, Washington, DC, 2004.
- [7] Mora L, Gadgil AJ, Wurtz E. Comparing zonal and CFD model predictions of isothermal indoor airflows to experimental data. *Indoor Air* 2003;13(2):77–85.
- [8] Persily AK, Ivy EM. Input data for multizone airflow and IAQ analysis. Gaithersburg, MD: National Institute of Standards and Technology, NISTIR 6585; 2001.
- [9] Goldberg DE. Genetic algorithm in search, optimization and machine learning. Reading, Massachusetts: Addison–Wesley Pub. Co.; 1989.
- [10] Mathworks A. Genetic algorithm and direct search toolbox. Natick, MA: The Mathworks Inc.; 2004.
- [11] Institute of Medicine and Medical Research Council. Chemical and biological terrorism—research and development to improve civilian medical response. Washington, DC: Institute of Medicine and Medical Research Council, National Academies Press; 1999.
- [12] Price BA, Smith TF. Description of the Iowa Energy Center Energy Resource Station: facility Update III, Technical report: ME-TFS-00-001. Department of Mechanical Engineering, The University of Iowa, Iowa City, IA. 2000.



Comparison of sensor systems designed using multizone, zonal, and CFD data for protection of indoor environments

Y. Lisa Chen*, Jin Wen

Civil, Architectural, and Environmental Engineering, Drexel University, Philadelphia, PA 19104, USA

ARTICLE INFO

Article history:

Received 3 April 2009

Received in revised form

17 October 2009

Accepted 20 October 2009

Keywords:

Indoor airflow modeling

Multizone model

Zonal model

Computational fluid dynamics (CFD)

Sensor system design

ABSTRACT

Sensors that detect chemical and biological warfare agents can offer early warning of dangerous contaminants. However, current sensor system design is mostly by intuition and experience rather than by systematic design. To develop a sensor system design methodology, the proper selection of an indoor airflow model is needed. Various indoor airflow models exist in the literature, from complex computational fluid dynamics (CFD) to simpler approaches such as multizone and zonal models. Airflow models provide the contaminant concentration data, to which an optimization method can be applied to design sensor systems. The authors utilized a subzonal modeling approach when using a multizone model and were the first to utilize a zonal model for systematic sensor system design. The objective of the study was to examine whether or not data from a simpler airflow model could be used to design sensor systems capable of performing just as well as those designed using data from more complex CFD models. Three test environments, a small office, a large hall, and an office suite were examined. Results showed that when a unique sensor system design was not needed, sensor systems designed using data from simpler airflow models could perform just as well as those designed using CFD data. Further, only for the small office did the common engineering sensor system design practice of placing a sensor at the exhaust result in sensor system performance that was equivalent to one designed using CFD data.

© 2009 Elsevier Ltd. All rights reserved.

1. Introduction

Sensors are currently used in the building environment to monitor parameters such as temperature, humidity, and contaminant levels. Recently, the public and those involved in heating, ventilating, and air conditioning (HVAC) design have begun to focus on safety issues in the building environment, for instance, the potential for terrorist attack from the release of a chemical and biological warfare (CBW) agent inside buildings. Since HVAC systems circulate air throughout buildings, they can also serve to spread released CBW agents very rapidly. Properly designed sensor systems can help to reduce the impacts of such attacks by alerting building occupants.

To design sensor systems for building environments, indoor airflow and contaminant dispersion patterns need to be known. This information can be collected experimentally, such as by tracer gas test. But these are often cumbersome and not cost effective. Therefore, it is advantageous to use airflow and contaminant dispersion simulation models in order to obtain such data. Airflow

models provide the contaminant concentration data, to which an optimization method can be applied to design sensor systems with given design objectives and constraints. Several airflow models exist in the literature, such as multizone, zonal, and computational fluid dynamics (CFD) models.

Multizone models represent any building as a network of well-mixed zones, i.e., temperature, humidity, mass flow and contaminant concentration are spatially uniform within each zone. Zones are connected by discrete flow paths, such as doors, windows, and cracks. Though easy to setup and computationally efficient compared to CFD models, multizone models cannot provide detailed airflow or contaminant dispersion information within a zone.

Zonal models subdivide larger zones into subzones in order to offer an improved representation of actual airflow and contaminant dispersion within zones. Many classes of zonal models have been reported in the literature and are summarized by the authors in Ref. [1]. The approaches are: power-law (PL), power-law with specific driven flow (PL-SDF), surface drag (SD), and surface drag with specific driven flow (SD-SDF). PL models exhibit dependence of pressure drop on the number of cells, while SD models eliminate this dependence. SDF modeling addresses the representation of jets and plumes. When compared to CFD data, zonal calculations of

* Corresponding author. Tel.: +1 215 895 2280; fax: +1 215 895 1363.
E-mail address: yhc22@glink.drexel.edu (Y.L. Chen).

airflow elements, such as recirculation and entrainment of room air into the inlet jet, are more accurate than multizone calculations [1]. Like multizone models, zonal models are easy to setup and computationally efficient.

Lastly, CFD numerically solves the partial differential equations governing fluid flow and contaminant dispersion, unlike multizone and zonal models which algebraically solve the governing equations. Thus, CFD is a computationally intense method for solving indoor airflow. Performing a CFD simulation also requires the user to have knowledge of fluid mechanics and numerical techniques. Nevertheless, countless studies have validated CFD results with experimental data. It is the most accurate of the three airflow models.

All of the above three modeling approaches have been used to design sensor systems to protect the indoor environment. However, there is no systemic study reported that examines how data from different airflow modeling approaches affects the performance of the designed sensor systems. In the literature, the average predictions of contaminant concentration of a multizone model were used to determine the location of a limited number of sensors in an office level using genetic algorithm (GA) as the optimization method [2]. In another study, detailed contaminant concentration results from a CFD model provided data for optimal sensor placement [3,4]. However, in the studies using CFD, no systematic approach to sensor placement was used. Sensor placement was based on concentration profiles at a few select locations. Further, the airflow model used in these and other sensor system design studies is often selected based on either convenience of using or accuracy of the airflow model. Thus, for an easy case setup and fast calculation, one would choose to use a multizone model to simulate the contaminant distribution needed for sensor system design. To conduct sensor system design based on more accurate contaminant distribution results, one would choose to use a CFD model.

Contaminant concentration data, for which an optimization method is applied to design sensor systems, should be gathered for different release events, covering the range of possible events. Using the simpler airflow models, multiple release events can be simulated in a relatively short amount of time. However, the accuracy of the contaminant data is not guaranteed. On the other hand, using more sophisticated CFD models, fewer events can be simulated in the same amount of time. However, the contaminant data is more accurate. Nevertheless, how the differences in accuracy of the calculated contaminant concentrations impact the performance of sensor systems designed using data from the various airflow models has not been discussed in the literature. Thus, a systematic comparison of the effects of using different airflow models on sensor system performance is the purpose of this study.

In a previous study conducted by the authors, both multizone and zonal model data were used to design sensor systems for two test spaces [5]. Small differences were found between sensor systems designed using multizone and zonal model data for a typical office. Greater differences were observed for a larger hall. The present study is a continuation of that work, which is to systematically compare the effects of using data from different airflow models on resulting sensor system design performance. The objective of this study was to determine whether or not data from a simpler airflow model could be used to design sensor systems capable of performing just as well as those designed using more accurate CFD data for various indoor environments.

2. Study approach

In this study, airflow and contaminant dispersion were simulated for three test environments: a small office, a large hall, and an

office suite. The airflow models used were the multizone model COMIS [6], the zonal model COWZ [7], and the CFD model Airpak [8]. A subzonal approach was taken when using the multizone and zonal models, meaning each physical zone was first subdivided into subzones. The relationship between flow and pressure of adjacent non-physical subzones was assigned a power-law relation with a flow coefficient of $0.83 \text{ m s}^{-1} \text{ Pa}^{-n}$ and exponent, n , of 0.5 [9]. Pressure differences between horizontal and vertical interfaces were distinguished by different relationships [10]. When using CFD, grid and time step sensitivity analyses were completed in order to determine the optimal mesh size and time step for each test environment. Mesh size analyses were not performed for the multizone and zonal models since the models have been shown to be relatively unaffected by changes in subzone size for test spaces similar to the ones in this study [9]. Time step sensitivity analyses were performed for the multizone and zonal models. Airflow was modeled in CFD using the indoor zero equation turbulence model since it has been shown to be appropriate for indoor airflow, for various indoor ventilation types, and is also computationally less intense than other turbulence models [11]. All simulations were performed on a 32-bit Dell Dimension desktop with Intel Duo-Core Processor and 3GB RAM.

A gaseous CBW agent was released at a constant rate from various locations in each test environment. Release locations were selected based on possible targets for effective dispersion or ease of accessibility. Sensor systems were then designed using the contaminant dispersion data calculated by each airflow model for each test environment. A "sensor system design" in this study refers to the arrangement of the sensors (i.e., their locations) given the design objective. The total number of sensors was used as a constraint. Sensor systems were designed to meet either one of two design objectives: minimize detection time or minimize occupant exposure. Genetic algorithm (GA) was the optimization approach used to design the sensor systems.

Once a sensor system is designed, data from CFD models are used as synthetic experimental data to evaluate the detection times and occupant exposures (more generally referred to as "objective function values") associated with each sensor system design. These objective function values are given different descriptive names in this study. The terminologies used are: multizone-optimal, zonal-optimal, CFD-optimal, and CFD-benchmarked objective function values. They differ in the airflow model data used to design the sensor system and the airflow model data used to calculate the objective function values associated with that sensor system. Fig. 1 demonstrates the connection between each name and the associated airflow models.

When CFD data served as synthetic experimental data, volume-averaged CFD concentration data was calculated based on the subzone sizes used for the multizone and zonal models. Comparing CFD-benchmarked values of detection time and occupant exposure to CFD-optimal ones shows whether or not data from simpler airflow models could be used to design sensor systems capable of performing just as well as those designed using more accurate CFD data. Thus, the CFD-benchmarked values represent the potential performance of the simpler airflow models, whereas the multizone- and zonal-optimal values respectively represent the current capabilities of the multizone and zonal models.

3. Test environments

Three test environments were modeled in this study: a small office, a large hall, and office suite. The dimensions, number of subzones, and boundary conditions used to simulate each of the test environments are summarized in Fig. 2 and Table 1. In Table 1, the space names under "Office suite" are followed by brackets. Inside the brackets is the designation used to identify that space

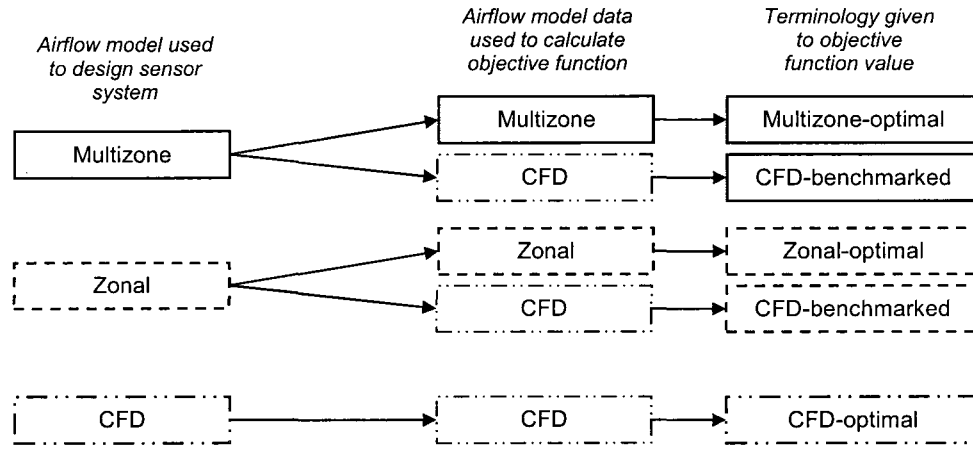


Fig. 1. Connection between terminologies in study and associated airflow models.

when discussing the sensor systems later in the study. To use the multizone and zonal models, each zone was subdivided into subzones. Subdivision of the small office and large hall are shown in Fig. 3. Subdivision of the individual spaces in the office suite was similar to that for the small office in Fig. 3 and is not shown for brevity. The division of the subzones was designed to capture each inlet jet by following general guidelines provided in Ref. [10]. A study on a 2-D space using the subzonal approach with two subzone sizes, 0.8×2.0 m and 0.4×1.0 m, was performed [9]. The study reported insignificant differences in the calculated airflow using these two subzone sizes. Since the subzones in this study were similar to the sizes in Ref. [9], no grid sensitivity analyses were performed. Airflow simulation results would not have changed significantly with the use of subzones of a slightly different size. The doors simulated were 0.9×2.1 m high. For all of the test environments, it was assumed that the pressure and temperature inside the space was equal to that of the outside. Therefore, infiltration from the outdoor environment was not modeled. For the office suite, cracks were modeled between each space. Each crack was modeled with an air mass flow coefficient of 0.001 kg/s@1 Pa and exponent of 0.65 [6]. Table 1 lists the locations of the cracks in the office suite. Inlet jets were modeled as isothermal and delivering 400 cfm through a 0.7 m-diameter diffuser. In the small office

and large hall, none of the return air was recirculated back into the test space. For the office suite, 80% of the return air was mixed with 20% outdoor air before being recirculated back into each space.

Steady state airflow simulations were performed in CFD for all three test environments in order to perform mesh size analyses (Section 4). Time step analyses were then performed using the optimal mesh size. For CFD, a total simulation period of 4 min was used. Transient airflow and contaminant distribution simulations were performed for all three test environments using the multizone and zonal models. For the multizone and zonal model, a time step of 1 min was used for a total simulation period of 2 h. Time steps of 1 and 30 s were also tested. When different time steps were used, the multizone- and zonal-optimal objective function values and sensor locations may or may not change. However, the general conclusions reported later were not affected. The difference in simulation periods for the multizone, zonal, and CFD models does not affect the results of this study. As long as the simulation period is longer than the contaminant release, the conclusions from this study will not be affected.

The air change rate (ACH) is defined as the air changes per hour, which is calculated by dividing volumetric flow rate supplied to a space (m^3/h) by the volume of that space (m^3). For each of the test environments, the airflow rate through a diffuser was kept constant

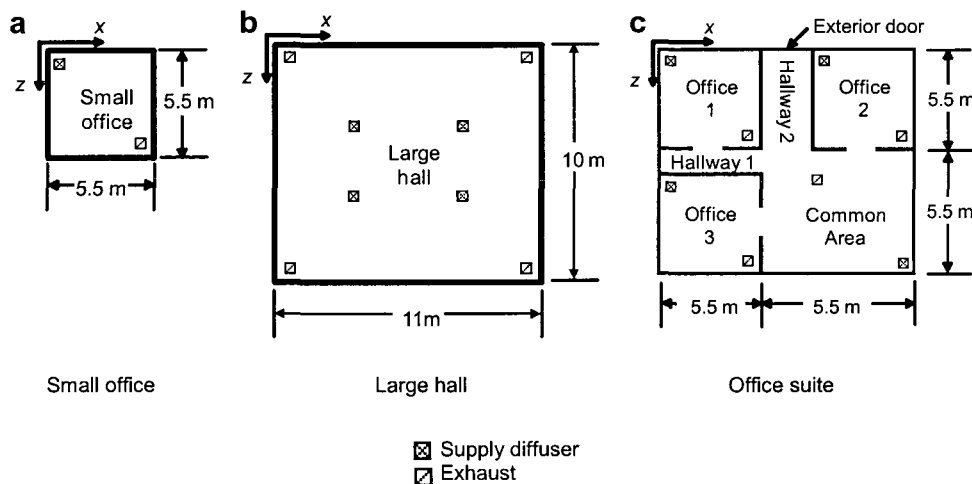


Fig. 2. Test environments.

Table 1
Boundary conditions of test environments.

Test environment	Dimensions (L × W × H), m	Subzones	Doors	Crack location ^a	No of inlets	No of exhausts
Small office	5.5 × 5.5 × 2.6	5 × 4 × 4	0	N/A	1	1
Large hall	11 × 10 × 3.6	9 × 9 × 6	0	N/A	4	4
Office suite						
Office 1 [1]	5.5 × 5.5 × 2.6	5 × 4 × 4	1	[H2]	1	1
Office 2 [2]	5.5 × 4.5 × 2.6	4 × 4 × 4	1	[H2]	1	1
Office 3 [3]	5.5 × 4.5 × 2.6	5 × 4 × 4	1	[H1]	1	1
Common Area [C]	5.5 × 5.5 × 2.6	5 × 5 × 4	0	N/A	1	1
Hallway 1 [H1]	5.5 × 1.0 × 2.6	5 × 1 × 4	0	[3]	0	0
Hallway 2 [H2]	1.0 × 5.5 × 2.6	1 × 4 × 4	1	[1], [2]	0	0

^a Cracks were modeled only for the office suite. The crack connects the space under column "Test space" and the space that is in brackets listed in this column. For instance, a crack connects Office 1, designated [1], and Hallway 2 [H2]. Thus, a crack also connects Hallway 2 to Office 1 as specified in the last row.

at 400 cfm. The Reynolds number for each test environment was maintained at approximately 24,000 in order that turbulent effects in the CFD model would be similar. The Reynolds number was calculated using the velocity through the diffuser and its diameter as the characteristic length. The small office and office suite had air change rates of 8.7 ACH, while the large hall had an air change rate of 6.9 ACH. In the literature on indoor sensor system design, ACH values of 4 [3] and 30 [2] were found. According to Ref. [12], typical ACH for commercial spaces is between 4 and 10. Thus, the ACH simulated for this study were within the general guidelines for commercial spaces and also reasonable compared to the values found in the literature. Further, the time step used was several times smaller than the time constant (1/ACH) for each space.

3.1. Contaminant release

The release of a CBW agent was modeled as a constant source (5 mg/s) that was present from $t=0$ to $t=1.0$ min. Four release locations were considered in the small office, five for the large hall, and six for the office suite (Fig. 4). For the small office, release location 1 was under the supply diffuser. Release location 2 was near the center of the room. Release location 3 was chosen near an occupant. Release location 4 was chosen along the wall where a door may be located.

For the large hall, release location 1 was under a supply diffuser. Release locations 2 and 3 were near the wall, close to the

exhausts. Release location 4 was near an inlet. Release location 5 was in the center of the large hall. In the office, one contaminant was released in Offices 1, 2, and 3, respectively. Two contaminant release locations were in the Common Area. All contaminants were released on the floor. The release locations were designed for effective dispersion or ease of accessibility. They were also designed to test the simpler models based on differences in the airflow calculated by the three models. Large differences in airflow could lead to large differences in contaminant dispersion. Thus, by specifying contaminant releases in the subzones where the largest differences between the calculated airflow of the simpler airflow model and CFD model exist, it can be shown whether or not even the largest differences between the airflow models affect sensor system design.

In this study, subzone location names are given by their respective x, z, and y cell index. For instance, in Fig. 4a, the first releasing location is in subzone 111. The second releasing location is in subzone 321, and so on. In CFD, the contaminants are modeled as volumetric sources of size $0.25 \times 0.25 \times 0.25$ m.

4. CFD grid and time step sensitivity analyses

The grid size used to model typical indoor spaces found in the literature varies widely. Therefore, an optimal mesh size and time step must be determined on a case by case basis. Structured meshes were used in this study. For the small office, results from using several mesh sizes and time steps were considered. The meshes used were: $10 \times 10 \times 10$ cm uniform, $8 \times 8 \times 8$ cm uniform, $6 \times 6 \times 6$ cm uniform, and each uniform mesh with three refinements (R1, R2, and R3). The "refined meshes" included different levels of clustering around the inlet, outlet, and contaminant sources. For each refinement, the initial grid perpendicular to the surface(s) of the inlet, outlet, and contaminants was 3.0 cm. For the R1 meshes, the grid sizes continued to increase toward the center of the test space at a ratio of 1.2. For the R2 meshes, the ratio decreased to 1.05, and for the R3 meshes, the ratio decreased to 1.03.

For the large hall, results from the following meshes were considered: $12 \times 12 \times 12$ cm uniform, $10 \times 10 \times 10$ cm uniform, $8 \times 8 \times 8$ cm uniform, and each uniform mesh with three refinements. A $6 \times 6 \times 6$ cm uniform mesh and its refinements were not considered for simulation of the large hall because the number of grids (>3 million) would have exceeded the 32-bit capacity of the software and computer used for performing the simulations. For the office suite, results from the following meshes were considered:

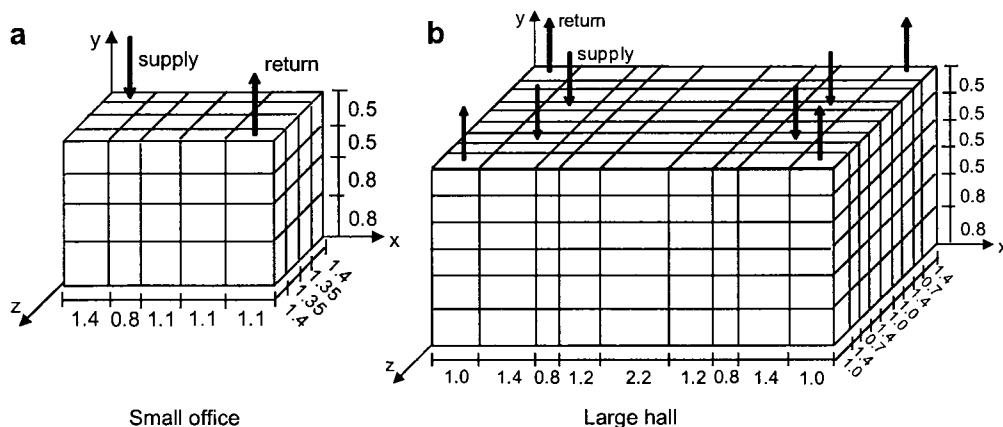


Fig. 3. Subdivision of test environments into subzones for multizone and zonal modeling.

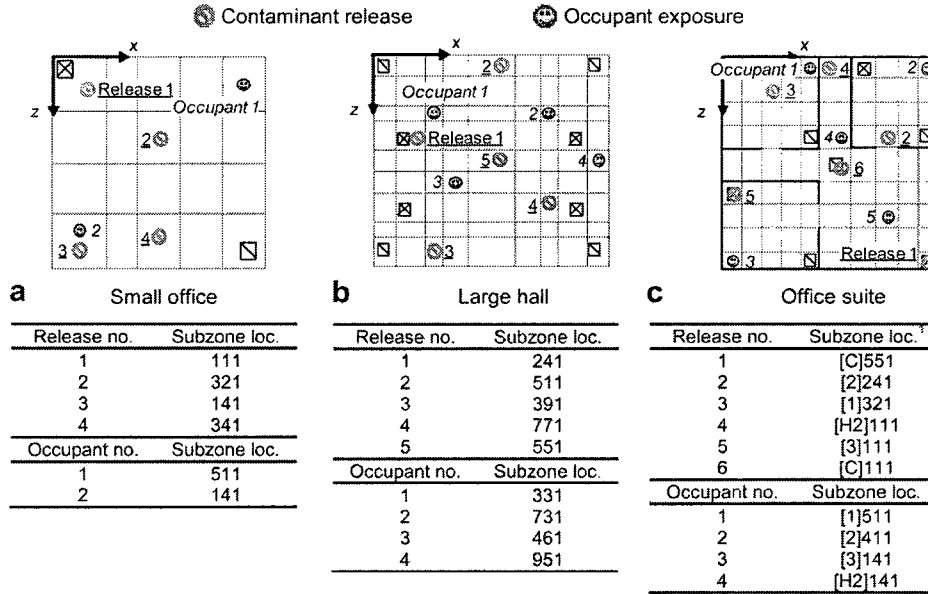


Fig. 4. Locations of contaminant releases (underlined) and occupant exposures (italicized) for three test environments. Subdivisions shown (not to scale). Note 1: see Table 1 and text for naming convention.

10 × 10 × 10 cm uniform, 8 × 8 × 8 cm uniform, and 6 × 6 × 6 cm uniform, and each uniform mesh with three refinements.

The CFD solutions in this study were considered converged when the sum of the solution residuals (for both flow and contaminant species) between iteration, *i*, and the one before it, *i* – 1, is 1e-03. For transient solutions, each time step was considered converged when the sum of the solution residuals was 1e-03.

The number of nodes in the meshes considered varied from 0.085 to 1.1 million for the small office, 0.535 to 1.9 million for the large hall, and 0.935 to 1.9 million for the office suite. The time steps (Δt) used were 0.25, 0.125, and 0.01 s.

Resulting velocity profiles from the various meshes were compared for several locations around the room. It was found that velocity profiles under the inlet were more affected by the change in grid size than locations farther from the inlet. This result was also found for the airflow in the large hall and office suite. Thus, only velocity profiles under inlets were used in the selection of an optimal mesh for each test environment. When the largest difference between the velocity profiles was less than 5%, the result was

considered grid and time step independent. It was found that the 8 cm (R2) mesh was an optimal mesh for the simulation of the small office with $\Delta t = 0.125$ s. It was found that the 10 cm (R2) mesh was an optimal mesh for the simulation of the large hall with $\Delta t = 0.125$ s. This same mesh was found optimal for the simulation of the office suite as well, with $\Delta t = 0.25$ s.

5. Simulation results

Steady state airflow was first computed in each test environment before the contaminant was released. It was assumed that the contaminant release would not affect the airflow. Fig. 5 shows the airflow results through the diffuser in the small office. The striking difference between the multizone and the zonal model results is the representation of the inlet jet. The influence of the supply air is more pronounced in the zonal model result and agrees more with the CFD result. The reason for this difference is that multizone models only account for the pressure drop at the inlet, using a power-law equation. Thus, the incoming inlet jet loses its

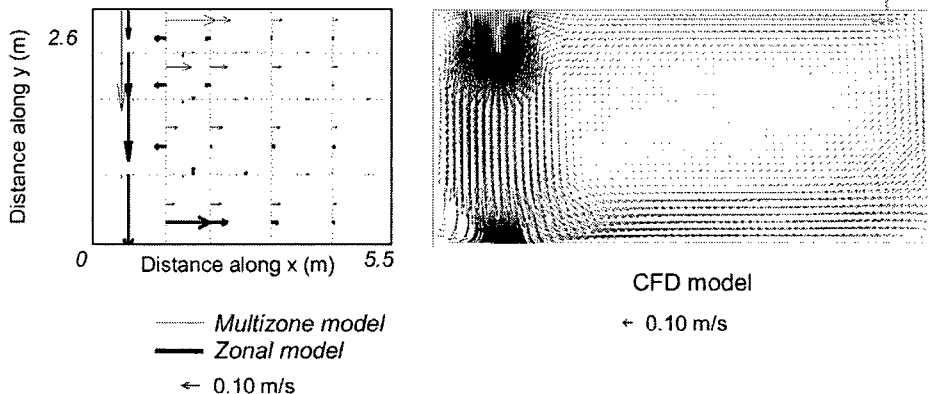


Fig. 5. Resulting airflow patterns from different airflow models through the supply diffuser in the small office (not to scale).

momentum upon entering the space. On the other hand, zonal models explicitly calculate the momentum of the inlet jet, along its axis. It is an empirical equation, which is a function of inlet area, inlet air speed, and distance from the inlet. Furthermore, the recirculation pattern predicted by the zonal model more resembles that predicted by the CFD model.

Elsewhere in the small office, the airflow patterns calculated by the zonal model also matched more closely with the CFD results than the multizone model results. Similar to the airflow results, the contaminant dispersion calculated by the zonal model matched more closely with that of the CFD results than the multizone model results. These trends were also observed in the large hall and office suite. Airflow and contaminant dispersion results for the large hall and office suite are not shown for brevity.

Intuition indicates that the differences in airflow and contaminant distribution calculated by the three airflow models will affect the performance of sensor systems designed using data from the respective airflow models. However, a sensor detects the presence of a contaminant once the concentration at a sensor is above the sensor threshold. The time at which detection occurs is not affected by the actual value of the concentration, as long as the value is above the sensor threshold. Therefore, it is possible that the differences in accuracy of the calculated contaminant concentrations will not affect the performance of sensor systems designed using data from the various airflow models.

6. Sensor system design results

Sensor systems were optimally designed using the Matlab GA optimization toolkit [13] based on the contaminant data calculated by the various airflow models. Either of two objective functions was applied to GA: (1) minimize detection time or (2) minimize occupant exposure. The objective function based on detection time, J_{det} , is defined as [14]:

$$J_{det} = \sum_{k=1}^N p_k \times t_{det-k} \quad (1)$$

where p_k is the probability for the k th release location to occur, t_{det-k} is the detection time for scenario k , and N is the number of release locations. t_{det-k} for a particular release location k given a multiple-sensor system is the minimum detection time of all of the sensors. For example, for a 2-sensor system, the detection time for four release locations may be (1) for sensor one: 1.0, 2.0, 1.5, and 1.0; and (2) for sensor two: 2.0, 1.0, 1.0, and 2.0. Thus, the detection time for each release location, t_{det-k} , given this 2-sensor system would be 1.0, 1.0, 1.0, and 1.0. In this study, p_k is $1/N$ for all release locations. Therefore the objective function value, J_{det} , is essentially the average detection time over all release locations, i.e., $\frac{1}{4}(1.0 + 1.0 + 1.0 + 1.0) = 1.0$ min in the above example. The detection time for each release location is the time when the measured contaminant concentration reaches the sensor threshold at a sensor location. The sensor threshold was a fixed value, 0.03 mg/m^3 [15], for all sensor system designs. Total occupant exposure, E_k , for the k th releasing location is defined as [14]:

$$E_k = \sum_{m=1}^S \sum_{t=0}^{t_{det-k}} \text{Exp}(m, t) \quad (2)$$

where $\text{Exp}(m, t)$ is the occupant exposure for the m th occupant at time t and S is the number of occupants. For each occupant, the exposure is the total inhaled concentration up to the time when the sensor alarms, i.e., when the contaminant concentration measured reaches the sensor threshold at the sensor location,

$$E_k = \sum_{m=1}^S \sum_{t=0}^{t_{det-k}} B \cdot C(m, t) \quad (3)$$

where B is the inhalation rate, which was assumed to be constant for all occupants and all times, and $C(m, t)$ the local concentration at each occupant location. Thus, for all N releasing locations, the objective function based on total occupant exposure, J_{exp} , is defined as [14]:

$$J_{exp} = \sum_{k=1}^N p_k \times E_k \quad (4)$$

Occupant exposures were evaluated at different locations in each test space (Fig. 4). In the small office, exposures were evaluated at opposite corners of the space. In the large hall, four exposures were evenly distributed throughout the space. Finally, in the office suite, one occupant exposure was evaluated in each of the three offices, Hallway 2, and the Common Area. All occupant exposures were evaluated at the breathing level.

The candidate sensor locations for which the contaminant concentration did not reach the sensor sensitivity within the simulation time period were penalized with a value of 1000 for both detection time and occupant exposure. A penalty of 1000 was used since it is at least an order of magnitude greater than the time for which concentration data is available. If the penalty value were set to be a value other than 1000, some reported objective function values would change (those with a value larger than 100). However, as long as the penalty value is greater than the time for which concentration data is available, the results of this study would not change.

Previous work by the authors showed that when the sensor quantity is equal to the number of releasing locations, numerous sensor systems exist [14]. In other words, no unique sensor system would exist. Therefore, this study evaluated the performance of sensor systems with sensor quantities less than the number of releasing locations.

Tables 2–7 summarize the sensor systems designed using multizone and zonal model data for each test space. The concepts of multizone-optimal, zonal-optimal, CFD-optimal, and CFD-benchmarked objective function values were introduced in Section 2. The “Objective function” column in these tables refers to the design objective of the sensor systems designed using contaminant dispersion data simulated either by multizone or zonal models. Since minimizing detection time did not always guarantee that occupant exposure was also minimized and vice versa, a “complementary” objective function value was defined (denoted in parenthesis). They refer to the occupant exposure when “ D ” was the objective function used to design the sensor system or detection time when “ E ” was the objective function value used.

The column “Locations using CFD data” are the sensor locations designed using CFD data alone (Tables 4–7). Some of these locations are also shown in Fig. 6. The last column indicates whether or not the CFD-benchmarked objective function value for each sensor system was equivalent to the CFD-optimal value for the same number of sensors. A “Y” indicates that the two values were equivalent, and thus the sensor system designed using data from the simpler airflow model could perform just as well as one designed using more accurate CFD data. A “Y” also indicates that the sensor locations designed using either multizone or zonal model data were the same as those designed using CFD data.

If there is one and only one sensor system that gives the minimum objective function value, that sensor system is given the description “unique”. They are marked with an “*” in Tables 2, 6 and 7. If there are multiple-sensor systems that give the same minimum

Table 2
Sensor design for small office using multizone model data.

Sensor sys. design	Sens. qty	Obj. func.	Locations using multizone data	Objective function value			Col. [6] equiv. to [7]?
				Multizone-optimal	CFD-benchmarked	CFD-optimal	
[1]	[2]	[3]	[4]	[5]	[6]	[7]	[8]
1	2	<i>D</i>	211,342	1.0	1.0	1.0	Y
		<i>E</i>		6.18e-5	1.34e-3	1.34e-3	Y
2	1	<i>D</i>	341*	1.0	1.0	1.0	Y
		<i>E</i>		6.18e-5	1.34e-3	1.34e-3	Y
Eng	1	<i>D</i>	544	1.75	1.0	1.0	Y
		<i>E</i>		1.10e-4	1.34e-3	1.34e-3	Y

Note (applies to Tables 2–7): “*D*” indicates a detection time objective function and is in units of minutes. “*E*” indicates an occupant exposure objective function and is in units of kg/kg. An “*” indicates a unique sensor system. “Eng” indicates a common engineering design practice.

objective function value, only one of the possible sensor systems is listed in Tables 2–7. The one listed was chosen based on similarity to the sensor systems designed using data from the other airflow models, thus allowing for a clearer comparison. In general, some 1-sensor systems were found to be unique in this study, while multiple-sensor systems were found to be non-unique.

6.1. Results for small office

Tables 2 and 3 summarize the sensor systems designed using the multizone and zonal model data, respectively, for the small office. Sensor sys. designs 1–2 were designed in this study during the optimization process. Sensor sys. “Eng” is one sensor placed at the exhaust, which is a common engineering design practice [16]. Because the sensor systems that were designed to minimize detection time also minimized occupant exposure, only one sensor system is listed for each sensor quantity. As indicated in Tables 2 and 3, even as the total number of sensors decreased, the multizone-, zonal-, and CFD-optimal detection times and occupant exposures remained the same value. The CFD-benchmarked objective function values were equivalent to the CFD-optimal values for all sensor systems, whether designed using multizone or zonal model data. Thus, it could be concluded that a sensor system designed using data from a simpler airflow model could perform just as well as one designed using more accurate CFD data for this small office.

Since neither the multizone-, zonal-, nor CFD-optimal detection times and occupant exposures changed when the number of sensors was reduced from two to one, it could also be concluded that the optimal number of sensors for the small office is one. Using both multizone and zonal model data, this location was near the exhaust, but not directly under the exhaust (subzone 341). The location for a 1-sensor system designed using CFD data was also subzone 341 (Tables 2 and 3).

Common engineering design practice is to place a single sensor under the exhaust since most of the air inside a room will return to

the exhaust (Sensor sys. Eng). Tables 2 and 3 indicate that using multizone and zonal model data, respectively, the objective function values calculated at this location were greater than the multizone- and zonal-optimal values for a 1-sensor system. Nevertheless, the objective function value calculated at this location using CFD data is equivalent to the CFD-optimal value for a 1-sensor system. Thus, using CFD data for sensor system design shows that the common engineering design practice of placing a sensor at the exhaust for a small office is optimal.

6.2. Results for large hall

Procedures for determining sensor systems for the large hall were similar to those used for the small office. Tables 4 and 5 summarize the sensor systems designed using the multizone and zonal model data, respectively, for the large hall. As the number of sensors decreased, the multizone-, zonal- and CFD-optimal detection times and occupant exposures increased. However, for the 1-sensor systems, the multizone- and zonal-optimal objective function values were much higher than the respective values for the 2-, 3-, and 4-sensor systems. This was due to the penalty of a value of 1000 for candidate sensor locations where contaminant concentrations did not reach the sensor threshold during at least one of the contaminant releases. As discussed earlier, as long as the penalty value is greater than the time for which concentration data is available, the results of this study would not change.

Fig. 6a shows that for the 2- and 3-sensor systems designed using either multizone (black-filled box) or zonal model data (gray-filled box), the sensor locations were close to the locations designed using CFD data (hashed box). Nevertheless, the CFD-benchmarked values were not equivalent to the CFD-optimal values for any of the sensor systems listed, except the 4-sensor systems, whether designed using multizone or zonal model data. As the number of sensors was reduced, data from the simpler airflow models was less appropriate for sensor system design in the case of the large hall. The inherent differences in the airflow models, and thus

Table 3
Sensor design for small office using zonal model data.

Sensor sys. design	Sens. qty	Obj. func.	Locations using multizone data	Objective function value			Col. [6] equiv. to [7]?
				Multizone-optimal	CFD-benchmarked	CFD-optimal	
[1]	[2]	[3]	[4]	[5]	[6]	[7]	[8]
1	2	<i>D</i>	443,523	1.0	1.0	1.0	Y
		<i>E</i>		5.65e-6	1.34e-3	1.34e-3	Y
2	1	<i>D</i>	341	1.0	1.0	1.0	Y
		<i>E</i>		5.65e-5	1.34e-3	1.34e-3	Y
Eng	1	<i>D</i>	544	1.5	1.0	1.0	Y
		<i>E</i>		9.15e-5	1.34e-3	1.34e-3	Y

Table 4
Sensor design for large hall using multizone model data.

Sensor sys. design	Sens. qty	Obj. func.	Locations using zonal data	Objective function value (complementary obj. func. value)			Locations using CFD data	Col. [6] equiv. to [7]?
				Multizone-optimal	CFD-benchmarked	CFD-optimal		
[1]	[2]	[3]	[4]	[5]	[6]	[7]	[8]	[9]
1	4	D	211,394,411,571	1.4 (5.30e-6)	1.0	1.0	211,394,411,571	Y
2	4	E	222,481,554,571	5.30e-6 (2.2)	1.08e-4	1.08e-4	222,481,554,571	Y
3	3	D	211,392,571	1.6 (5.30e-6)	1.2	1.0	386,422,662	N (+0.2)
4	3	E	121,471,541	4.04e-6 (2.8)	1.11e-4	1.08e-4		N (+3e-6)
5	2	D	211,481	2.2 (8.12e-6)	1.6	1.0	222,592	N (+0.6)
6	2	E	211,471	5.41e-6 (2.4)	2.00e-4	1.08e-4		N (+9e-5)
7	1	D	471	200	1.9	1.4	552	N (+0.5)
		E		200	2.30e-4	1.09e-4		N (+1e-4)
Eng-1	4	D	116,916,196,996	8.0	1.6	1.0	211,394,411,571	N (+0.6)
		E		7.29e-5	1.98e-4	1.08e-4		N (+9e-5)
Eng-2	1	D	551	400	1.6	1.4	552	N (+0.2)
		E		400	1.66e-4	1.09e-4		N (+6e-5)
Eng-3	1	D	556	1000	1.8	1.4		N (+0.4)
		E		1000	1.97e-4	1.09e-4		N (+9e-5)

contaminant transport and detection time, could be compensated for when the number of sensors was relatively large. More sensors increased the likelihood that at least one of the sensors in a system designed using data from a simpler airflow model would be able to detect each contaminant release with the same detection time as a sensor system designed using CFD data. The reduction in the number of sensors placed more weight on each sensor location in determining the detection time of the entire sensor system. Differences in contaminant transport between the models would be amplified with the reduction of sensors. Thus, it could be concluded that a sensor system designed for the large hall using data from a simpler airflow model could perform just as well as one designed using more accurate CFD data when the total number of sensors exceeded a minimum value, i.e., 3 when using either multizone or zonal model data.

When multizone model data was used to design sensor systems, one notices that the same occupant exposure could be expected from different detection times. Sensor sys.-1 in Table 4 was designed to minimize detection time. The minimum detection time was 1.4 min for a 4-sensor system. Sensor sys.-2 was designed to minimize occupant exposure. Its detection time was 2.2 min for a 4-sensor system. Nevertheless, both the occupant exposures for Sensor sys.-1 and 2 were equal (5.30e-6 kg/kg). This can be explained by the definition of occupant exposure (Eq. (3)), which depends on both the local inhaled concentration of each occupant

and the detection time of each sensor in a sensor system. In many regions of the large hall, the airflow patterns calculated by the multizone model were in the opposite direction of those calculated by the zonal and CFD models. For instance, through release location 2, the multizone model calculated more airflow moving along the walls ($x = 0$, $x = 11$ m) than up the middle ($x = 5.5$ m) (Fig. 7). This resulted in much of the contaminant leaving through two of the exhausts, which were located at $x = 1.7$ and $x = 9.3$ m. The contaminant was not distributed to the rest of the large hall and to the occupants. Thus, no matter the detection time of a sensor, the local concentration at each occupant was always 0 mg/m³, resulting in occupant exposure always being 0 kg/kg for release 2. Airflow results and subsequent occupant exposure values for release 3 were similar to those for release 2 and are not shown for brevity. Minimizing occupant exposure could not guarantee that detection time was also minimized since occupant exposure is evaluated at each occupant and the detection time is evaluated at the sensors.

In contrast, the zonal and CFD models calculated distribution of releases 2 and 3 to more areas of the large hall and the occupants than the multizone model. Thus, for each sensor location and for each release location, every detection time had a distinct value for occupant exposure. Thus, minimizing occupant exposure did guarantee that detection time was also minimized.

When multizone model data was used to design sensor systems, one also notices that the lowest detection time for a specific

Table 5
Sensor design for large hall using zonal model data.

Sensor sys. design	Sens. qty	Obj. func.	Locations using zonal data	Objective function value			Locations using CFD data	Col. [6] equiv. to [7]?
				Zonal-optimal	CFD-benchmarked	CFD-optimal		
[1]	[2]	[3]	[4]	[5]	[6]	[7]	[8]	[9]
1	4	D	396,511,542,785	1.0	1.0	1.0	396,511,542,785	Y
		E		2.68e-6	1.08e-4	1.08e-4		Y
2	3	D	196,551,511	1.0	1.2	1.0	386,422,662	N (+0.2)
		E		2.68e-6	1.96e-4	1.08e-4		N (+9e-5)
3	2	D	495,522	1.6	1.4	1.0	222,592	N (+0.4)
		E		2.73e-6	1.98e-4	1.08e-4		N (+9e-5)
4	1	D	522	200	200	1.4	552	N (+200)
		E		200	200	1.09e-4		N (+200)
Eng-1	4	D	116,916,196,996	1.6	1.6	1.0	396,511,542,785	N (+0.6)
		E		2.70e-6	1.98e-4	1.08e-4		N (+9e-5)
Eng-2	1	D	551	400	1.6	1.4	552	N (+0.2)
		E		400	1.66e-4	1.09e-4		N (+6e-5)
Eng-3	1	D	556	400	1.8	1.4		N (+0.4)
		E		400	1.97e-4	1.09e-4		N (+9e-5)

Table 6
Sensor design for office suite using multizone model data.

Sensor sys. design	Sens. qty	Obj. func.	Locations using multizone data	Objective function value (complementary obj. func. value)			Locations using CFD data	Col. [7] equiv. to [7]?
				Multizone-optimal	CFD-benchmarked	CFD-optimal		
[1]	[2]	[3]	[4]	[5]	[6]	[7]	[8]	[9]
1	5	D	[1]321, [3]111, [H1]511, [H2]111, [C]331	1.0	1.0	1.0	{1}442, [3]411, [H1]511, [H2]111, [C]452	Y
		E		1.04e-5	3.89e-3	3.89e-3		Y
2	4	D	[2]114, [3]511, [H2]111, [C]421	1.17	1.0	1.0	[2]114, [3]511, [H2]111, [C]421	Y
		E		1.05e-5	3.89e-3	3.89e-3		Y
3	3	D	[1]342, [C]111, [H2]111	1.5 (2.26e-5)	1.0	1.0	[1]342, [C]111, [H2]111	Y
4	3	E	[3]511, [H2]111, [C]451	1.12e-5 (1.5)	3.89e-3	3.89e-3	[3]511, [H2]111, [C]451	Y
5	2	D	[3]221, [H2]111	2.0 (3.00e-5)	2.17	1.0	[H2]121, [C]113	N (+1.17)
6	2	E	[H2]111, [C]131	1.84e-5 (2.33)	4.97e-3	3.89e-3	[H2]121, [C]112	N (+1e-3)
		D	[2]113	168	168	1.5	[2]111*	N (+168)
Eng	4	D	[1]544, [2]444, [3]544, [C]111	168	168	1.0	[2]114, [3]511, [H2]111, [C]421	N (+168)
		E		168	168	3.89e-3		N (+168)

number of sensors did not guarantee the lowest occupant exposure. Sensor sys.-3 in Table 4 was designed to minimize detection time. The minimum detection time was 1.6 min for a 3-sensor system. Sensor sys.-4 was designed to minimize occupant exposure. Its detection time was 2.8 min for a 3-sensor system. Nevertheless, Sensor sys.-3 had a larger occupant exposure than Sensor sys.-4.

The detection time of Sensor sys.-3, for each respective release, was 1.0, 2.0, 1.0, 2.0, and 2.0. The detection time of Sensor sys.-4, for each respective release, was 1.0, 5.0, 4.0, 3.0, and 1.0. For release 1, the detection times were both 1.0 min, so the associated occupant exposure would be equal as well. As discussed above, no matter the detection time for releases 2 and 3, the occupant exposures were always 0 kg/kg because the local concentration at each occupant was always 0 mg/m³. Thus, the only difference, with regards to the calculation of the occupant exposure, between these two sensor systems were the detection times for releases 4 and 5. They are respectively [2.0, 2.0 min] and [3.0, 1.0 min], for which the respective averages are both 2.0 min. The respective occupant exposures are [1.49e-7, 8.24e-6 kg/kg] and [6.96e-7, 1.40e-6 kg/kg], for which the respective averages are 4.19e-5 and 1.05e-6 kg/kg. This demonstrates that even if the overall detection time were minimized, the local concentration at each occupant for each respective release determines whether or not the occupant exposure is also minimized. Therefore, if more than one combination of individual detection times can result in the same overall detection

time, minimizing occupant exposure cannot be guaranteed. Therefore, both minimizing detection time and occupant exposure, along with other possible design criteria, should be considered when designing sensor systems in order to ensure that occupants are being protected.

Sensors are typically placed near exhausts for contaminant detection since most of the air inside a room will return to the exhaust. Therefore, the locations of the four exhausts in the large hall were selected as a 4-sensor system (Sensor sys. Eng-1). The detection times calculated using multizone, zonal, and CFD model data for Sensor sys. Eng-1 were greater than the respective optimal values for a 4-sensor system. Thus, it could be concluded that Sensor sys. Eng-1 is not an optimal one. Two more possible engineering design practices were tested. Sensor sys. Eng-2 was a 1-sensor system with a sensor placed in the center of the large hall on the floor. Sensor sys. Eng-3 was a 1-sensor system with a sensor placed in the center of the large hall on the ceiling. The detection times calculated using multizone, zonal, and CFD model data for Sensor sys. Eng-2 and 3 were greater than the respective optimal values for a 1-sensor system. Nevertheless, for Sensor sys. Eng-2 and 3, the CFD-benchmarked objective function values were no more than 30 s greater for detection time and no more than 1e-4 kg/kg greater for occupant exposure. As more data on the risk of exposure to CBW agents becomes available, how these differences could affect actual building occupants should be evaluated.

Table 7
Sensor design for office suite using zonal model data.

Sensor sys. design	Sens. qty	Obj. func.	Locations using zonal data	Objective function value			Locations using CFD data	Col. [7] equiv. to [8]?
				Zonal-optimal	CFD-benchmarked	CFD-optimal		
[1]	[2]	[3]	[4]	[5]	[6]	[7]	[8]	[9]
1	5	D	[1]542, [3]141, [H2]111, [C]111 [C]341	1.0	1.0	1.0	[1]542, [3]141, [H2]111, [C]111, [C]341	Y
		E		1.28e-5	3.89e-3	3.89e-3		Y
2	4	D	[1]531, [3]411, [H2]111, [C]211	1.0	1.0	1.0	[1]531, [3]411, [H2]111, [C]211	Y
		E		1.28e-5	3.89e-3	3.89e-3		Y
3	3	D	[3]411 [H2]111 [C]552	1.17	1.0	1.0	[3]411, [H2]111, [C]552	Y
		E		1.29e-5	3.89e-3	3.89e-3		Y
4	2	D	[H2]111 [C]552	1.33	1.0	1.0	[H2]111, [C]552,	Y
		E		1.49e-5	3.89e-3	3.89e-3		Y
5	1	D	[C]551	168	168	1.5	[2]111*	N (+168)
		E		168	168	4.76e-3		N (+168)
Eng	4	D	[1]544, [2]444, [3]544, [C]111	168	168	1.0	[2]114, [3]511, [H2]111, [C]421	N (+168)
		E		168	168	3.89e-3		N (+168)

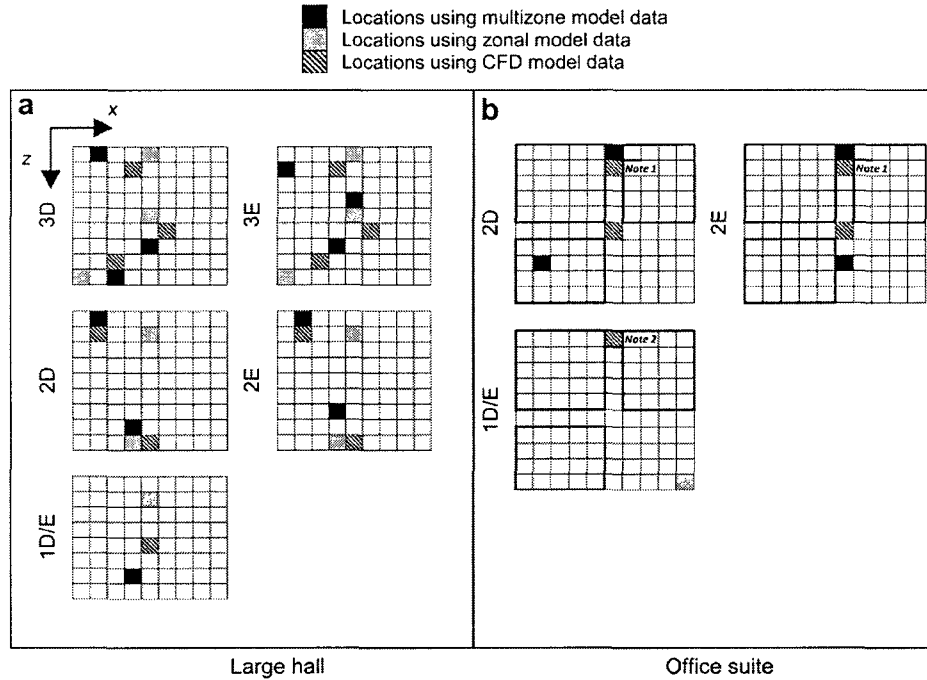


Fig. 6. Sensor systems designed using multizone, zonal, and CFD data for (a) large hall and (b) office suite. Number-letter designation refers to total number of sensors and design objective (D = minimize detection time, E = minimize occupant exposure, D/E = location for both minimizing detection time and occupant exposure are the same). Locations from Tables 4–7. Note 1: 2-sensor systems designed using zonal and CFD model data overlap in plan view and are at the same height above the floor. Note 2: 1-sensor system designed using multizone and CFD model data overlap in plan view. Location designed using multizone model data at $y = 1.6$. Location designed using CFD model data at $y = 0$.

6.3. Results for office suite

Procedures for determining sensor systems for the office suite were similar to those used for the small office and large hall. Tables 6 and 7 summarize the sensor systems designed using the multizone and zonal model data, respectively, for the office suite. The number in brackets before the subzone number indicates the room in which the sensor is located (see Table 1). For instance, [1]111 means Office 1, subzone 111. [H] indicates the hallway, and [C] indicates the Common Area.

Similar to the large hall, as the number of sensors was reduced, data from the simpler airflow models was less appropriate for sensor system design in the case of the office suite. Further, even sensor systems designed either using multizone or zonal model data that were similar to those designed using CFD data did not result in equivalent objective function values (Fig. 6b). For the

2-sensor system designed using multizone model data, each location designed using multizone model data (black-filled box) was close to the locations designed using CFD data (hatched box). Note that the locations designed using zonal model data overlapped with those designed using CFD data for the 2-sensor systems. Thus, it could be concluded that a sensor system designed for the office suite using data from a simpler airflow model could perform just as well as one designed using more accurate CFD data when the total number of sensors exceeded a minimum value, i.e., 2 when using multizone model data and 1 when using zonal model data.

Also similar to the large hall, when multizone model data was used to design the sensor systems for the office suite, minimizing occupant exposure could not always guarantee that detection time was also minimized. The multizone model did not calculate distribution of release 4 to the rest of the office suite, and thus no contaminant reached the occupants. No matter the detection time,

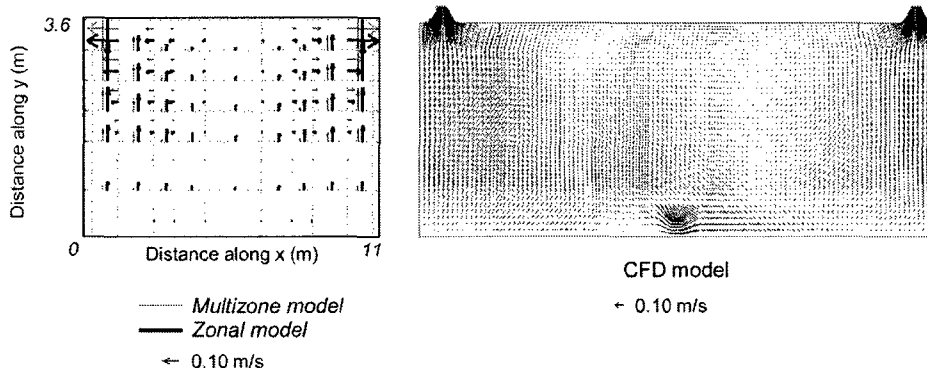


Fig. 7. Resulting airflow patterns from different airflow models through release 2 in the large hall (not to scale).

occupant exposure was always 0 kg/kg because the local concentration at each occupant was always 0 mg/m³ for release 4. Thus, two different detection times could result in the same occupant exposure.

The reason that minimizing detection time did not guarantee occupant exposure for the 4- and 5-sensor systems in Table 6 was because the sensor systems reported are not unique. The reported 4- and 5-sensor systems coincidentally minimized detection time and occupant exposure. Minimizing detection time did not guarantee minimization of occupant exposure for the 2- and 3-sensor systems for reasons similar to those for the large hall. Thus, additional constraints on the objective functions should be incorporated in order to utilize multizone model data for sensor system design irrespective of the test environment.

Again, the locations of the four exhausts in the office suite were selected as a 4-sensor system (Sensor sys. Eng). The multizone-optimal, zonal-optimal, and CFD-benchmarked detection time values for this 4-sensor system were all 168 min. These high values were due to the penalty of a value of 1000 and indicate that the designed sensor system could not detect a containment release for at least one of the releasing scenarios. The CFD-optimal value was 1.0 min for any 4-sensor system. Thus, the 4-sensor system with sensors placed at the four exhausts is not an optimal design.

7. Conclusions

Indoor air sensor system design to protect a building from CBW attack was discussed in this study. Contaminant dispersion was simulated using multizone, zonal, and CFD airflow models for three test environments: a small office, a large hall, and an office suite. Four releasing locations were simulated in the small office, five in the large hall, and six in the office suite. GA was used to design the sensor systems that minimized either detection time or occupant exposure. This study sought to examine whether or not, despite inherent differences in airflow and contaminant dispersion results, data from a simpler airflow model could be used to design sensor systems capable of performing just as well as those designed using more accurate CFD data. It was found that (1) unless a unique sensor system is needed, sensor systems designed using data from simpler airflow models performed just as well as those designed using more accurate CFD data; and (2) additional constraints to the sensor system design problem should be incorporated in order to guarantee that when minimizing detection time, occupant exposure is also minimized and vice versa, especially when using multizone model data to design sensor systems.

Future work should study the limitations on the characteristics of a space (size, shape, layout, etc.) for which data from a multizone and/or zonal model can be used to design sensor systems capable of performing just as well as those designed using more accurate CFD data. This would involve a systematic approach by changing the various characteristics of a space and observing the performance of sensor systems designed using different airflow model data.

Acknowledgements

Support for this work has been provided by a National Science Foundation Graduate Research Fellowship.

References

- [1] Mora L, Gadgil AJ, Wurtz E. Comparing zonal and CFD model predictions of isothermal indoor airflows to experimental data. *Indoor Air* 2003;13(2):77–85.
- [2] Arvelo J, Brandt A, Roger RP, Saksena A. An enhanced multizone model and its application to optimum placement of CBW sensors. *ASHRAE Transactions* 2002;108(2):818–25.
- [3] Zhai Z, Srebric J, Chen Q. Application of CFD to predict and control chemical and biological agent dispersion in buildings. *International Journal of Ventilation* 2003;2(3):251–64.
- [4] Zhang TF, Chen Q, Lin C-H. Optimal sensor placement for airborne contaminant detection in an aircraft cabin. *HVAC&R Research* 2007;13(5):683–96.
- [5] Chen YL, Wen J. Application of zonal model on indoor air sensor network design. In: *Proceedings of sensors and smart structures technologies for civil, mechanical, and aerospace systems*. San Diego, CA: SPIE; 2007 [6529].
- [6] Feustal HE, Smith BV. COMIS 3.0-user's guide. Lawrence Berkeley National Laboratory; 1997.
- [7] Ren Z, Stewart J. COWZ user's guide: zonal indoor source emission and dispersion model, version 1. The School of Computer Science and QUESTOR Centre; 2003.
- [8] FLUENT. Airpak 2.1 user's guide. Fluent Inc; 2002.
- [9] Wurtz E, Nataf J-M, Winkelmann F. Two- and three-dimensional natural and mixed convection simulation using modular zonal models in buildings. *International Journal of Heat and Mass Transfer* 1999;42(5):923.
- [10] Ren Z. Enhanced modelling of indoor air flows, temperatures, pollutant emission and dispersion by nesting sub-zones within a multizone model. The United Kingdom: Queen's University; 2002.
- [11] Chen Q, Xu W. Zero-equation turbulence model for indoor airflow simulation. *Energy and Buildings* 1998;28(2):137–44.
- [12] ASHRAE. 1995 ASHRAE handbook HVAC applications. American Society of Heating, Refrigerating and Air-Conditioning Engineers; 1995.
- [13] Mathworks. Genetic algorithm and direct search toolbox. The Mathworks Inc.; 2004.
- [14] Chen YL, Wen J. Sensor system design for building indoor air protection. *Building and Environment* 2008;43(7):1278–85.
- [15] Institute of Medicine. *Chemical and biological terrorism – research and development to improve civilian medical response*. Washington, D.C.: National Academies Press; 1999.
- [16] Schell M, Int-Hout D. Demand control ventilation using CO₂. *ASHRAE Journal* 2001 February 2001:18–29.


APPENDIX B Sensor system design results for Test Cases in Chapter 2

Figure B-1 to Figure B-22 are contaminant contour plots for each test case simulated using three airflow models for Zone A[-], which had the ceiling-mounted diffuser and exhaust, for each release number. Contour plots are shown for $t = 1.0$ min and 3.0 min. They illustrate the differences between the contaminant transport calculated by each of the three airflow models.

They also demonstrate: (1) *only* for release #1 was *at least* one occupant exposed to the contaminant when simulated with either the multizone or zonal model. Note that even though the contour lines may fall within the subzone of an occupant, the concentration there was always zero; (2) no matter the release location, *at least* one occupant was exposed to the contaminant when simulated with the CFD model; and (3) differences between the contaminant transport calculated by each of the three airflow models.

Contour plots for selected test cases were reported in Chapter 2 and will not be repeated here. Contour plots for Test Case 1, Release #3 on page 77. Contour plots for Test Case 7, Release #1 on page 83.

 Contaminant release

 Occupant exposure

* Symbols for Figure B-1 to Figure B-22.

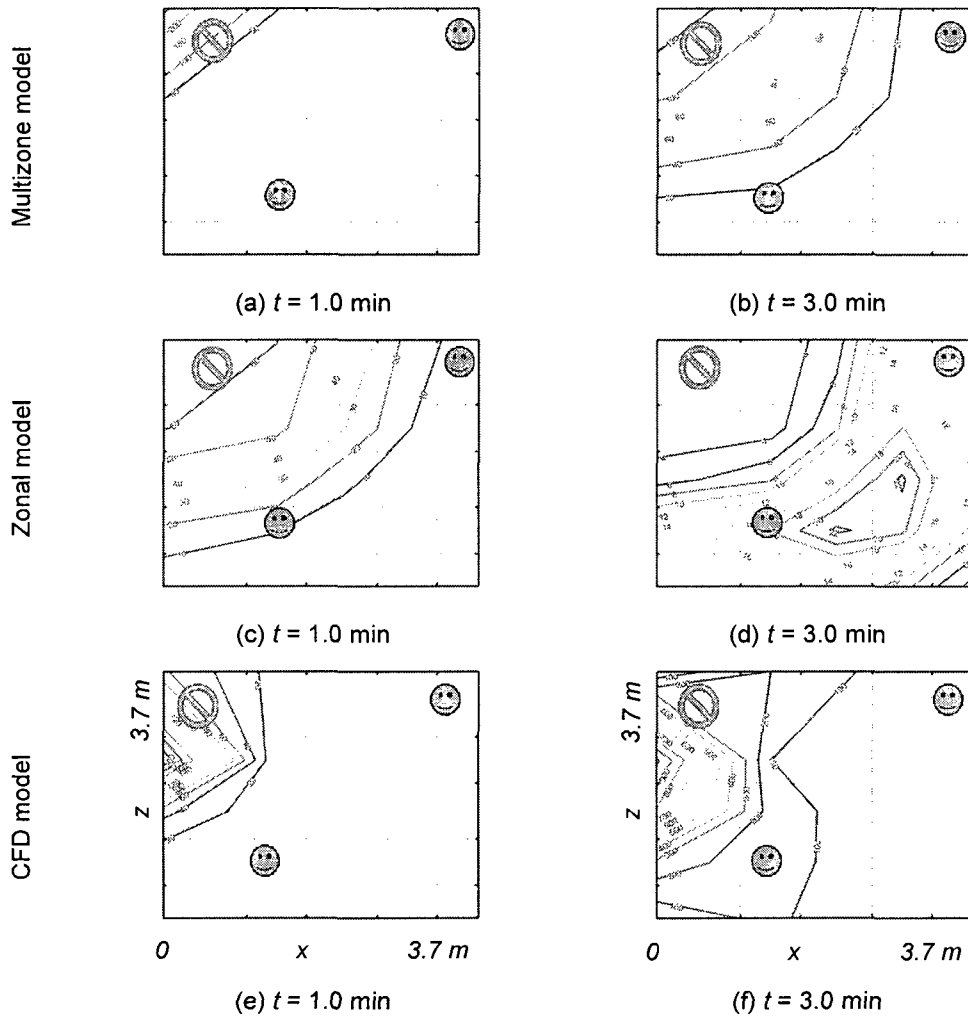


Figure B-1. Contaminant contour plots for Test Case 1, Release #1

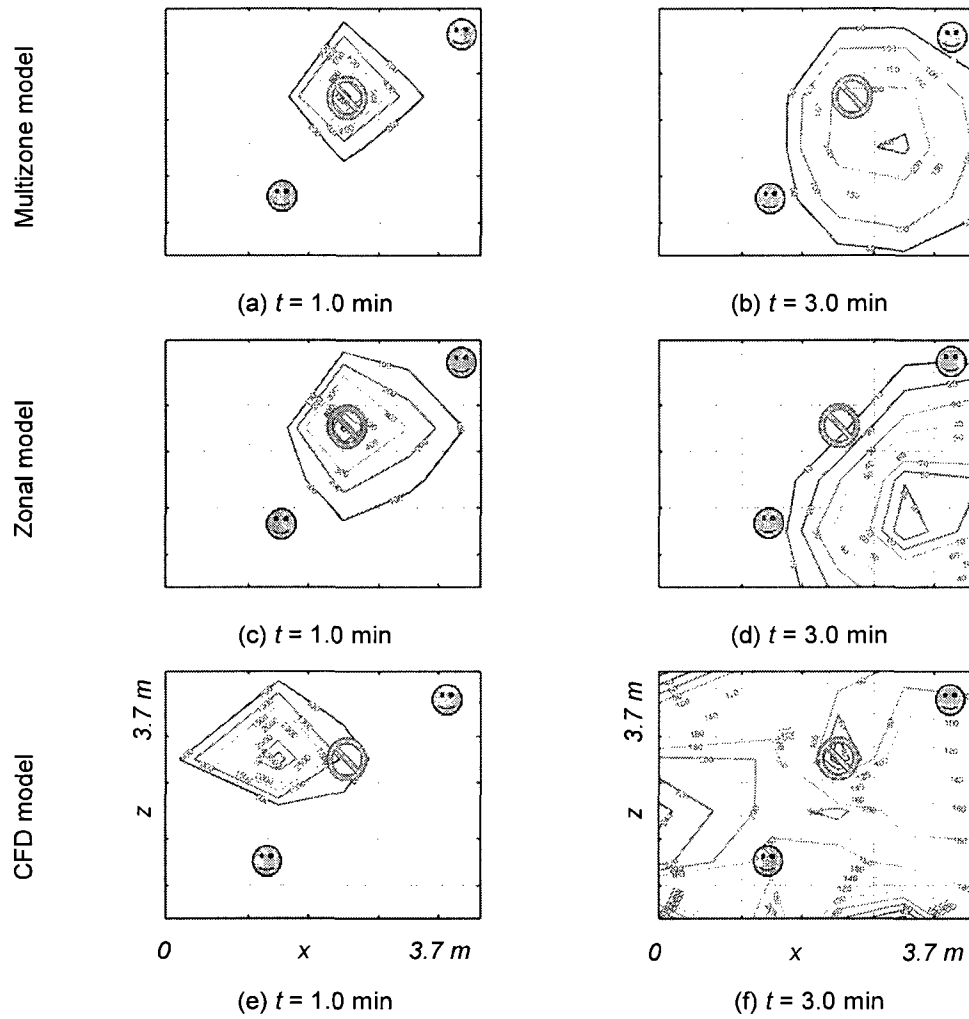


Figure B-2. Contaminant contour plots for Test Case 1, Release #2

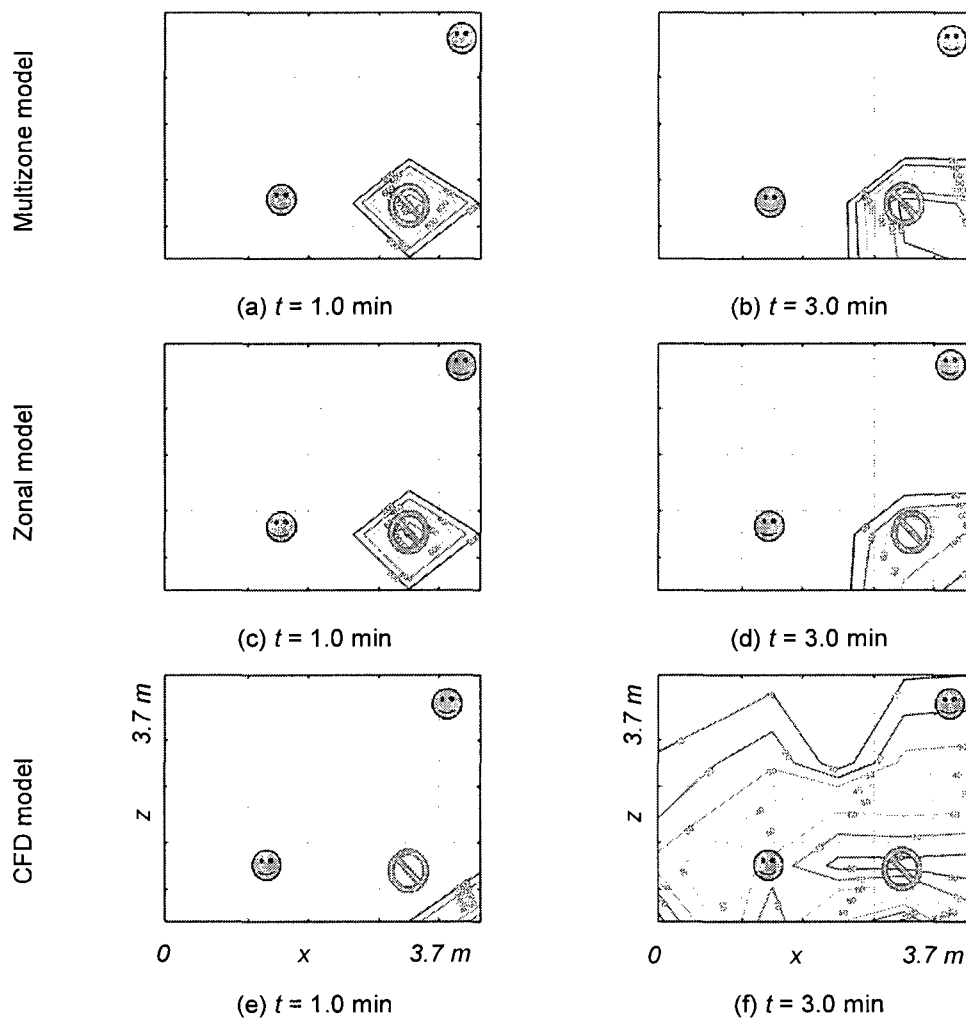


Figure B-3. Contaminant contour plots for Test Case 1, Release #4

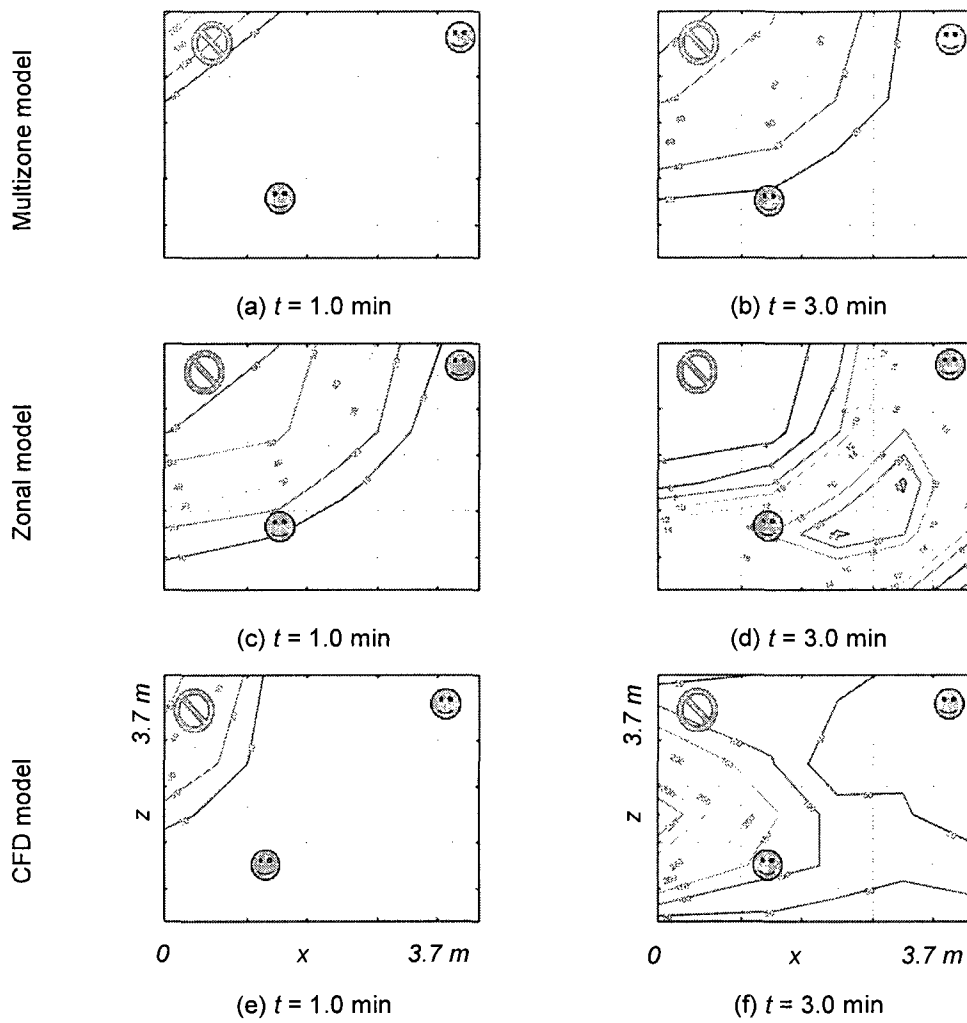


Figure B-4. Contaminant contour plots for Test Case 2, Release #1

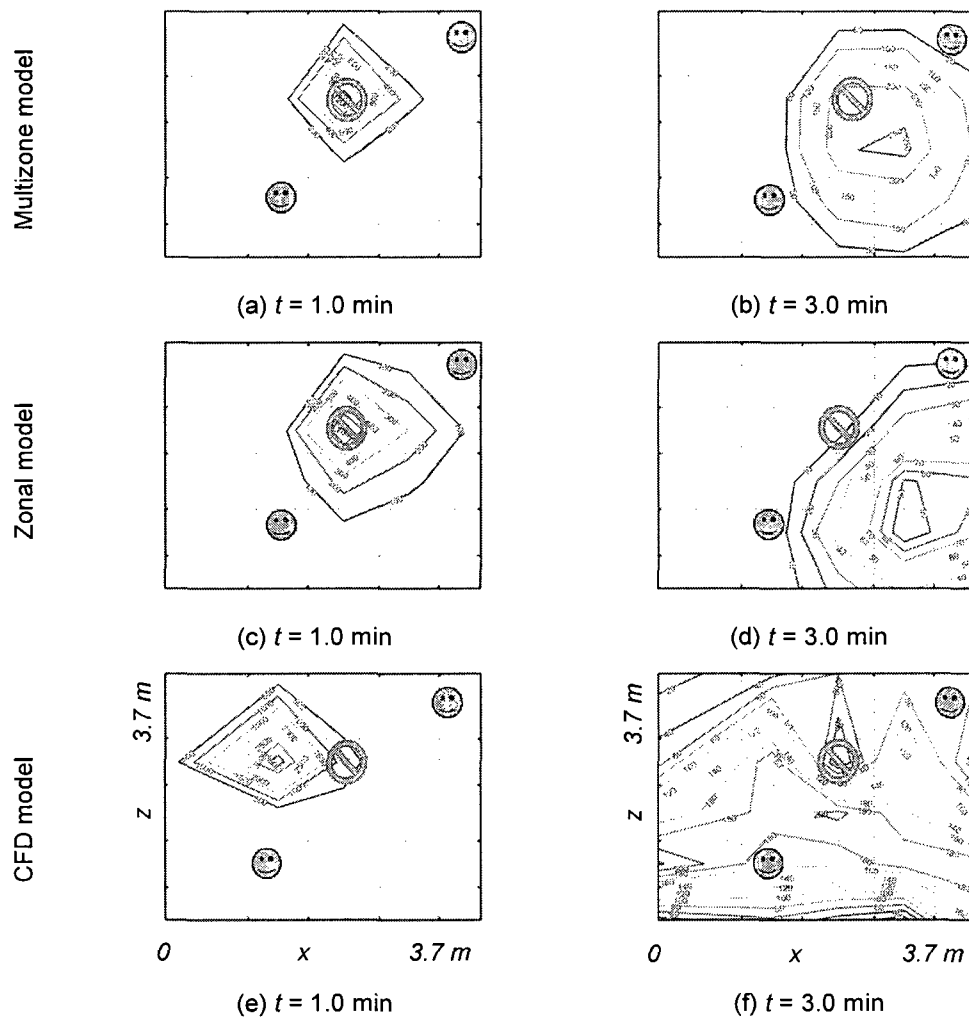


Figure B-5. Contaminant contour plots for Test Case 2, Release #2

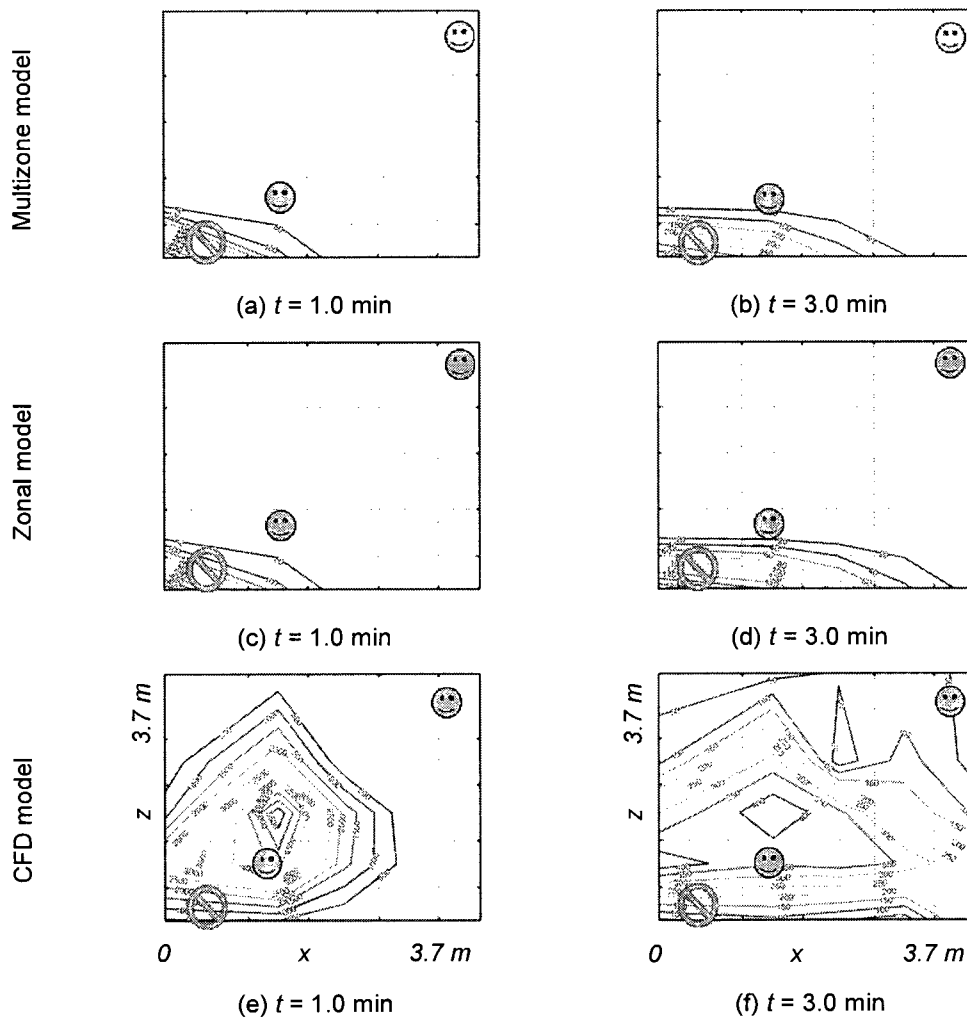


Figure B-6. Contaminant contour plots for Test Case 2, Release #3

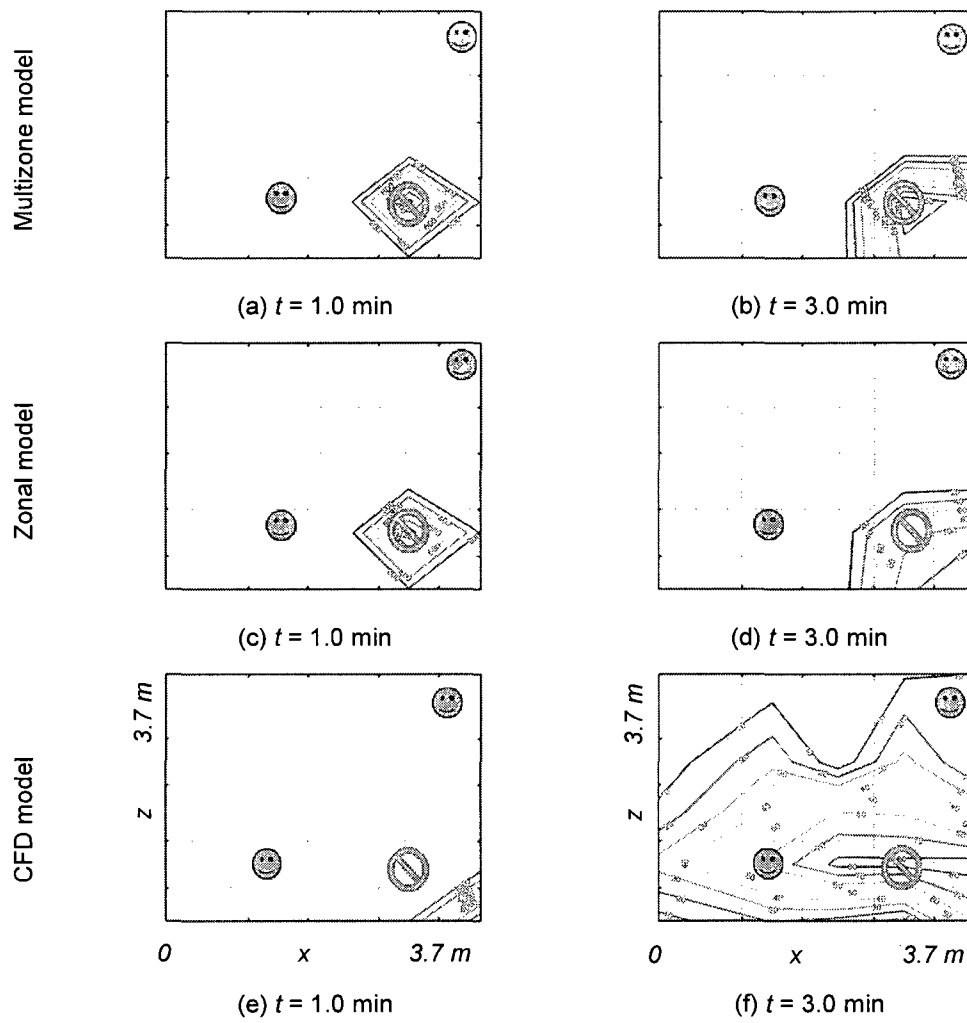


Figure B-7. Contaminant contour plots for Test Case 2, Release #4

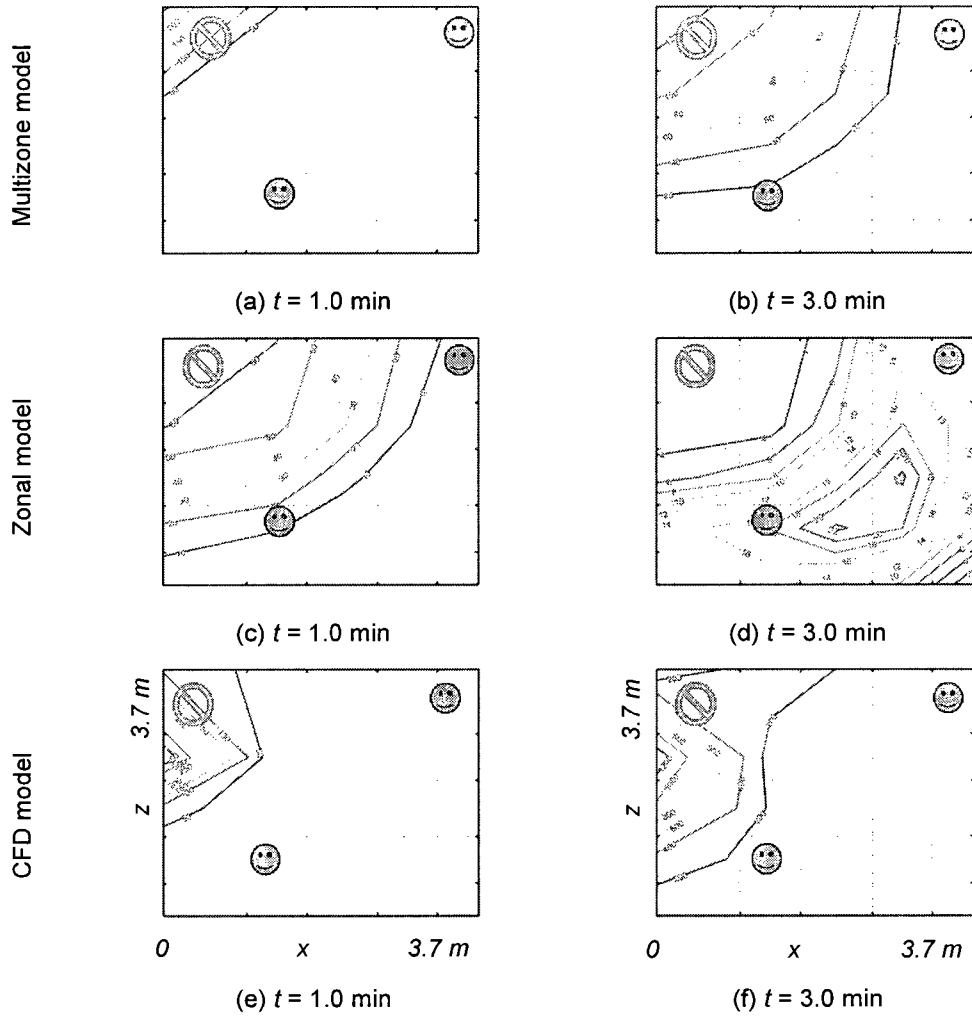


Figure B-8. Contaminant contour plots for Test Case 5, Release #1

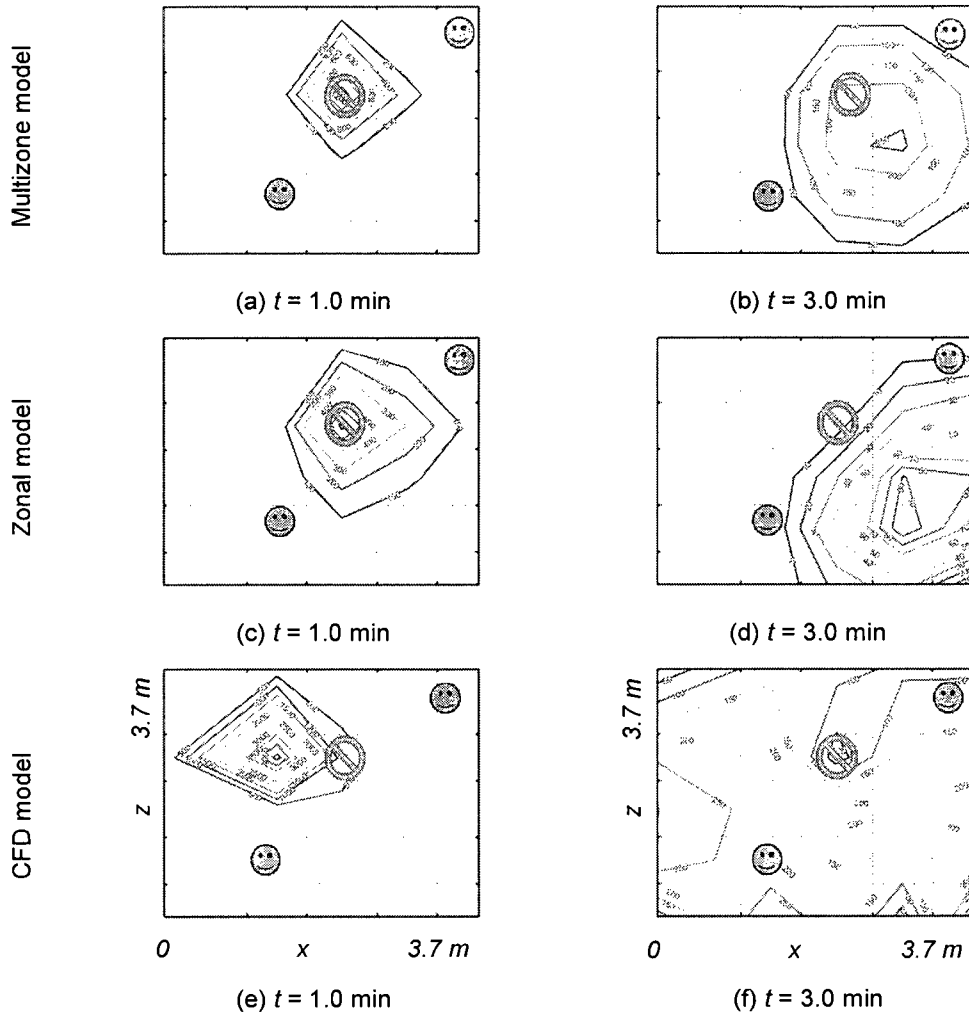


Figure B-9. Contaminant contour plots for Test Case 5, Release #2

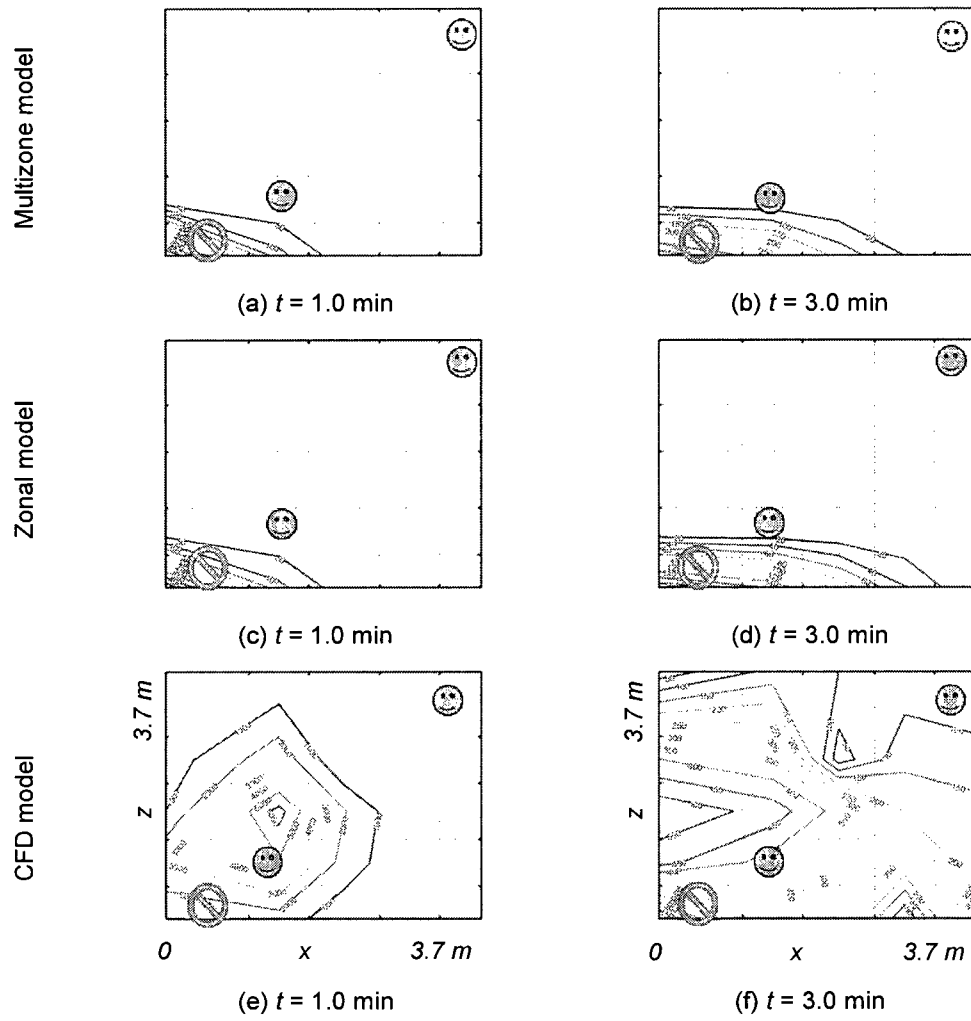


Figure B-10. Contaminant contour plots for Test Case 5, Release #3

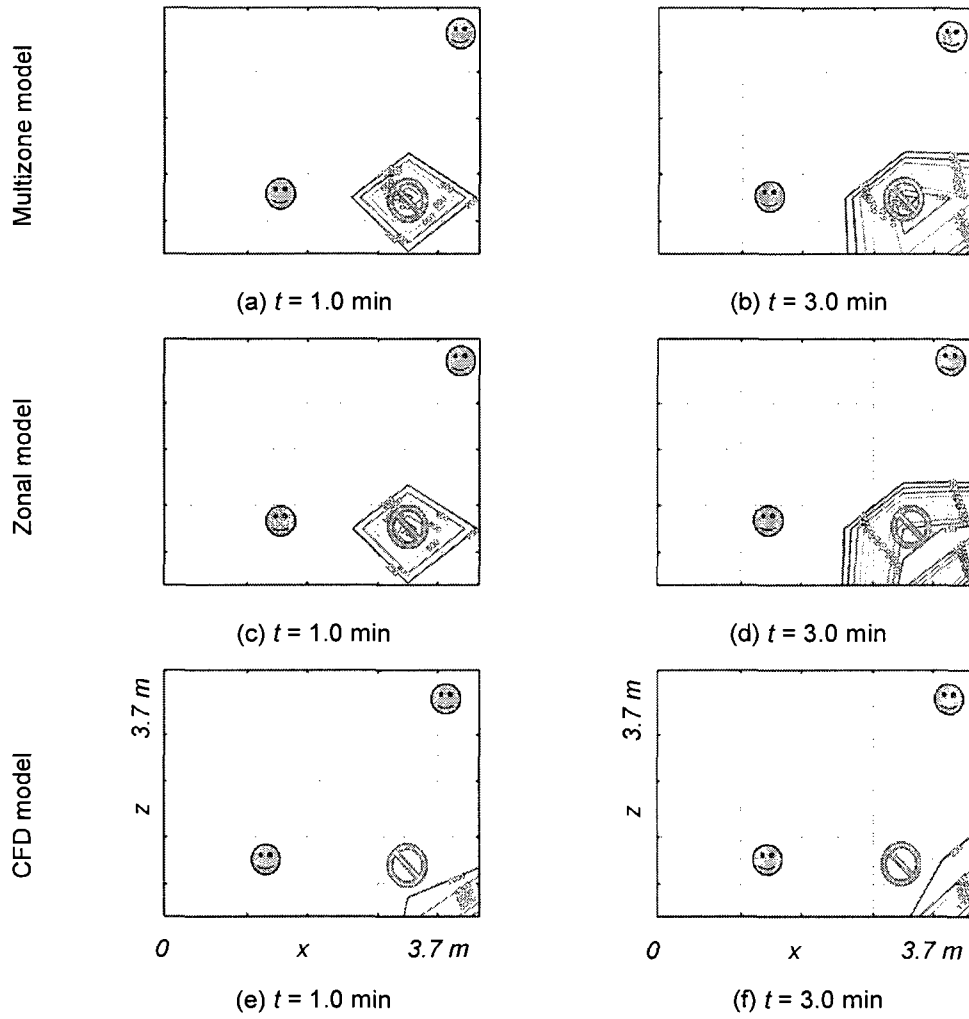


Figure B-11. Contaminant contour plots for Test Case 5, Release #4

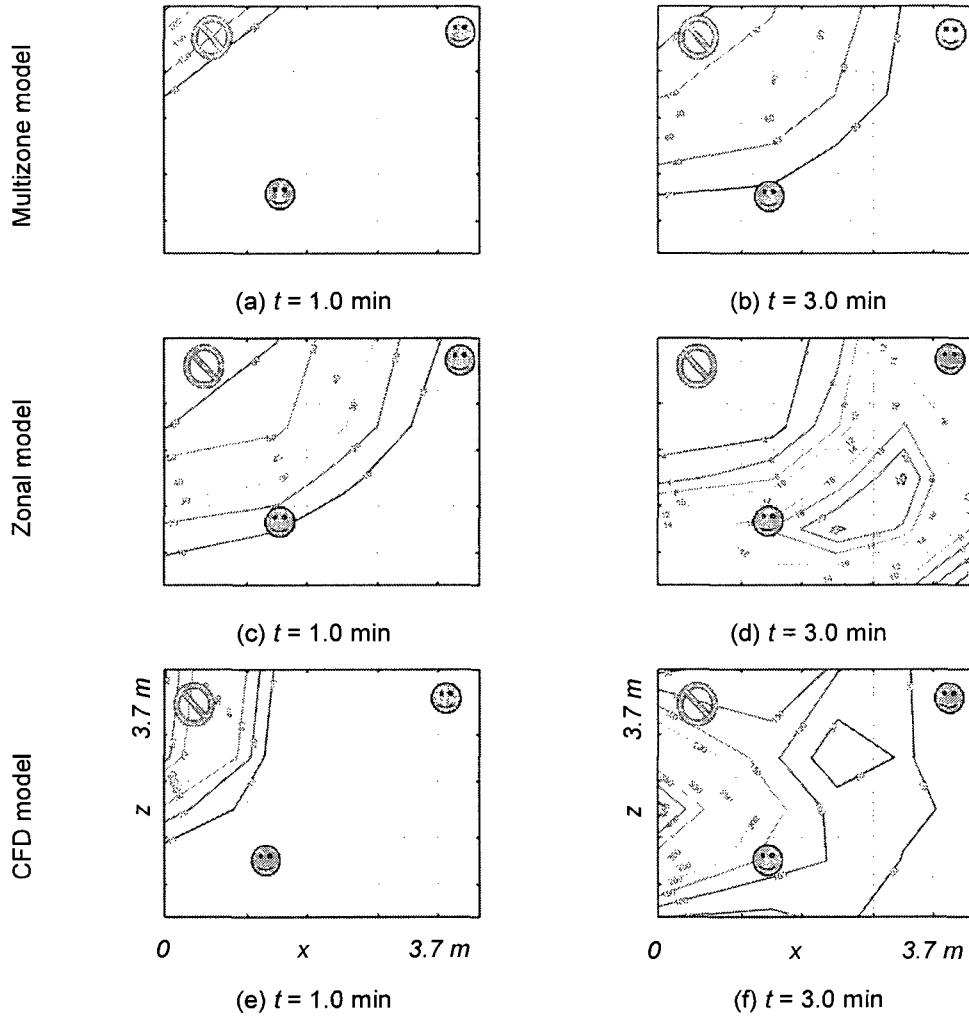


Figure B-12. Contaminant contour plots for Test Case 6, Release #1

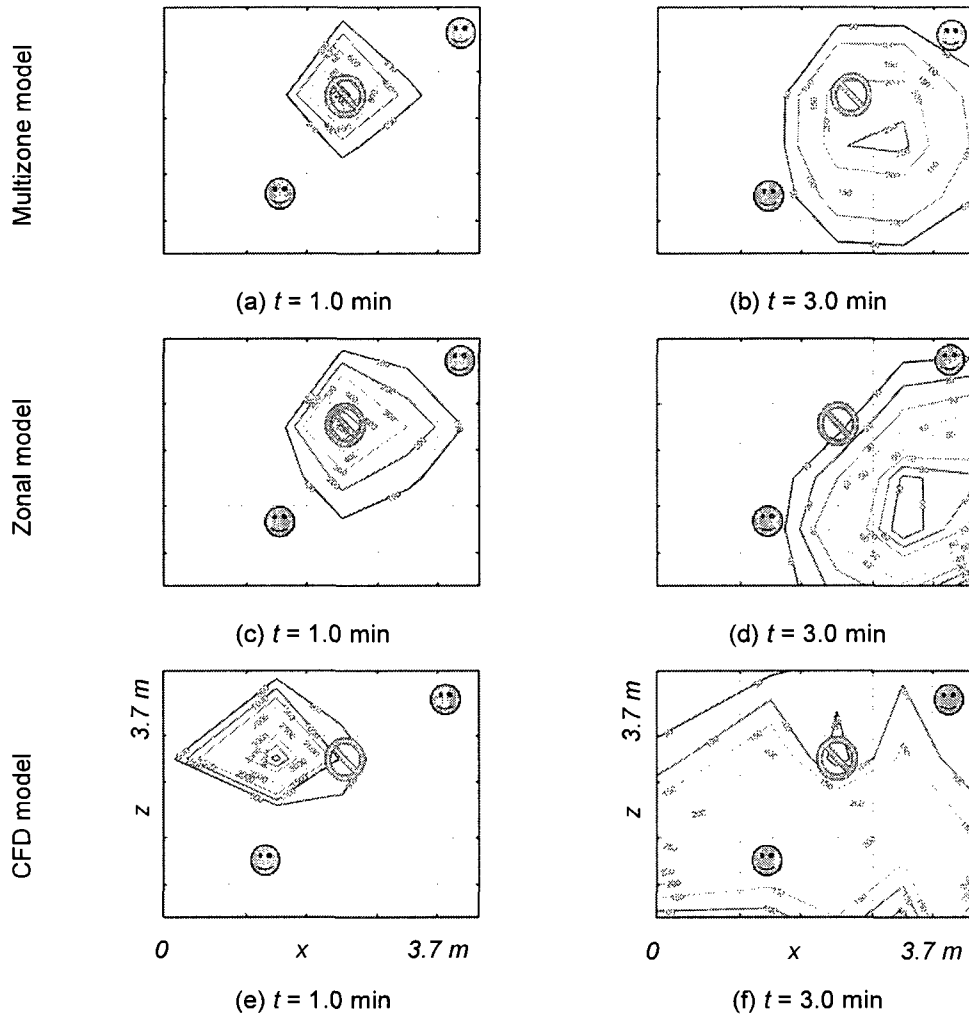


Figure B-13. Contaminant contour plots for Test Case 6, Release #2

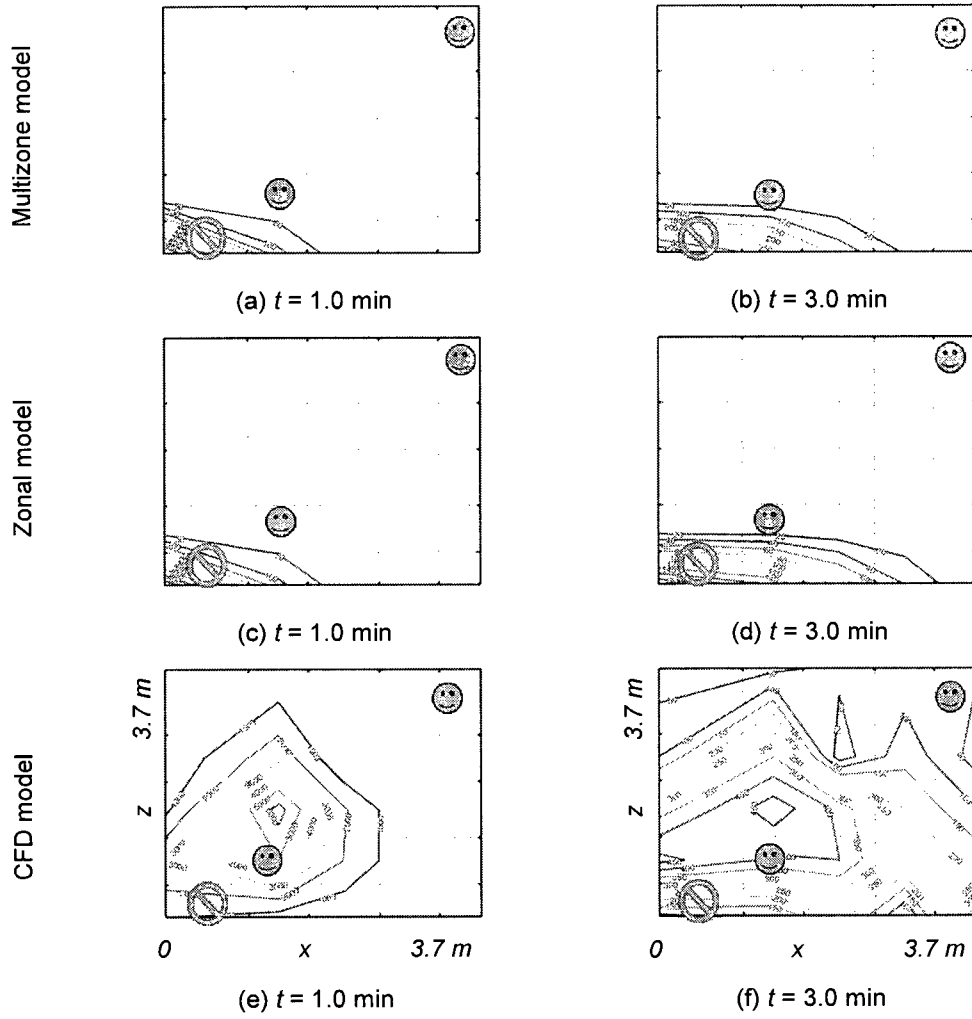


Figure B-14. Contaminant contour plots for Test Case 6, Release #3

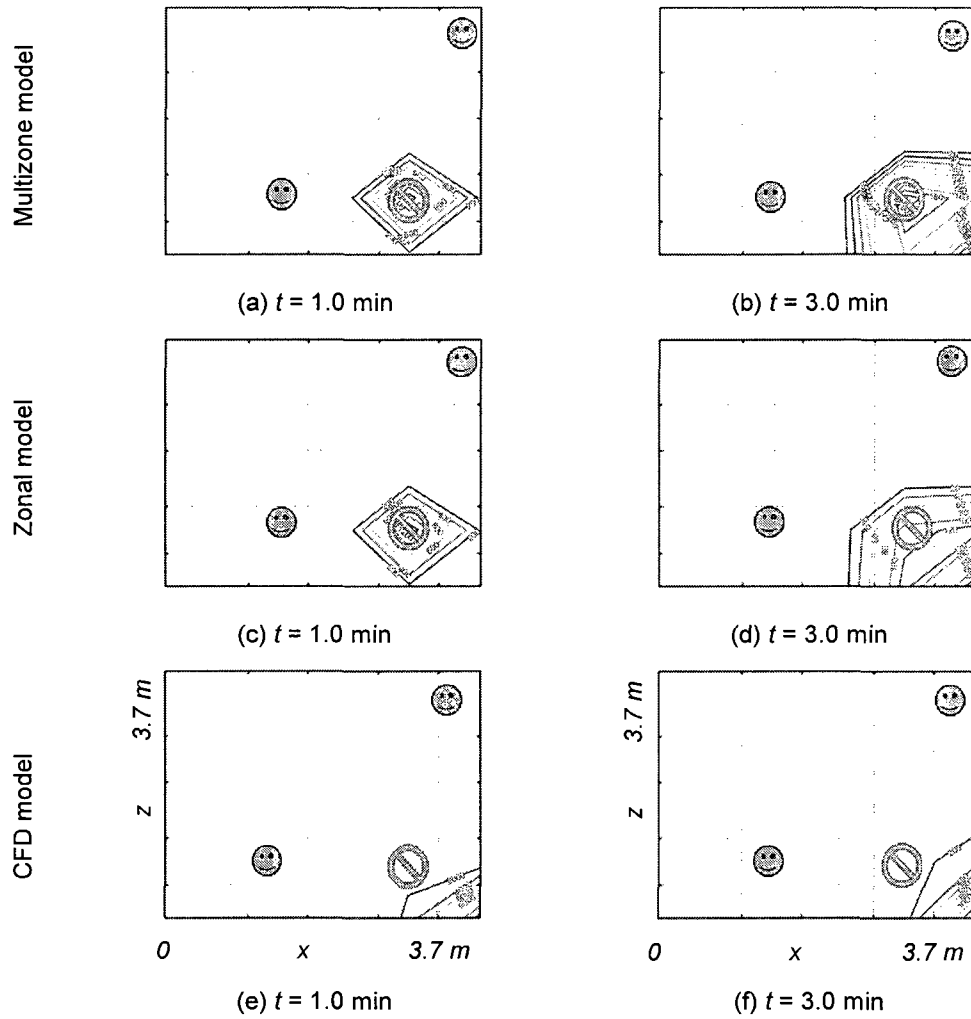


Figure B-15. Contaminant contour plots for Test Case 6, Release #4

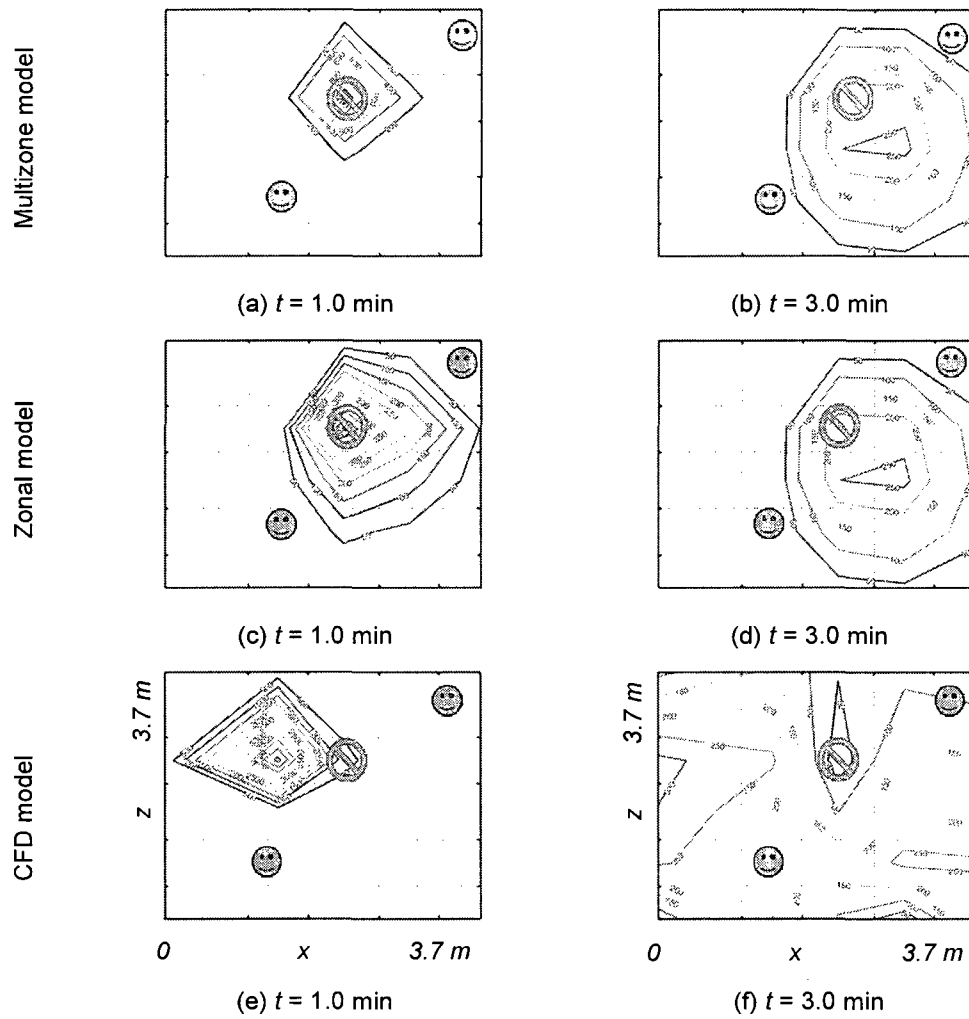


Figure B-16. Contaminant contour plots for Test Case 7, Release #1

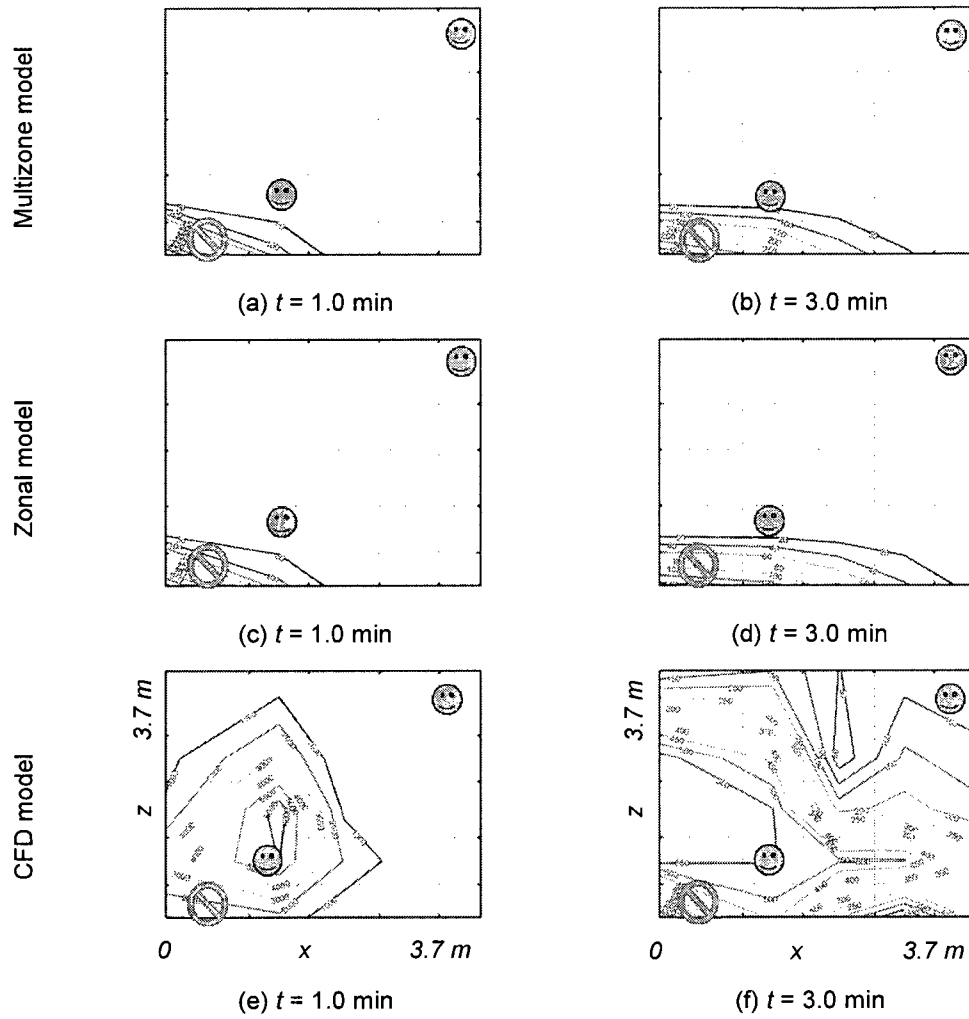


Figure B-17. Contaminant contour plots for Test Case 7, Release #3

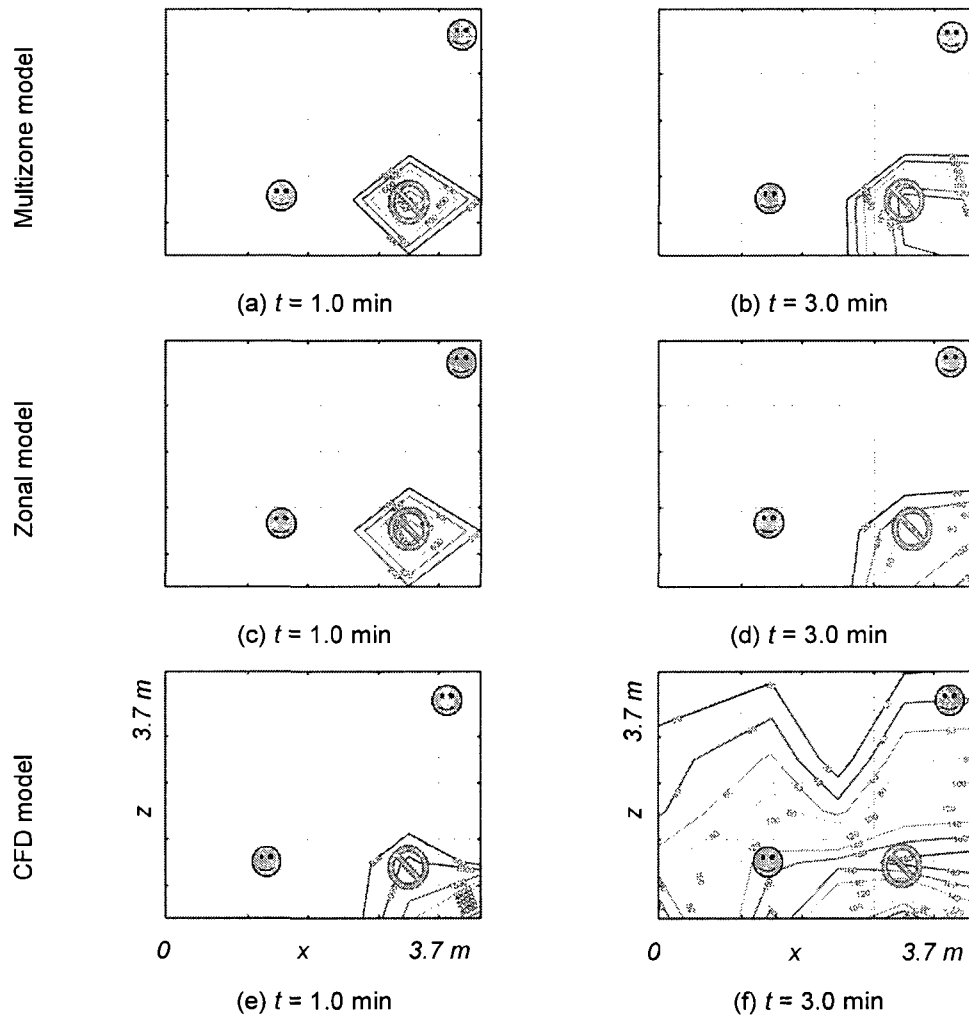


Figure B-18. Contaminant contour plots for Test Case 7, Release #4

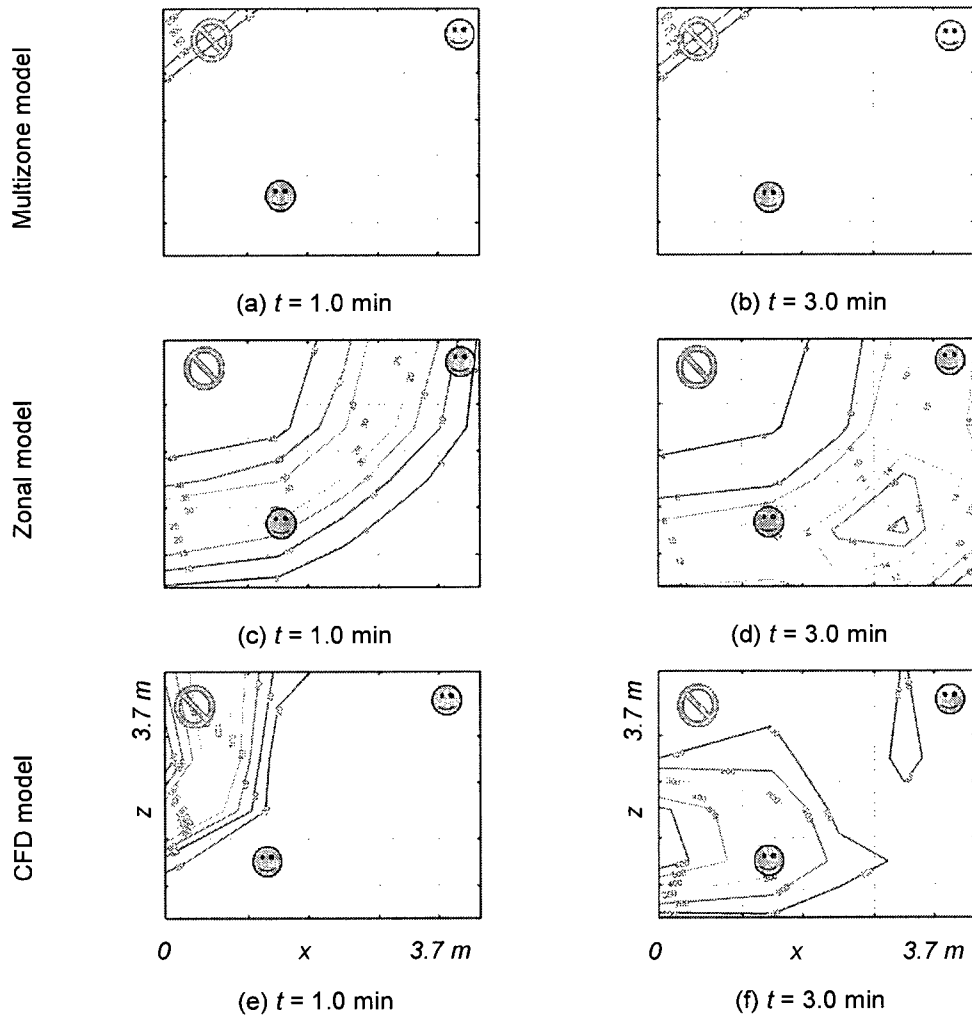


Figure B-19. Contaminant contour plots for Test Case 8, Release #1

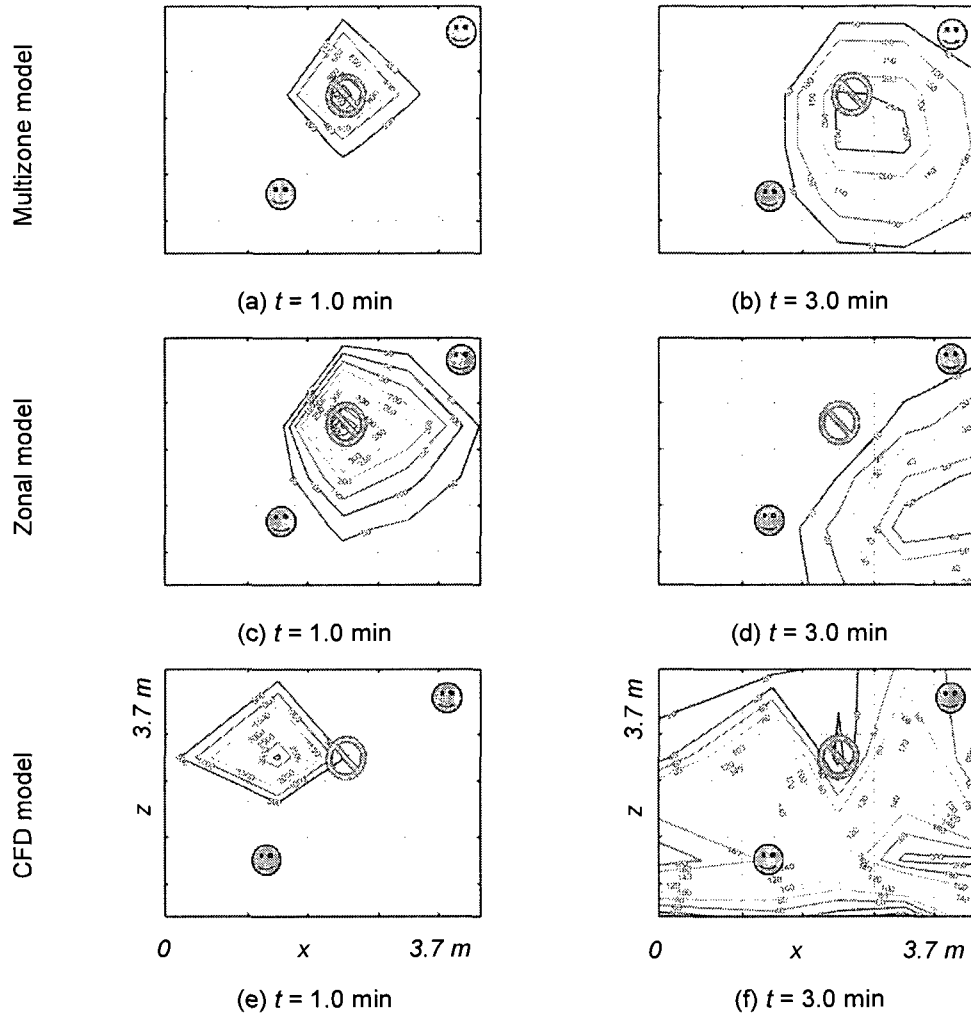


Figure B-20. Contaminant contour plots for Test Case 8, Release #2

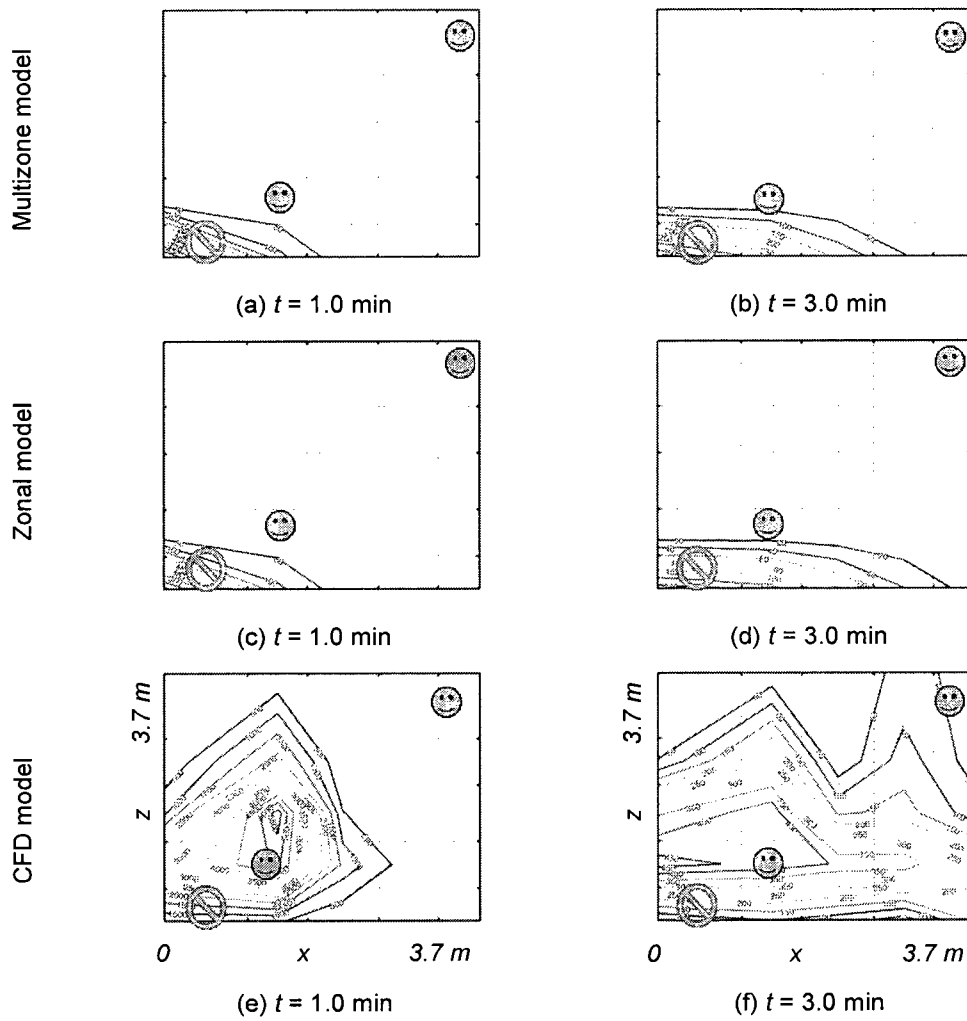


Figure B-21. Contaminant contour plots for Test Case 8, Release #3

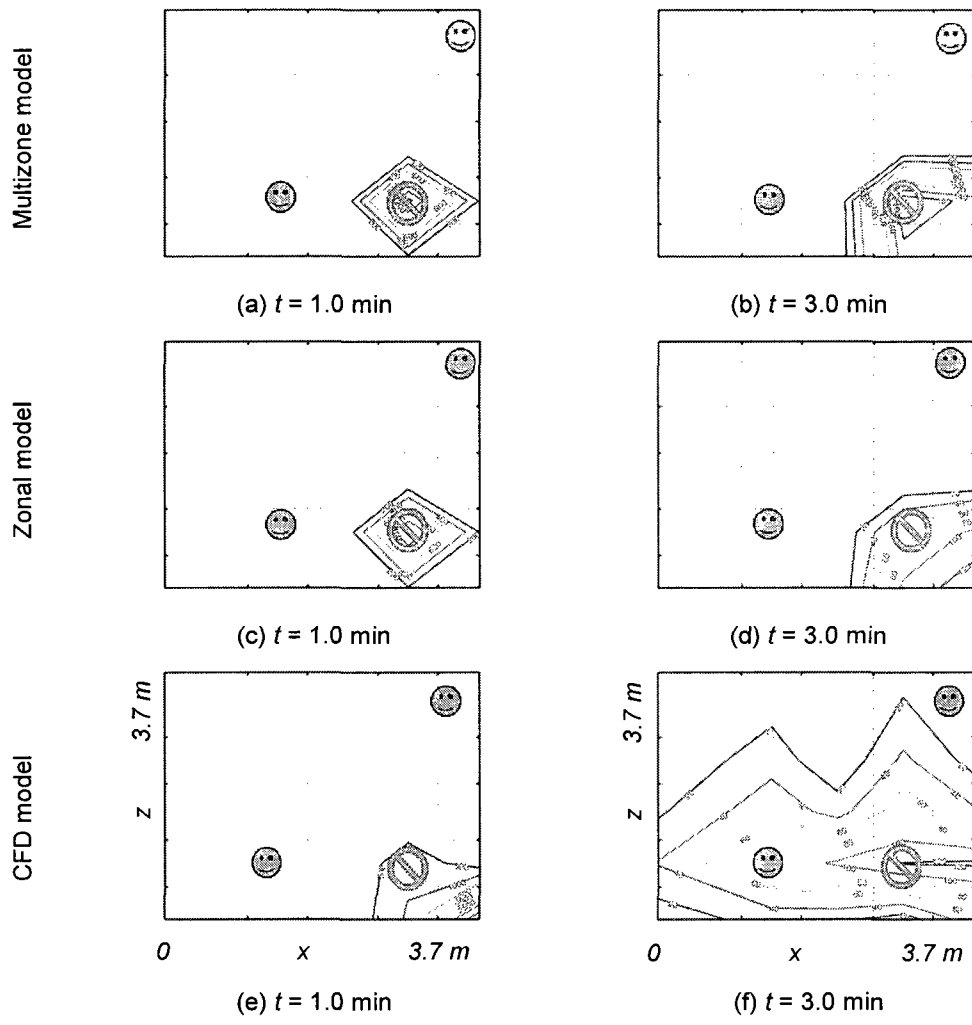


Figure B-22. Contaminant contour plots for Test Case 8, Release #4

Figure B-23 to Figure B-46 are contaminant contour plots for each test case simulated using three airflow models for Zone A[+], which had the wall-mounted diffuser and exhaust, for each release number. Contour plots are shown for $t = 1.0$ min and 3.0 min. They illustrate the differences between the contaminant transport calculated by each of the three airflow models.

They also demonstrate: (1) *only* for release #1 was *at least* one occupant exposed to the contaminant when simulated with either the multizone or zonal model. Note that even though the contour lines may fall within the subzone of an occupant, the concentration there was always zero; (2) no matter the release location, *at least* one occupant was exposed to the contaminant when simulated with the CFD model; and (3) CFD model data indicates that *every* subzone location is an *optimal* sensor location, *except* for the cases where furniture is placed below the diffuser (Test Cases 15 and 16); and (4) differences between the contaminant transport calculated by each of the three airflow models.

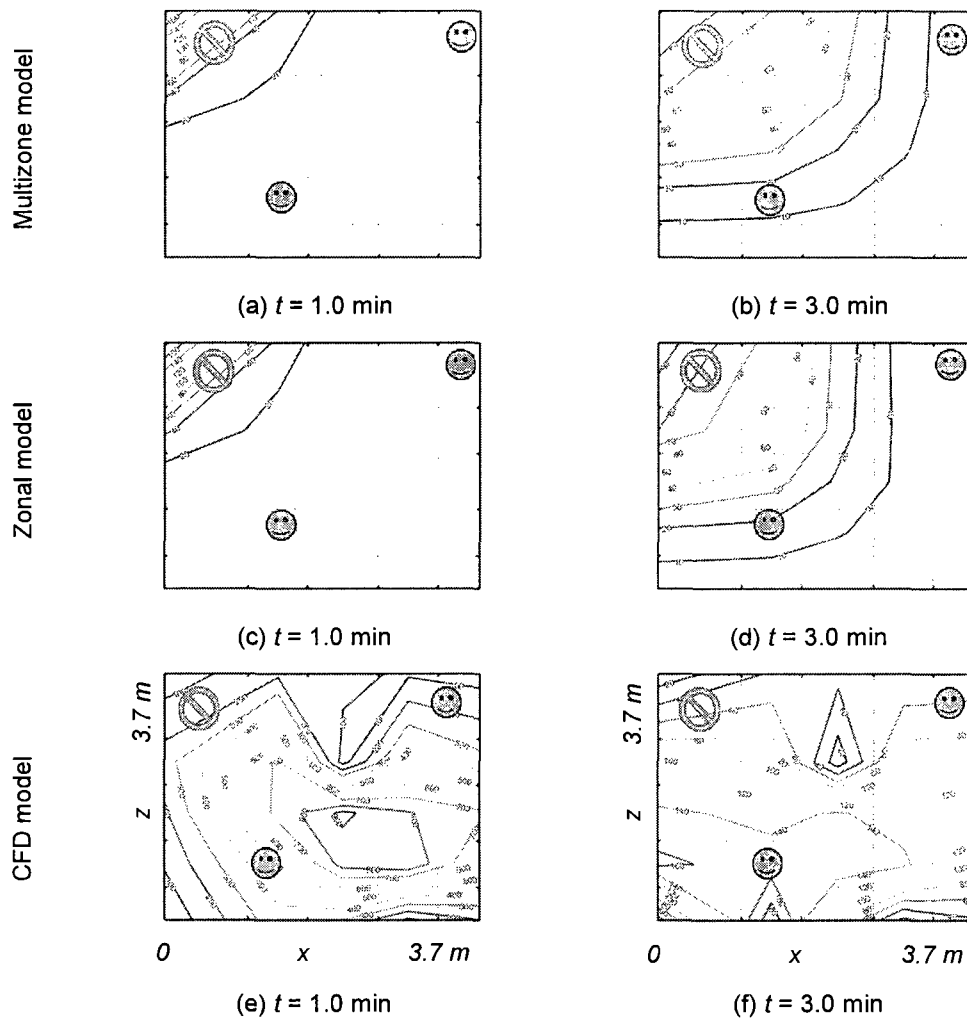


Figure B-23. Contaminant contour plots for Test Case 9, Release #1

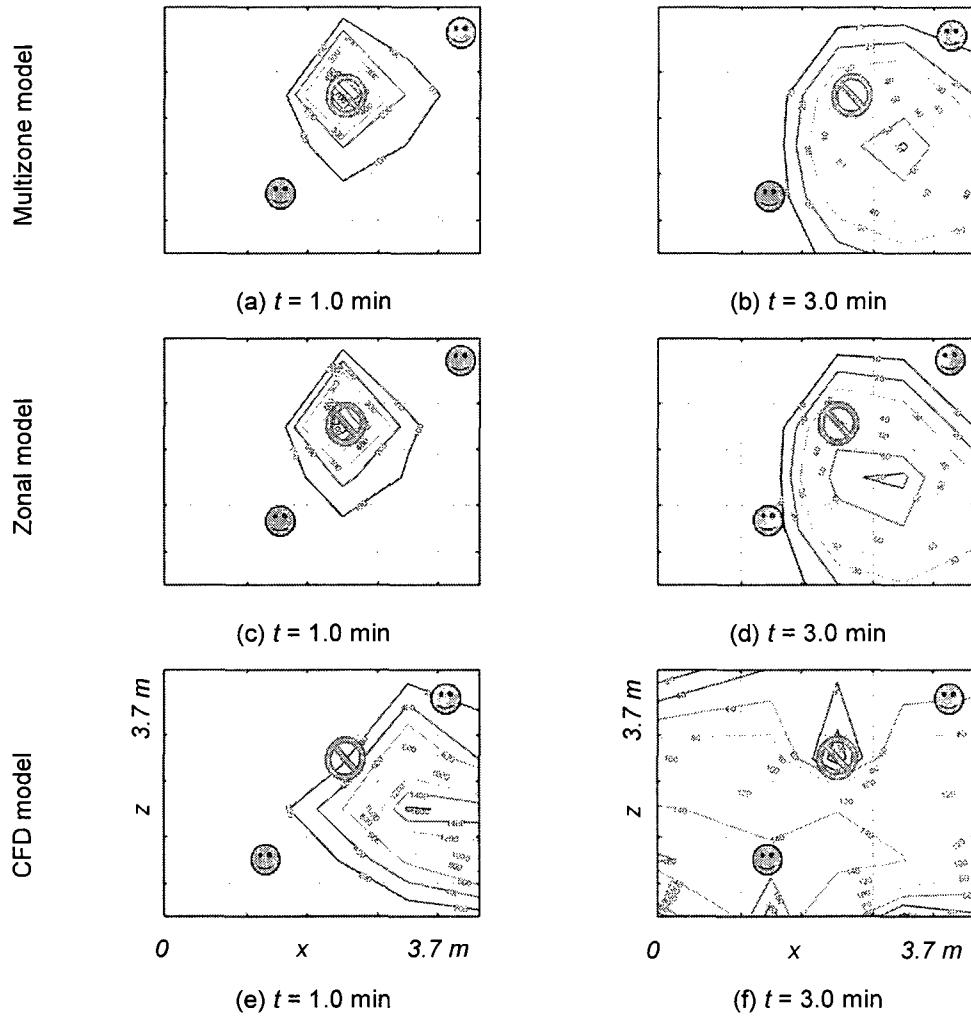


Figure B-24. Contaminant contour plots for Test Case 9, Release #2

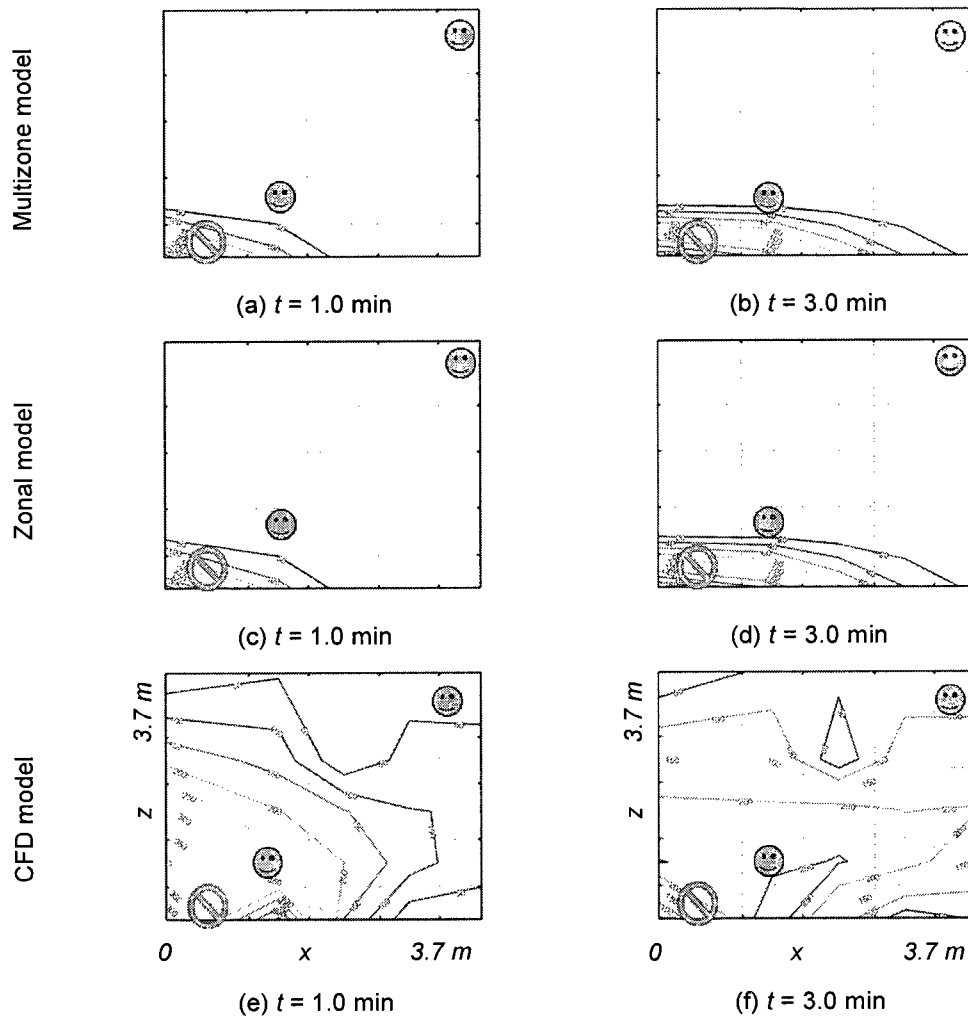


Figure B-25. Contaminant contour plots for Test Case 9, Release #3

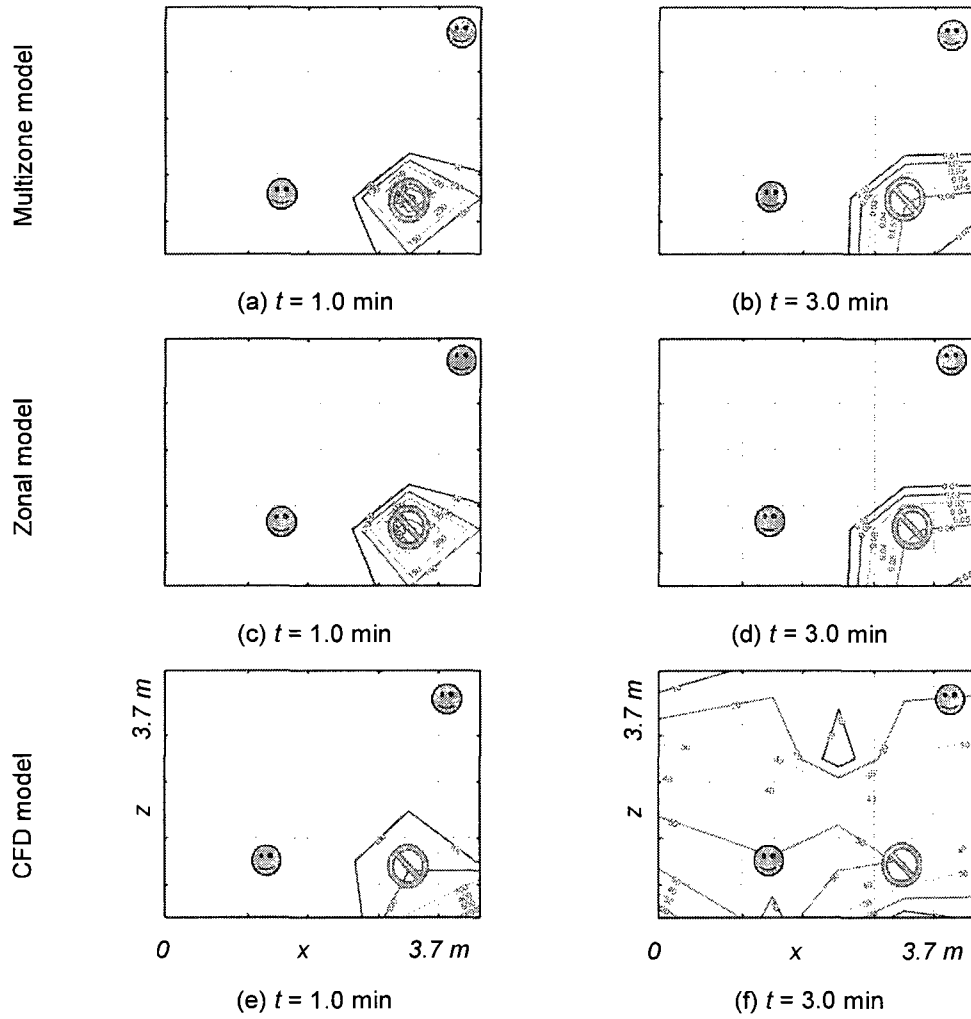


Figure B-26. Contaminant contour plots for Test Case 9, Release #4

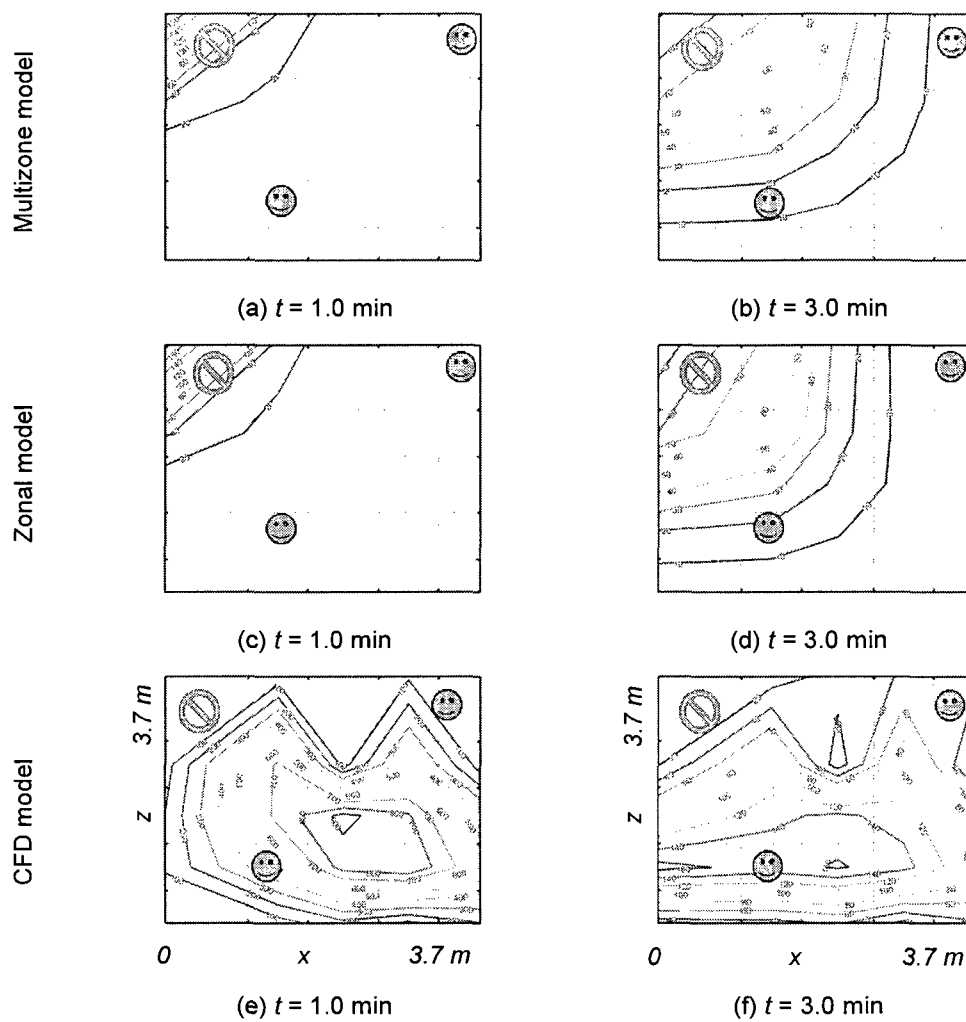


Figure B-27. Contaminant contour plots for Test Case 10, Release #1

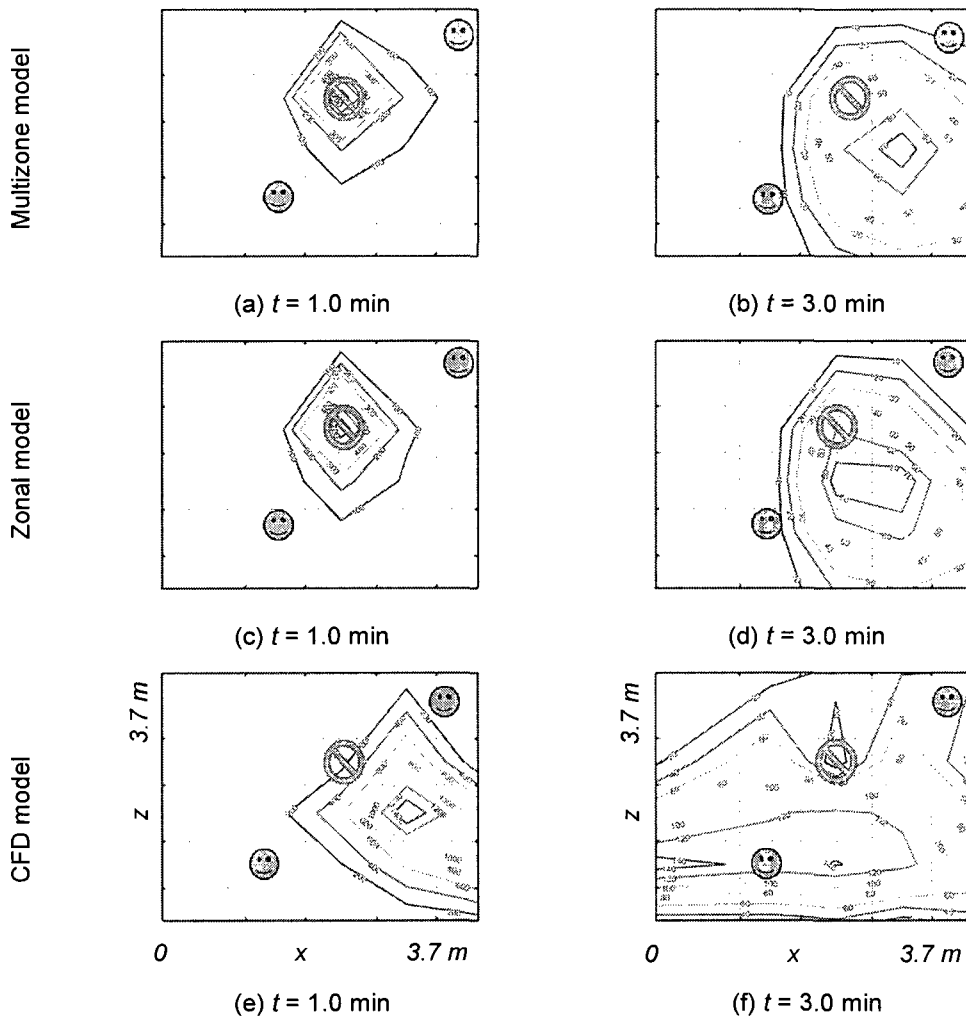


Figure B-28. Contaminant contour plots for Test Case 10, Release #2

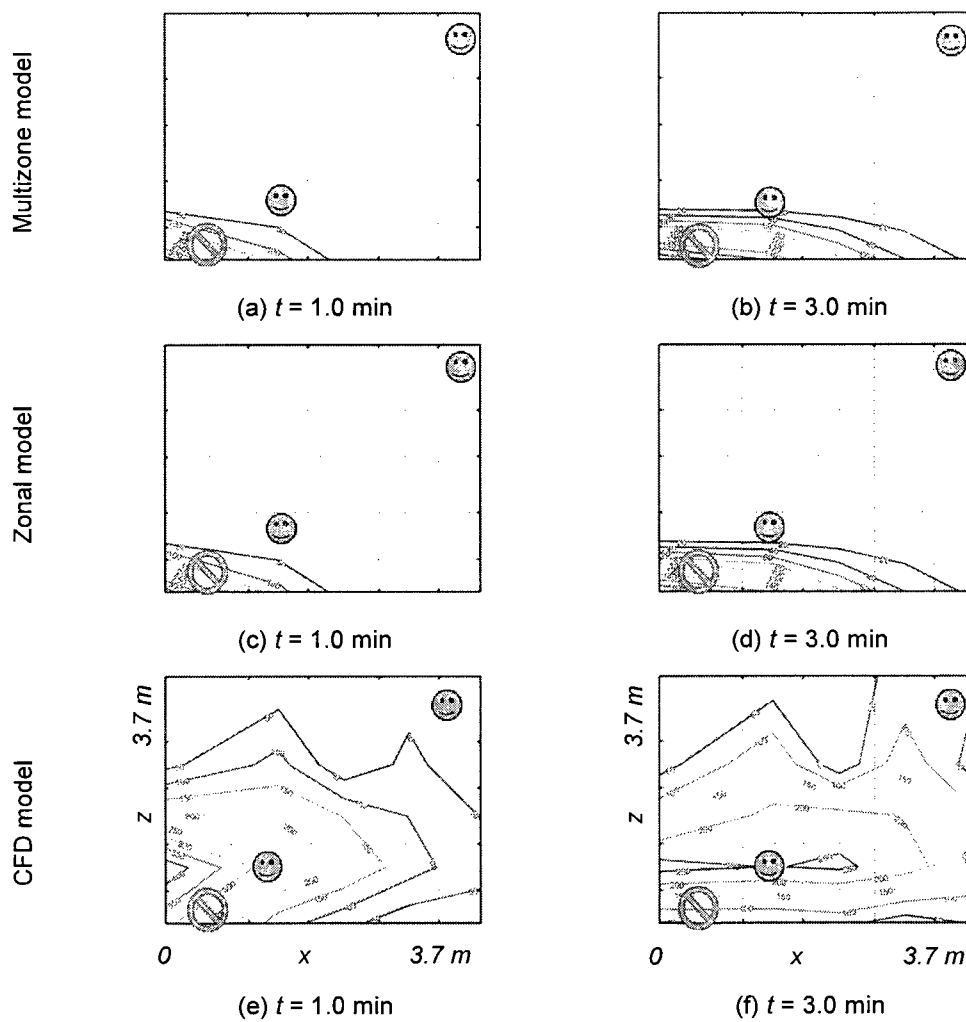


Figure B-29. Contaminant contour plots for Test Case 10, Release #3

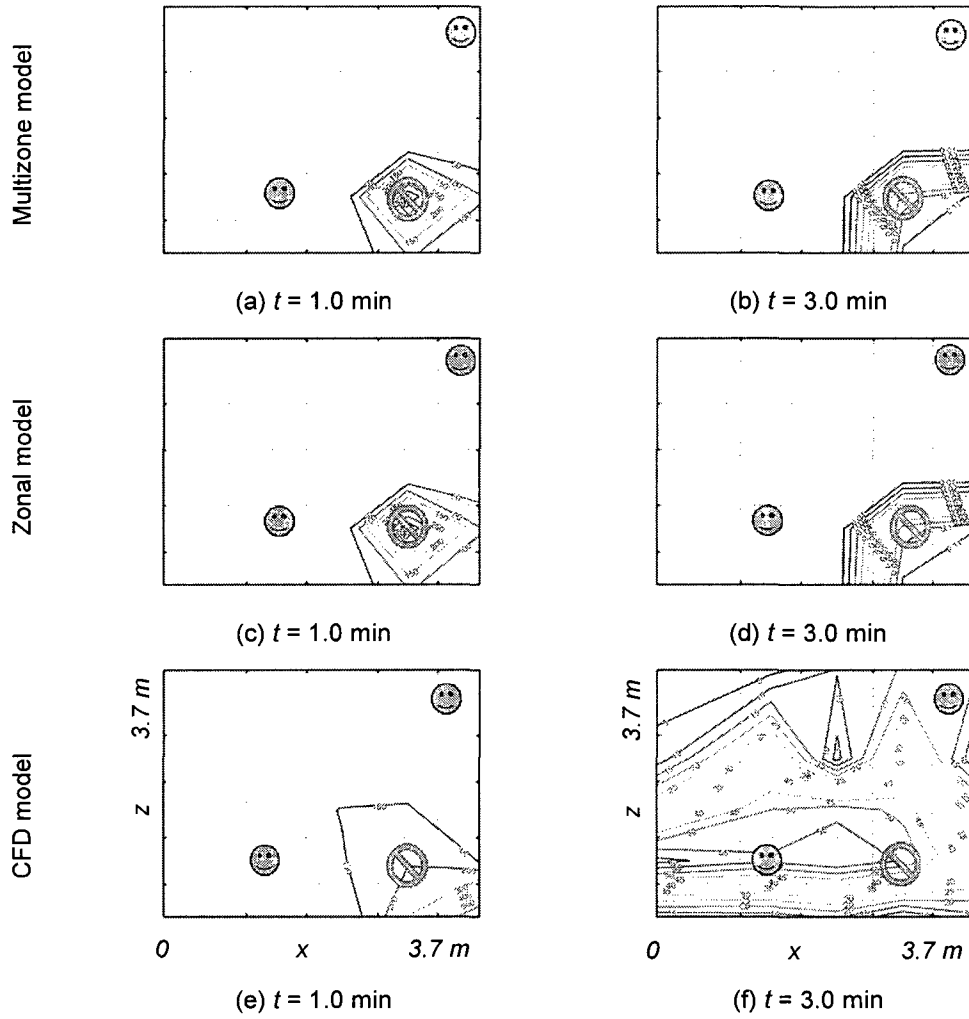


Figure B-30. Contaminant contour plots for Test Case 10, Release #4

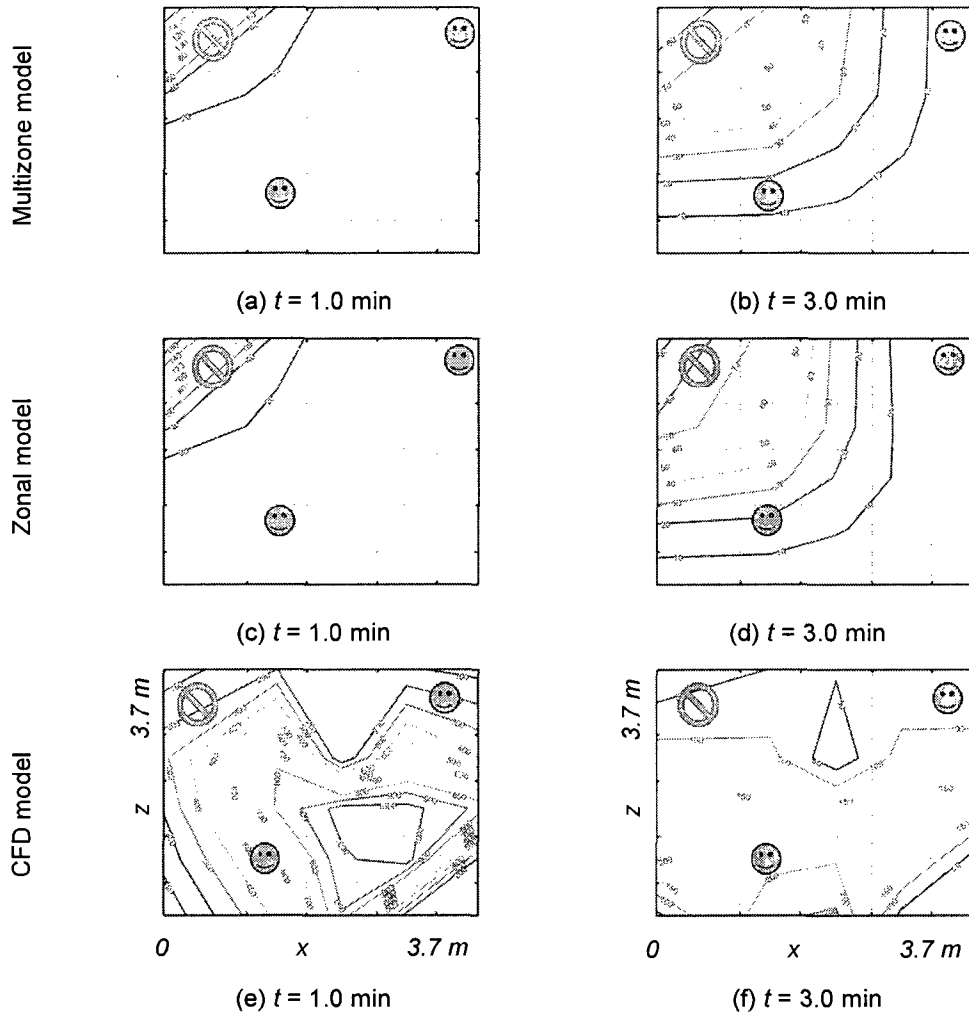


Figure B-31. Contaminant contour plots for Test Case 13, Release #1

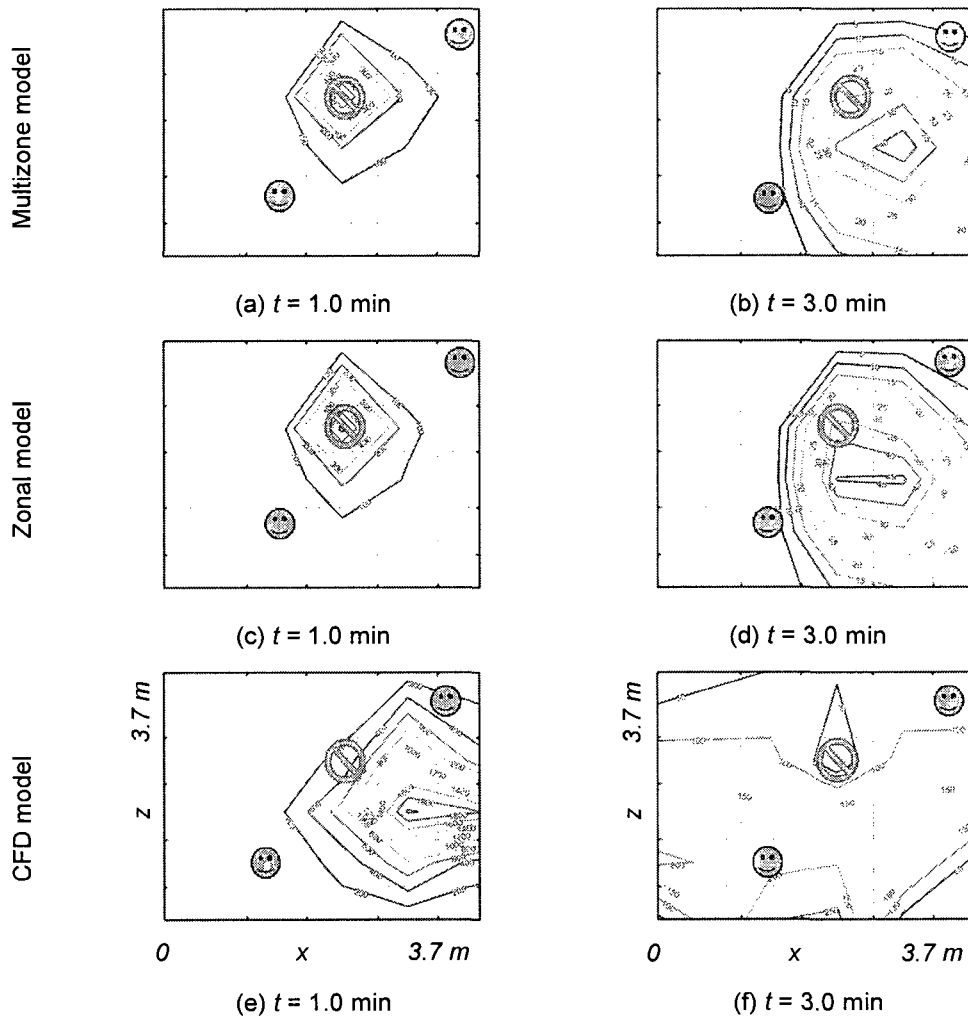


Figure B-32. Contaminant contour plots for Test Case 13, Release #2

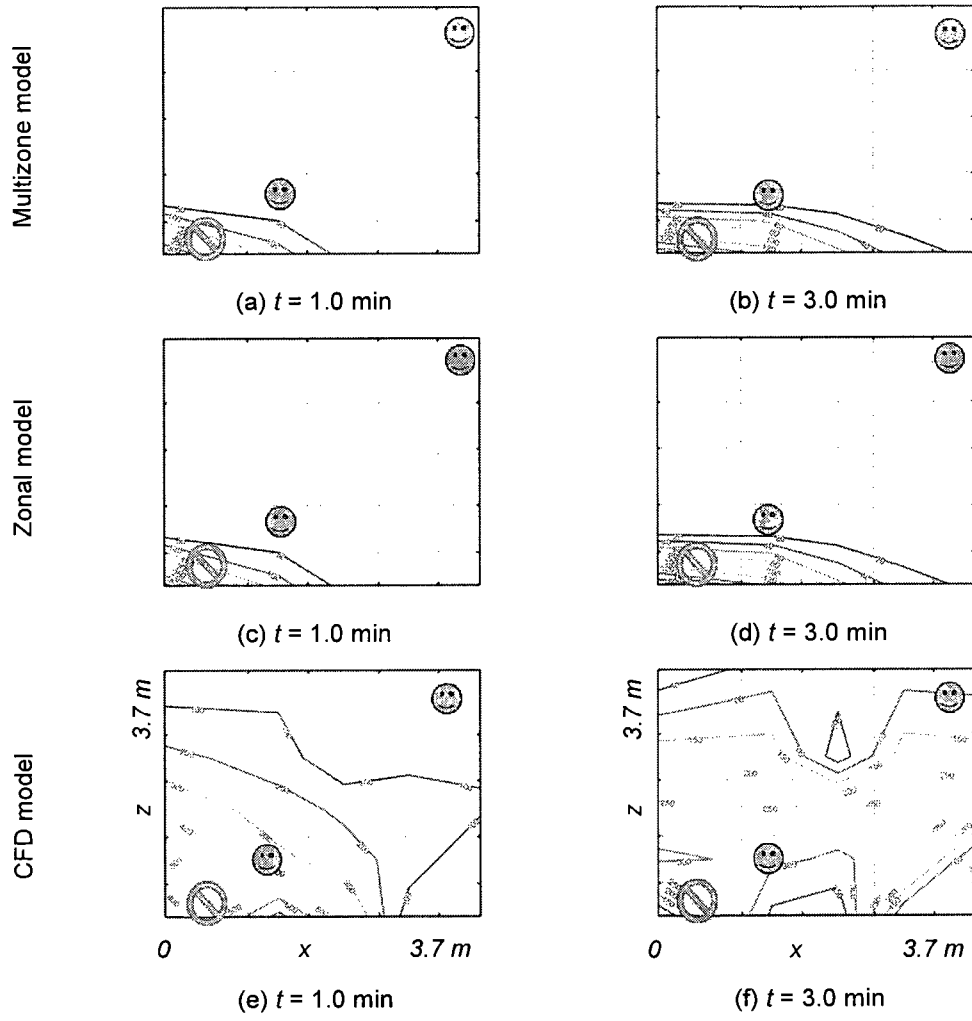


Figure B-33. Contaminant contour plots for Test Case 13, Release #3

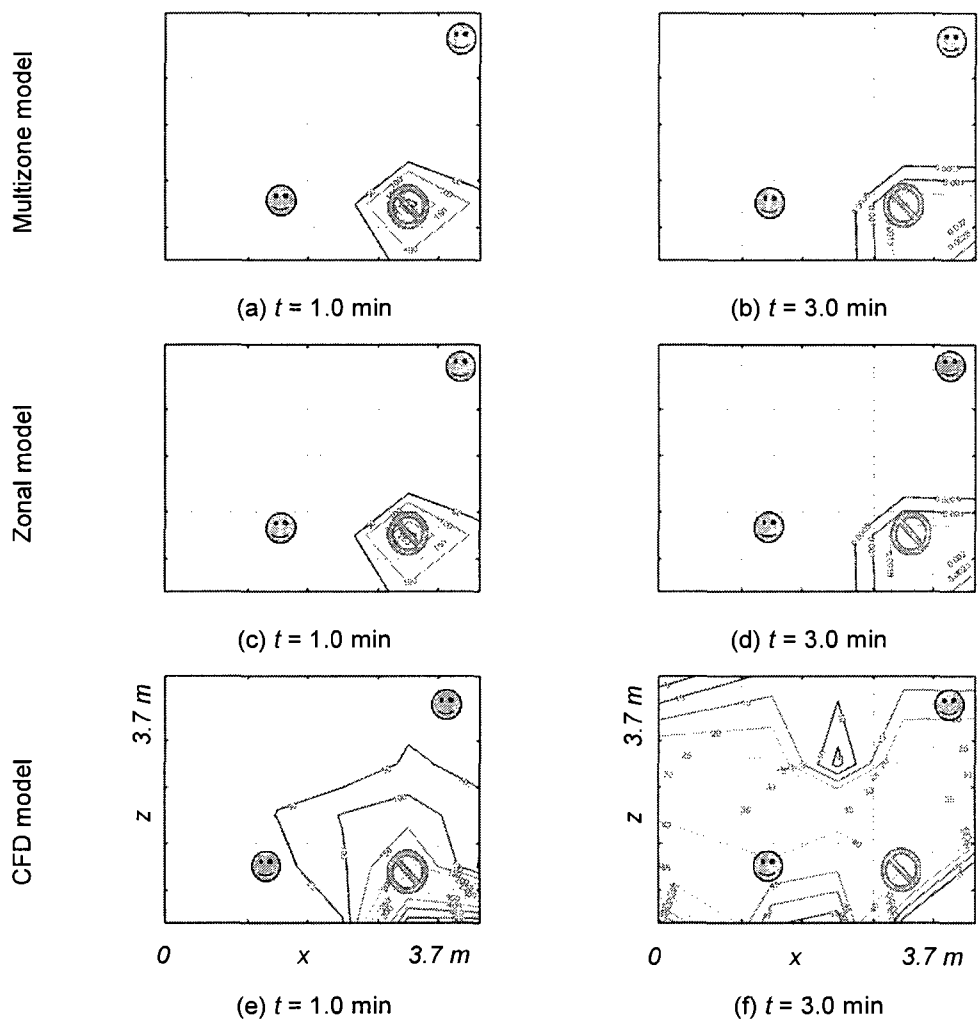


Figure B-34. Contaminant contour plots for Test Case 13, Release #4

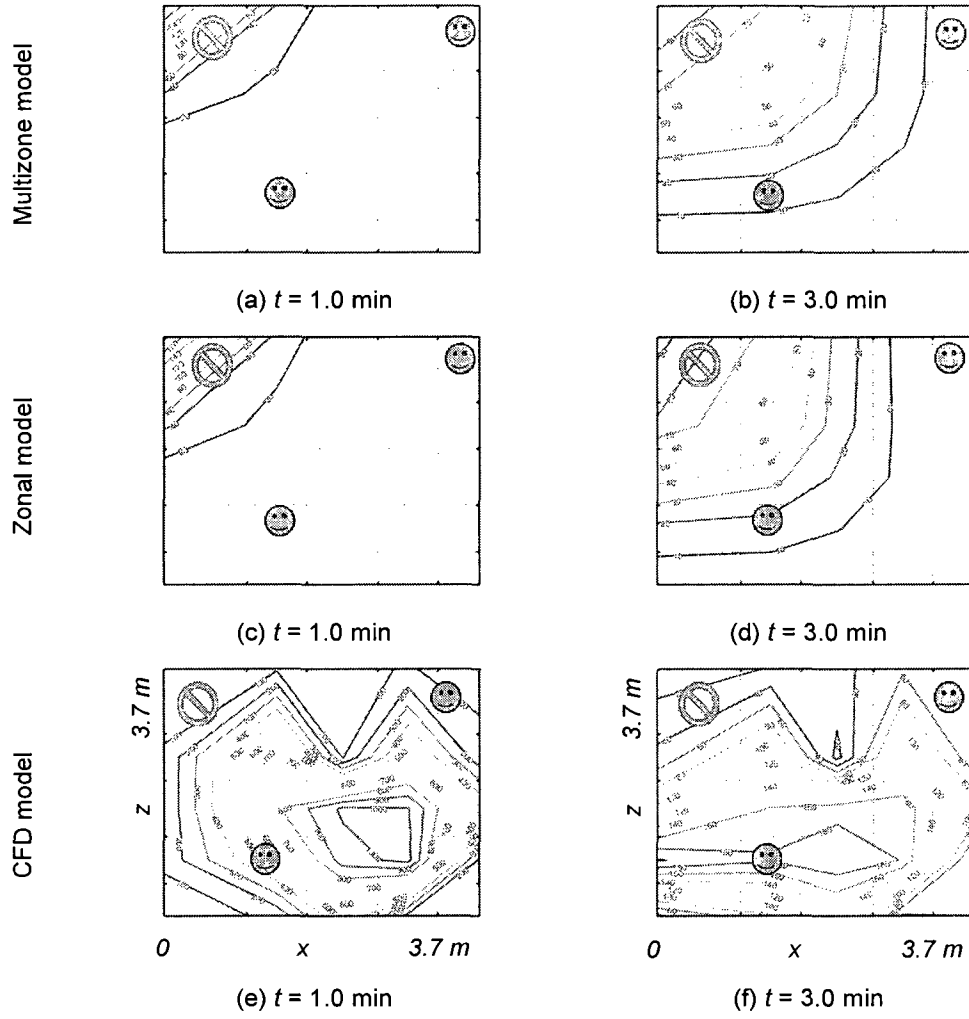


Figure B-35. Contaminant contour plots for Test Case 14, Release #1

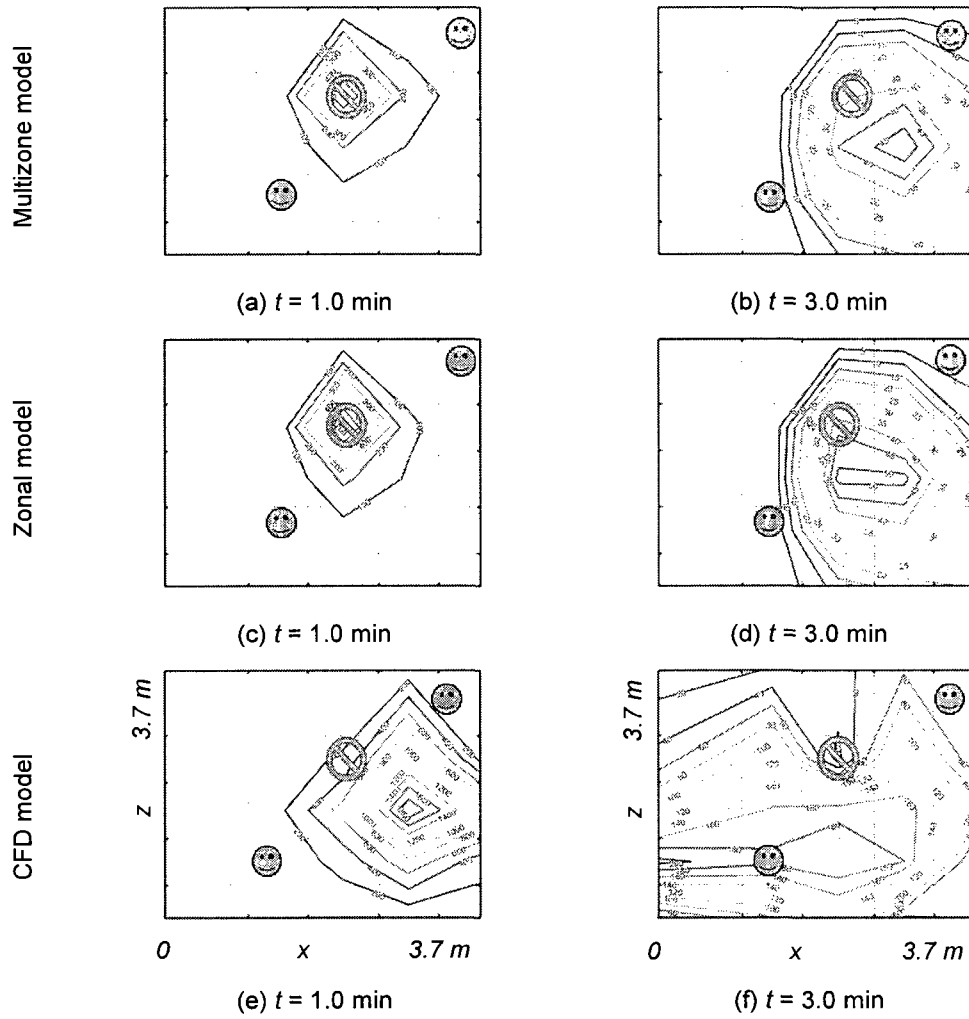


Figure B-36. Contaminant contour plots for Test Case 14, Release #2

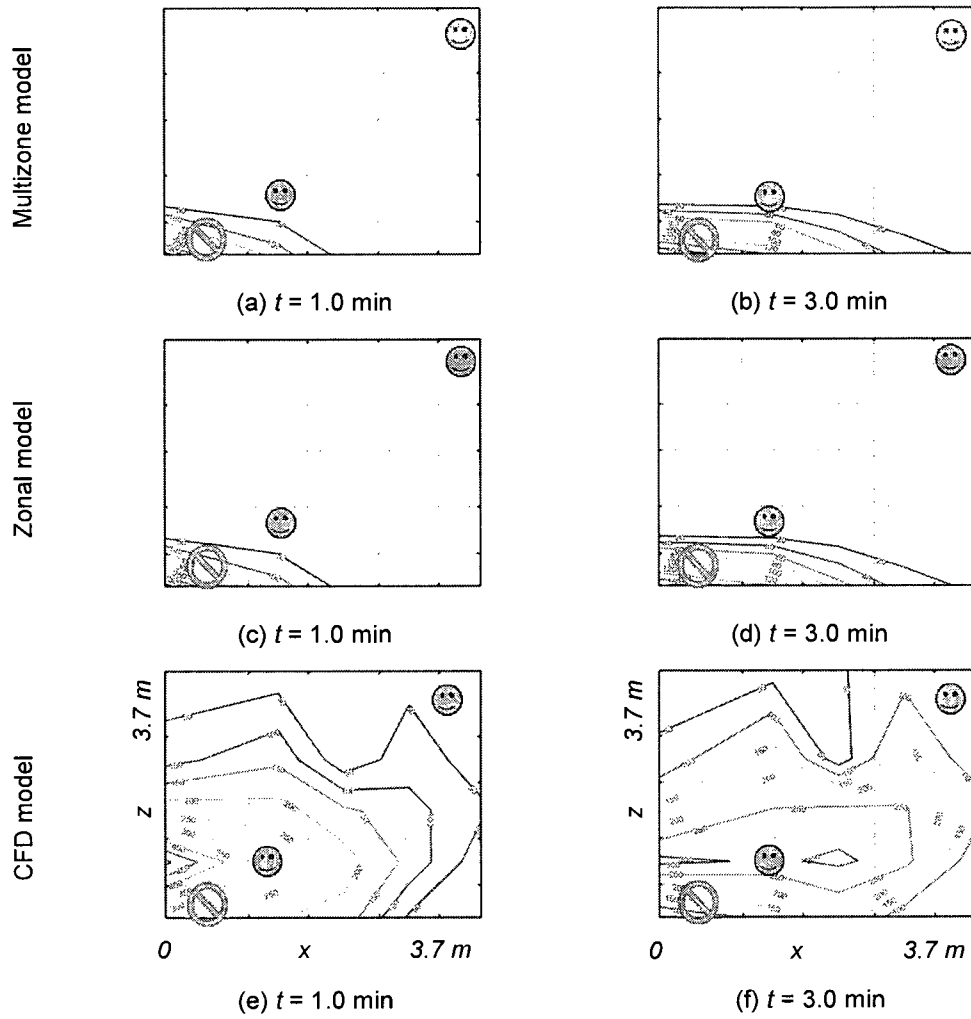


Figure B-37. Contaminant contour plots for Test Case 14, Release #3

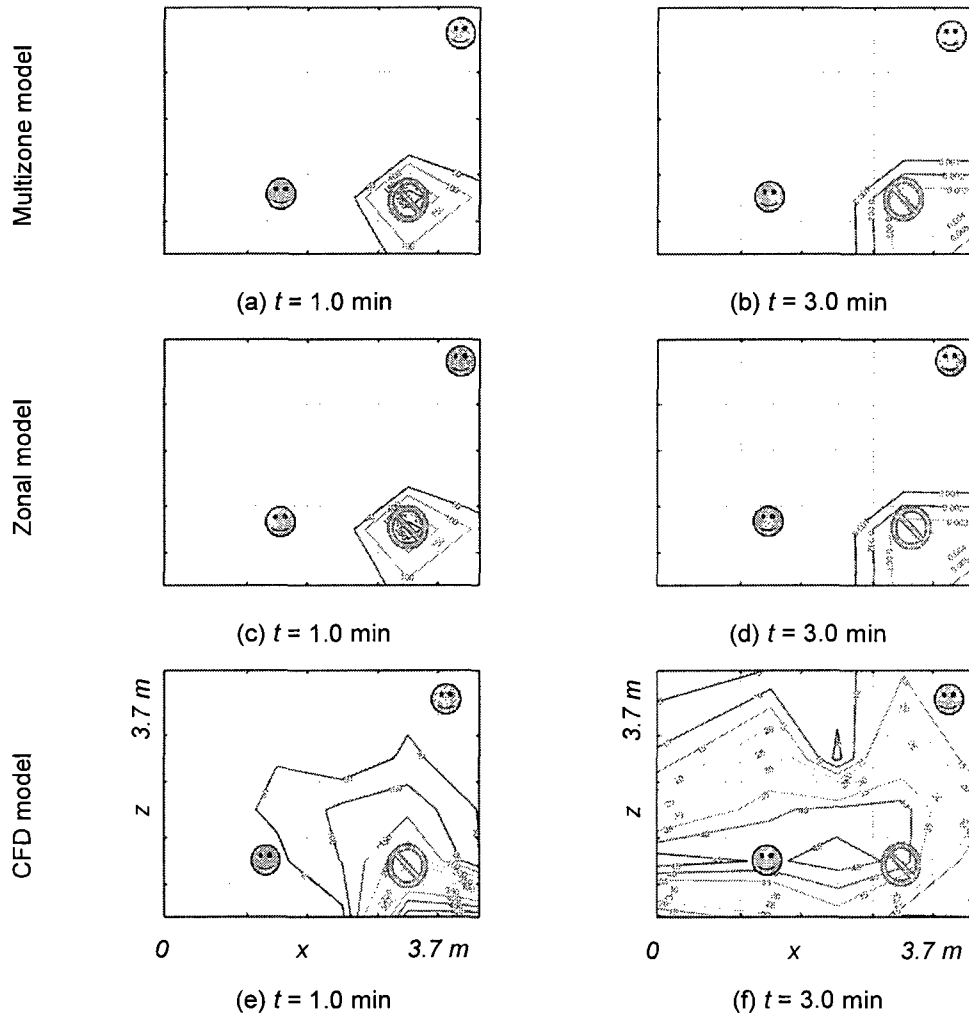


Figure B-38. Contaminant contour plots for Test Case 14, Release #4

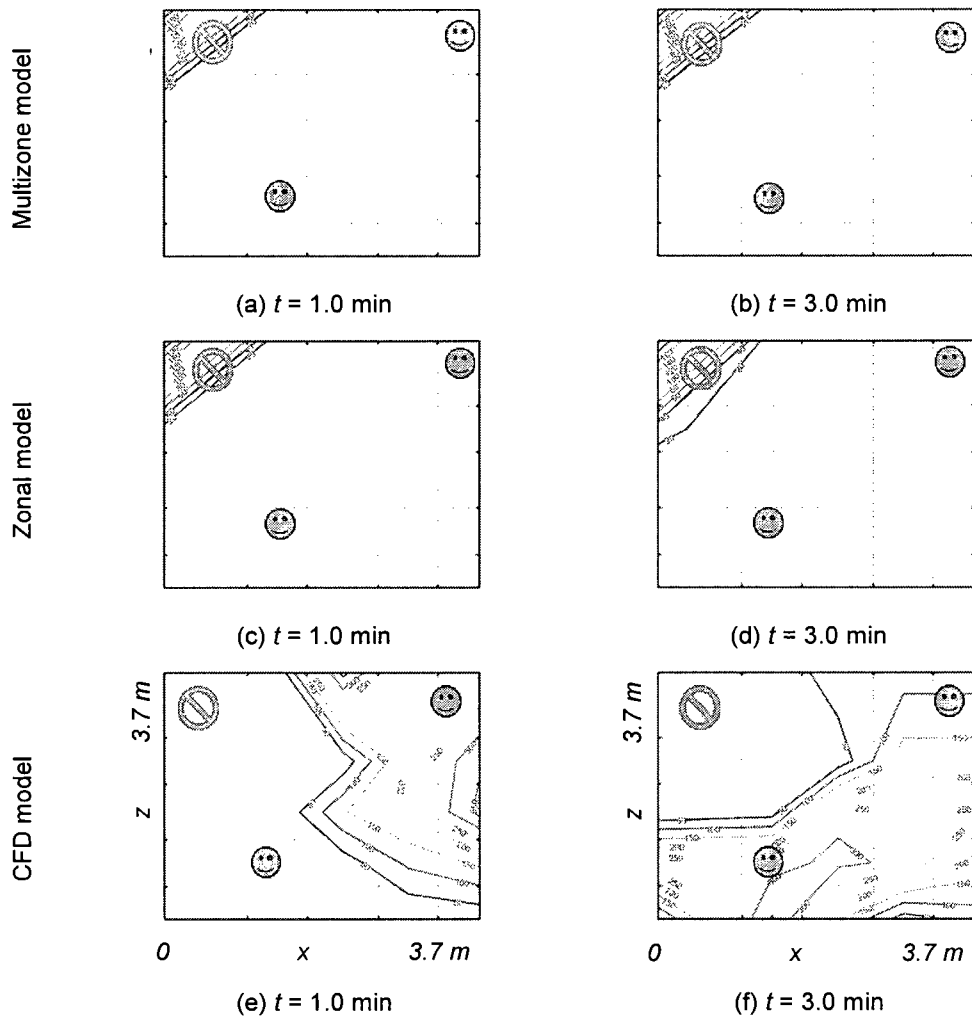


Figure B-39. Contaminant contour plots for Test Case 15, Release #1

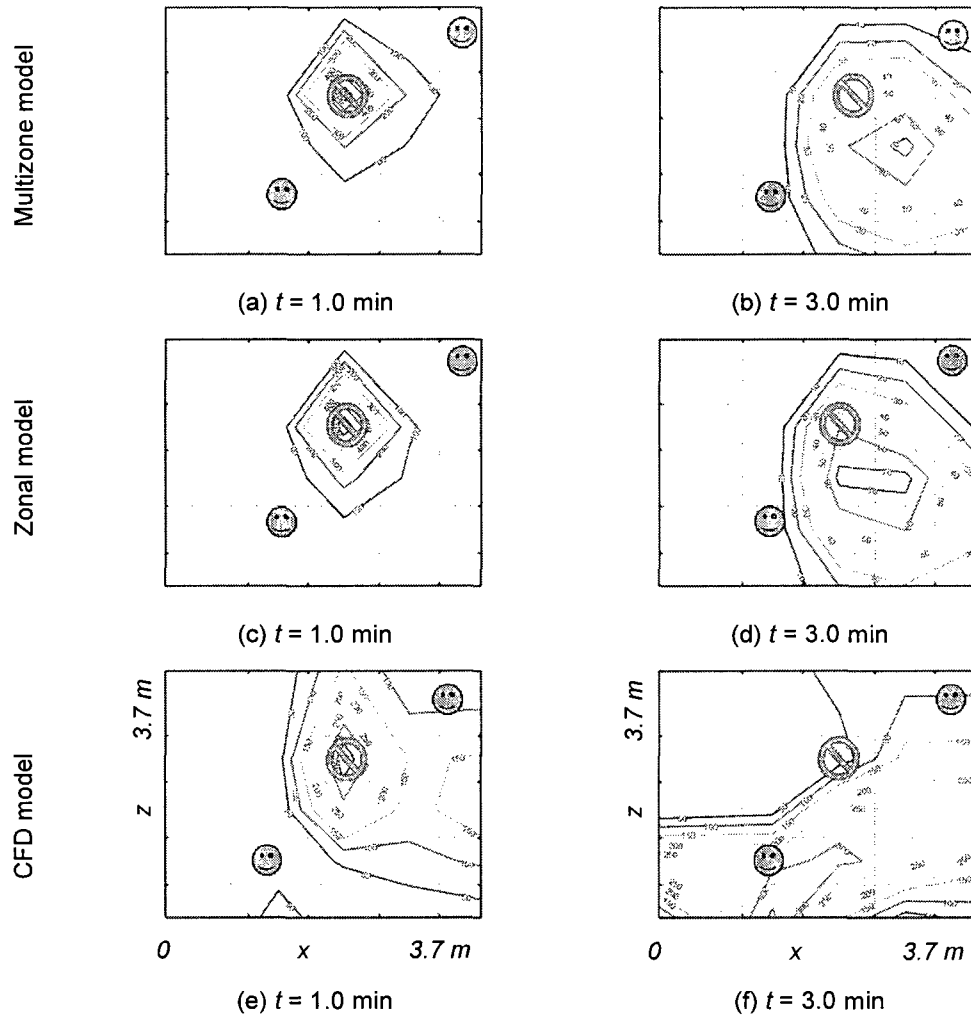


Figure B-40. Contaminant contour plots for Test Case 15, Release #2

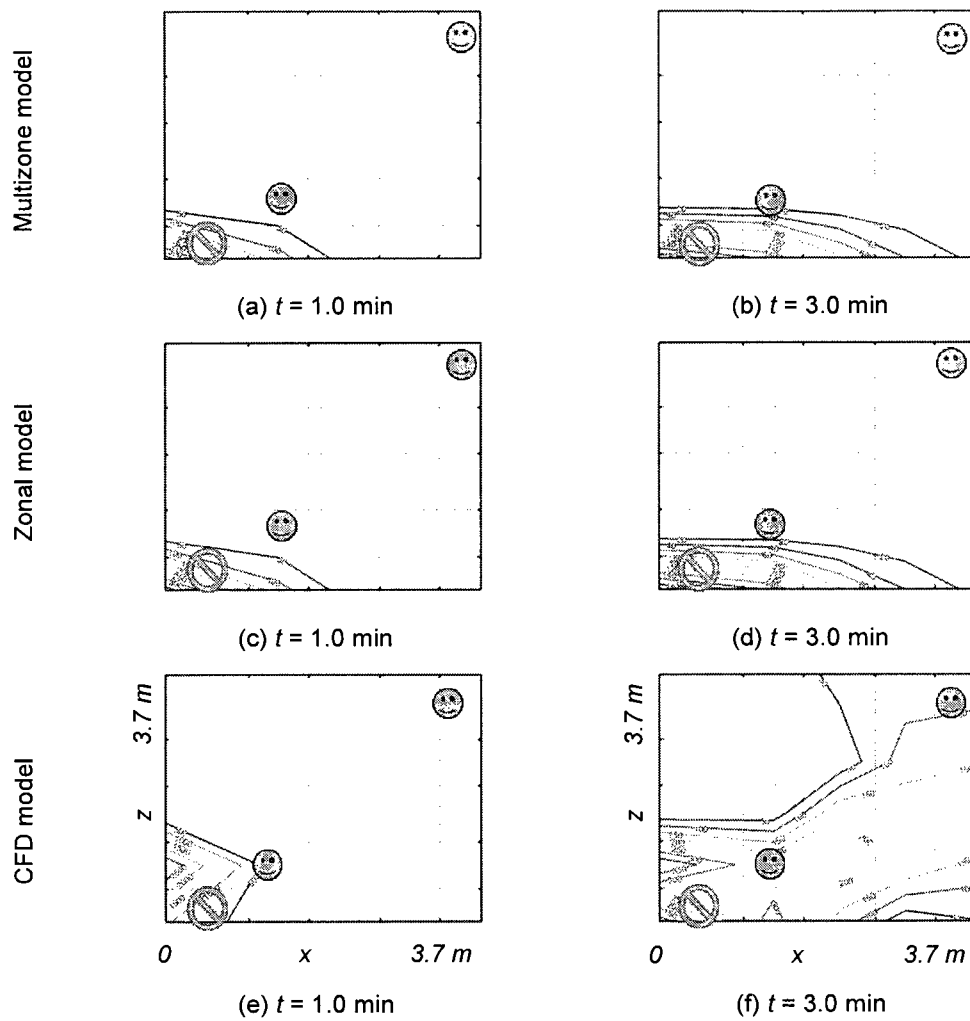


Figure B-41. Contaminant contour plots for Test Case 15, Release #3

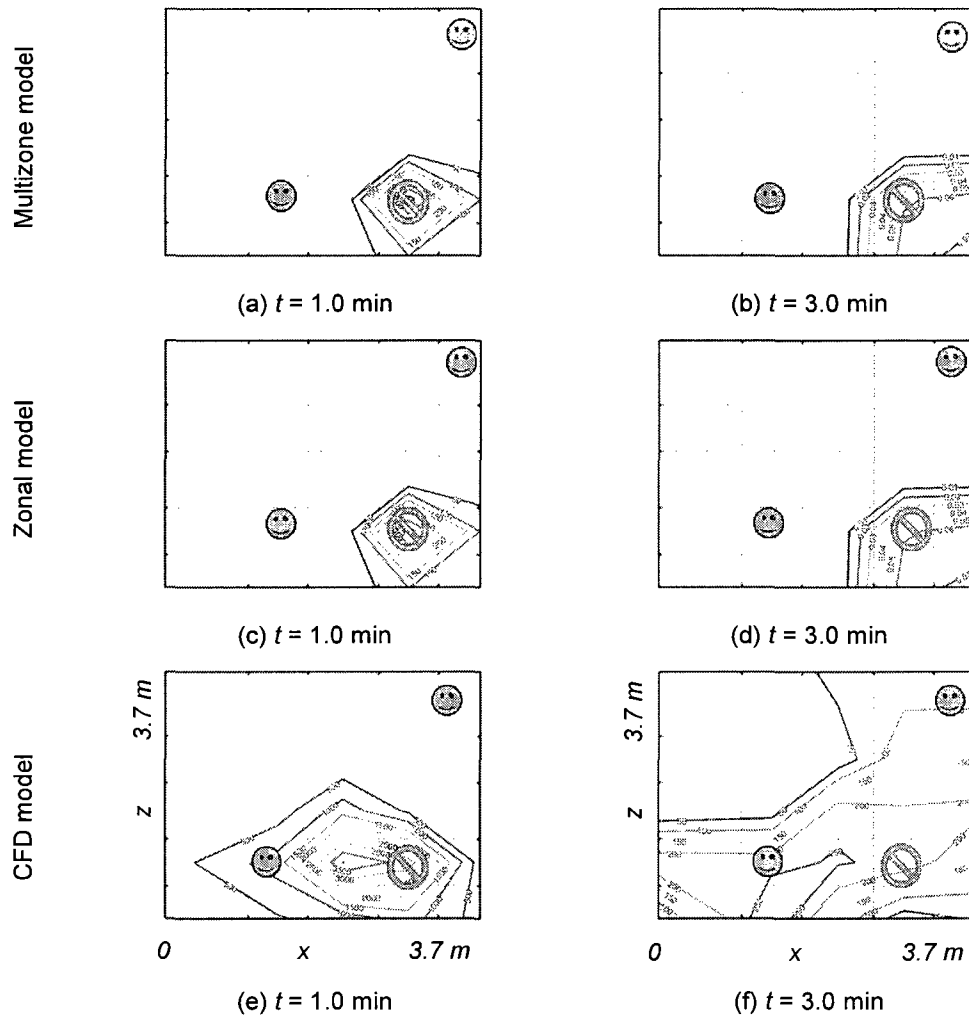


Figure B-42. Contaminant contour plots for Test Case 15, Release #4

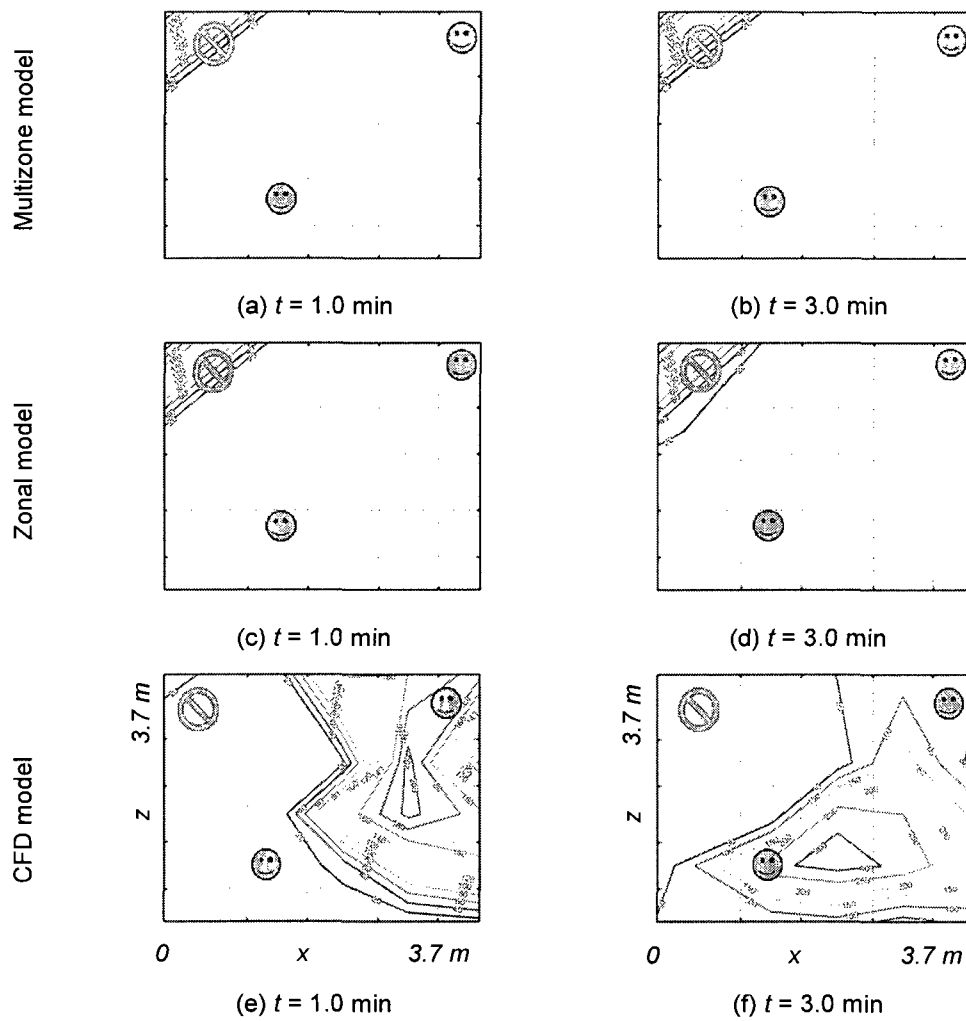


Figure B-43. Contaminant contour plots for Test Case 16, Release #1

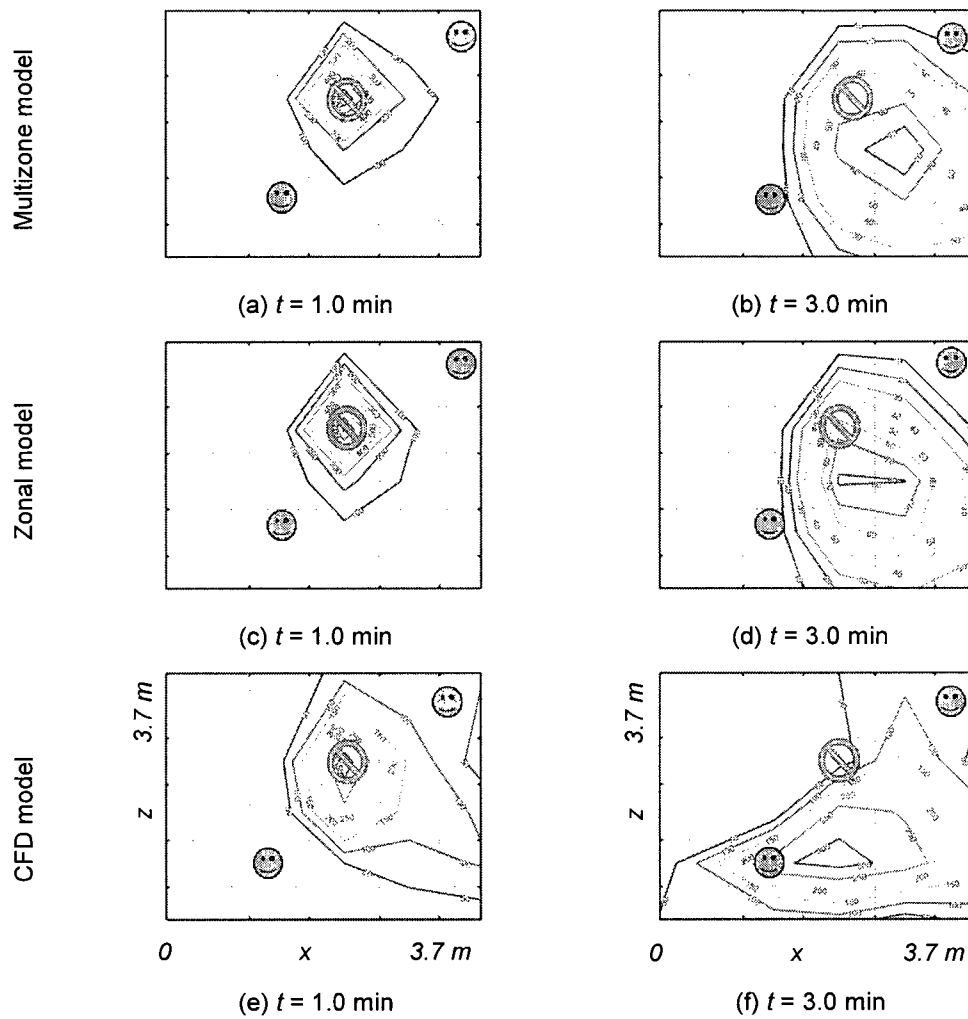


Figure B-44. Contaminant contour plots for Test Case 16, Release #2

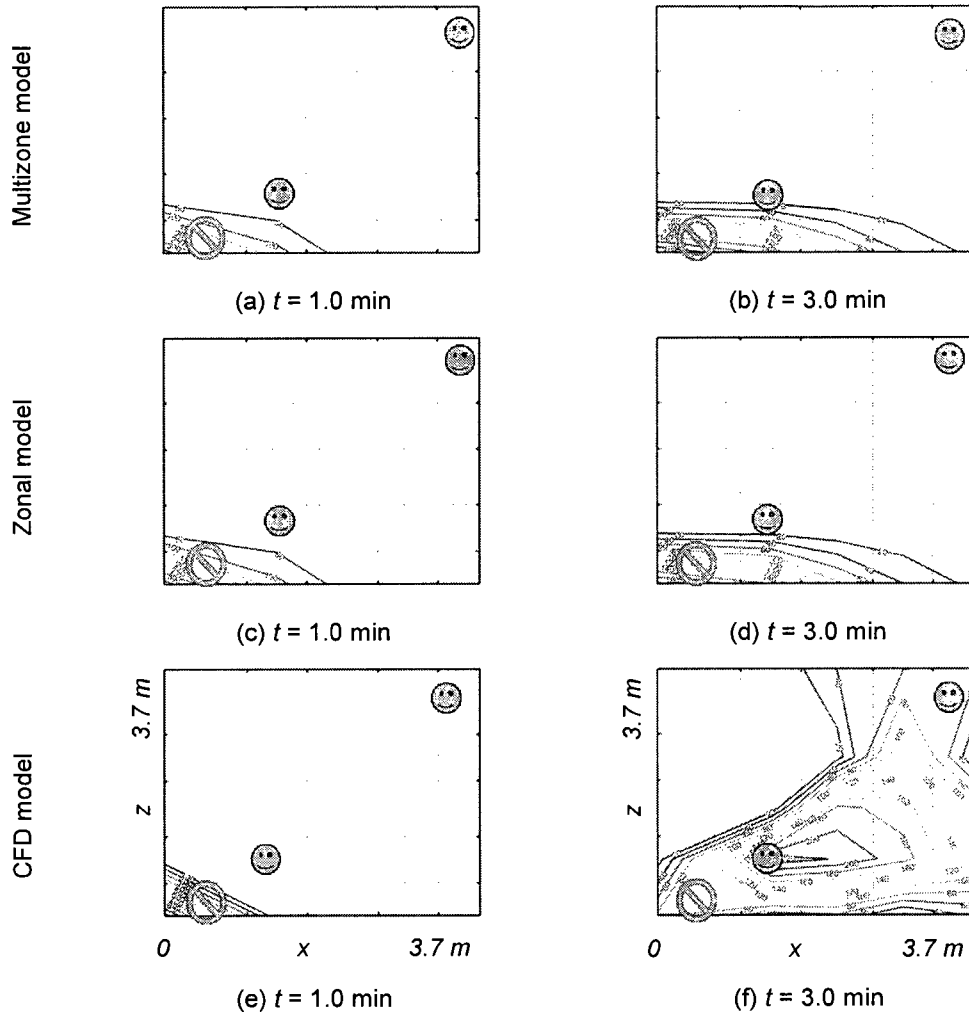


Figure B-45. Contaminant contour plots for Test Case 16, Release #3

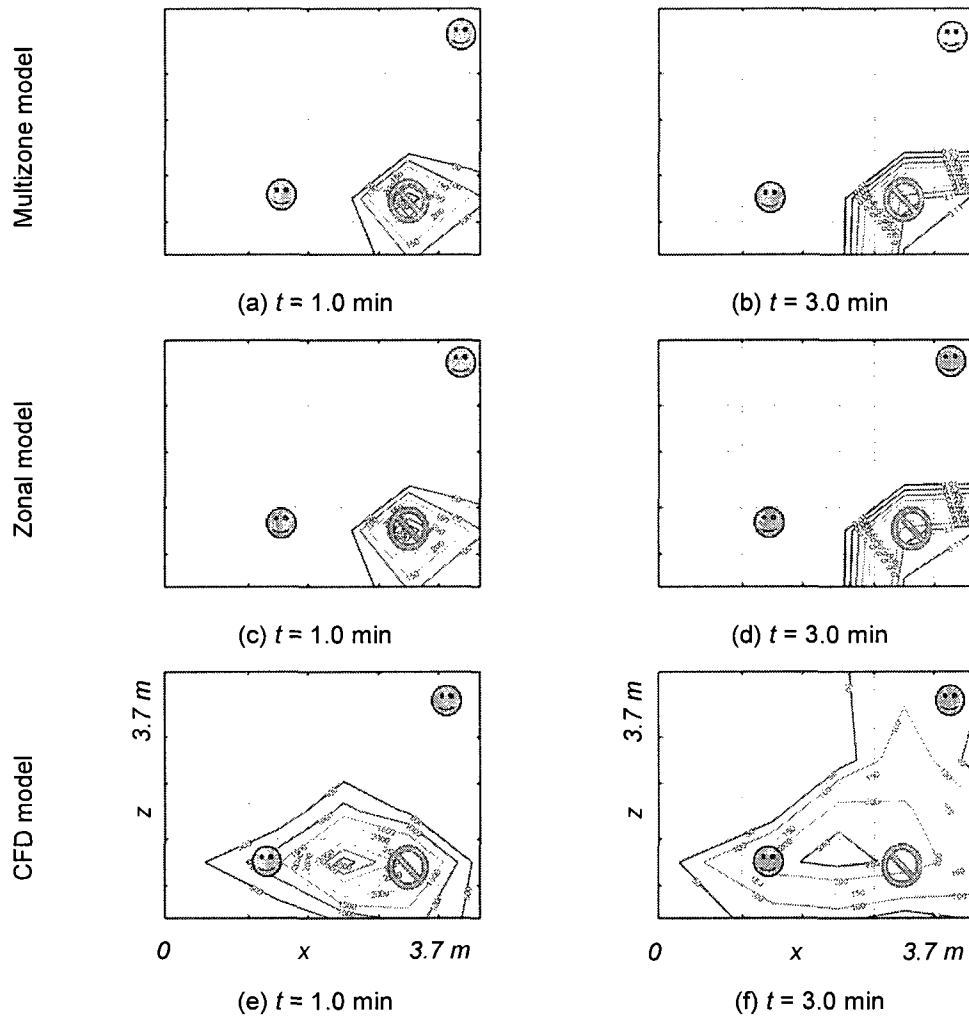


Figure B-46. Contaminant contour plots for Test Case 16, Release #4

Figure B-47 to Figure B-54 compares the respective test cases for each test zone *with* infiltration. There is a figure for each contaminant release (#1 to #4). They are shown for $t = 1.0$ min. In general, contaminant transport is *greater* for the test cases with the wall-mounted diffuser. Though not obviously apparent from observing the figures, every *subzone* location was an *optimal* sensor location for the test cases with the wall-mounted diffuser, *except* for Test Cases 15 and 16 (both furniture under the diffuser).

Further, the test cases *with* infiltration showed *less effective* contaminant transport than the test case *without* infiltration. The test cases with *furniture under the exhaust* show *more effective* (or about the same) contaminant transport than the test cases with *no furniture*. Lastly, the test cases with *furniture under the diffuser* show *less effective* contaminant transport than the test cases with *no furniture* (except for Release #4 since it was close to the exhaust. Its transport was not *as affected* by furniture under the diffuser).

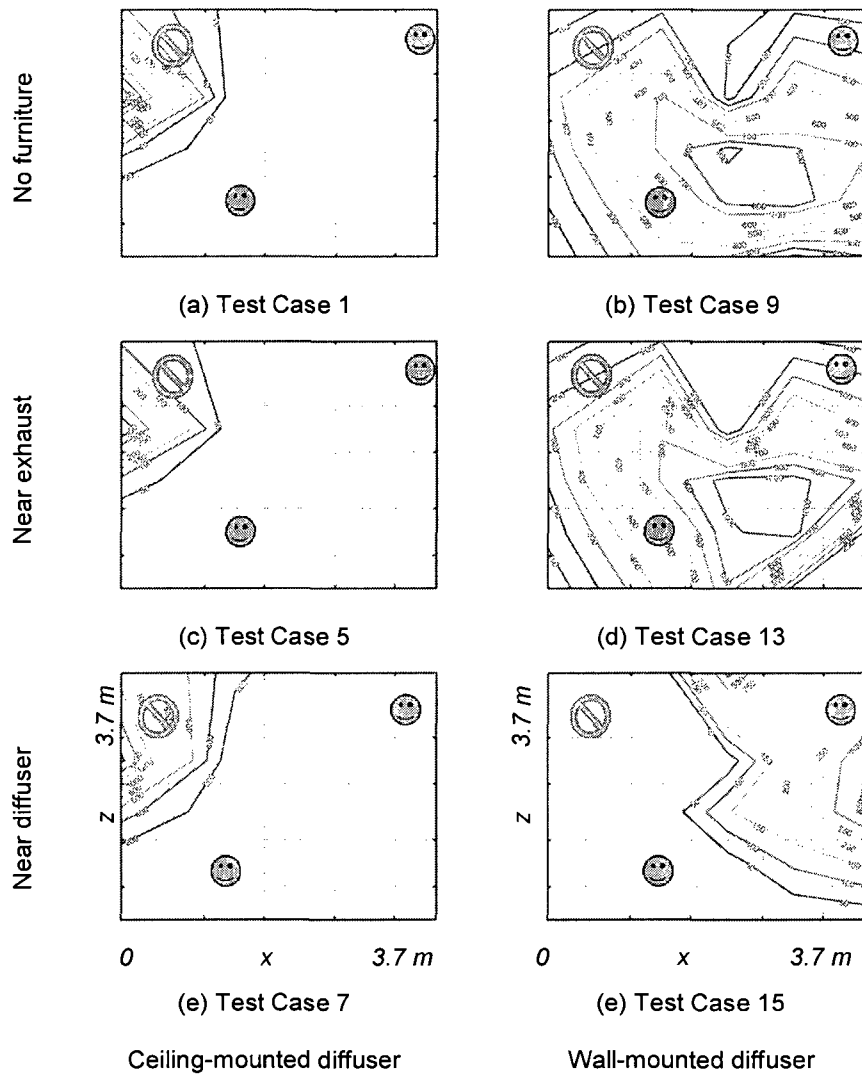


Figure B-47. Contaminant contour plots for Release #1 without infiltration

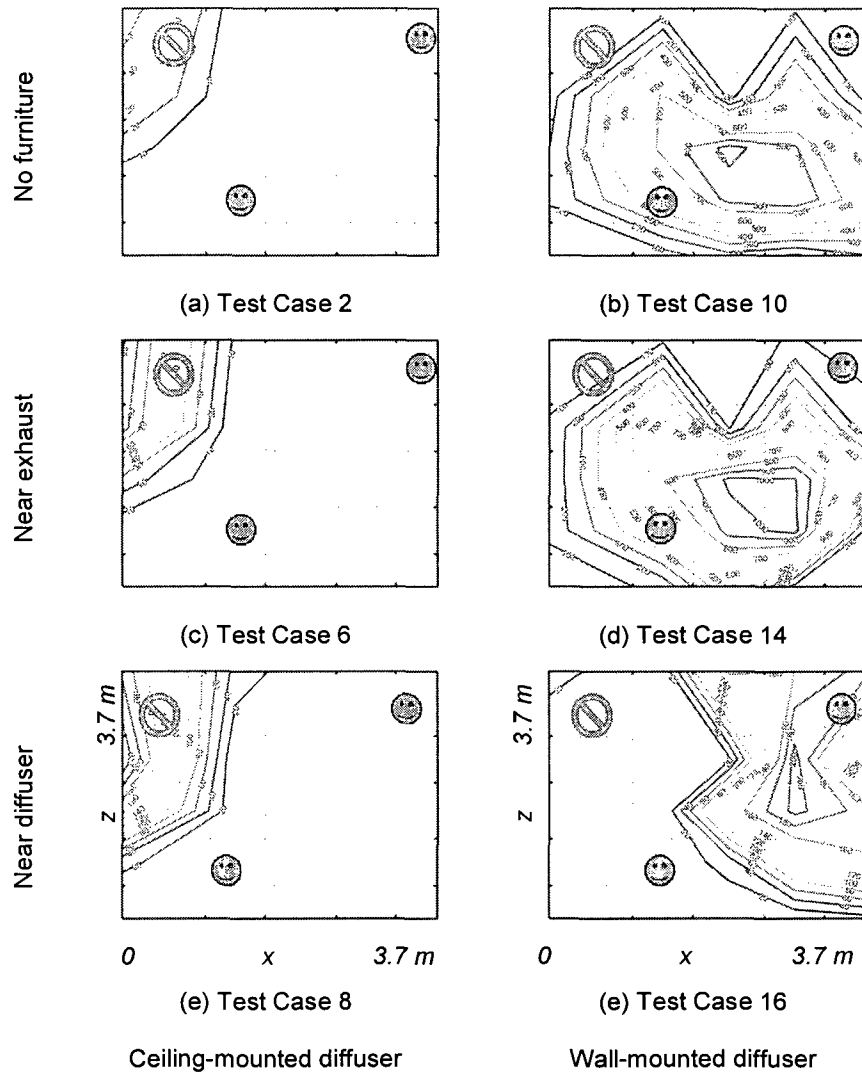


Figure B-48. Contaminant contour plots for Release #1 with infiltration

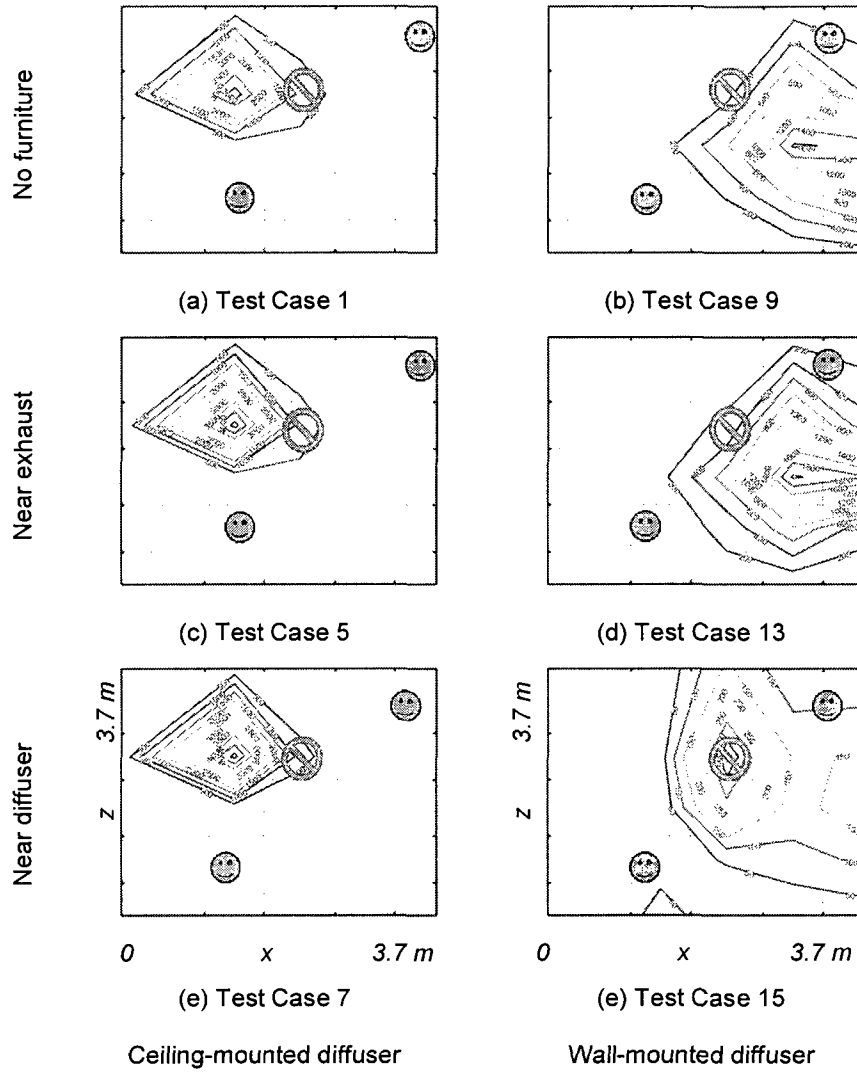


Figure B-49. Contaminant contour plots for Release #2 without infiltration

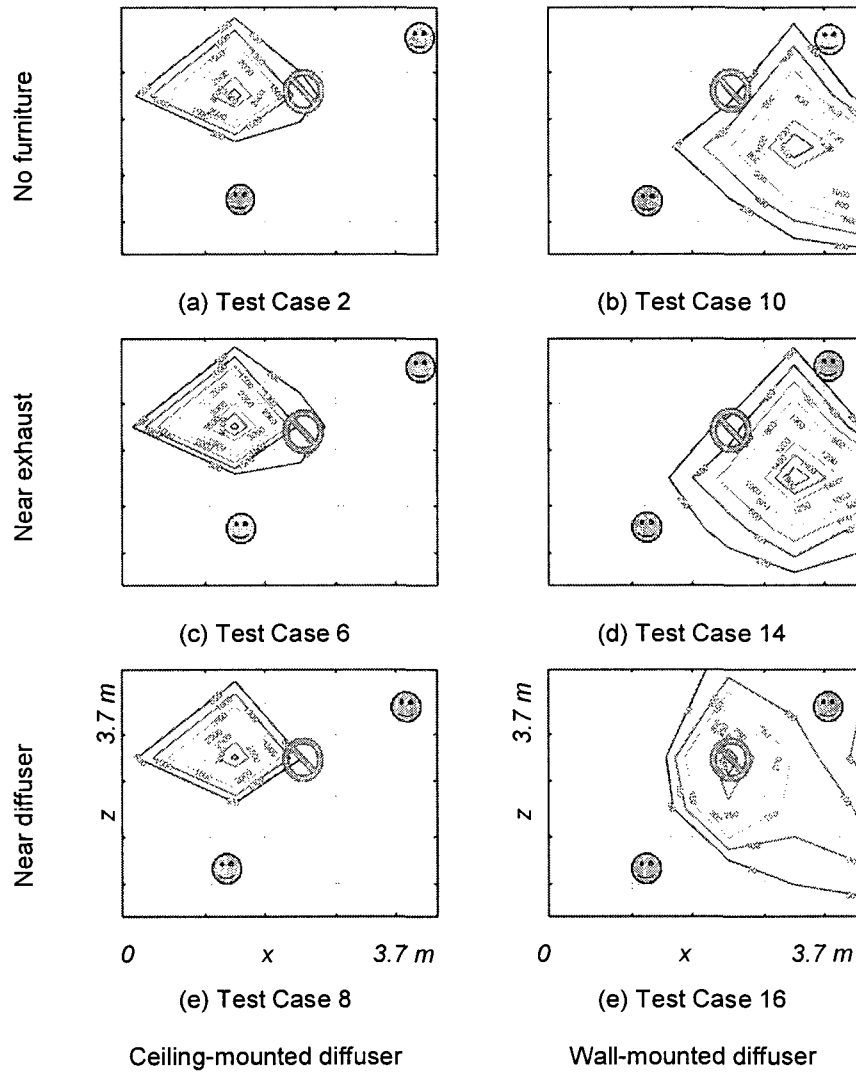


Figure B-50. Contaminant contour plots for Release #2 with infiltration

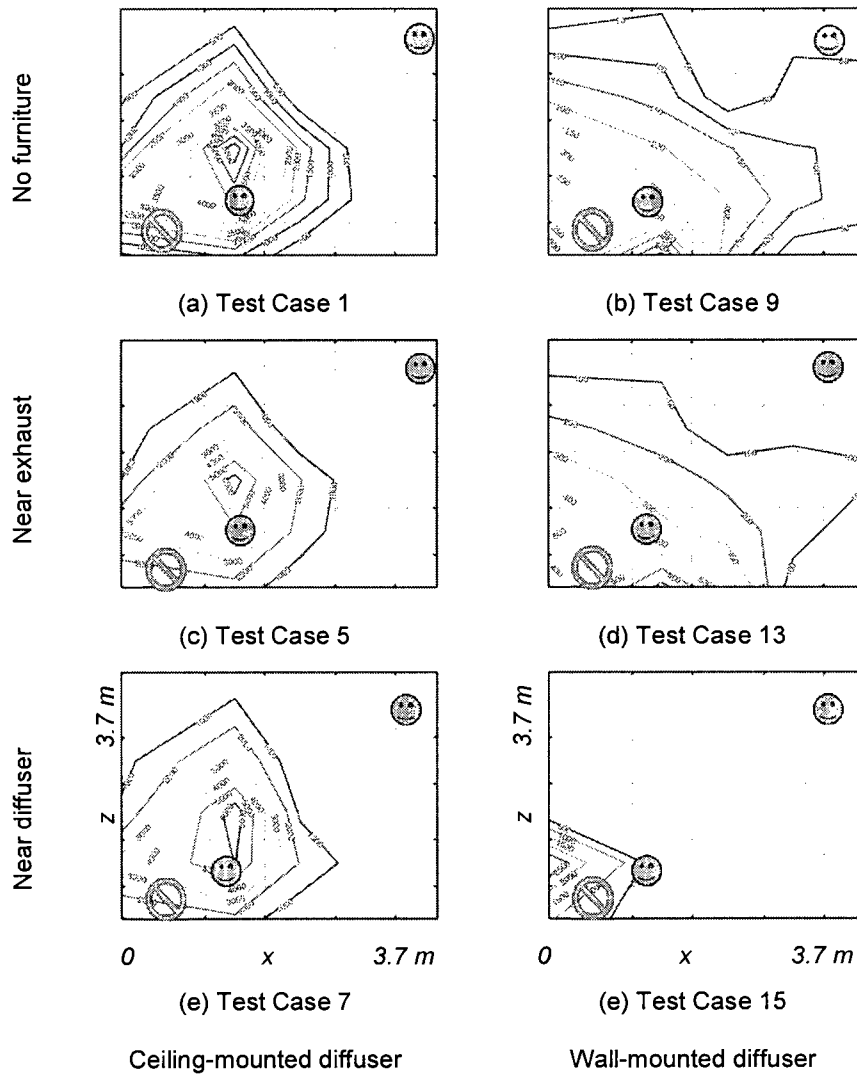


Figure B-51. Contaminant contour plots for Release #3 without infiltration

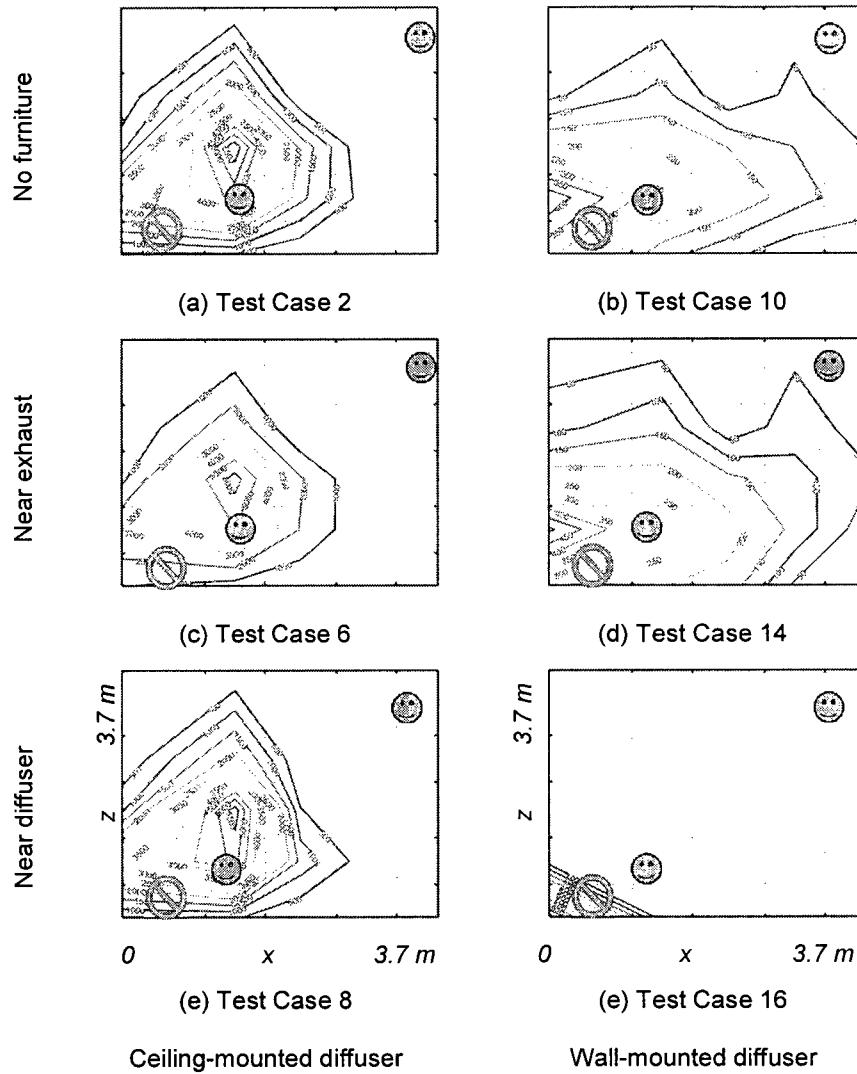


Figure B-52. Contaminant contour plots for Release #3 with infiltration

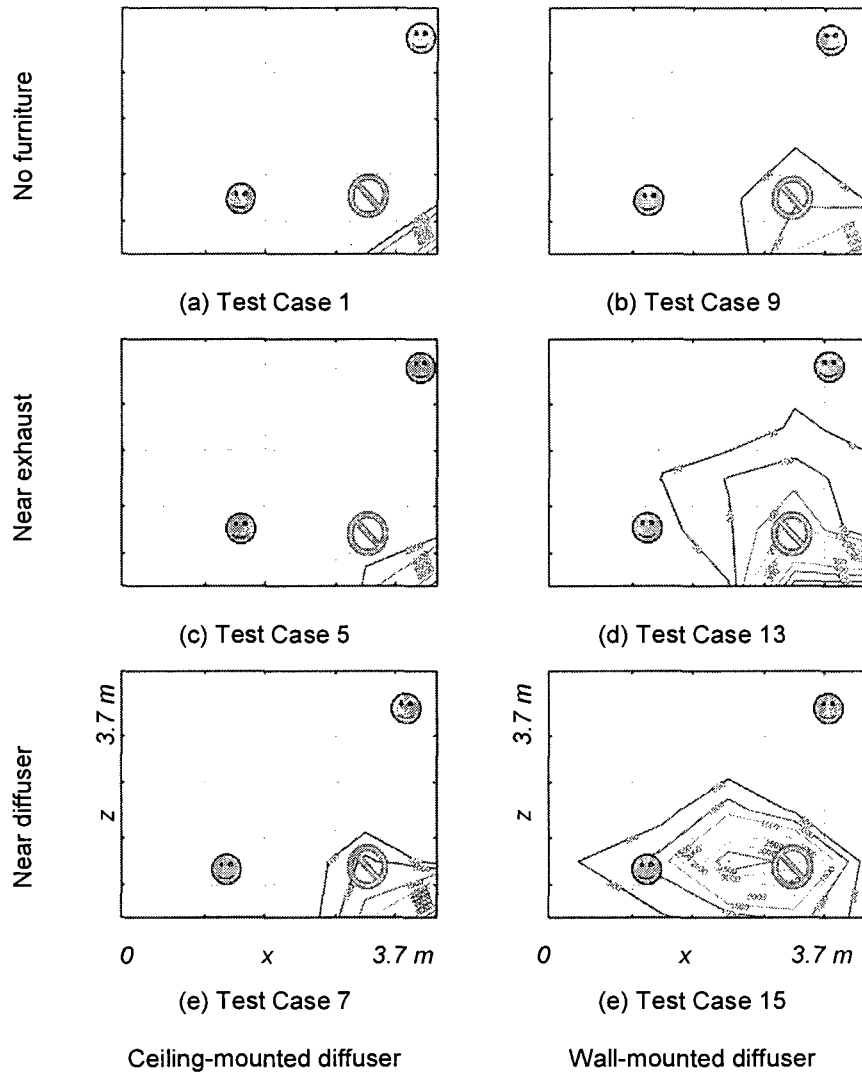


Figure B-53. Contaminant contour plots for Release #4 without infiltration

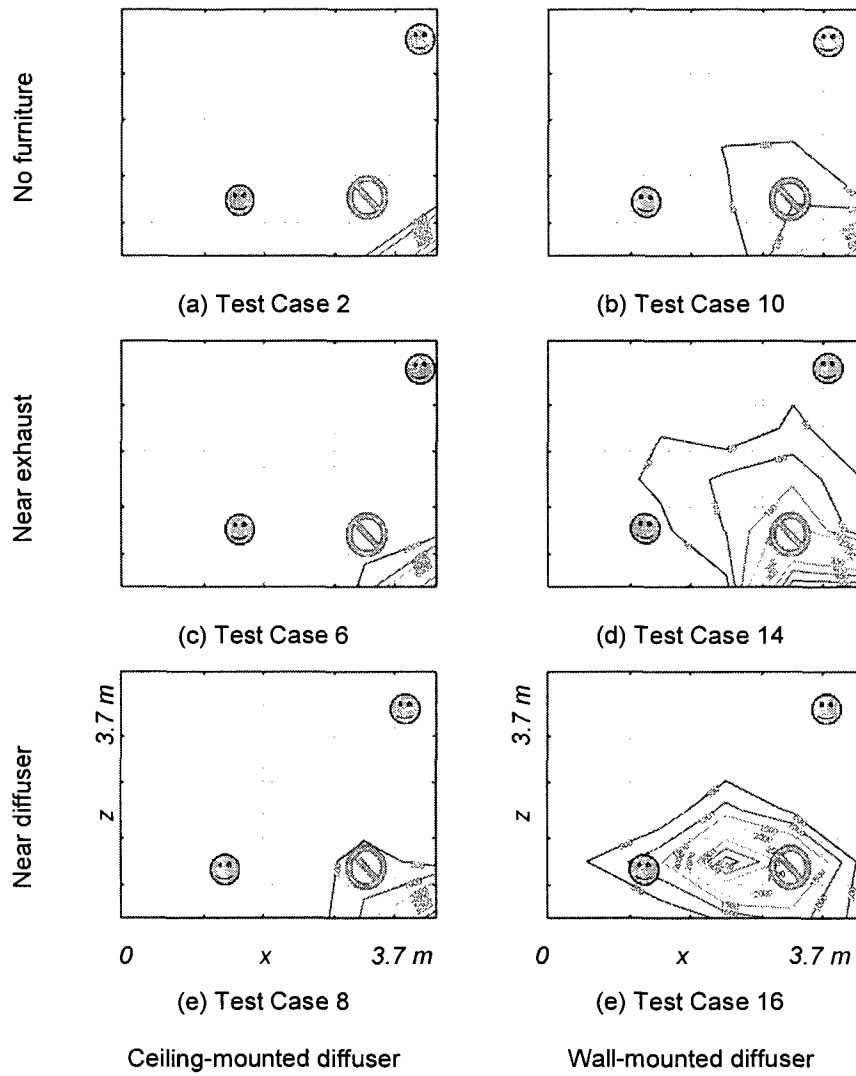


Figure B-54. Contaminant contour plots for Release #4 with infiltration

Table B-1 to Table B-8 summarize the sensor systems designed using the simpler airflow models for each test case simulated for zone $A[-]$, $B[-]$, which has the ceiling-mounted diffuser and exhaust.

Tables for selected test cases were reported in Chapter 2 and will not be repeated here. Sensor system designs for Test Case 1 using multizone and zonal model data are given on page 75 and 75, respectively. Those for Test Case 7 using multizone and zonal model data are given on page 80 and 80, respectively.

Table B-1. Sensor system designs for Test Case 2 using multizone model data.

Sensor sys. [1]	Qty [2]	Obj. func. [3]	Locations using multizone data [4]	Objective function value (complementary obj. func. value)			Locations using CFD data [8]	Col. [6] equiv. to [7]? [9]
				Multizone-optimal [5]	CFD-benchmarked [6]	CFD-optimal [7]		
1	4	D	231,351, 445,535	1.0 (5.6e-8)	1.0	1.0		Y
2	4	E	141,213, 322,552	5.6e-8 (1.0)	9.5e-4	9.5e-4		Y
3	3	D	151,331, 442	1.0 (5.6e-8)	1.0	1.0		Y
4	3	E	221,523, 551	5.6e-8 (1.0)	9.5e-4	9.5e-4		Y
5	2	D	151,551	1.0 (5.6e-8)	1.0	1.0		Y
6	2	E	131,552	5.6e-8 (1.0)	9.5e-4	9.5e-4		Y
7	1	D	451*	1.25 (9.8e-7)	1.5	1.0	252	N
8	1	E	431	5.6e-8 (500.5)	9.6e-4	9.5e-4	252	N
Eng	1	D (E)	555	2.25 (1.2e-5)	1.5 (1.1e-3)	1.0 (9.5e-4)	255	N

* unique sensor system

Table B-2. Sensor system designs for Test Case 2 using zonal model data.

Sensor sys. [1]	Qty [2]	Obj. func. [3]	Locations using zonal data [4]	Objective function value (complementary obj. func. value)			Locations using CFD data [8]	Col. [6] equiv. to [7]? [9]
				Zonal-optimal [5]	CFD-benchmarked [6]	CFD-optimal [7]		
1	4	D	114,212, 324,453	1.0 (2.6e-6)	1.0	1.0		Y
2	4	E	122,324, 513,551	2.6e-6 (1.0)	9.5e-4	9.5e-4		Y
3	3	D	112,355, 553	1.0 (2.6e-6)	1.0	1.0		Y
4	3	E	213,321, 454	2.6e-6 (1.0)	9.5e-4	9.5e-4		Y
5	2	D	132,452	1.0 (2.6e-6)	1.0	1.0		Y
6	2	E	214,554	2.6e-6 (1.0)	9.5e-4	9.5e-4		Y
7	1	D	451 or 452*	1.0 (2.6e-6)	1.5 or 1.25	1.0	252	N
8	1	E	451 or 452	2.6e-6 (500.5)	1.10e-3 or 9.58e-4	9.6e-4	252	N
Eng	1	D (E)	555	1.5 (1.1e-5)	1.5 (1.1e-3)	1.0 (9.5e-4)	255	N

* almost unique sensor system

Table B-3. Sensor system designs for Test Case 5 using multizone model data.

Sensor sys. [1]	Qty [2]	Obj. func. [3]	Locations using multizone data [4]	Objective function value (complementary obj. func. value)			Locations using CFD data [8]	Col. [6] equiv. to [7]? [9]
				Multizone-optimal [5]	CFD-benchmarked [6]	CFD-optimal [7]		
1	4	D	112,341, 453,523	1.0 (5.8e-8)	1.0	1.0		Y
2	4	E	113,241, 453,551	5.8e-8 (1.0)	9.95e-4	9.95e-4		Y
3	3	D	152,411, 541	1.0 (5.8e-8)	1.0	1.0		Y
4	3	E	222,331, 453	5.8e-8 (1.0)	9.95e-4	9.95e-4		Y
5	2	D	131,552	1.0 (5.8e-8)	1.0	1.0		Y
6	2	E	211,452	5.8e-8 (1.0)	9.95e-4	9.95e-4		Y
7	1	D	451*	1.25 (1.02e-6)	1.25	1.0	251	N
8	1	E	431	5.8e-8 (500.5)	1.0e-3	9.95e-4	251	N
Eng	1	D (E)	555	2.25 (1.2e-5)	1.5 (1.2e-3)	1.0 (9.95e-4)	355	N

* unique sensor system

Table B-4. Sensor system designs for Test Case 5 using zonal model data.

Sensor sys. [1]	Qty [2]	Obj. func. [3]	Locations using zonal data [4]	Objective function value (complementary obj. func. value)			Locations using CFD data [8]	Col. [6] equiv. to [7]? [9]
				Zonal-optimal [5]	CFD-benchmarked [6]	CFD-optimal [7]		
1	4	D	115,242, 453,532	1.0 (2.6e-6)	1.0	1.0		Y
2	4	E	121,132, 243,552	2.6e-6 (1.0)	9.95e-4	9.95e-4		Y
3	3	D	155,411, 552	1.0 (2.6e-6)	1.0	1.0		Y
4	3	E	142,453, 211	2.6e-6 (1.0)	9.95e-4	9.95e-4		Y
5	2	D	222,554	1.0 (2.7e-6)	1.0	1.0		Y
6	2	E	151,545	2.6e-6 (1.0)	9.95e-4	9.95e-4		Y
7	1	D	451 or 452	1.0 (2.6e-6)	1.25	1.0	251 or 252	N
8	1	E	451 or 452	2.6e-6 (500.5)	1.00e-3	9.95e-4	251 or 252	N
Eng	1	D (E)	555	1.5 (1.1e-5)	1.5 (1.2e-3)	1.0 (9.95e-4)	355	N

Table B-5. Sensor system designs for Test Case 6 using multizone model data.

Sensor sys. [1]	Qty [2]	Obj. func. [3]	Locations using multizone data [4]	Objective function value (complementary obj. func. value)			Locations using CFD data [8]	Col. [6] equiv. to [7]? [9]
				Multizone-optimal [5]	CFD-benchmarked [6]	CFD-optimal [7]		
1	4	D	152,344, 431,543	1.0 (5.5e-8)	1.0	1.0		Y
2	4	E	112,322, 431,555	5.5e-8 (1.25)	1.0e-3	1.0e-3		Y
3	3	D	141,412, 453,	1.0 (5.5e-8)	1.0	1.0		Y
4	3	E	121,452, 541	5.5e-8 (1.25)	1.0e-3	1.0e-3		Y
5	2	D	221,452	1.0 (5.5e-8)	1.0	1.0		Y
6	2	E	121,453	5.5e-8 (1.25)	1.0e-3	1.0e-3		Y
7	1	D	451*	1.25 (9.7e-7)	1.25	1.0	252	N
8	1	E	431	5.5e-8 (500.5)	1.02e-3	1.0e-3	252	N
Eng	1	D (E)	555	2.25 (1.1e-5)	1.5 (1.2e-3)	1.0 (1.0e-3)	255	N

* unique sensor system

Table B-6. Sensor system designs for Test Case 6 using zonal model data.

Sensor sys. [1]	Qty [2]	Obj. func. [3]	Locations using zonal data [4]	Objective function value (complementary obj. func. value)			Locations using CFD data [8]	Col. [6] equiv. to [7]? [9]
				Zonal-optimal [5]	CFD-benchmarked [6]	CFD-optimal [7]		
1	4	D	115,252, 452,533	1.0 (2.6e-6)	1.0	1.0		Y
2	4	E	144,214, 452,515	2.6e-6 (1.0)	1.0e-3	1.0e-3		Y
3	3	D	112,155, 542	1.0 (2.6e-6)	1.0	1.0		Y
4	3	E	234,413, 554	2.6e-6 (1.25)	1.0e-3	1.0e-3		Y
5	2	D	113,552	1.0 (2.6e-6)	1.0	1.0		Y
6	2	E	125,455	2.6e-6 (1.25)	1.0e-3	1.0e-3		Y
7	1	D	451 or 452*	1.0 (2.6e-6)	1.25	1.0	252	N
8	1	E	451 or 452	2.6e-6 (1.0)	1.02e-3	1.0e-3	252	N
Eng	1	D (E)	555	1.5 (1.1e-5)	1.5 (1.2e-3)	1.0 (1.0e-3)	255	N

* almost unique sensor system

Table B-7. Sensor system designs for Test Case 8 using multizone model data.

Sensor sys. [1]	Qty [2]	Obj. func. [3]	Locations using multizone data [4]	Objective function value (complementary obj. func. value)			Locations using CFD data [8]	Col. [6] equiv. to [7]? [9]
				Multizone-optimal [5]	CFD-benchmarked [6]	CFD-optimal [7]		
1	4	D	111,232, 341,451	1.0	1.0	1.0		Y
2	4	E	See note					
3	3	D	111,255, 551	1.0	1.0	1.0		Y
4	3	E	See note					
5	2	D	111,551	1.0	1.0	1.0		Y
6	2	E	See note					
7	1	D	451,452, 453,551, or 552*	250.75	Range from 1.25 to 1.5	1.0	152 or 153	N
8	1	E	See note					
Eng	1	D (E)	555	251.25 (0)	1.75 (1.3e-3)	1.0 1.05e-3	144	N

Note: For *all* contaminant releases, occupant exposure is always 0 kg/kg. Therefore, all sensor systems designed using multizone model data result in the same occupant exposure, 0 kg/kg, and there are no "optimal" designs. * almost unique sensor system

Table B-8. Sensor system designs for Test Case 8 using zonal model data.

Sensor sys. [1]	Qty [2]	Obj. func. [3]	Locations using zonal data [4]	Objective function value (complementary obj. func. value)			Locations using CFD data [8]	Col. [6] equiv. to [7]? [9]
				Zonal-optimal [5]	CFD-benchmarked [6]	CFD-optimal [7]		
1	4	D	132,222, 453,534	1.0 (4.2e-6)	1.0	1.0		Y
2	4	E	212,255, 442,535	4.2e-6 (1.0)	1.05e-3	1.05e-3		Y
3	3	D	114,351, 545	1.0 (4.2e-6)	1.0	1.0		Y
4	3	E	233,324, 454	4.2e-6 (1.0)	1.05e-3	1.05e-3		Y
5	2	D	114,551	1.0 (4.2e-6)	1.0	1.0		Y
6	2	E	112,551	4.2e-6 (1.0)	1.05e-3	1.05e-3		Y
7	1	D	451,452, or 453*	1.0 (4.2e-6)	Range from 1.25 to 1.5	1.0	152 or 153	N
8	1	E	451,452, or 453	4.2e-6 (1.0)	Range from 1.07e-3 to 1.22e-3	1.05e-3	152 or 153	N
Eng	1	D (E)	555	1.5 (1.2e-5)	1.75 (1.3e-3)	1.0 1.05e-3	144	N

* almost unique sensor system

Table B-9 to Table B-14 summarize the sensor system designs for each test case simulated for Zone A[+], which had the wall-mounted diffuser and exhaust.

Tables for selected test cases were reported in Chapter 2 and will not be repeated here. Sensor system designs for Test Case 9 using multizone and zonal model data are given on page 86 and 86, respectively. Those for Test Case 15 using multizone and zonal model data are given on page 91 and 91, respectively. And those for Test Case 16 using multizone and zonal model data are given on page 91 and 92, respectively.

Table B-9. Sensor system designs for Test Case 10 using multizone model data.

Sensor sys. [1]	Qty [2]	Obj. func. [3]	Locations using multizone data [4]	Objective function value (complementary obj. func. value)			Locations using CFD data [8]	Col. [6] equiv. to [7]? [9]
				Multizone-optimal [5]	CFD-benchmarked [6]	CFD-optimal [7]		
1	4	D	113,141, 251,441	1.0 (7.3e-8)			See note	
2	4	E	131,242, 452,525	7.3e-8 (1.0)				
3	3	D	211,451, 541	1.0 (7.3e-8)				
4	3	E	131,215, 541	7.3e-8 (1.0)				
5	2	D	211,551	1.0 (7.3e-8)				
6	2	E	211,551	7.3e-8 (1.0)				
7	1	D	451 or 551*	1.25 (1.1e-6)				
8	1	E	441	7.3e-8 (250.75)				
Eng	1	D (E)	551	1.25 (1.1e-6)				

Note: Using CFD data, every sensor location (i.e., subzone locations) was an optimal location to place a sensor. Note applicable to this table and following one. * almost unique sensor system

Table B-10. Sensor system designs for Test Case 10 using zonal model data.

Sensor sys. [1]	Qty [2]	Obj. func. [3]	Locations using multizone data [4]	Objective function value (complementary obj. func. value)			Locations using CFD data [8]	Col. [6] equiv. to [7]? [9]
				Multizone-optimal [5]	CFD-benchmarked [6]	CFD-optimal [7]		
1	4	D	123,211, 344,451	1.0 (7.5e-8)			See note	
2	4	E	141,231, 441,551	7.5e-8 (1.0)				
3	3	D	131,421, 551	1.0 (7.5e-8)				
4	3	E	221,335, 551	7.5e-8 (1.0)				
5	2	D	131,451	1.0 (7.5e-8)				
6	2	E	241,551	7.5e-8 (1.0)				
7	1	D	451 or 551*	1.25 (1.1e-6)				
8	1	E	441	7.5e-8 (250.75)				
Eng	1	D (E)	551	1.25 (1.1e-6)				

* almost unique sensor system

Table B-11. Sensor system designs for Test Case 13 using multizone model data.

Sensor sys. [1]	Qty [2]	Obj. func. [3]	Locations using multizone data [4]	Objective function value (complementary obj. func. value)			Locations using CFD data [8]	Col. [6] equiv. to [7]? [9]
				Multizone-optimal [5]	CFD-benchmarked [6]	CFD-optimal [7]		
1	4	D	153,322, 421,551	1.0 (9.0e-8)			See note	
2	4	E	151,215, 322,441	9.0e-8 (1.0)				
3	3	D	211,322, 451	1.0 (9.0e-8)				
4	3	E	211,341, 551	9.0e-8 (1.0)				
5	2	D	221,451	1.0 (9.0e-8)				
6	2	E	221,551	9.0e-8 (1.0)				
7	1	D	451 or 551*	1.25 (1.3e-6)				
8	1	E	441	9.0e-8 (250.75)				
Eng	1	D (E)	551	1.25 (1.3e-6)				

Note: Using CFD data, *every* sensor location (i.e., subzone locations) was an optimal location to place a sensor. Note applicable to this table and following one. * almost unique sensor system

Table B-12. Sensor system designs for Test Case 13 using zonal model data.

Sensor sys. [1]	Qty [2]	Obj. func. [3]	Locations using zonal data [4]	Objective function value (complementary obj. func. value)			Locations using CFD data [8]	Col. [6] equiv. to [7]? [9]
				Zonal-optimal [5]	CFD-benchmarked [6]	CFD-optimal [7]		
1	4	D	151,222, 521,552	1.0 (9.3e-8)			See note	
2	4	E	112,231, 455,551	9.3e-8 (1.0)				
3	3	D	111,435, 551	1.0 (9.3e-8)				
4	3	E	111,433, 551	9.3e-8 (1.0)				
5	2	D	121,451	1.0 (9.3e-8)				
6	2	E	111,451	9.3e-8 (1.0)				
7	1	D	451 or 551*	1.25 (1.3e-6)				
8	1	E	441	9.3e-8 (250.75)				
Eng	1	D (E)	551	1.25 (1.3e-6)				

* almost unique sensor system

Table B-13. Sensor system designs for Test Case 14 using multizone model data.

Sensor sys. [1]	Qty [2]	Obj. func. [3]	Locations using multizone data [4]	Objective function value (complementary obj. func. value)			Locations using CFD data [8]	Col. [6] equiv. to [7]? [9]
				Multizone-optimal [5]	CFD-benchmarked [6]	CFD-optimal [7]		
1	4	D	121,231, 351,441	1.0 (8.4e-8)			See note	
2	4	E	121,255, 451,533	8.4e-8 (1.0)				
3	3	D	231,332, 451	1.0 (8.4e-8)				
4	3	E	133,441, 551	8.4e-8 (1.0)				
5	2	D	311,451	1.0 (8.4e-8)				
6	2	E	221,551	8.4e-8 (1.0)				
7	1	D	451 or 551*	1.25 (1.2e-6)				
8	1	E	441	8.4e-8 (250.75)				
Eng	1	D (E)	551	1.25 (1.2e-6)				

Note: Using CFD data, *every* sensor location (i.e., subzone locations) was an optimal location to place a sensor. Note applicable to this table and following one. * almost unique sensor system

Table B-14. Sensor system designs for Test Case 14 using zonal model data.

Sensor sys. [1]	Qty [2]	Obj. func. [3]	Locations using zonal data [4]	Objective function value (complementary obj. func. value)			Locations using CFD data [8]	Col. [6] equiv. to [7]? [9]
				Zonal-optimal [5]	CFD-benchmarked [6]	CFD-optimal [7]		
1	4	D	111,221, 432,551	1.0 (8.6e-8)			See note	
2	4	E	121,351, 425,541	8.6e-8 (1.0)				
3	3	D	113,221, 451	1.0 (8.6e-8)				
4	3	E	121,451, 541	8.6e-8 (1.0)				
5	2	D	211,551	1.0 (8.6e-8)				
6	2	E	221,551	8.6e-8 (1.0)				
7	1	D	451 or 551*	1.25 (1.2e-6)				
8	1	E	441	8.6e-8 (250.75)				
Eng	1	D (E)	551	1.25 (1.2e-6)				

* almost unique sensor system

**APPENDIX C Published portions of Chapter 3 (in Proceedings of Indoor Air
2008 and ANCRiSST)**

Application of singular value decomposition for estimating indoor airflow

Y. Lisa Chen,^{*} and Jin Wen

Drexel University, Philadelphia, PA, USA

**Corresponding email: yhc22@drexel.edu*

SUMMARY

Indoor airflow is governed by a set of nonlinear, coupled partial differential equations (PDEs). Analytical solutions to these PDEs rarely exist for real-life applications. Thus, numerical approaches such as numerical integration and algebraic methods exist in the literature. Computational fluid dynamics (CFD) is the most widely used numerical integration approach. It is often cumbersome to setup and computationally expensive. In contrast, multizone and zonal models that utilize algebraic methods are relatively simple to setup and are computationally efficient. Though not as accurate as CFD results, algebraic methods have proven adequacy for many applications. In this paper another algebraic approach, singular value decomposition (SVD), was evaluated (1) as a method to predict indoor airflow, and (2) as a method to back-estimate indoor airflow given information about actual airflow. Part 1 showed airflow results that compared favorably with a steady state multizone model. Part 2 showed SVD as a promising reverse-modelling method when given additional velocity data.

KEYWORDS

Indoor airflow modelling, Singular value decomposition, Sensor locations

INTRODUCTION

Simulating indoor airflow is important for ventilation design and control, which affect building energy use, the safety of the indoor environment, and indoor air quality (IAQ). These factors are important to building owners and occupants. There are three main types of indoor airflow simulation models: multizone, zonal, and CFD. Multizone models consider a building as a network of interconnected nodes (Walton, 1989). Each node is a well-mixed zone, wherein IAQ parameters such as temperature, contaminant concentration, and pressure, are spatially uniform. The flow network is solved using algebraic pressure relationships. Since the well-mixed assumption is not valid in most indoor air applications, the second type of airflow model, the zonal model, further subdivides each physical zone into subzones. This is not unlike meshing in CFD models. However, subzones in zonal models are not nearly quite as small as those used in CFD models. Zonal models also incorporate mass flow equations for driving elements such as velocity jets and thermal plumes. The inclusion of driving elements improves the zonal model's accuracy over multizone models. Lastly, CFD models use numerical integration to iteratively solve the governing equations of airflow and contaminant dispersion. Given the inherent complexity of numerical integration over algebraic methods, CFD models are thus more computationally intensive. Nevertheless, CFD models produce the most accurate results of the three models when compared to experimental data.

Multizone, zonal, and CFD models are forward-modelling techniques. Given boundary conditions, these models calculate indoor airflow and/or contaminant distribution. Airflow calculations are performed by first specifying a pressure field. In multizone and zonal models, the relationship between airflow and pressure has been empirically determined. Even though the empirical constants in these relationships have been widely accepted, they can affect the solution of airflow when changed (Jiru and Haghighat, 2006). In CFD, the pressure field is updated iteratively until the solution of the flow field converges. It is not a trivial task to obtain convergence, nor is it computationally efficient. All forward-modelling techniques require the user to specify initial and boundary conditions. These parameters are not always easy to specify correctly.

Another modelling technique is reverse-modelling. These models use field measurements (experimental or synthetic) to estimate unknown parameters or past states in the model. Once these parameters or states are determined, the reverse-model can then provide additional information about current conditions or make predictions about the future. Miller (1997) utilized nonlinear least-squares minimization and tracer gas data to determine interzonal airflow rates from mass-balance relationships. This model may be limited to small buildings/zone configurations since the number of mass-balance relationships multiplies with the size of the building/zone. Using artificial neural networks and historic contaminant dispersion data, Hasham et al. (2004) predicted hourly contaminant concentrations. This study required gathering complete sets of historic contaminant data. Lastly, Zhang and Chen (2007) used "reverse CFD" equations to estimate source characteristics within a single enclosed space. Performing a reverse CFD simulation was met with the same complexity and computational effort as performing a forward CFD simulation.

Using multizone (or zonal) models is attractive because of their ease in setup and computational efficiency. Using CFD models is attractive because it provides more accurate results than do multizone and zonal models. Nevertheless, CFD models are complex and computationally intense. Thus, it is desirable to take advantage of the efficiency of multizone and zonal models while simultaneously attaining accuracy comparable to that of CFD models for estimating indoor airflow and contaminant dispersion. Reverse-modelling may have the potential to do this. The proposed reverse-modelling method is singular value decomposition (SVD). Its performance in estimating indoor airflow is studied in this paper. In the future, its performance in estimating contaminant dispersion and source characteristics after a release could be explored.

Objectives

This study proposes to: (1) evaluate the performance of SVD as a forward-modelling approach for predicting indoor airflow; and (2) evaluate the performance of SVD as a reverse-modelling approach for estimating indoor airflow within a single space given additional airflow information from within that space. The performance of SVD as a forward airflow model will be compared to multizone and CFD models in Part 1. The performance of SVD as a reverse airflow model will be compared to a CFD model in Part 2. Future work will include the use of a multizone model for reverse-modelling in Part 2.

METHODS

Singular value decomposition

The space inside a single room can be subdivided into $H \times L \times D$ control volumes. The net mass flow (in minus out) for each control volume must equal to zero, satisfying continuity. The system of mass balance equations, comprised of one expression per control volume, becomes underdetermined as H , L , and D increase (i.e., the number of unknown mass flow rates > the number of mass balance equations). To solve this underdetermined system, a method called singular value decomposition (SVD) (Golub and Kahan, 1965) can be employed. The general representation of any linear system is:

$$\mathbf{Ax} = \mathbf{b} \quad (1)$$

where \mathbf{A} is an $m \times n$ matrix, \mathbf{x} contains the variables, and \mathbf{b} contains solutions to the system. Normally, this system is easily solved by matrix inversion. However, if the system is underdetermined, there are an infinite number of solutions to \mathbf{x} . Thus, to solve an underdetermined system, SVD uses the pseudoinverse of \mathbf{A} . \mathbf{A} can be factorized into:

$$\mathbf{A} = \mathbf{U}\mathbf{\Sigma}\mathbf{V}^T \quad (2)$$

where $\mathbf{\Sigma}$ contains the singular values of \mathbf{A} on its diagonal, \mathbf{U} and \mathbf{V} are orthogonal matrices containing corresponding singular vectors in their columns, and the superscript T is the transpose. These elements are used to find the pseudoinverse of \mathbf{A} , \mathbf{A}^* .

$$\mathbf{A}^* = \mathbf{V}\mathbf{\Sigma}^+\mathbf{U}^T \quad (3)$$

where $\mathbf{\Sigma}^+$ is the transpose of $\mathbf{\Sigma}$ with every non-zero entry replaced by its reciprocal. Thus, the original system represented by Eq. (1) can be solved by:

$$\mathbf{x} = \mathbf{A}^* \times \mathbf{b} \quad (4)$$

The accuracy of SVD can be checked by comparing the original "right hand side", \mathbf{b} , with the one obtained by multiplying \mathbf{A} with the \mathbf{x} from Eq. (4).

Study approach

The airflow models described in the "Introduction" satisfy mass conservation upon completion of the solution process. Their ultimate objective is to solve for airflow rates, but all take an indirect approach. In contrast, SVD is used in this study to directly solve for mass flow rates. To demonstrate this, first a test room is selected and subdivided into subzones. Boundary conditions and subzone dimensions are also specified. In Part 1, the airflow network will be solved using SVD and the results compared to the multizone model, CONTAM (Walton and Dols, 2005), and the CFD model, AIRPAK (FLUENT, 2002). In Part 2, synthetic velocity data from the benchmark CFD simulation will be given as additional known conditions to the airflow network that was setup in Part 1. Performing the study in two parts helps to determine if SVD is better suited for forward- or reverse-modelling.

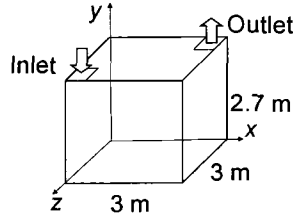


Figure 1. Test case room.

Test case setup

Consider a room which is 3m×2.7m×3m (Figure 1). The room has one inlet and outlet. Both are 0.6m×0.6m. Flow is isothermal. The inlet velocity is 1 m/s and the density of air is constant throughout the room at 1.225 kg/m³. The test room size and airflow conditions were taken from a study by Murakami and Kato (1989). It is also comparable to a small office. Three simulation methods were used: SVD, multizone, and CFD. Zonal modelling is saved for future studies. The exiting air flow rate was assumed to be equal to the entering air flow rate. Neither leakage nor other sources of airflow exchange were considered in this study. Future work would place the test room inside a larger building where a multizone model could provide boundary airflow exchange with surrounding zones.

Airflow models used

To use SVD, the room in Figure 1 was subdivided into 4×4×4 subzones. The width of the subzones in the x- and z - directions were 0.6, 0.9, 0.9, and 0.6m. The height of each subzone was 0.675m. This spacing ensured that the inlet and outlet were contained in a single subzone. The face areas associated with each control volume were easily calculated given the subzone dimensions. Additional configurations of subzone size and number were evaluated as well. Unlike CFD modeling, however, the number and size of the subzones in algebraic models do not affect the result greatly. This conclusion was also reported by Mora et al. (2003). For any subzone (or control volume), the net mass flow, \dot{m} , must equal zero. Mathematically:

$$\sum_{i=1}^6 \dot{m}_i = \sum_{i=1}^6 \rho v_i A_i = 0 \quad (5)$$

where i is the face of a control volume, ρ is the density of air in kg/m³, v is the velocity of air in m/s, and A is the cross-sectional area through which the air passes. The system is thus:

$$\mathbf{A} \left[\rho \sum_{n=1}^N \mathbf{v} \right] = 0 \quad (6)$$

for N subzones, where \mathbf{A} contains the face areas for each respective control volume. The boundary conditions and unknowns are contained in the quantity $\rho \Sigma \mathbf{v}$.

In CONTAM, the airflow between adjacent subzones was represented by a two-way, single opening model whose discharge coefficient was 0.78 and the exponent 0.5. The grid size for the CFD model was 30×26×30, roughly 0.1m×0.1m×0.1m cells. The standard k - ϵ turbulence model

was used to solve the steady state airflow. The grid size and turbulence model here were also used by Murakami and Kato (1989).

Part 1: SVD as a forward-modelling approach

The performance of the SVD and multizone models was evaluated. Qualitative assessments were performed by comparing the airflow patterns predicted by each model to the CFD benchmark. Quantitative assessments were performed by calculating the error between each model and CFD using:

$$\frac{\text{CFD result} - \text{model result}}{\text{CFD result}} \times 100\% \quad (7)$$

Part 2: SVD as a reverse-modelling approach

To use SVD as a reverse-modelling approach, various amounts of synthetic velocity data was provided to the model as known conditions. For convenience, synthetic velocity data was taken from the CFD simulation in Part 1. Future work would use actual velocity sensor data. Eighteen cases (Figure 2) were run in order to determine the amount and location of synthetic velocity data that had the most influence on the accuracy of the reverse-modelling capability of SVD. Synthetic velocity data was taken from "poles" located around the room. Each pole had four sensors, measuring velocities either both in the x - and y -direction, only in the x -direction, or only in the y -direction.

RESULTS

Part 1: Results of SVD as a forward-modelling approach

The SVD model predicted airflow just as well as the multizone model, but no better, when compared to the CFD model. However, one striking difference is in the last column along the x -direction (see dashed oval in Figure 3). The multizone model predicted zero flow, whereas the SVD model did predict some flow.

As is shown in Figure 4, the error distributions of the SVD and multizone models nearly overlapped. Both error distributions peaked in the 51% to 100% error range. The meaning of the other lines will be discussed later.

Part 2: Results of SVD as a reverse-modelling approach

As mentioned previously, the SVD model with no incorporated velocity data performed no better than the multizone model. The next step was to incorporate velocity data and observe whether or not SVD fared better as a reverse-modelling approach. Figure 4 shows the error distribution using Eq. (7) for the SVD model (no synthetic velocity data provided), the multizone model, and the cases shown in Figure 2 (velocity data provided). Cases 1 and 4 showed vast improvement to the accuracy of the airflow estimation compared to the SVD model with no additional velocity data. Both distributions were skewed right, peaking in the lower ranges of percentage error. When the number of poles was reduced to four, the accuracy of the airflow estimation was reduced except for Cases 17 and 18. This was indicated by higher frequency in the higher ranges of percentage error (Cases 7, 10, 13, and 16).

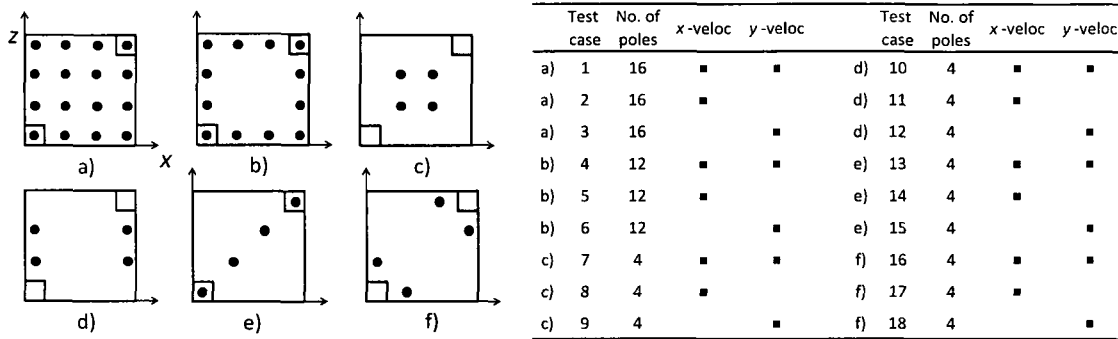


Figure 2. "Pole" locations where synthetic velocity data were taken.

The amount of velocity data collected at each sensor also affected the accuracy of the airflow estimation using SVD. When 16 measurement poles (Cases 1-3) were available, merely given x - or y -velocity data was sufficient to obtain a reasonably accurate description of the airflow in the test room. This was also the case when the number of measurement poles was reduced to 12, placed along the perimeter of the room (Cases 4-6). Here, the y -velocities were more helpful in improving the accuracy of the airflow estimation. This may be since under the inlet and outlet, which were along the perimeter of the room, the bulk of air was traveling in the vertical direction. In contrast, x -velocities were more helpful in improving the accuracy of the airflow estimation when the poles were placed in the center of the room (e.g., Cases 7-9).

The next step was to observe which pole locations and which sensors attributed most to the accuracy of the airflow estimation using SVD. One pole at a time, up to four sensors were removed one at a time from Case 4. When sensors were being removed from one pole, the remaining 11 poles still had all of their sensors. Both x - and y -velocities were available to SVD in the following cases. Observing the error distribution (results not shown), it was determined that one sensor atop each pole (except for the pole to the right of the inlet) could be removed independently without causing a more than 5% drop in accuracy. The accuracy of the airflow estimation was measured by the drop in the peak frequency value (compared to Case 4) of the error distribution. When one sensor was removed atop each pole simultaneously (Case 19), the accuracy decreased 23%. Nevertheless, qualitatively the resulting airflow pattern was still reasonable when compared to the CFD benchmark. It was also determined that removing the poles, one at a time, along the left and right walls (except for the pole on the left wall closest to the inlet) could be removed without causing a more than 5% drop in accuracy. When these poles were removed simultaneously (Case 20), the accuracy decreased 16%. Although quantitatively Case 20 fared better than Case 19, qualitatively Case 19 fared better than Case 20 (results not shown). Thus, other measures of model performance should be considered in addition to airflow rates.

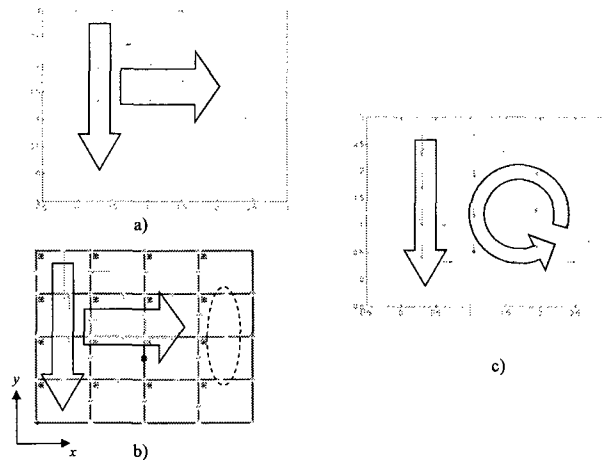


Figure 3. Airflow results under inlet. a) SVD, b) multizone, c) AIRPAK model.

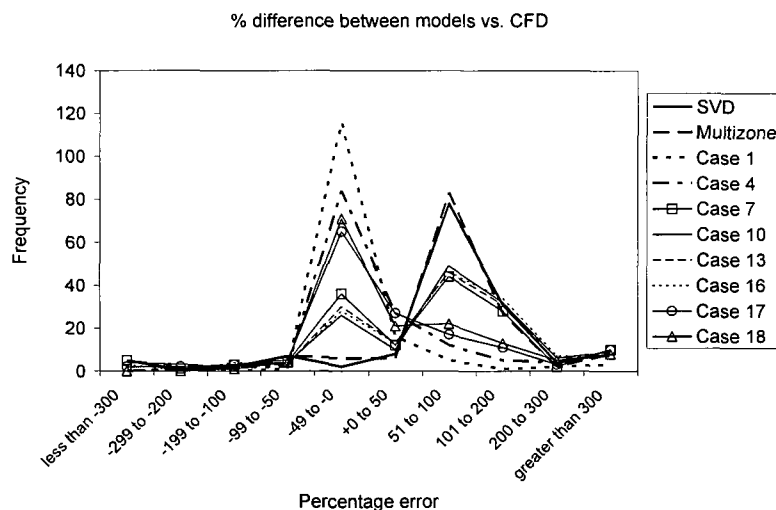


Figure 4. Histogram showing frequency of percentage difference from CFD model.

DISCUSSION

The solution of indoor airflow has been approached using numerical integration of the governing equations of fluid flow and with algebraic solutions using pressure difference relationships. The former method can be both complex to setup and computationally intensive, whereas the latter method, though easy to setup and computationally efficient, does not provide as accurate of solutions. When these approaches are used for reverse-modelling, the same advantages and drawbacks when forward-modelling also apply. Thus, it was desirable to take advantage of the efficiency of multizone and zonal models while simultaneously attaining accuracy comparable to that of CFD models for the application of reverse-modelling. The proposed approach utilized SVD, a solution method that exhibited the same attractive qualities as the multizone and zonal

models, but also showed promise to be an appropriate alternative to using CFD for accurate reverse-modelling. The velocity data for this study came from a CFD simulation, but actual sensor data may also be used.

To best improve the reverse-modelling performance of SVD, it was desirable to have as much sensor data as possible. But realistically, the amount of sensor data available would be constrained by availability, cost, and other factors. Thus, this study concluded that sensor data from the perimeter of the room was much more helpful in improving reverse-modelling performance than sensors placed in the centre of the room. The elimination of the measurement poles in the centre of the room is also an economic and efficient simplification for future experimental studies. Furthermore, since the inlet and outlet were along the perimeter of the test room, the bulk of air moved in the vertical direction along the perimeter. On these poles, measuring y -velocity helped more to improve the accuracy of the airflow estimation by SVD than measuring x -velocity. The poles closest to the inlet were more influential to the accuracy of the airflow estimation than poles elsewhere. More cases could be run in the future to determine if more sensors can be removed from the remaining poles.

The proposed method proved to be easy to setup, efficient, and fairly accurate in reverse-modelling airflow when given additional information. The proposed method can be implemented in real-time applications where a CFD simulation was not previously performed and a limited number of sensor data is available. The resulting airflow patterns back-estimated by SVD can be used to evaluate indoor air quality and, in the future, locate contaminant releases.

The full range of capabilities of the proposed approach has not yet been fully explored and is saved for future work. First, comparison of its reverse-modelling capability to that of a multizone model with the same velocity sensor data should be compared. Second, the proposed method should be extended to transient applications. Third, more cases using different sensor locations and sensor quantities should be considered in order to determine the optimal sensor configuration for best back-predicting airflow. Fourth, if for instance exact airflow prediction is not necessary in determining contaminant concentration, the proposed approach should be extended to estimating contaminant dispersion. Fifth, if the velocity sensors were replaced with temperature sensors, how would the accuracy of the airflow estimation using SVD model change. Since temperature sensors are both more economical and accurate than velocity sensors, they would be more commonly found in actual indoor environments.

CONCLUSIONS

The reverse-modelling of indoor airflow need not rely on complex CFD techniques or simple, but oftentimes, inadequate multizone or zonal modelling techniques. The proposed method using SVD has been shown to be as attractive as the multizone and zonal models for ease and efficiency, but with additional information can estimate airflow comparable to a CFD model. Further development of the proposed method could lead to better estimation of real-time indoor airflow. This information would be useful for evaluating indoor air quality and could also provide a quick estimate of contaminant dispersion. The proposed method has application in areas where the health and safety of building occupants is a priority.

ACKNOWLEDGEMENT

The authors would like to thank the National Science Foundation (NSF) for providing support of this work through the NSF Graduate Research Fellowship Program (GRFP).

REFERENCES

- FLUENT. 2002. Airpak 2.1 User's Guide. Report for Fluent Inc., Lebanon, NH pages.
- Golub G. and Kahan W. 1965. Calculating the Singular Values and Pseudo-Inverse of a Matrix. *Journal of the Society for Industrial and Applied Mathematics: Series B, Numerical Analysis*, 2(2), 205-224.
- Hasham F.A., Kindzierski W.B. and Stanley S.J. 2004. Modeling of hourly NO_x concentrations using artificial neural networks. *Journal of Environmental Engineering and Science*, 3, S111-S119.
- Jiru T.E. and Haghghat F. 2006. A new generation of zonal models. *ASHRAE Transactions*, 112(2).
- Miller S.L., Leiserson K. and Nazaroff W.W. 1997. Nonlinear Least-Squares Minimization Applied to Tracer Gas Decay for Determining Airflow Rates in a Two-Zone Building. *Indoor Air*, 7(1), 64-75.
- Mora L., Gadgil A.J. and Wurtz E. 2003. Comparing zonal and CFD model predictions of isothermal indoor airflows to experimental data. *Indoor Air*, 13(2), 77-85.
- Murakami S. and Kato S. 1989. Numerical and experimental study on room airflow - 3-D predictions using the *k-ε* turbulence model. *Building and Environment*, 24(1), 85-97.
- Walton G.N. 1989. AIRNET - A Computer Program for Building Airflow Network Modeling. Report for NISTIR 89-4072, National Institute of Standards and Technology, Gaithersburg, MD, 83 pages.
- Walton G.N. and Dols W.S. 2005. CONTAM 2.4 User Guide and Program Documentation. Report for NISTIR 7251, National Institute of Standards and Technology, Gaithersburg, MD, 313 pages.
- Zhang T.F. and Chen Q. 2007. Identification of contaminant sources in enclosed environments by inverse CFD modeling. *Indoor Air*, 17(3), 167-177.

Sensor System and Inverse Model Development for Indoor Airflow Estimation

Y. Lisa Chen¹ and Jin Wen²

¹*Department of Civil, Architectural, and Environmental Engineering, Drexel University, USA*

²*Department of Civil, Architectural, and Environmental Engineering, Drexel University, USA*
yhc22@drexel.edu, jinwen@drexel.edu

ABSTRACT

Indoor airflow, which is governed by a set of nonlinear, coupled partial differential equations (PDEs), is often the basis for demand ventilation control, indoor contamination risk analysis, and indoor air quality control. Analytical solutions to these PDEs rarely exist for real-life applications. Thus, numerical approaches such as numerical integration and algebraic methods exist in the literature. Computational fluid dynamics (CFD) is the most widely used numerical integration approach. It is often cumbersome to setup and computationally expensive. In contrast, multizone and zonal models that utilize algebraic methods are relatively simple to setup and are computationally efficient. Though not as accurate as CFD results, algebraic methods have proven adequacy for many applications. In this paper, several algebraic approaches, including singular value decomposition (SVD), were evaluated as methods to inversely estimate indoor airflow given limited sensor measurements of actual airflow. The case studies showed SVD as a promising inverse modeling method when given additional data. In lieu of actual sensor data, this study provided synthetic velocity and temperature data to the inverse models. Depending on the type of data provided, the estimation accuracy of the proposed method varied. It was also found that the location of the provided data also affected the estimation accuracy of the proposed inversed airflow model. In situations where real sensor data is available, the identified inverse method has the potential to efficiently and accurately estimate indoor airflow. This information can then be used in the applications of estimating indoor air quality, detecting harmful contaminants, and guide future sensor placement.

¹ PhD candidate

² Assistant professor, presenter

INTRODUCTION

Information about indoor airflow is important for ventilation design and control, which affect building energy use, the safety of the indoor environment, and indoor air quality (IAQ). These factors are important to building owners and occupants. There are three main types of forward indoor airflow simulation models: multizone, zonal, and computational fluid dynamics (CFD). Multizone models consider a building as a network of interconnected nodes (Walton 1989). Each node is a well-mixed zone, wherein IAQ parameters such as temperature, contaminant concentration, and pressure, are spatially uniform. The flow network is solved using algebraic pressure relationships. Since the well-mixed assumption is not valid in most indoor air applications, the second type of airflow model, the zonal model, further subdivides each physical zone into subzones. This is not unlike meshing in CFD models. However, subzones in zonal models are not nearly as small as those used in CFD models. Zonal models incorporate mass flow equations for driving elements such as velocity jets and thermal plumes. The inclusion of driving elements improves the zonal model's accuracy over multizone models. Lastly, CFD models use numerical integration to iteratively solve the governing equations of airflow and contaminant dispersion. Given the inherent complexity of numerical integration over algebraic methods, CFD models are thus more computationally intensive. Nevertheless, CFD models produce the most accurate results of the three airflow models when compared to experimental data.

Multizone, zonal, and CFD models are forward modeling techniques. Given boundary conditions, these models calculate indoor airflow and/or contaminant distribution. Airflow calculations are performed by first specifying a pressure field. In multizone and zonal models, the relationship between airflow and pressure is assumed to be non-linear and empirically determined. Even though the empirical constants in these relationships have been widely accepted, they can affect the solution of airflow when changed (Jiru and Haghighat 2006). In CFD, the pressure field is updated iteratively until the solution of the flow field converges. It is not a trivial task to obtain convergence, nor is it computationally efficient. All forward modeling techniques require the user to specify initial and boundary conditions. These parameters are not always easy to specify correctly.

Another modeling technique is inverse modeling. These models use field measurements (experimental or synthetic) to estimate unknown parameters or past states in the model. Once these parameters or states are determined, the inverse model can then provide additional information about current conditions or make predictions about the future. Miller *et al.* (1997) utilized nonlinear least-squares minimization and tracer gas data to determine interzonal airflow rates from mass balance relationships. This method of inverse modeling may be case-specific, as it requires a significant amount of measured data for each particular building case for model fitting. Using artificial neural networks and historic contaminant dispersion data, Hasham *et al.* (2004) predicted hourly contaminant concentrations. This study required gathering complete sets of historic contaminant data. Lastly, Zhang and Chen (2007) used "inverse CFD" equations to estimate source characteristics within a single enclosed space. Performing an inverse CFD simulation was met with the same complexity and computational effort as performing a forward CFD simulation.

Fast development of indoor sensors and communication technology will make larger and larger amounts of sensor data available for use in indoor air applications. There is potential to include this sensor data in simplified, inverse airflow models in order to quickly obtain an accurate solution of indoor airflow. The development of such an inverse model and the design of a sensor system to collect the appropriate data are worth discussing. In this study, both singular value decomposition (SVD) and a multizone model are evaluated as potential inverse airflow models. Multizone models consider indoor airflow as a non-linear process. In this study, however, a linear approach was taken and singular value decomposition (SVD) was used to inversely solve

for indoor airflow. Both are attractive because of their ease in setup and computational efficiency. How sensor quantity and location affect the estimation accuracy of the inverse models is also discussed.

STUDY APPROACH

This study proposes to: (1) compare the performance of SVD and a multizone model as inverse modeling approaches for estimating indoor airflow given velocity data (discussed in Part I of this study); (2) optimize the quantity and location of velocity data provided to the inverse model that maximizes the indoor airflow estimation accuracy (Part II); and (3) compare the performance of the proposed inverse model using temperature sensor measurements to using velocity data (Part III). In lieu of experimental data, velocity and temperature data from CFD simulations will be provided to the inverse models representing sensor measurements. The performance of each inverse model will be evaluated by comparing model predictions with CFD data.

In the study of indoor airflow, for any control volume of air, the net mass flow, \dot{m} , must equal zero in order to satisfy continuity. For a system of N control volumes,

$$\mathbf{A} \left[\rho \sum_{n=1}^N \mathbf{v} \right] = \mathbf{0} \quad (1)$$

where ρ is the density of air in kg/m^3 , \mathbf{v} is the velocity of air in m/s , and A is the cross-sectional area through which the air passes. The boundary conditions and unknowns are contained in the quantity $\rho \Sigma \mathbf{v}$. Another set of equations, for energy balance, can be used to solve for indoor airflow:

$$\sum_{n=1}^N (\dot{m}cT + \sum h_k A_k (T_{w,k} - T_i)) = 0 \quad (2)$$

where \dot{m} is the mass flow rate of air, c is the specific heat of air, T is temperature of a subzone, h_k is the convection coefficient for each surface (such as wall, floor, etc.) of a subzone, A_k is the area of each surface, and $T_{w,k}$ is the temperature of each surface. Since there are up to six unknown \mathbf{v} or \dot{m} (left, right, up, down, front and back velocities) for any control volume, as N increases, the system becomes underdetermined. To solve an underdetermined system, a method called singular value decomposition (SVD) (Golub and Kahan 1965) will be employed. For the first objective (Part I of this study), airflow results using SVD (Chen and Wen 2008) and the multizone model, CONTAM (Walton and Dols 2005), as inverse airflow models will be compared. The performance of each inverse model will be evaluated using CFD data simulated by Airpak (FLUENT 2002). For the second objective (Part II of this study), genetic algorithm (GA) (Goldberg 1989) will be used to optimize the quantity and location of synthetic velocity data introduced to the inverse model in order to maximize its airflow estimation accuracy. For the third objective (Part III of this study), only the performance of the SVD model, incorporating temperature measurements, will be evaluated.

Test rooms

Consider a room which is $3\text{m} \times 2.7\text{m} \times 3\text{m}$ with one inlet and outlet. Both are $0.6\text{m} \times 0.6\text{m}$. Incoming flow is isothermal for Parts I and II. For Part III, the incoming air is 13°C , the walls of

the room are held constant at 21°C, and the initial temperature inside each subzone is 21°C. The inlet velocity is 1 m/s and the density of air is constant throughout the room at 1.225 kg/m³. The test room size and airflow conditions were taken from Murakami and Kato (1989), which are comparable conditions for a small office. Three configurations for the location of the inlet and outlet are considered (Fig. 1).

Airflow models used

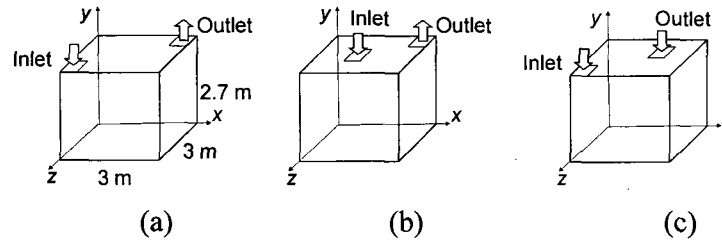


Fig. 1. Test rooms A, B, and C.

Three airflow simulation methods were used: inverse SVD (invSVD), inverse CONTAM (invC), and CFD. Both invSVD and invC were used to inversely solve for indoor airflow. The CFD simulations provided synthetic sensor data to the inverse airflow models and was also used to evaluate the performance of the inverse airflow models. The performance of invSVD was evaluated both with and without infiltration. A constant infiltration rate of -0.04 kg/s was considered. The invSVD model that included infiltration will be referred to as invSVD1. The invSVD model that did not include infiltration will be referred to as invSVD0. Infiltration was always considered when using invC. Infiltration was not considered in the CFD model. CFD studies in the literature of indoor air modeling oftentimes neglect infiltration as well. First, it is assumed that when a space is mechanically ventilated, the higher-than-outdoor indoor air pressure prevents infiltration of outdoor air into the room (Zhai *et al.* 2003). Thus, even if infiltration were included, it would not disrupt indoor airflow. Second, the location of the paths of infiltration, such as small cracks in walls and around doors and windows, are often not visible to the eye. Not knowing the location of each infiltration path thus makes it challenging to accurately include infiltration in CFD models. For simplification, one study assumed infiltration to be uniformly distributed on an exterior wall (Wang *et al.* 2006). However, this method still does not represent actual infiltration.

Each of the test rooms in Fig. 1 was subdivided into 4×4×4 control volumes (henceforth referred to as "subzones"). The width of the subzones was either 0.6 or 0.9m. The height of each subzone was 0.675m. This spacing ensured that the inlet and outlet were contained in a single subzone. Additional configurations of subzone size and number were evaluated as well. Unlike CFD modeling, however, the number and size of the subzones in algebraic models do not affect the result greatly (Mora *et al.* 2003).

The invC model requires specifying the pressure-flow relationship between subzones where no physical boundary, such as a wall, exists. The literature on zonal modeling uses the power-law relationship with a discharge coefficient was 0.78 and the exponent 0.5 to do so (Mora *et al.* 2003). The grid size for the CFD model was 30×26×30, roughly 0.1m×0.1m×0.1m cells. The standard *k-ε* turbulence model was used to solve the steady state airflow. The grid size and turbulence model here were also used by Murakami and Kato (1989).

Part I: Comparing inverse SVD and inverse CONTAM

The performance of the invSVD and invC models was evaluated with CFD data. Various amounts of synthetic velocity data, which was taken from a CFD simulation, was provided to each model as additional known conditions. Future work could use velocity data collected from actual sensors. Eighteen test cases were run for each test room (Fig. 2). Synthetic velocity data was taken from "poles" located around the room. Each pole had four sensors, measuring velocities either both in the x - and y -direction, only in the x -direction, or only in the y -direction. The locations of the poles in Fig. 2 were selected based on ideal situations, such as having a large number of sensors evenly distributed throughout the entire test room (Fig. 2a), and based on more practical limitations on available sensor quantity (Fig. 2d-f). The airflow solutions resulting from the use of these respective configurations provide insight into the relative importance of locating sensors close to the diffuser or exhaust and the relative importance of sensor measurements from the perimeter versus from the center of the room.

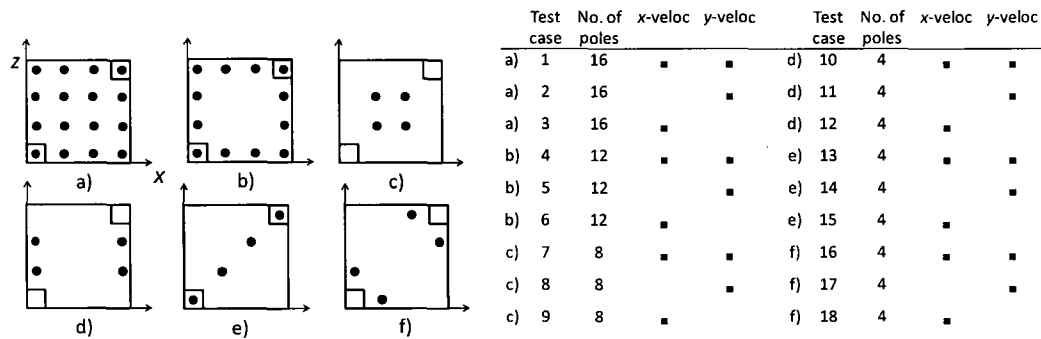


Fig. 2. Pole locations where synthetic velocity data were taken.

The absolute error between the airflow results of each inverse airflow model and CFD at the interface between all of the subzones was calculated. Using these values, a histogram or error distribution, was created for each test case. The skewness was then calculated for each error distribution, defined as:

$$\frac{N}{(N-1)(N-2)} \sum_{i=1}^N \left(\frac{\bar{x}_i - x_i}{s} \right)^3 \quad (3)$$

where \bar{x}_i is the mean error, x_i is the error in each bin, N is the number of bins, and s is the sample standard deviation. Seven bins are defined for this study. The more positive the skewness of an error distribution, the more the distribution peaked in the bins of smaller error, which is an initial indicator of more accurate airflow estimation when compared to the CFD airflow results.

Part II: Optimizing sensor location for inverse SVD model

Genetic algorithm (GA) was used to optimize the quantity and location of velocity data provided to the inverse model that maximizes the indoor airflow estimation accuracy. All of the subzones were candidate locations. Two trials were performed. In Trial 1, for each candidate location, only velocity measurements in one direction, either vertical or horizontal, were provided to each inverse airflow model as additional known data. In Trial 2, for each candidate location, *both* vertical and horizontal measurements were available. Given a specific number of sensors,

the objective function to be minimized was the *negative* of skewness in Eq. (4), which is also the same as maximizing skewness.

Part III: Using temperature data for inverse SVD model

Similar to Part I, here, SVD will be used to solve a set of energy balance equations (Eq. 3) given T and $T_{w,k}$. The same measure of estimation accuracy, skewness, in Part I will be applied in Part III.

RESULTS AND DISCUSSION

Part I: Comparing inverse SVD and inverse CONTAM

The estimation accuracy of invSVD, with and without considering infiltration (invSVD0 and invSVD1, respectively), was compared to that of invC for the test cases shown in Fig. 2. Table 1 shows that except for a few test cases (14 and 17), the difference between the skewness of the error distributions resulting from the use of the invSVD0 and invSVD1 models were small (<5%) for test room A. Similar results for found for test rooms B and C. Thus, it was concluded that including infiltration as a known boundary condition in the invSVD model neither degraded nor improved its estimation accuracy for the test cases in this study. Further, plots of the error

Table 1. Summary of skewness of error distributions resulting from use of invSVD0, invSVD1, and invC models to inversely estimate airflow for test room A.

Test case	<u>Skewness</u>			Model with highest skewness	% diff between invSVD models	% diff between invSVD1 and invC
	invSVD0	invSVD1	invC			
1	2.645	2.646	2.594	invSVD1	<1%	
2	2.641	2.645	2.584	invSVD1	<1%	
3	1.763	1.746	1.880	invC	<1%	7.692%
4	2.623	2.623	2.548	invSVD	<1%	
5	2.623	2.623	2.501	invSVD	<1%	
6	1.137	1.123	1.328	invC	<5%	18.29%
7	1.696	1.616	1.610	invSVD0	<5%	
8	0.951	0.998	1.281	invC	5.031%	28.29%
9	1.488	1.372	1.263	invSVD0	<5%	
10	1.378	1.396	1.500	invC	<5%	7.450%
11	1.451	1.439	1.839	invC	<1%	27.81%
12	0.804	0.866	0.894	invC	7.717%	<5%
13	1.178	1.767	1.835	invC	<1%	<5%
14	1.539	1.713	1.710	invSVD1	11.337%	
15	1.139	1.094	0.723	invSVD0	<5%	
16	1.903	1.546	1.072	invSVD0	<1%	
17	1.546	1.625	1.531	invSVD1	5.073%	
18	1.072	1.063	1.104	invC	<1%	<5%

distributions and airflow results from the use of the invSVD1 and invC models showed little difference (plots not shown for brevity). Thus, it was concluded that the invSVD and invC models demonstrated comparable airflow estimation accuracy for the test cases shown. Lastly, it was concluded that the best test cases among the ones tested in this study were 1, 2, 4, and 5 for test room A. Even though there were more sensor data available in test case 1 than in test case 4, the difference between the skewness of the resulting error distributions was <1%. Thus, it was concluded that sensors placed around the perimeter subzones of test room A provided sufficient data to estimate indoor airflow as accurately as placing sensors in every subzone. This offers a practical and cost effective simplification in both experimental set ups and field tests for future work in inverse airflow modeling since sensors are more readily installed on walls than in the center of a room. In a previous study published by the authors (Chen and Wen 2008), it was shown that if sensors were placed along the perimeter of the room (Fig. 2b), the major circulation patterns predicted by CFD are well-captured. Other test cases where the skewness of the resulting error distributions was high were test cases 13-15, where sensors were placed directly beneath the diffuser and exhaust. Thus, it was concluded that measurements below these airflow elements can improve the airflow estimation accuracy of the inverse models in this study. Similar conclusions were found for test rooms B and C. Details are not presented for brevity.

Part II: Optimizing sensor location for inverse SVD model

The invSVD1 model was chosen for the optimization process since (1) the invSVD1 model had comparable performance with the invSVD0 and invC models (Part I discussion) and (2) either of the invSVD models was more easily incorporated into the optimization process than invC. Fig. 3 shows the skewness of the error distributions resulting from the incorporation of an increasing number of sensors for test room A. For both Trials 1 and 2, as the number of sensors increased, the skewness increased as well, which was to be expected. The difference between the skewness values for Trials 1 and 2 were never greater than 5% for any sensor quantity. Thus, it could be concluded that the extra measurement (and thus the extra sensor in an experimental setup) would not greatly improve the estimation accuracy of the invSVD1 model.

As the number of sensors increase, the skewness stabilized. For Trial 1, there is <5% improvement in skewness above nine sensors in test room A. For both test rooms B and C, it was four sensors. Thus, depending on the flow condition, the minimum number of sensors to achieve optimal estimation accuracy varies. With a limited number of sensors, the optimization process found locations that were more critical to the improvement of skewness. As the number of available sensors was increased, the additional measurements only provided marginal improvement to skewness. Knowing the optimal quantity of sensors for a specific test room necessary for acceptable inverse airflow estimation is important in most situations where sensor quantity is limited. For optimal sensor configurations up to and including nine sensors, the optimization process selected a majority of the sensors (91%) to be located on the walls for test room A. Forty percent of these were found to be located in the z -plane closest to the outlet ($z=4$) since the outlet in test room A was adjacent to a wall. However, in test room C, where the outlet was placed off the wall in $z=3$, the majority of the sensors were shown to be placed in the z -plane adjacent to the outlet ($z=4$, a wall). Thus, it was concluded that, up to the minimum optimal number of sensors for each respective test room, the majority of sensors will be placed on the wall *closest* to the outlet no matter the location of the inlet. Further, the majority of the optimally selected sensors will measure velocity in direction of the bulk airflow.

Part III: Using temperature data for inverse SVD model

A value of $4 \text{ W/m}^2\cdot\text{K}$ for h_k is assumed for all subzone surfaces {El Mankibi, 2006 #770}.

The temperature of the incoming air and that of the surfaces is known. Therefore, the only unknown in Eq. (8) is the indoor airflow, which can be inversely solved for using invSVD. Given the sensor locations in Fig. 2a, it was found that the skewness of the error distribution (0.8136) was better than the case when no velocity data was included in the invSVD model, but not better than the case when no velocity data was included in the invC model. Improvements could be made by specifying more accurate values of h_k .

CONCLUSIONS

Inverse modeling techniques provide opportunities to take advantage of fast-developments in sensing and communicating technologies, using sensor data for efficient and accurate estimation and prediction of indoor airflow and contaminant distribution. However, for the capabilities of inverse models to reach their full potential, proper inverse model structure and sensor system design (such as quantity and type) need to be examined. In this study, (1) the feasibility of using SVD as an inverse modeling approach was studied, where indoor airflow was represented as a linear system, (2) the performances of inverse SVD models and inverse CONTAM model, where indoor airflow is represented as a non-linear system, were compared, (3) the need for including infiltration in these inverse models was evaluated, and (4) optimal sensor system design to best provide sensor measurements for inverse models was examined. It was found that the inverse SVD models performed comparably to the inverse CONTAM model when provided with velocity data. It was found that infiltration data did not affect inverse model performance greatly. Using genetic algorithm to optimize the estimation accuracy, or skewness, of the inverse SVD model, it was found that most sensors should be placed on the wall closest to the outlet and measure velocity in the vertical direction. These conclusions can be beneficial for simplifying and maximizing the effectiveness of indoor airflow experiments and measurements. This information would be useful for evaluating indoor air quality and could also provide an estimate of contaminant dispersion. When using temperature data for estimating indoor airflow, it was found that the airflow estimation was better than the case when no velocity data was provided to the inverse SVD model but no better the case when no velocity data was provided to the inverse CONTAM model. Further studies should be performed using other types of data, such as contaminant concentration, and observing the effect on inverse model performance.

ACKNOWLEDGEMENTS

Support for this work has been provided by a National Science Foundation Graduate Research Fellowship.

REFERENCES

- Chen, Y. L. and J. Wen, "Application of singular value decomposition for estimating indoor airflow ", Proceedings from Indoor Air 2008, Copenhagen, Denmark, 2008.
- FLUENT, *Airpak 2.1 User's Guide*, Fluent Inc., 2002, Lebanon, NH.
- Goldberg, D. E., *Genetic Algorithm in Search, Optimization and Machine Learning*, Reading, MA, 1989, Addison-Wesley Pub. Co.
- Golub, G. and W. Kahan, "Calculating the Singular Values and Pseudo-Inverse of a Matrix", *Journal of the Society for Industrial and Applied Mathematics: Series B, Numerical Analysis*, Vol. 2, No. 2, 1965, pp. 205-224.
- Hasham, F. A., W. B. Kindzierski and S. J. Stanley, "Modeling of hourly NO_x concentrations using artificial neural networks", *Journal of Environmental Engineering and Science*, Vol. 3, No. 2004, pp. S111-S119.
- Jiru, T. E. and F. Haghighat, "A new generation of zonal models", *ASHRAE Transactions*, Vol.

Accepted for publication in Proceedings of Fifth International Workshop on Advanced Smart Structures and Technology

- 112, No. 2, 2006, pp. 163-174.
- Miller, S. L., K. Leiserson and W. W. Nazaroff, "Nonlinear Least-Squares Minimization Applied to Tracer Gas Decay for Determining Airflow Rates in a Two-Zone Building", *Indoor Air*, Vol. 7, No. 1, 1997, pp. 64-75.
- Mora, L., A. J. Gadgil and E. Wurtz, "Comparing zonal and CFD model predictions of isothermal indoor airflows to experimental data", *Indoor Air*, Vol. 13, No. 2, 2003, pp. 77-85.
- Murakami, S. and S. Kato, "Numerical and experimental study on room airflow - 3-D predictions using the $k-\epsilon$ turbulence model", *Building and Environment*, Vol. 24, No. 1, 1989, pp. 85-97.
- Walton, G. N., *AIRNET - A Computer Program for Building Airflow Network Modeling*, National Institute of Standards and Technology, 1989, Gaithersburg, MD.
- Walton, G. N. and W. S. Dols, *CONTAM 2.4 User Guide and Program Documentation*, National Institute of Standards and Technology, 2005, Gaithersburg, MD.
- Wang, A., Y. Zhang, J. L. Topmiller, J. S. Bennett and K. H. Dunn, "Tracer study of airborne disease transmission in an aircraft cabin mock-up", *ASHRAE Transactions*, Vol. 112, No. 2, 2006, pp. 697-705.
- Zhai, Z., J. Srebric and Q. Chen, "Application of CFD to Predict and Control Chemical and Biological Agent Dispersion in Buildings", *International Journal of Ventilation*, Vol. 2, No. 3, 2003, pp. 251-264.
- Zhang, T. F. and Q. Chen, "Identification of contaminant sources in enclosed environments by inverse CFD modeling", *Indoor Air*, Vol. 17, No. 3, 2007, pp. 167-177.

APPENDIX D Detailed RSS values for airflow estimates in Chapter 3

Table D-1. Summary of RSS values from use of invSVD0, invSVD1, and invC models to inversely estimate airflow for Zone A

Pole configuration	Skewness			Model with lowest RSS	% diff between invSVD models	% diff between invSVD1 and invC
	invSVD0	invSVD1	invC			
0 (base case)	1.430	1.413	1.268			
1	0.016	0.009	0.159	invSVD1	<5%	
2	0.077	0.065	0.147	invSVD1	70%	
3	0.741	0.731	0.831	invSVD1	19%	
4	0.268	0.262	0.322	invSVD1	<5%	
5	0.319	0.307	0.322	invSVD1	<5%	
6	1.104	1.094	1.066	invC	<1%	<5%
7	1.069	1.055	1.016	invC	<5%	<5%
8	1.376	1.357	1.246	invC	<5%	<10%
9	1.104	1.090	1.050	invC	<5%	<5%
10	1.136	1.119	1.076	invC	<5%	<5%
11	1.178	1.159	1.066	invC	<5%	<10%
12	1.320	1.304	1.195	invC	<5%	<10%
13	0.854	0.832	1.193	invSVD1	<5%	
14	0.939	0.924	1.098	invSVD1	<5%	
15	1.251	1.228	1.369	invSVD1	<5%	
16	1.020	0.994	0.965	invC	<5%	<5%
17	1.049	1.030	1.045	invSVD1	<5%	
18	1.341	1.318	1.181	invC	<5%	12%

Table D-2. Summary of RSS values from use of invSVD0, invSVD1, and invC models to inversely estimate airflow for Zone B

Pole configuration	Skewness			Model with lowest RSS	% diff between invSVD models	% diff between invSVD1 and invC
	invSVD0	invSVD1	invC			
0 (base case)	2.821	2.800	2.747			
1	3.157	3.140	4.334	invSVD1	<1%	
2	2.382	2.395	1.293	invC	<1%	85%
3	2.004	1.996	3.717	invSVD1	<1%	
4	2.082	2.065	2.991	invSVD1	<1%	
5	1.877	1.850	1.385	invC	<5%	34%
6	2.082	2.535	3.251	invSVD0	22%	
7	2.173	2.162	1.681	invC	<1%	29%
8	1.810	1.798	1.008	invC	<1%	78%
9	2.620	2.598	3.071	invSVD1	<1%	
10	2.388	2.370	2.667	invSVD1	<1%	
11	2.633	2.612	2.616	invSVD1	<1%	
12	2.706	2.686	2.667	invC	<1%	<1%
13	2.007	1.987	1.722	invC	<5%	15%
14	1.875	1.857	1.523	invC	<5%	22%
15	2.724	2.701	2.817	invSVD1	<1%	
16	2.644	2.613	3.044	invSVD1	<5%	
17	2.756	2.732	2.982	invSVD1	<1%	
18	2.753	2.722	2.916	invSVD1	<5%	

Table D-3. Summary of RSS values from use of invSVD0, invSVD1, and invC models to inversely estimate airflow for Zone C

Pole configuration	Skewness			Model with lowest RSS	% diff between invSVD models	% diff between invSVD1 and invC
	invSVD0	invSVD1	invC			
0 (base case)	1.037	1.022	0.977			
1	0.699	0.681	1.587	invSVD1	<5%	
2	0.589	0.592	0.467	invC	<1%	27%
3	0.866	0.811	2.050	invSVD1	7%	
4	0.547	0.530	1.823	invSVD1	<5%	
5	0.563	0.552	0.697	invSVD1	<5%	
6	0.868	0.818	1.674	invSVD1	6%	
7	1.040	1.020	1.261	invSVD1	<5%	
8	1.039	1.024	1.092	invSVD1	<5%	
9	1.034	1.015	1.240	invSVD1	<5%	
10	0.997	0.980	0.975	invC	<5%	<1%
11	0.993	0.979	0.866	invC	<5%	13%
12	1.018	1.001	1.058	invSVD1	<5%	
13	0.887	0.868	1.225	invSVD1	<5%	
14	0.877	0.865	0.978	invSVD1	<5%	
15	1.063	1.036	1.116	invSVD1	<5%	
16	0.830	0.809	1.457	invSVD1	<5%	
17	0.894	0.878	0.818	invC	<5%	7%
18	0.884	0.865	1.430	invSVD1	<5%	

APPENDIX E Matlab codes for Chapter 4

Matlab code for sensor models

```

conc_err = zeros(nzones,1);
c_out = 0;
c_supply = 0;

if sens_error == 0
    filter_conc_kp = conc_kp;
    filter_c_out = c0;
    filter_c_supply = cs;
elseif sens_error == 1 (precision error) | sens_error == 2 (precision error & bias)
    if sens_error == 2
% used only once to get bias errors, subsequent runs, use file
%     bias_error_z = ((ae + (be-ae)*rand(nzones,1)));
%     bias_error_o = ((ae + (be-ae)*rand(1,1)));
%     bias_error_s = ((ae + (be-ae)*rand(1,1)));
        bias_error_z = csvread(['bias_error_z(' num2str(nzones) ').txt']);
        bias_error_o = csvread(['bias_error_o(' num2str(nzones) ').txt']);
        bias_error_s = csvread(['bias_error_s(' num2str(nzones) ').txt']);
    end
    for i = 1:size(conc_kp,2)
        if sens_error == 1
            conc_err(:,i) = conc_kp(:,i).*(1-(ae + (be-ae)*rand(nzones,1)));
            c_out(1,i) = c0(1,i).*(1-(ae + (be-ae)*rand(1,1)));
            c_supply(1,i) = cs(1,i).*(1-(ae + (be-ae)*rand(1,1)));
        elseif sens_error == 2
            conc_err(:,i) = conc_kp(:,i).*(1-sqrt(((ae + (be-ae)*rand(nzones,1)).^2+bias_error_z.^2)));
            c_out(1,i) = c0(1,i).*(1-sqrt(((ae + (be-ae)*rand(1,1)).^2+bias_error_o.^2)));
            c_supply(1,i) = cs(1,i).*(1-sqrt(((ae + (be-ae)*rand(1,1)).^2+bias_error_s.^2)));
        end
    end
    end
    filter_conc_kp = zeros(size(conc_err,1),size(conc_err,2));
    filter_c_out = zeros(size(c_out,1),size(c_out,2));
    filter_c_supply = zeros(size(c_supply,1),size(c_supply,2));
    if trans == 1
        windowSize = 6;
        for jk = 1:nzones
            filter_conc_kp(jk,:) = filter(ones(1,windowSize)/windowSize,1,conc_err(jk,:));
        end
        filter_c_out(1,:) = filter(ones(1,windowSize)/windowSize,1,c_out);
        filter_c_supply(1,:) = filter(ones(1,windowSize)/windowSize,1,c_supply);

        filter_conc_kp = filter_conc_kp(:,windowSize+1:end);
        filter_c_out = filter_c_out(1,windowSize+1:end);
        filter_c_supply = filter_c_supply(1,windowSize+1:end);
    elseif trans == 0
        filter_conc_kp = conc_err;
        filter_c_out = c_out;
        filter_c_supply = c_supply;
    end
end

if trans == 0
    filter_conc_kp = filter_conc_kp(:,1:timetime);
    filter_c_out = filter_c_out(:,1:timetime);
    filter_c_supply = filter_c_supply(:,1:timetime);
end
end

```


Matlab code for LSQ inverse model

```

global volumes q_act dt occup_kp diff_method v filter_conc_kp filter_c_out
filter_c_supply nzones AHS_supply sens_error model nparam err timetime

conc_used = filter_conc_kp;
c0_used = filter_c_out;
cs_used = filter_c_supply;

% do not alter
if nzones == 3
    A = sign(c_c(1:nzones,:));
    B = zeros(nzones,1);

    A = [A;ones(1,nzones)*-1 repmat([1 zeros(1,nzones-1)],1,nzones) zeros(1,nzones*2) -1
1;...
        zeros(1,nparam-nzones*2) ones(1,nzones)*-1 ones(1,nzones) 1 -1];
    B = [B;0;0];

    if trans == 1
        % write two more equations since 100% OA system
        A = [A;zeros(1,nparam-nzones*2) ones(1,nzones) zeros(1,nzones) -1 0;...
            zeros(1,nparam-nzones*2) zeros(1,nzones) ones(1,nzones) 0 -1];
        B = [B;0;0];
    end
end

LHS = [c_c;A];
RHS = [y_c;B];

% equality constraints (known flow rates)
nparam = nparam + 2;

lb = zeros(nparam,1);
ub = repmat(AHS_supply,nparam,1);
options = optimset('MaxIter',10000);

b = zeros(nparam,1);
A_add = zeros(nparam,nparam);
B_add = zeros(nparam,1);
if nzones == 3
    if trans == 0
        ind_knw = [13:16 19:20];
    elseif trans == 1
        ind_knw = [13:16 20];
    end
elseif nzones == 6
    if trans == 0
        ind_knw = [15 21 17 33 18 39 24 40 29 35 30 41 43:49 55:56];
    elseif trans == 1
        ind_knw = [15 21 17 33 18 39 24 40 29 35 30 41 43:49 56];
    end
end
ind_knw = sort(ind_knw);
for i = 1:size(ind_knw,2)
    A_add(ind_knw(i),ind_knw(i)) = 1;
    B_add(ind_knw(i),1) = q_act(ind_knw(i));
end
Aeq = A_add;
beq = B_add;
thetahat = lsqlin(LHS,RHS,[],[],Aeq,beq,lb,ub,[],options);

```

Matlab code for RLS inverse model

```

function [thetahat,corr,excited] = myfun_2_rls(thetainit,Pinit,constrained,gamma)
global volumes q_act dt occup_kp diff_method v filter_conc_kp filter_c_out
filter_c_supply nzones AHS_supply sens_error model nparam err occ_error % for other
models to change CONTAM data
% constrained = 0 = unconstrained
% constrained = 1 = linear equalities
% constrained = 2 = linear inequalities
% constrained = 3 = CRI with equality + inequality

P = eye(18)*Pinit;
x = filter_conc_kp;
c0 = filter_c_out;
cs = filter_c_supply;

timetime = 288*3;

thetahat(1:18,1) = thetainit;
if constrained == 0 | constrained == 3
    thetahat(13:16,1) = q_act(13:16,1);
end
nparam = size(thetahat,1);

% linear constraints A*theta = B
% (1) continuity
A = [1 0 0 -1 -1 -1 0 1 0 0 1 0 1 0 0 -1 0 0 ;...
     0 1 0 0 1 0 -1 -1 -1 0 0 1 0 1 0 0 -1 0 ;...
     0 0 1 0 0 1 0 0 1 -1 -1 -1 0 0 1 0 0 -1 ];
B = zeros(3,1);
% (2) known values
ind_knw = [13:16];
A_add = zeros(3,nparam);
for i = 1:size(ind_knw,2)
    A_add(i,ind_knw(i)) = 1;
    B_add(i,1) = q_act(ind_knw(i));
end
if constrained == 1
    A = [A;A_add];
    B = [B;B_add];
end

P_st = eye(nparam) - A\A;
k = 1;
C(:,k) = [c0(1,k) 0 0 -x(1,k) -x(1,k) -x(1,k) 0 x(2,k) 0 0 x(3,k) 0 cs(1,k) 0 0 -x(1,k)
0 0 ;...
          0 c0(1,k) 0 0 x(1,k) 0 -x(2,k) -x(2,k) -x(2,k) 0 0 x(3,k) 0 cs(1,k) 0 0 -
x(2,k) 0 ;...
          0 0 c0(1,k) 0 0 x(1,k) 0 0 x(2,k) -x(3,k) -x(3,k) -x(3,k) 0 0 cs(1,k) 0 0 -
x(3,k) ];

for i = 2:timetime
    y(:,i) = [(x(:,i)-x(:,i-1))/dt.*v-occup_kp(:,i-1)];
    phi_transp(:,i) = [c0(1,i) 0 0 -x(1,i-1) -x(1,i-1) -x(1,i-1) 0 x(2,i-1) 0 0 x(3,i-1)
0 cs(1,i) 0 0 -x(1,i-1) 0 0;...
                    0 c0(1,i) 0 0 x(1,i-1) 0 -x(2,i-1) -x(2,i-1) -x(2,i-1) 0 0
x(3,i-1) 0 cs(1,i) 0 0 -x(2,i-1) 0;...
                    0 0 c0(1,i) 0 0 x(1,i-1) 0 0 x(2,i-1) -x(3,i-1) -x(3,i-1) -
x(3,i-1) 0 0 cs(1,i) 0 0 -x(3,i-1)];
    phi(:,i) = phi_transp(:,i)';
    K(:,i) = P(:,i-1)*phi(:,i)/[gamma*eye(size(phi_transp,1)) +
phi_transp(:,i)*P(:,i-1)*phi(:,i)];
    corr(:,i) = y(:,i) - phi_transp(:,i)*thetahat(:,i-1);
    excited(:,i) = phi_transp(:,i)*P(:,i-1)*phi(:,i);
    P(:,i) = P(:,i-1)*(eye(nparam)-K(:,i)*phi_transp(:,i))/gamma;
    if min(abs(corr(:,i))) < 1.9e-5
        if constrained == 0 | constrained == 3

```

```

        thetahat(:,i) = thetahat(:,i-1) + K(:,i)*corr(:,i);
elseif constrained == 1
    thetahat(:,i) = A\B + P_st*K(:,i)*[y(:,i) - phi_transp(:,i)*thetahat(:,i-
1)];
end
if constrained == 3
    % equality constraints (continuity)
    P_EC = P(:,i);
    W = inv(A*P_EC*A');
    thetahat_EC(:,i) = thetahat(:,i) - P_EC*A'*W*(A*thetahat(:,i)-B(:,1));
    thetahat_EC(:,i) = thetahat(:,i);
    % inequality constraints (non-negativity)
    H = P_EC - P_EC*A'*W*A*P_EC;
    H_diag = diag(H);
    for ih = 1:nparam
        Hii(ih,1) = 1/H_diag(ih,1);
    end
    D = diag(Hii);
    miu_star_orig = -D*thetahat_EC(:,i);
    miu_star = miu_star_orig;
    for mi = 1:nparam
        if miu_star_orig(mi,1) < 0
            miu_star(mi,1) = 0; % truncate negative values
        end
    end
    thetahat_IC(:,i) = thetahat_EC(:,i) + H*miu_star;
    % enforce inequality constraints, if necessary
    for fi = 1:nparam
        if thetahat_IC(fi,i) < 0
            thetahat_IC(fi,i) = 0; % truncate negative values
        end
    end
    thetahat(:,i) = thetahat_IC(:,i);
end
else
    thetahat(:,i) = thetahat(:,i-1);
    P(:,i) = P(:,i-1);
end
end
end

```

Matlab code for NONLINOPTIM & SDE inverse models

```

function [x,fval,exitflag,output] = runnested(x0,lb,ub)
options = optimset('MaxFunEval',100000,'MaxIter',100000,'TolFun',1e-
8,'FinDiffType','central','Display','iter');

[x,fval,exitflag,output] = fmincon(@myfun_2,x0,[],[],[],[],lb,ub,@confun,options);

function [fval] = myfun_2(x)

global volumes q_act dt occup_kp diff_method v filter_conc_kp filter_c_out
filter_c_supply nzones AHS_supply sens_error model nparam err occ_error% for other models
to change CONTAM data

    conc_used = filter_conc_kp;
    c0_used = filter_c_out;
    cs_used = filter_c_supply;

    timetime = 288*1; % 288*ndays or size(conc_used,2)

    if model == 1 (SDE inverse model) & sens_error == 0
        sigma = sqrt(0.025^2+0.025^2);
    elseif model == 1 (SDE inverse model) & sens_error == 1
        sigma = 0.05;
    elseif model == 1 (SDE inverse model) & sens_error == 2
        sigma = sqrt(0.025^2+0.025^2);
    end

```

```

q_estim = [-x(5)-x(6)-x(4)-x(16) x(8) x(11) x(1) x(13);...
           x(5) -x(8)-x(9)-x(7)-x(17) x(12) x(2) x(14);...
           x(6) x(9) -x(11)-x(12)-x(10)-x(18) x(3) x(15)];
toler = 0.05;
wts = [1;1;1]; % weighting

c_model(:,1) = conc_used(:,1);
conc(:,1) = [c_model(:,1);c0_used(1,1);cs_used(1,1)];
for ic = 2:timetime
    if model == 1 (SDE inverse model)
        dW(:,ic) = 0 + sqrt(dt)*randn(3,1);
        rand_error(:,ic) = volumes*(q_estim*conc(:,ic-1)*sigma).*dW(:,ic);
        if occ_error == 0
            c_model(:,ic) = c_model(:,ic-1) + volumes*(q_estim*conc(:,ic-1)+occup_kp(:,ic-1))*dt+rand_error(:,ic);
        elseif occ_error == 1
            end
        elseif model == 3 (NONLINOPTIM inverse model)
            c_model(:,ic) = c_model(:,ic-1) + volumes*(q_estim*conc(:,ic-1)+occup_kp(:,ic-1))*dt;
        end
        for jc = 1:size(c_model,1)
            if c_model(jc,ic) < 0
                c_model(jc,ic) = 0;
            end
        end
        conc(:,ic) = [c_model(:,ic);c0_used(1,ic);cs_used(1,ic)];
        c_act(:,ic) = conc_used(:,ic);
        error(:,ic) = wts.*(c_model(:,ic) - c_act(:,ic)).^2;
    end
    ic;
    fval = sum(sum(error));

function [c, ceq] = confun(x)
global q_act nzones
% Nonlinear inequality constraints
c = [];
% Nonlinear equality constraints
if nzones == 3
    ceq = [x(13)-q_act(13);x(14)-q_act(14);x(15)-q_act(15);x(16)-q_act(16);...
           x(8)+x(11)+x(1)+x(13)-x(5)-x(6)-x(4)-x(16);...
           x(5)+x(12)+x(2)+x(14)-x(8)-x(9)-x(7)-x(17);...
           x(6)+x(9)+x(3)+x(15)-x(11)-x(12)-x(10)-x(18)];
end

```

**APPENDIX F Detailed reports of building airflow network estimates for
transient test case for Chapter 4**

**Table F-1. Estimated building airflow network using synthetic perfect CO₂
measurements (transient, LSQ model).**

	Synthetic airflow rate, m ³ /h (cfm)	Estimated airflow rate, m ³ /h (cfm)	Percentage error in Q
Q _{0A}	0	0	0%
Q _{A0}	151 (89)	160 (94)	6%
Q _{0B}	0	0	0%
Q _{B0}	144 (85)	0	100%
Q _{0C}	0	0	0%
Q _{C0}	130 (76)	266 (156)	104%
Q _{AB}	71 (42)	67 (39)	6%
Q _{BA}	0	0	0%
Q _{AC}	0	0	0%
Q _{CA}	222 (130)	226 (133)	2%
Q _{BC}	0	24 (14)	100%
Q _{CB}	0	1 (1)	100%
Q _{RB}	178 (104)	293 (172)	64%
Q _{RC}	822 (482)	708 (415)	14%
ΣQ _{jA}	222 (130)	226 (133)	2%
ΣQ _{Aj}	222 (130)	227 (133)	2%
ΣQ _{jB}	321 (188)	317 (186)	1%
ΣQ _{Bj}	322 (189)	317 (186)	2%
ΣQ _{jC}	1176 (689)	1201 (704)	2%
ΣQ _{Cl}	1175 (688)	1201 (704)	2%

Table F-2. Estimated building airflow network using 1,000 sets of synthetic imperfect CO₂ measurements with precision error only (transient, LSQ model).

	Synthetic airflow rate, m ³ /h (cfm)	Estimated airflow rate, m ³ /h (cfm)		Synthetic value within estimated range? (If N, percentage difference)
		Min	Max	
Q _{0A}	0	0	0	Y
Q _{A0}	151 (89)	177 (104)	208 (122)	N (17-37%)
Q _{0B}	0	0	4 (2)	Y
Q _{B0}	144 (85)	45 (27)	269 (157)	Y
Q _{0C}	0	0	9 (5)	Y
Q _{C0}	130 (76)	0	190 (111)	Y
Q _{AB}	71 (42)	3 (2)	21 (12)	N (71-95%)
Q _{BA}	0	0	2 (1)	Y
Q _{AC}	0	0	0	Y
Q _{CA}	222 (130)	192 (112)	216 (127)	N (3-14%)
Q _{BC}	0	0	10 (6)	Y
Q _{CB}	0	0	2 (1)	Y
Q _{RB}	178 (104)	0	216 (127)	Y
Q _{RC}	822 (482)	784 (459)	1011 (592)	Y
ΣQ _{jA}	222 (130)	192 (112)	219 (128)	N (2-14%)
ΣQ _{Aj}	222 (130)	180 (105)	228 (134)	Y
ΣQ _{jB}	321 (188)	253 (148)	276 (162)	N (14-21%)
ΣQ _{Bj}	322 (189)	45 (27)	497 (291)	Y
ΣQ _{jC}	1176 (689)	1176 (689)	1195 (700)	Y
ΣQ _{Cj}	1175 (688)	976 (572)	1419 (832)	Y

Table F-3. Estimated building airflow network using 1 set of synthetic imperfect CO₂ measurements with precision error only (transient, LSQ model).

	Synthetic airflow rate, m ³ /h (cfm)	Estimated airflow rate, m ³ /h (cfm)	Percentage error in Q
Q _{0A}	0	0	0%
Q _{A0}	151 (89)	197 (115)	30%
Q _{0B}	0	0	0%
Q _{B0}	144 (85)	0	100%
Q _{0C}	0	0	0%
Q _{C0}	130 (76)	230 (135)	77%
Q _{AB}	71 (42)	9 (5)	88%
Q _{BA}	0	0	0%
Q _{AC}	0	0	0%
Q _{CA}	222 (130)	205 (120)	8%
Q _{BC}	0	22 (13)	100%
Q _{CB}	0	0	0%
Q _{RB}	178 (104)	237 (139)	33%
Q _{RC}	822 (482)	763 (447)	7%
ΣQ _{jA}	222 (130)	205 (120)	8%
ΣQ _{Aj}	222 (130)	205 (120)	8%
ΣQ _{jB}	321 (188)	258 (151)	19%
ΣQ _{Bj}	322 (189)	259 (152)	20%
ΣQ _{jC}	1176 (689)	1198 (702)	2%
ΣQ _{Cj}	1175 (688)	1198 (702)	2%

Table F-4. Estimated building airflow network using 1,000 sets of synthetic imperfect CO₂ measurements with precision error & bias (transient, LSQ model).

	Synthetic airflow rate, m ³ /h (cfm)	Estimated airflow rate, m ³ /h (cfm)		Synthetic value within estimated range? (If N, percentage difference)
		Min	Max	
Q _{0A}	0	0	0	Y
Q _{A0}	151 (89)	196 (115)	202 (119)	N (29-34%)
Q _{0B}	0	2 (1)	4 (3)	N (100%)
Q _{B0}	144 (85)	127 (74)	324 (190)	Y
Q _{0C}	0	35 (20)	41 (24)	N (100%)
Q _{C0}	130 (76)	0	141 (83)	Y
Q _{AB}	71 (42)	23 (13)	26 (15)	N (63-68%)
Q _{BA}	0	0	0	Y
Q _{AC}	0	0	0	Y
Q _{CA}	222 (130)	221 (130)	226 (132)	Y
Q _{BC}	0	0	0	Y
Q _{CB}	0	0	0	Y
Q _{RB}	178 (104)	0	150 (88)	N (15-100%)
Q _{RC}	822 (482)	850 (498)	1047 (613)	N (3-27%)
ΣQ _{jA}	222 (130)	221 (130)	226 (132)	Y
ΣQ _{Aj}	222 (130)	219 (128)	229 (134)	Y
ΣQ _{jB}	321 (188)	275 (161)	280 (164)	N (13-14%)
ΣQ _{Bj}	322 (189)	127 (74)	474 (278)	Y
ΣQ _{jC}	1176 (689)	1211 (710)	1218 (714)	N (3-4%)
ΣQ _{Cj}	1175 (688)	1071 (628)	1414 (828)	Y

Table F-5. Estimated building airflow network using 1 set of synthetic imperfect CO₂ measurements with precision error & bias (transient, LSQ model).

	Synthetic airflow rate, m ³ /h (cfm)	Estimated airflow rate, m ³ /h (cfm)	Percentage error in Q
Q _{0A}	0	0	0%
Q _{A0}	151 (89)	197 (116)	30%
Q _{0B}	0	3 (1)	100%
Q _{B0}	144 (85)	275 (161)	91%
Q _{0C}	0	45 (26)	100%
Q _{C0}	130 (76)	0	100%
Q _{AB}	71 (42)	28 (16)	60%
Q _{BA}	0	0	0%
Q _{AC}	0	0	0%
Q _{CA}	222 (130)	225 (132)	1%
Q _{BC}	0	0	0%
Q _{CB}	0	0	0%
Q _{RB}	178 (104)	5 (3)	97%
Q _{RC}	822 (482)	996 (584)	21%
ΣQ _{jA}	222 (130)	225 (132)	1%
ΣQ _{Aj}	222 (130)	225 (132)	1%
ΣQ _{jB}	321 (188)	280 (164)	13%
ΣQ _{Bj}	322 (189)	280 (164)	13%
ΣQ _{jC}	1176 (689)	1211 (716)	4%
ΣQ _{Cj}	1175 (688)	1211 (716)	4%

Table F-6. Estimated building airflow network using synthetic perfect CO₂ measurements (transient, NONLINOPTIM model).

	Synthetic airflow rate, m ³ /h (cfm)	Estimated airflow rate, m ³ /h (cfm)	Percentage error in Q
Q _{0A}	0	0	0%
Q _{A0}	151 (89)	210 (123)	38%
Q _{0B}	0	0	0%
Q _{B0}	144 (85)	217 (127)	51%
Q _{0C}	0	0	0%
Q _{C0}	130 (76)	391 (229)	201%
Q _{AB}	71 (42)	33 (19)	53%
Q _{BA}	0	40 (24)	100%
Q _{AC}	0	0	0%
Q _{CA}	222 (130)	202 (119)	9%
Q _{BC}	0	0	0%
Q _{CB}	0	193 (113)	100%
Q _{RB}	178 (104)	217 (127)	22%
Q _{RC}	822 (482)	391 (229)	52%
ΣQ _{iA}	222 (130)	243 (142)	9%
ΣQ _{Aj}	222 (130)	243 (142)	9%
ΣQ _{jB}	321 (188)	475 (278)	48%
ΣQ _{Bj}	322 (189)	475 (278)	47%
ΣQ _{jC}	1176 (689)	1176 (689)	0%
ΣQ _{Cl}	1175 (688)	1177 (690)	0%

Table F-7. Estimated building airflow network using 1,000 sets of synthetic imperfect CO₂ measurements with precision error only (transient, NONLINOPTIM model).

	Synthetic airflow rate, m ³ /h (cfm)	Estimated airflow rate, m ³ /h (cfm)		Synthetic value within estimated range? (If N, percentage difference)
		Min	Max	
Q _{0A}	0	0	0	Y
Q _{A0}	151 (89)	209 (123)	209 (123)	N (38%)
Q _{0B}	0	0	0	Y
Q _{B0}	144 (85)	217 (127)	217 (127)	N (51%)
Q _{0C}	0	0	0	Y
Q _{C0}	130 (76)	391 (229)	391 (229)	N (201%)
Q _{AB}	71 (42)	33 (19)	33 (19)	N (53%)
Q _{BA}	0	40 (24)	40 (24)	N (100%)
Q _{AC}	0	0	0	Y
Q _{CA}	222 (130)	202 (119)	202 (119)	N (9%)
Q _{BC}	0	0	0	Y
Q _{CB}	0	192 (113)	192 (113)	N (100%)
Q _{RB}	178 (104)	217 (127)	217 (127)	N (22%)
Q _{RC}	822 (482)	391 (229)	391 (229)	N (52%)
ΣQ _{iA}	222 (130)	243 (142)	243 (142)	N (9%)
ΣQ _{Aj}	222 (130)	243 (142)	243 (142)	N (9%)
ΣQ _{jB}	321 (188)	475 (278)	475 (278)	N (48%)
ΣQ _{Bj}	322 (189)	475 (278)	475 (278)	N (47%)
ΣQ _{jC}	1176 (689)	1176 (689)	1176 (689)	Y
ΣQ _{Cl}	1175 (688)	1176 (689)	1176 (689)	Y

Table F-8. Estimated building airflow network using 1 set of synthetic imperfect CO₂ measurements with precision error only (transient, NONLINOPTIM model).

	Synthetic airflow rate, m ³ /h (cfm)	Estimated airflow rate, m ³ /h (cfm)	Percentage error in Q
Q _{0A}	0	0	0%
Q _{A0}	151 (89)	209 (123)	38%
Q _{0B}	0	0	0%
Q _{B0}	144 (85)	217 (127)	51%
Q _{0C}	0	0	0%
Q _{C0}	130 (76)	391 (229)	201%
Q _{AB}	71 (42)	33 (19)	53%
Q _{BA}	0	40 (24)	100%
Q _{AC}	0	0	0%
Q _{CA}	222 (130)	202 (119)	9%
Q _{BC}	0	0	0%
Q _{CB}	0	192 (113)	100%
Q _{RB}	178 (104)	217 (127)	22%
Q _{RC}	822 (482)	391 (229)	52%
ΣQ _{jA}	222 (130)	243 (142)	9%
ΣQ _{Aj}	222 (130)	243 (142)	9%
ΣQ _{jB}	321 (188)	475 (278)	48%
ΣQ _{Bj}	322 (189)	475 (278)	47%
ΣQ _{jC}	1176 (689)	1176 (689)	0%
ΣQ _{Cj}	1175 (688)	1176 (689)	0%

Table F-9. Estimated building airflow network using 1,000 sets of synthetic imperfect CO₂ measurements with precision error & bias (transient, NONLINOPTIM model).

	Synthetic airflow rate, m ³ /h (cfm)	Estimated airflow rate, m ³ /h (cfm)		Synthetic value within estimated range? (If N, percentage difference)
		Min	Max	
Q _{0A}	0	0	0	Y
Q _{A0}	151 (89)	209 (123)	209 (123)	N (38%)
Q _{0B}	0	0	0	Y
Q _{B0}	144 (85)	217 (127)	217 (127)	N (51%)
Q _{0C}	0	0	0	Y
Q _{C0}	130 (76)	391 (229)	391 (229)	N (201%)
Q _{AB}	71 (42)	33 (19)	33 (19)	N (53%)
Q _{BA}	0	40 (24)	40 (24)	N (100%)
Q _{AC}	0	0	0	Y
Q _{CA}	222 (130)	202 (119)	202 (119)	N (9%)
Q _{BC}	0	0	0	Y
Q _{CB}	0	192 (113)	192 (113)	N (100%)
Q _{RB}	178 (104)	217 (127)	217 (127)	N (22%)
Q _{RC}	822 (482)	391 (229)	391 (229)	N (52%)
ΣQ _{jA}	222 (130)	243 (142)	243 (142)	N (9%)
ΣQ _{Aj}	222 (130)	243 (142)	243 (142)	N (9%)
ΣQ _{jB}	321 (188)	475 (278)	475 (278)	N (48%)
ΣQ _{Bj}	322 (189)	475 (278)	475 (278)	N (47%)
ΣQ _{jC}	1176 (689)	1176 (689)	1176 (689)	Y
ΣQ _{Cj}	1175 (688)	1176 (689)	1176 (689)	Y

Table F-10. Estimated building airflow network using 1 set of synthetic imperfect CO₂ measurements with precision error & bias (transient, NONLINOPTIM model).

	Synthetic airflow rate, m ³ /h (cfm)	Estimated airflow rate, m ³ /h (cfm)	Percentage error in Q
Q _{DA}	0	0	0%
Q _{AD}	151 (89)	209 (123)	38%
Q _{DB}	0	0	0%
Q _{BD}	144 (85)	217 (127)	51%
Q _{DC}	0	0	0%
Q _{CD}	130 (76)	391 (229)	201%
Q _{AB}	71 (42)	33 (19)	53%
Q _{BA}	0	40 (24)	100%
Q _{AC}	0	0	0%
Q _{CA}	222 (130)	202 (119)	9%
Q _{BC}	0	0	0%
Q _{CB}	0	192 (113)	100%
Q _{RB}	178 (104)	217 (127)	22%
Q _{RC}	822 (482)	391 (229)	52%
ΣQ _{jA}	222 (130)	243 (142)	9%
ΣQ _{Aj}	222 (130)	243 (142)	9%
ΣQ _{jB}	321 (188)	475 (278)	48%
ΣQ _{Bj}	322 (189)	475 (278)	47%
ΣQ _{jC}	1176 (689)	1176 (689)	0%
ΣQ _{Cj}	1175 (688)	1176 (689)	0%

Table F-11. Estimated building airflow network using synthetic perfect CO₂ measurements (transient, SDE model).

	Synthetic airflow rate, m ³ /h (cfm)	Estimated airflow rate, m ³ /h (cfm)	Percentage error in Q
Q _{DA}	0	0	0%
Q _{AD}	151 (89)	212 (124)	40%
Q _{DB}	0	0	0%
Q _{BD}	144 (85)	234 (137)	62%
Q _{DC}	0	0	0%
Q _{CD}	130 (76)	366 (215)	182%
Q _{AB}	71 (42)	8 (4)	89%
Q _{BA}	0	30 (17)	100%
Q _{AC}	0	0	0%
Q _{CA}	222 (130)	190 (112)	14%
Q _{BC}	0	0	0%
Q _{CB}	0	243 (142)	100%
Q _{RB}	178 (104)	237 (139)	33%
Q _{RC}	822 (482)	377 (221)	54%
ΣQ _{jA}	222 (130)	220 (129)	1%
ΣQ _{Aj}	222 (130)	220 (129)	1%
ΣQ _{jB}	321 (188)	500 (293)	56%
ΣQ _{Bj}	322 (189)	500 (293)	55%
ΣQ _{jC}	1176 (689)	1176 (689)	0%
ΣQ _{Cj}	1175 (688)	1176 (689)	0%

Table F-12. Estimated building airflow network using synthetic imperfect CO₂ measurements with precision error only (transient, 1,000 iterations of SDE model).

	Synthetic airflow rate, m ³ /h (cfm)	Estimated airflow rate, m ³ /h (cfm)		Synthetic value within estimated range? (If N, percentage difference)
		Min	Max	
Q _{0A}	0	0	0.40 (14)	Y
Q _{A0}	151 (89)	159 (93)	4.46 (157)	N (5-77%)
Q _{0B}	0	0	0.80 (28)	Y
Q _{B0}	144 (85)	157 (92)	4.78 (168)	N (9-99%)
Q _{0C}	0	0	0.60 (21)	Y
Q _{C0}	130 (76)	347 (203)	7.88 (277)	N (167-264%)
Q _{AB}	71 (42)	8 (4)	1.60 (56)	Y
Q _{BA}	0	11 (6)	1.64 (58)	N (100%)
Q _{AC}	0	0	0.61 (22)	Y
Q _{CA}	222 (130)	162 (95)	4.45 (156)	Y
Q _{BC}	0	0	0.70 (24)	Y
Q _{CB}	0	132 (78)	4.12 (145)	N (100%)
Q _{RB}	178 (104)	156 (91)	4.72 (166)	Y
Q _{RC}	822 (482)	340 (199)	7.74 (272)	N (44-59%)
ΣQ _{jA}	222 (130)	173 (101)	6.49 (228)	Y
ΣQ _{Aj}	222 (130)	167 (98)	6.68 (235)	Y
ΣQ _{jB}	321 (188)	390 (228)	10.68 (376)	N (22-100%)
ΣQ _{Bj}	322 (189)	323 (189)	11.84 (416)	Y
ΣQ _{jC}	1176 (689)	1176 (689)	21.52 (757)	Y
ΣQ _{Cj}	1175 (688)	981 (575)	24.18 (850)	Y

Table F-13. Estimated building airflow network using synthetic imperfect CO₂ measurements with precision error only (transient, 1 iteration of SDE model).

	Synthetic airflow rate, m ³ /h (cfm)	Estimated airflow rate, m ³ /h (cfm)	Percentage error in Q
Q _{0A}	0	1 (1)	100%
Q _{A0}	151 (89)	168 (99)	11%
Q _{0B}	0	2 (1)	100%
Q _{B0}	144 (85)	208 (122)	44%
Q _{0C}	0	3 (2)	100%
Q _{C0}	130 (76)	441 (258)	239%
Q _{AB}	71 (42)	8 (4)	89%
Q _{BA}	0	0	0%
Q _{AC}	0	0	0%
Q _{CA}	222 (130)	175 (102)	22%
Q _{BC}	0	0	0%
Q _{CB}	0	120 (70)	100%
Q _{RB}	178 (104)	169 (99)	5%
Q _{RC}	822 (482)	446 (261)	46%
ΣQ _{jA}	222 (130)	176 (103)	21%
ΣQ _{Aj}	222 (130)	176 (103)	21%
ΣQ _{jB}	321 (188)	378 (222)	18%
ΣQ _{Bj}	322 (189)	378 (222)	17%
ΣQ _{jC}	1176 (689)	1180 (692)	0%
ΣQ _{Cj}	1175 (688)	1180 (692)	0%

Table F-14. Estimated building airflow network using synthetic imperfect CO₂ measurements with precision error & bias (transient, 1,000 iterations of SDE model).

	Synthetic airflow rate, m ³ /h (cfm)	Estimated airflow rate, m ³ /h (cfm)		Synthetic value within estimated range? (If N, percentage difference)
		Min	Max	
Q _{0A}	0	0	18 (11)	Y
Q _{A0}	151 (89)	171 (100)	252 (148)	N (13-66%)
Q _{0B}	0	0	37 (22)	Y
Q _{B0}	144 (85)	174 (102)	266 (156)	N (21-84%)
Q _{0C}	0	0	35 (20)	Y
Q _{C0}	130 (76)	354 (207)	455 (267)	N (172-250%)
Q _{AB}	71 (42)	7 (4)	81 (47)	Y
Q _{BA}	0	9 (5)	86 (51)	N (100%)
Q _{AC}	0	0	37 (22)	Y
Q _{CA}	222 (130)	170 (99)	255 (150)	Y
Q _{BC}	0	0	35 (20)	Y
Q _{CB}	0	146 (85)	234 (137)	N (100%)
Q _{RB}	178 (104)	170 (100)	265 (155)	Y
Q _{RC}	822 (482)	349 (205)	458 (268)	N (44-58%)
ΣQ _{jA}	222 (130)	179 (105)	360 (211)	Y
ΣQ _{Aj}	222 (130)	178 (104)	370 (217)	Y
ΣQ _{jB}	321 (188)	405 (236)	602 (353)	N (22-88%)
ΣQ _{Bj}	322 (189)	354 (207)	652 (382)	N (10-102%)
ΣQ _{jC}	1176 (689)	1176 (689)	1283 (752)	Y
ΣQ _{Cj}	1175 (688)	1018 (597)	1403 (822)	Y

Table F-15. Estimated building airflow network using synthetic imperfect CO₂ measurements with precision error & bias (transient, 1 iteration of SDE model).

	Synthetic airflow rate, m ³ /h (cfm)	Estimated airflow rate, m ³ /h (cfm)	Percentage error in Q
Q _{0A}	0	0	0%
Q _{A0}	151 (89)	226 (133)	50%
Q _{0B}	0	0	0%
Q _{B0}	144 (85)	188 (110)	30%
Q _{0C}	0	0	0%
Q _{C0}	130 (76)	373 (219)	187%
Q _{AB}	71 (42)	15 (9)	79%
Q _{BA}	0	10 (6)	100%
Q _{AC}	0	0	0%
Q _{CA}	222 (130)	232 (136)	4%
Q _{BC}	0	2 (1)	100%
Q _{CB}	0	173 (101)	100%
Q _{RB}	178 (104)	238 (139)	34%
Q _{RC}	822 (482)	402 (235)	51%
ΣQ _{jA}	222 (130)	242 (142)	9%
ΣQ _{Aj}	222 (130)	242 (142)	9%
ΣQ _{jB}	321 (188)	437 (256)	36%
ΣQ _{Bj}	322 (189)	438 (257)	36%
ΣQ _{jC}	1176 (689)	1180 (691)	0%
ΣQ _{Cj}	1175 (688)	1180 (691)	0%

APPENDIX G Published portions of Chapter 4
(in proceedings of 1st International High Performance Buildings Conference)

Estimating a Building Airflow Network using CO₂ Measurements from a Distributed Sensor Network

Y. Lisa CHEN^{1*}, Jin WEN²

¹Department of Civil, Architectural, and Environmental Engineering, Drexel University
Philadelphia, PA, USA
215-895-2280 (tel), yhc22@drexel.edu

¹Department of Civil, Architectural, and Environmental Engineering, Drexel University
Philadelphia, PA, USA
215-895-4911 (tel), jinwen@drexel.edu

* Corresponding Author

ABSTRACT

An appropriate estimate of a building airflow network, which consists of infiltration and interzonal airflow, is important when determining indoor air quality, energy use, and for detecting contaminants. The objective of this study was to estimate the airflow network of a commercial building using CO₂ as a tracer. CO₂ is naturally present in the environment and is generated inside buildings by occupants. In Part I of this study, various sets of "perfect" CO₂ measurements were simulated under different occupancy schedules. In Part II of this study, the effect of CO₂ sensor uncertainty on airflow estimation was evaluated. Linear least squares was used in both parts of this study to estimate the building airflow network. This study demonstrated (1) the feasibility of using CO₂ as a tracer to estimate a building airflow network and (2) that a good estimate of the building airflow network can be made even under sensor uncertainty.

1. INTRODUCTION

An appropriate estimate of a building airflow network, which consists of infiltration and interzonal airflow, is important when determining indoor air quality, energy use, and for detecting contaminants. Fan pressurization tests are used to determine the airtightness of a building envelope, which is characteristic of the envelope construction. Tracer gas tests, on the other hand, are used to determine the infiltration through a building envelope under specific outdoor and indoor conditions. Tracer gas tests can also be used to determine interzonal airflows.

ASTM Standard E779 specifies test conditions for blower-door tests and is intended for single-zone buildings or multi-zone buildings that can be considered a single-zone (ASTM, 2003). Canadian Standard CGSB149.15 specifies testing conditions for a fan pressurization test using a building's own air handling system (CGSB, 1999). It has been applied to commercial buildings with limitations (Jeong *et al.*, 2008). Bahnfleth *et al.* (1999) compared these two test standards in two multi-zone, multi-story buildings. The researchers found that neither method was easy to implement. Wind and stack effects were difficult to control in multi-story buildings. Further, the sealing of leakage paths between floors via shaft penetrations was challenging. Therefore, the results of the fan pressurization tests may be inaccurate.

ASTM Standard E741 specifies test conditions for tracer gas tests, as well as how to then determine air exchange rates (ASTM, 2000). Studies in the literature using CO₂ as a tracer have only been performed on single-zone or small multi-zone residences (Aglan, 2003; Lu *et al.*, 2010; Penman, 1980; Penman *et al.*, 1982; Roulet *et al.*, 2002;

Smith, 1988; Yan *et al.*, 2007). Most of these tests determined overall air exchange rates with the outdoors and not the specific airflow rate through the building envelope or between zones (interzonal airflow). In order to estimate interzonal airflow rates, either multiple tracers are needed (Miller *et al.*, 1997) or multiple tracer tests must be performed (Afonso *et al.*, 1986).

1.1 Study Objectives

The objective of this study was to estimate the airflow network of a commercial building using CO₂ as a tracer. It offers several advantages over the traditional blower-door and tracer gas tests just discussed. First, this study presents a method that can be implemented on multi-zone, commercial buildings, which is currently challenging given their size and the complexity of their building airflow network. Second, the method presented is able to determine airflow rates across the building envelope in each zone and also between zones. Third, the use of CO₂ is advantageous as it is a naturally present tracer. CO₂ sensors are readily available and relatively inexpensive compared to the equipment needed to measure a traditional tracer gas such as SF₆. And lastly, the method presented provides a fast estimate of the building airflow network. It requires less time to set-up than a traditional blower-door or tracer gas test and has the potential to determine a building airflow network in real-time.

1.2 Study Applications

This building airflow network estimation method presented in this study has several applications. First, it can be used to determine the building airtightness at specific parts of a building, not just the overall building airtightness. Second, once the building airflow network is estimated, it can be used to provide a quick estimate of the dispersion of other unmeasured contaminants. Third, an understanding of the building airflow network can provide insight into the pressure distribution of a building. This information is critical in spaces such as laboratories and hospitals. Lastly, it can be used for building commissioning.

2. STUDY METHODS

In Part I of this study, various sets of "perfect" CO₂ measurements were simulated under different occupancy schedules. In Part II of this study, the effect of CO₂ sensor uncertainty on airflow estimation was evaluated. Linear least squares was used in both parts of this study to estimate the building airflow network.

2.1 Synthetic Test Building

In lieu of experimental data, a three-zone commercial building was modeled in CONTAM (Walton *et al.*, 2005). Figure 1 shows the location of Zones A (common area), B (office), and C (conference room), along with their respective volumes. The exterior wall is modeled as brick veneer with a leakage property of 1.14 cm²/m². The interior walls are modeled with leakage of 1.12 cm²/m². The inoperable closed windows are modeled with leakage 0.86 cm²/m of sash. The interior open doors are modeled as 2.1 m² openings. One-way flow through each of these leakage paths is governed by a power-law equation of the form $F = K(\Delta P)^n$, where F is the airflow rate (kg/s), ΔP is the pressure difference calculated by CONTAM (Pa), and K and n are empirical constants. In this study, $K=1$ and $n=0.65$ for all of the leakage paths. The leakage properties of each leakage path, along with air density, are then used to convert F (kg/s) to Q (m³/s).

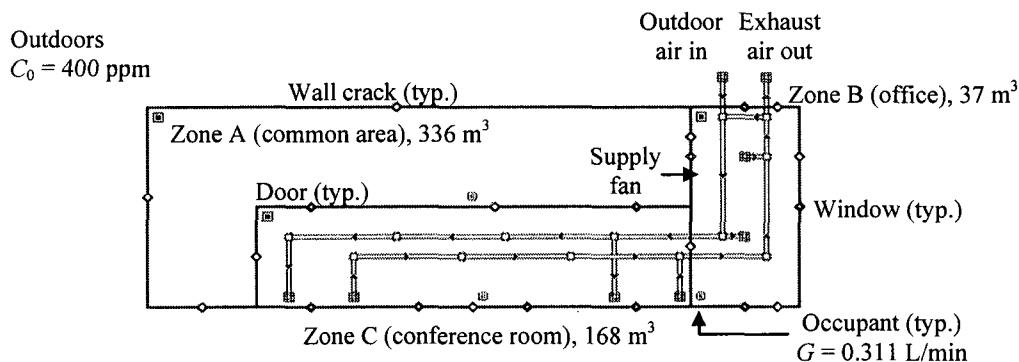


Figure 1: CONTAM model of three-zone test building.

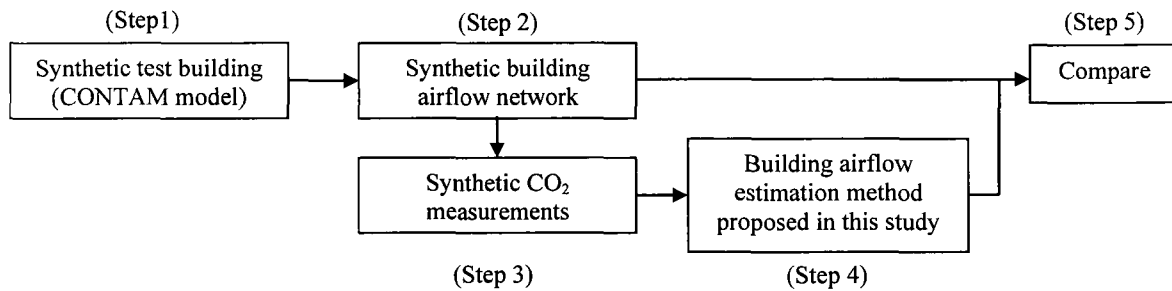


Figure 2: Flow diagram of study process.

A recirculation ventilation system was modeled with 20% outdoor air. The location of the outdoor air intake and total exhaust are shown in Figure 1. The supply fan delivers 4 m³/h (145 cfm) to Zone B and 20 m³/h (690 cfm) to Zone C, which are approximately 7 air changes per hour (ACH). Because Zone A was not mechanically ventilated and has a relatively large volume, the whole building air exchange rate is about 1 ACH. The figure shows the location of ductwork, diffusers, and exhausts. CO₂ is present in the outdoors (Zone 0) with a constant concentration of 400 ppm (DOC, 2010). CO₂ is generated by occupants in each zone at a rate of $G = 0.311$ L/min (ASHRAE, 1990).

Figure 2 summarizes the study process. In lieu of experimental data, the first step was to generate synthetic CO₂ measurements using CONTAM (Step 1). CONTAM first determines the pressure distribution. It then utilizes nonlinear pressure relationships, such as power-law equations, to determine the airflow rate through each leakage path and ductwork (Step 2). This synthetic building airflow network is then used to calculate synthetic CO₂ measurements (Step 3). This study then utilized linear least squares to back-estimate the building airflow network in Step 4 using the synthetic CO₂ measurements provided by CONTAM in Step 3. Lastly, the estimated building airflow network from Step 4 is compared to the one that actually generated the synthetic CO₂ measurements (CONTAM model, Step 2). Keep in mind that CONTAM utilizes nonlinear relationships between pressure and airflow to calculate airflow, whereas in this study, linear relationships between contaminant concentration and airflows were utilized to back-calculate airflow.

2.2 Building Airflow Network

The building airflow network can be estimated using the general contaminant mass balance equation is given in Equation (1). For this study, synthetic steady-state CO₂ measurements are available from CONTAM. Therefore, the left hand side of Equation (1) is zero. The use of transient measurements is saved for future work.

$$V_i \frac{dC_i}{dt} = 0 = \sum_{j \neq i} Q_{ji} C_j - \sum_{j \neq i} Q_{ij} C_i + \sum G_i \quad (1)$$

Q_{ji} is the airflow rate from zone j to zone i (m³/s), Q_{ij} is the airflow rate from zone i to zone j (m³/s), C_j is the CO₂ concentration in zone j (kg/m³), C_i is the CO₂ concentration in zone i (kg/m³), and $\sum G_i$ is the total CO₂ generated in zone i (kg/s). Thus, for N zones, the system of contaminant mass balance equations can be written as:

$$-\mathbf{G} = \mathbf{Q}\mathbf{C} \quad (2)$$

where \mathbf{Q} are the parameters to be estimated (building airflow network), \mathbf{C} are the CO₂ concentrations in each of the N zones, the supply concentration, C_s , and the ambient concentration, C_0 . \mathbf{B} are sources of CO₂ in each of the N zones. Equation (2) can be expanded as:

$$-\begin{bmatrix} \sum G_1 \\ \sum G_2 \\ \dots \\ \sum G_N \end{bmatrix} = \begin{bmatrix} -\sum_j Q_{1-j} & Q_{2-1} & \dots & Q_{N-1} \\ Q_{1-2} & -\sum_j Q_{2-j} & & Q_{N-2} \\ \dots & \dots & \dots & \dots \\ Q_{1-N} & Q_{2-N} & \dots & -\sum_j Q_{N-j} \end{bmatrix} \begin{bmatrix} C_1 \\ C_2 \\ \dots \\ C_N \\ C_S \\ C_0 \end{bmatrix} \quad (3)$$

In order to estimate the parameters, \mathbf{Q} , the system of equations should be just- or over-determined. Thus, various occupancy schedules were modeled to generate different sets of CO₂ data. Airflow remained constant. The occupancy schedules modeled are given in Table 1. Thus, as an example, ΣG_A (total CO₂ generated in Zone A) would be 1·0.311 L/min, ΣG_B (total CO₂ generated in Zone B) would be 1·0.311 L/min, and ΣG_C (total CO₂ generated in Zone C) would be 5·0.311 L/min for Test 1. The resulting steady-state CO₂ concentrations are given in Table 2. In Tests 1-6, Zone A had the highest steady-state CO₂ concentration, even though it had the same occupancy as Zone B, because it was not mechanically ventilated. The more total occupants inside the synthetic building, the higher the steady-state CO₂ concentrations were (see Tests 1 and 9).

Table 1: Number of occupants modeled in CONTAM.

	Test 1	Test 2	Test 3	Test 4	Test 5	Test 6	Test 7	Test 8	Test 9
Zone A	1	1	1	1	1	1	1	1	1
Zone B	1	1	1	1	1	1	2	3	4
Zone C	5	4	3	2	1	0	1	2	3
Total	7	6	5	4	3	2	4	6	8

Table 2: Synthetic steady-state CO₂ measurements (ppm) calculated by CONTAM.

	Test 1	Test 2	Test 3	Test 4	Test 5	Test 6	Test 7	Test 8	Test 9
Zone A	786	741	695	650	604	558	627	696	765
Zone B	720	687	653	620	588	554	669	784	900
Zone C	698	653	607	562	516	471	539	608	677
Supply	611	583	555	527	499	471	522	573	625

2.3 Parameter Estimation

The parameters, \mathbf{Q} , were estimated using linear least squares, which minimizes a function, J :

$$J = |\mathbf{Q}\mathbf{C} + \mathbf{G}|^2 \quad (4)$$

which is the absolute difference between the left and right hand side of Equation (2). \mathbf{Q} must: (a) satisfy air mass balance in each zone (incoming air – outgoing air = 0); (b) be non-negative; and (c) satisfy additional known conditions. The additional known conditions were: (c-1) supply airflow rates into Zones B and C were provided, as was the incoming outdoor air and total exhausted airflow rates; and (c-2) since Zone A was not mechanically ventilated, its supply and exhaust airflow rates were zero.

Part I of this study consisted of using "perfect" CO₂ measurements taken directly from the CONTAM model. Thus, Equation (4) was used in parameter estimation. Part II of this study consisted of observing the effects of CO₂ sensor uncertainty on airflow estimation. Therefore, \mathbf{C} in Equation (4) was replaced with $\tilde{\mathbf{C}}$, where $\tilde{\mathbf{C}} = \mathbf{C} \pm \varepsilon$. ε is the sensor uncertainty, which was assumed to be 5% of the "perfect" measurement. A Monte Carlo simulation with 1,000 iterations was employed to observe the effect of CO₂ sensor uncertainty on airflow estimation. For each

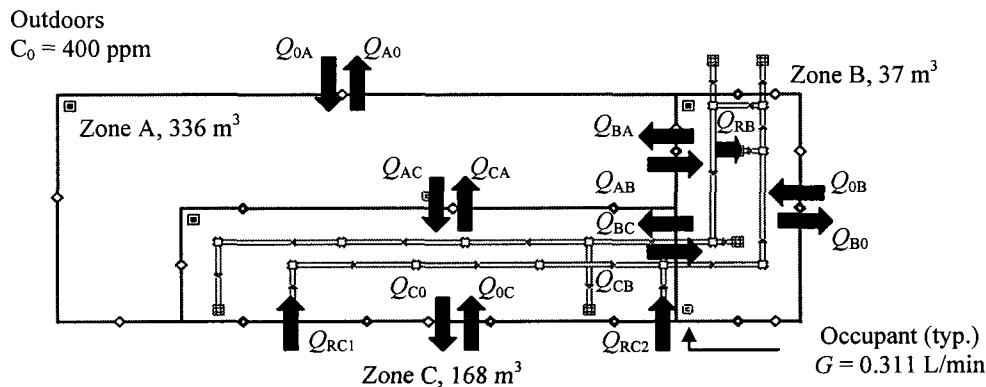


Figure 3: Building model showing parameters (airflow rates) estimated.

iteration, a single error value is sampled to determine \tilde{C} . Thus, at the end of 1,000 iterations, the building airflow network will include mean (μ) and standard deviation values (σ) (reported as min and max values, which are $\mu - \sigma$ and $\mu + \sigma$, respectively). The results of Part I and II are presented in the following section.

3. RESULTS

Figure 3 shows that 14 unknown parameters (airflow rates) were determined. There are two exhausts in Zone C (Q_{RC1} and Q_{RC2}), but only the total exhaust rate, Q_{RC} , was estimated. The airflow rate between two zones, including the outdoors, was the total airflow rate through all of the leakage paths between them. For example, there were two open doors and two interior wall leakage paths between Zones A and C. However, the airflow rate that was estimated between them was represented only by Q_{AC} or Q_{CA} . Each of the leakage paths in CONTAM was modeled as one-way flow, and each parameter must be non-negative (an imposed constraint). Therefore, only one of each pair of airflows between two zones will have a non-negative value. For example, between Zones A and C, either Q_{AC} or Q_{CA} will be non-negative and the other zero. In real buildings, two-way flow in leakage paths may exist between two zones. This situation is saved for future work.

3.1 Part I: Parameter Estimation using Perfect Sensor Measurements

Table 3 shows that airflow estimates from parameter estimation are mostly in good agreement with the synthetic values from CONTAM. The airflow estimates met all of the required constraints. Specifically, they (a) satisfied air mass balance in each zone (last six rows of Table 3), (b) were all non-negative, and (c) only one of each pair of airflows between two zones had a non-negative value.

The mean absolute difference in estimated airflows was $0.50 \text{ m}^3/\text{h}$ (17 cfm), which is < 1 ACH difference in any zone. The largest percentage difference in estimated airflows was for Q_{CO} (100%), Q_{BO} (81%), and Q_{RB} (48%). Though these differences were considerable, steady-state CO_2 concentrations calculated using the estimated airflows differed $< 1\%$ with those calculated by the CONTAM model. Thus, even relatively large differences in the estimation of the building airflow network resulted in small, if not negligible, differences in the calculation (or prediction) of contaminant concentration. Therefore, it could be concluded that CO_2 can be used as a tracer to estimate a building airflow network when steady-state measurements are available. A similar estimation procedure using transient CO_2 measurements is saved for future work.

3.2 Part II: Parameter Estimation using Sensor Measurements with Uncertainty

Table 4 shows the airflow estimates from parameter estimation using sensor measurements with uncertainty. Instead of a single value for each airflow estimate, the min and max values are given. The last column of Table 4 indicates whether or not the synthetic airflow from CONTAM fell within the range of the estimated airflows. For most of the

Table 3: Results of parameter estimation using perfect sensor measurements.

	Synthetic airflow from CONTAM, m ³ /h (cfm)	Airflow from parameter estimation, m ³ /h (cfm)	Percentage difference (Synthetic – Estimate)/Synthetic × 100
Q_{0A}	0	0	0%
Q_{A0}	2.25 (79)	2.25 (79)	0.11%
Q_{0B}	0	0	0%
Q_{B0}	2.15 (75)	3.88 (137)	80.93%
Q_{0C}	0	0	0%
Q_{C0}	1.73 (61)	0	100%
Q_{AB}	1.62 (57)	1.63 (57)	0.15%
Q_{BA}	0	0	0%
Q_{AC}	0	0	0%
Q_{CA}	3.88 (136)	3.88 (136)	0%
Q_{BC}	0	0	0%
Q_{CB}	0	0	0%
Q_{RB}	3.63 (128)	1.89 (66)	47.89%
Q_{RC}	14.01 (493)	15.74 (554)	12.38%
ΣQ_{jA}	3.88 (136)	3.88 (136)	0%
ΣQ_{Aj}	3.88 (136)	3.88 (136)	0%
ΣQ_{jB}	5.77 (203)	5.77 (203)	0%
ΣQ_{Bj}	5.77 (203)	5.77 (203)	0%
ΣQ_{jC}	19.62 (690)	19.62 (690)	0%
ΣQ_{Cj}	19.62 (690)	19.62 (690)	0%

Table 4: Results of parameter estimation using sensor measurements with uncertainty.

	Synthetic airflow from CONTAM, m ³ /h (cfm)	Range of airflow from parameter estimation, m ³ /h (cfm)		Does synthetic value fall within estimated range? (If N, percentage difference)
		Min	Max	
Q_{0A}	0	0	0.04 (1)	Y
Q_{A0}	2.25 (79)	1.97 (69)	2.41 (85)	Y
Q_{0B}	0	0	0.03 (1)	Y
Q_{B0}	2.15 (75)	2.99 (105)	4.73 (166)	N (39-120%)
Q_{0C}	0	0	0.50 (18)	Y
Q_{C0}	1.73 (61)	0	1.21 (42)	N (30-100%)
Q_{AB}	1.62 (57)	0.98 (35)	2.18 (77)	Y
Q_{BA}	0	0	0	Y
Q_{AC}	0	0	0.27 (9)	Y
Q_{CA}	3.88 (136)	3.29 (116)	4.49 (158)	Y
Q_{BC}	0	0	0.81 (28)	Y
Q_{CB}	0	0	1.09 (38)	Y
Q_{RB}	3.63 (128)	0.68 (24)	3.14 (111)	N (13-81%)
Q_{RC}	14.01 (493)	14.5 (509)	17.0 (596)	N (3-21%)
ΣQ_{jA}	3.88 (136)	3.29 (116)	4.53 (159)	Y
ΣQ_{Aj}	3.88 (136)	2.95 (104)	4.87 (171)	Y
ΣQ_{jB}	5.77 (203)	5.13 (180)	7.45 (262)	Y
ΣQ_{Bj}	5.77 (203)	3.67 (129)	8.68 (305)	Y
ΣQ_{jC}	19.62 (690)	19.62 (690)	21.20 (745)	Y
ΣQ_{Cj}	19.62 (690)	17.78 (625)	23.74 (835)	Y

flows, the synthetic airflow from CONTAM does fell within the range of the estimated airflows. Similar to the airflow estimation results with perfect sensor measurements, the estimated range of airflows for Q_{CO} , Q_{BO} , and Q_{RB} did not cover the synthetic values from CONTAM. Neither was it covered for Q_{RC} , though the difference was smaller than for the other three inconsistent airflows. Overall, the magnitude of percentage difference between the synthetic and estimated airflows using sensor measurements with uncertainty was similar to the differences found when using perfect sensor measurements. Therefore, it could be concluded that sensor error did not greatly affect the accuracy of the building airflow network estimate.

The mean absolute difference in estimated airflows was between 0.54 and 0.76 m³/h (19-21 cfm), which is still < 1 ACH difference in any zone. The largest difference between the steady-state CO₂ concentrations calculated using the estimated airflows and those calculated by the CONTAM model was between 0.4 and 1.1%. This range of error, as a result of using sensor measurements with uncertainty, was very similar to the error as a result of using perfect sensor measurements. Therefore, it could be concluded that sensor error also did not greatly affect the accuracy of the prediction of contaminant concentration.

4. DISCUSSION

Sec. 1.2 indicated four applications for the airflow estimation method presented in this study. First, this study was able to determine the airtightness of each zone, which was nearly identical to the synthetic result calculated by the CONTAM model. Using the estimated airflows, an exfiltration rate of 0.10 ACH existed in Zone B, 0.01 ACH exfiltration in Zone A, and 0 ACH exfiltration in Zone C. The CONTAM model calculated 0.06 ACH exfiltration in Zone B, and 0.01 ACH exfiltration in both Zones A and C. Given that the ventilation supplied 7 ACH to Zones B and C, the differences between the estimated and synthetic exfiltration rates were very small. Therefore, one could reasonably use the results of the estimation method presented in this study to improve the airtightness at specific locations in a building to reduce the amount of energy wasted through infiltration or exfiltration.

Second, this study was able to predict the steady-state CO₂ concentrations within 5% of the synthetic values from CONTAM. Therefore, it could also be reasonably used to predict the transport of other gaseous contaminants. Third, this study was able to determine the pressure distribution inside the synthetic building, which was nearly identical to the synthetic result calculated by the CONTAM model. Using the estimated airflows, it could be concluded that the pressure in Zone C was greater than in Zone A, and the pressure in Zone A was greater than in Zone B. Since it was estimated that there was little to no flow between Zones B and C, one might conclude that the pressures in Zones B and C were equal. However, if that were the case, then the estimate would have shown air from Zone B to Zone A when the opposite was estimated. Therefore, the pressure in Zone B must be the lowest of the three zones and some flow would exist from Zone C to Zone B. Thus, one could reasonably use the results of the estimation method presented in this study to redistribute pressure or select locations for specialized, pressure-sensitive spaces (like in laboratories and hospitals) during a building renovation.

Lastly, the airflow estimation method presented in this study could be used for building commissioning. The airtightness information can be used to help reduce energy waste, the prediction of contaminant dispersion can be used to improve indoor air quality, and the pressure distribution information can be used to verify ventilation performance.

5. CONCLUSIONS

The building airflow network of a synthetic three zone commercial building was estimated using linear least squares with constraints. Steady-state CO₂ measurements were obtained from CONTAM simulations under different occupancy schedules. In Part I of this study, "perfect" steady-state CO₂ measurements were used to estimate the building airflow network. In Part II of this study, the effect of CO₂ sensor uncertainty on the airflow estimate was evaluated. It was found that, no matter without or with sensor uncertainty, steady-state CO₂ measurements were able to be used to obtain a reasonable estimate of the building airflow network compared to the synthetic values from CONTAM. Furthermore, for both parts of this study, even large differences between the synthetic and estimated airflow rates resulted in good prediction of CO₂ concentrations.

6. FUTURE WORK

One area for future work includes utilizing transient CO₂ concentrations to estimate a building airflow network. Recursive least squares (RLS) can be used to estimate airflow based on incoming contaminant data from each zone. RLS offers several advantages over the linear least squares method used in this study. Namely, there is no need for matrix inversion, which is more computationally efficient. To study the effect of sensor uncertainty when utilizing transient CO₂ concentrations, Equation (1) can be rewritten as a stochastic differential equation and then RLS used. Another area for future work includes studying the limitations of the estimation method presented in this study by increasing the number of zones or ACH of the zones. The airflow estimation method presented in this study would also require validation.

REFERENCES

- Afonso, C. F. A., Maldonado, E. A. B. and Skåret, E., 1986, A single tracer-gas method to characterize multi-room air exchanges, *Energy and Buildings*, vol. 9, no. 4: p. 273-280.
- Aglan, H. A., 2003, Predictive model for CO₂ generation and decay in building envelopes, *J.App. Phys.*, vol. 93, no. 2: p. 1287-90.
- ASHRAE, 1990, *ANSI/ASHRAE Standard 62-1989: Ventilation for acceptable indoor air quality*, American Society of Heating, Refrigerating and Air-Conditioning Engineers.
- ASTM, 2000, *ASTM E741 - 00 Standard Test Method for Determining Air Change in a Single Zone by Means of a Tracer Gas Dilution*, American Society for Testing and Materials.
- ASTM, 2003, *ASTM E779 - 03 Standard Test Method for Determining Air Leakage Rate by Fan Pressurization*, American Society of Testing and Materials.
- Bahnfleth, W. P., Yuill, G. K. and Lee, B. W., 1999, Protocol for field testing of tall buildings to determine envelope air leakage rate, *ASHRAE Transactions*, vol. 105, no. 2: p. 27-38.
- CGSB, 1999, *Determination of the Overall Envelope Airtightness of Buildings by the Fan Pressurization Method Using the Building's Air Handling Systems*, Canadian General Standards Board.
- DOC, 2010, Trends in Atmospheric Carbon Dioxide, U. S. Department of Commerce, from <http://www.esrl.noaa.gov/gmd/ccgg/trends/>.
- Jeong, J., Firrantello, J., Bahnfleth, W., Freihaut, J. and Musser, A., 2008, Case studies of building envelope leakage measurement using an air-handler fan pressurisation approach, *Build. Serv. Eng.*, vol. 29, no. 2: p. 137-155.
- Lu, T., Knuutila, A., Viljanen, M. and Lu, X., 2010, A novel methodology for estimating space air change rates and occupant CO₂ generation rates from measurements in mechanically-ventilated buildings, *Build. Environ.*, vol. 45, no. 5: p. 1161-1172.
- Miller, S. L., Leiserson, K. and Nazaroff, W. W., 1997, Nonlinear Least-Squares Minimization Applied to Tracer Gas Decay for Determining Airflow Rates in a Two-Zone Building, *Indoor Air*, vol. 7, no. 1: p. 64-75.
- Penman, J. M., 1980, An experimental determination of ventilation rate in occupied rooms using atmospheric carbon dioxide concentration, *Build. Environ.*, vol. 15, no. 1: p. 45-47.
- Penman, J. M. and Rashid, A. A. M., 1982, Experimental determination of air-flow in a naturally ventilated room using metabolic carbon dioxide, *Build. Environ.*, vol. 17, no. 4: p. 253-256.
- Roulet, C. A. and Foradini, F., 2002, Simple and Cheap Air Change Rate Measurement Using CO₂ Concentration Decays, *Int. J. Vent.*, vol. 1, no. 1: p. 39-44.
- Smith, P. N., 1988, Determination of ventilation rates in occupied buildings from metabolic CO₂ concentrations and production rates, *Build. Environ.*, vol. 23, no. 2: p. 95-102.
- Walton, G. N. and Dols, W. S., 2005, *CONTAM 2.4 User Guide and Program Documentation*, National Institute of Standards and Technology.
- Yan, Y., Zhipeng, B., Chunrong, J., Zhaofeng, W., Wenting, R. and Jingjing, Z., 2007, Measuring air exchanges rates using continuous CO₂ sensors, *Symposium on Air Quality Measurement Methods and Technology 2007, April 30, 2007 - May 3, 2007*, Air and Waste Management Association: p. 101-108.

ACKNOWLEDGEMENT

The authors would like to thank the Koerner Family Foundation for support of this work. Partial support was also provided by the National Science Foundation Graduate Research Fellowship.

VITA

Y. Lisa Chen Ng
ylisachen@gmail.com
<http://www.pages.drexel.edu/~yhcn22/>

Education

Ph.D. Drexel University, Philadelphia, PA 2005-2010
 Civil/Architectural Engineering, July 2010

B.S. Drexel University, Philadelphia, PA 1998-2003
 Architectural Engineering, Magna Cum Laude, June 2003

Fellowships & Awards

- Koerner Family Fellowship 2009-2010
- National Science Foundation Graduate Research Fellow (GRFP) 2006-2009
- Otto Gessner Scholarship 2006
- Kling-Lindquist Engineering Scholarship 2006
- Graduate Assistance in Areas of National Need (GAANN) Fellow 2005

Publications

- Chen, Y. Lisa and Jin Wen (2010). "Comparison of sensor systems designed using multizone, zonal, and CFD data for protection of indoor environments." *Building and Environment*. 45(4): 1061-1071.
- Chen, Y. Lisa and Jin Wen (2009). "Sensor system and inverse model development for indoor air estimation." In *Proceedings of Fifth International Workshop on Advanced Smart Structures and Technology*, Boston, MA, Asian-Pacific Network of Centers for Research in Smart Structure Technology (ANCRiSST), Boston, MA. Jul 29-Aug 1.
- Chen, Y. Lisa and Jin Wen (2008). "Sensor system design for building indoor air protection." *Building and Environment*. 43(7): 1278-1285.
- Chen, Y. Lisa and Jin Wen (2008). "Application of singular value decomposition for estimating indoor airflow." In *Proceedings of Indoor Air 2008*, Copenhagen, Denmark. Aug 17-22.
- Chen, Y. Lisa and Jin Wen (2007). "Application of zonal model on indoor air sensor network design." *Sensors and Smart Structures Technologies for Civil, Mechanical, and Aerospace Systems 2007*, In *Proceedings of the SPIE*, Volume 6529. pp. 652911. San Diego, CA. Mar 18-22.
- Chen, Y. Lisa and Jin Wen (2006). "A Smart Indoor Air Quality Sensor Network – Modeling and Design." In *Proceedings for US-Taiwan Workshop on Smart Structural Technology for Seismic Hazard Mitigation*, Taipei, Taiwan. Oct 12-14.